



DISSERTATION

# Current limiting mechanisms in coated conductors

Ausgeführt zum Zwecke der Erlangung des akademischen Grades einer  
Doktorin der technischen Wissenschaften unter der Leitung von

Privatdoz. Dipl.-Ing. Dr. techn. Michael Eisterer  
E141  
Atominstitut

eingereicht an der Technischen Universität Wien  
Fakultät für Physik

von

Mayraluna Lao, MSc.  
Matrikelnummer: 1228679  
Margaretengürtel 6/19  
1050 Wien, Österreich

Wien, am 22 Februar 2017

This work was supported by



which has received funding from the European Union Seventh Framework Programme [FP7/2007-2013] under grant agreement no. NMP-LA-2012-280432.



## Abstract

The application of high temperature superconductors (HTS) for the generation of high magnetic fields and production of long-length wires for power transmission has now become a technological reality using the second-generation design of HTS wires also known as coated conductors (CCs). At the present, there are already quite a number of CC architectures available and the main challenge is to reduce the cost of production while keeping the superconducting properties optimized in terms of current carrying capacity. The main goal of this thesis is to assess current limiting mechanisms in different CC design.

The two main material aspects that influence the critical current density of CCs are grain boundaries (GB) and microstructural defects. The former can cause detrimental effects to  $J_c$  while the latter can increase  $J_c$  especially at high fields by acting as pinning centers that inhibit motion of flux lines that causes dissipation. In this thesis, it was found that despite successfully confining the GB misorientation angle to a few degrees ( $<10^\circ$ ), the current transport in CCs on rolling assisted biaxially textured (RABiTS) NiW substrate with pulsed laser deposited (PLD)  $\text{YBa}_2\text{Cu}_3\text{O}_{7-x}$  (YBCO) is still strongly influenced by its granular morphology. As confirmed by scanning Hall probe microscopy, the granular texture persists from temperatures of 4 K up to 77 K and applied magnetic fields of up to 5 T. Using local orientation mapping, it was found that the GBs are not the sole component that affects the current. The local degradation of  $J_c$  and the percolative current flow are also influenced by the local misorientation of the YBCO grains, varying porosity of the YBCO layer deposited on top of each NiW grain and grooved GBs due to trenches in the underlying template. Such granular morphology was also found to have drastic effects on the transport property. A peak in the field dependence of  $J_c$  was found to occur within a few Tesla. It depends on temperature and on the direction of the applied magnetic field. Using an existing model for Abrikosov-Josephson vortex lying in the GBs, the peak in  $J_c(B)$ , characterizes a well-defined transition from GB-limited regime, which persists up to fields of 1.5 T at 40 K, to grain-limited regime at high fields. By using chemical solution deposition of YBCO instead of PLD, the granularity was significantly reduced. Adding secondary phases such as  $\text{BaHfO}_3$

---

(BHO) and  $\text{BaYNb}_{0.5}\text{Ta}_{0.5}\text{O}_6$  (BYNTO) in the PLD process also results in a reduction of magnetic granularity opening further improvements in utilizing PLD with RABiTS templates.

The critical current density of CCs with textured buffer layer deposited either by the alternating beam assisted deposition technique (ABAD) or inclined substrate deposition technique (ISD) is found to be limited by vortex pinning. Granularity effects are not observed within the field and temperature range of the investigations.  $J_c$  turns out to have interesting anisotropic behavior at various fields and current orientations in the ISD-MgO buffered CC owing to the tilted crystallographic growth of the  $\text{GdBa}_2\text{Cu}_3\text{O}_{7-x}$  layer. The phenomenon of vortex channeling which was found in the past to be confined to temperatures below 50 K in vicinal YBCO films was observed to persist up to 77 K in the case of ISD-buffered tapes. The formation of BHO and BYNTO nanocolumns in PLD-grown YBCO films on ABAD textured template increases  $J_c$  and lowers the  $J_c$ -anisotropy when the orientation of the applied field is varied with respect to the sample. When the applied magnetic field is parallel to the nanocolumns, the BHO phase causes the highest increase in  $J_c$  of up to three times down to a temperature of 5 K.

The angle-dependence of  $J_c$  and N-value, which characterizes the steepness of the IV-curve, showed direct correlation at 77 K, an inverse correlation at 64 K and a narrow and sharp peak parallel to the  $ab$ -planes appeared in  $N(\phi)$  at 40 K. This behavior is consistent in all the CCs investigated despite the tilted crystallographic axes in ISD-buffered tapes and despite the presence of nanocolumns in the BHO and BYNTO doped samples. These observations are interpreted as manifestation of the kinked vortex state and a quasi lock-in state. Their onsets are the same for all the tapes and are therefore intrinsic to the layered structure of YBCO.

## Kurzfassung

Die Anwendung von Hochtemperatursupraleitern (HTSL) zur Erzeugung hoher Magnetfelder sowie großer Drahtlängen im Bereich der Energieübertragung ist mittlerweile durch die zweite Generation von HTSL-Drähten, den *coated conductors* (CC) oder Bandleitern, zur technologischen Realität geworden. Derzeit sind bereits verschiedene Bauweisen von CC verfügbar und die Herausforderung besteht nun darin, die Herstellungskosten zu reduzieren, aber gleichzeitig die ausgezeichneten supraleitenden Eigenschaften hinsichtlich des Stromtransportes beizubehalten. Das Ziel der vorliegenden Arbeit ist daher die Beurteilung und Abschätzung der stromlimitierenden Mechanismen in unterschiedlichen Ausführungen von CC.

Zu den wichtigsten Materialeigenschaften von CC, welche die kritische Stromdichte  $J_c$  limitieren, zählen Korngrenzen und mikrostrukturelle Defekte. Während sich erstere nachteilig auf  $J_c$  auswirken, können letztere  $J_c$  erhöhen, speziell in höheren Feldern, da Defekte im Kristallgitter als Verankerungszentren wirken und dadurch die Flusslinien an der Bewegung hindern, was zur Dissipation führen würde. Ein Ergebnis dieser Arbeit war, dass der Stromtransport in mittels gepulster Laserabscheidung (*pulsed laser deposition*, PLD)  $\text{YBa}_2\text{Cu}_3\text{O}_{7-x}$  (YBCO) auf biaxial texturierten (RABiTS) NiW-Substraten hergestellten Bandleitern trotz kleiner Korngrenzen-Verkippungswinkel ( $< 10^\circ$ ) stark vom granularen Aufbau beeinflusst wird. Mittels Rasterhallsondenmikroskopie wurde nachgewiesen, dass die granulare Textur bei Temperaturen von 4 K bis 77 K und in Magnetfeldern bis zu 5 T besteht. Elektronenrückstreubeugung (*Electron back scatter diffraction*, EBSD)-Messungen bestätigten, dass die lokale Herabsetzung von  $J_c$  sowie der perkolative Stromfluss durch Fehlorientierung der Körner, variierende Porosität der YBCO-Schicht auf einzelnen NiW-Körnern sowie gestörte Strukturen an den Korngrenzen aufgrund von Unebenheiten des darunter liegenden Templates verursacht werden. Diese granulare Morphologie hat ebenso drastische Auswirkungen auf die Transporteigenschaften. Ein Maximum in der Feldabhängigkeit von  $J_c$  tritt bereits bei wenigen Tesla auf und hängt sowohl der Feldrichtung als auch von der Temperatur ab. Aus einem schon bestehenden Modell für Abrikosov-Josephson-Flusslinien innerhalb einer Korngrenze lässt sich ableiten, dass das Maximum in  $J_c(B)$  einen

wohldefinierten Übergang zwischen einem von Korngrenzen limitierten Regime – bei Feldern bis 1,5 T und Temperaturen von 40 K repräsentiert – hin zu einem vom Korn selbst limitierten Bereich bei hohen Feldern. Bei der Abscheidung von YBCO aus chemischen Lösungen (*chemical solution deposition*, CSD) anstelle von PLD, kann die Granularität signifikant verkleinert werden. Die Hinzugabe sekundärer Phasen, wie BaHfO<sub>3</sub> (BHO) und BaYNb<sub>0.5</sub>Ta<sub>0.5</sub>O<sub>6</sub> (BYNTO) während des PLD-Prozesses resultiert ebenfalls in einer Reduktion der magnetischen Granularität und bietet die Möglichkeit für zukünftige Verbesserungen bei PLD auf RABiTS-Templates.

Die kritische Stromdichte von Bandleitern mit texturierten Pufferschichten, die entweder mittels Abscheidung unter alternierendem Ionenstrahl (*alternating beam assisted deposition*, ABAD) oder Wachstum auf verkippten Substrat (*inclined substrate deposition*, ISD) aufgetragen wurden, wird durch Flussverankerung begrenzt – Granularitätseffekte hingegen wurden in den untersuchten Feld- und Temperaturbereichen nicht beobachtet. Bandleiter mit ISD-MgO-Pufferschicht zeigen auf Grund des verkippten kristallographischen Wachstums der GdBa<sub>2</sub>Cu<sub>3</sub>O<sub>7-x</sub> Schichten für  $J_c$  ein interessantes anisotropes Verhalten bei verschiedenen Feldern und Stromrichtungen. Das Phänomen von Flusswirbelkanälen (*vortex channeling*), das bei YBCO-Filmen bisher nur im Temperaturbereich bis 50 K betrachtet worden ist bestand in ISD-Leitern hingegen bis zu 77 K. Die Ausbildung von stabförmigen BHO- und BYNTO-Nanostrukturen in PLD gewachsenen YBCO-Filmen auf ABAD texturierten Templates führt zu einer Erhöhung von  $J_c$  und einer Verringerung der  $J_c$ -Anisotropie, wenn die Richtung des Magnetfeldes in Bezug auf die Probe variiert. Im Falle eines zu den BHO-Nanostrukturen parallelen Feldes zeigt  $J_c$  eine bis zu dreifache Erhöhung bei Temperaturen bis 5 K hinab.

Die Winkelabhängigkeit von  $J_c$  und die Steilheit der Strom-Spannungskurve zeigen bei 77 K eine direkte Korrelation, bei 64 K hingegen eine indirekte und bei 40 K tritt eine scharfe Spitze auf wenn das Feld parallel zu den *ab*-Ebenen ist. Dieses Verhalten wurde bei allen CC beobachtet, auch bei ISD-Bändern mit verkippten kristallographischen Achsen sowie den BHO- und BYNTO-dotierten Proben. Diese Beobachtungen werden als Manifestation eines geknickten Flusswirbelzustandes (*kinked vortex state*) und beziehungsweise eines quasi-ingerastetenzustandes (*quasi lock-in state*) interpretiert, deren Einsetzen ab einem bestimmten Winkel bei allen Bändern gleich ist und deshalb eine intrinsische Eigenschaft der Schichtstruktur von YBCO darstellt.

# Contents

<b>List of figures</b>	<b>viii</b>
<b>List of tables</b>	<b>xviii</b>
<b>List of abbreviations and symbols</b>	<b>xix</b>
<b>1 Introduction</b>	<b>1</b>
<b>2 Background</b>	<b>5</b>
2.1 The coated conductors . . . . .	5
2.2 REBCO: A layered superconductor . . . . .	6
<b>3 Experimental Details</b>	<b>9</b>
3.1 Sample preparation . . . . .	9
3.1.1 ISD-MgO buffered tape . . . . .	9
3.1.2 PLD-YBCO tapes . . . . .	10
3.1.3 CSD-YBCO tapes . . . . .	12
3.2 Angle-resolved $J_c$ measurements . . . . .	15
3.2.1 Transport $J_c$ . . . . .	15
3.2.2 Magnetic measurement of $J_c$ . . . . .	18
3.3 Scanning Hall probe microscopy . . . . .	19
3.3.1 The cantilever . . . . .	19
3.3.2 SHPM in LN <sub>2</sub> bath . . . . .	20
3.3.3 High-resolution SHPM . . . . .	20
3.3.4 Spatial $J_c$ evaluation . . . . .	21
3.3.5 Application to coated conductors . . . . .	22
3.4 Microstructural analysis . . . . .	27
<b>4 REBCO films with tilted <math>c</math>-axis</b>	<b>29</b>
4.1 Microstructure . . . . .	29
4.1.1 YBCO on miscut SrTiO <sub>3</sub> substrate . . . . .	29
4.1.2 GdBCO on ISD-buffered coated conductor . . . . .	30
4.2 Magnetic field profiles . . . . .	31
4.3 Angular dependence of $J_c$ in longitudinal current direction . . . . .	34
4.3.1 $J_{c,L}$ at maximum Lorentz force . . . . .	34
4.3.2 $J_{c,L}$ at variable Lorentz force . . . . .	37



4.4	Angular dependence of $J_c$ in transverse current direction . . . . .	42
4.4.1	$J_{c,T}$ at maximum Lorentz force . . . . .	42
4.4.2	$J_{c,T}$ at variable Lorentz force . . . . .	44
4.5	Summary . . . . .	51
<b>5</b>	<b>Effects of the granular morphology of coated conductors</b>	<b>53</b>
5.1	PLD-YBCO on metallic substrate . . . . .	53
5.1.1	Microstructure . . . . .	53
5.1.2	Magnetic field profiles . . . . .	55
5.1.3	Spatial dependence of $J_c$ . . . . .	59
5.1.4	Transport $J_c$ . . . . .	66
5.1.5	Magnetic field profiles in the direction of $H_{\text{app}} \parallel ab$ . . . . .	69
5.1.6	Non-monotonic $J_c(B)$ behavior . . . . .	73
5.2	PLD-YBCO with secondary phases . . . . .	82
5.3	CSD-YBCO on RABiTS NiW . . . . .	86
5.3.1	Magnetic field profile . . . . .	86
5.3.2	Transport $J_c$ . . . . .	87
5.4	Summary . . . . .	90
<b>6</b>	<b><math>J_c</math>-enhancement by artificial pinning centers</b>	<b>91</b>
6.1	Pure YBCO on SS . . . . .	91
6.2	YBCO with $\text{BaHfO}_3$ addition . . . . .	95
6.3	YBCO with $\text{Ba}_2\text{YNb}_{0.5}\text{Ta}_{0.5}\text{O}_6$ addition . . . . .	98
6.4	Comparison of the APCs in PLD-YBCO on SS . . . . .	101
6.5	APCs in PLD-YBCO with RABiTS NiW . . . . .	105
6.6	Summary . . . . .	108
<b>7</b>	<b>Conclusions and further work</b>	<b>111</b>
7.1	Conclusions . . . . .	111
7.2	Future outlook . . . . .	113
	<b>Bibliography</b>	<b>115</b>

# List of figures

2.1	Diagram of two main coated conductor architectures [22]. . . . .	5
2.2	Schematic diagram of vortex states as the angle of the applied magnetic field is rotated towards the $ab$ -plane. . . . .	7
2.3	Angle-dependence of $J_c$ measured by B. Roas et al. at different temperatures and applied field [81]. . . . .	8
3.1	Schematic diagram of the ISD setup. . . . .	10
3.2	(a) TEM image of the longitudinal cross-section of GdBCO-ISD showing the buffer layers and the GdBCO layer. (b) Schematic diagram of the GdBCO layer showing the vectors $\hat{n}$ and $\hat{e}_c$ that corresponds to the direction normal to the tape surface and $c$ -axis, respectively and the angle $\theta_v = 24^\circ$ that denotes the tilt of the $c$ -axis with respect to $\hat{n}$ . . . . .	10
3.3	Schematic diagram of the PLD setup [40]. . . . .	11
3.4	Architecture of (a) YBCO on ABAD-YSZ/SS tape and (b) YBCO on RABiTS-Ni-5at%W tape. . . . .	12
3.5	Sketch of the two sample rods used for the angle-resolved transport $J_c$ measurements. (a) Single axis rod and (b) two axis rod. . . . .	16
3.6	(a) SEM image of a laser-structured bridge. (b) Optical image of a chemically etched bridge. . . . .	17
3.7	(a) Typical $V(I)$ curve obtained from the transport measurement. The lines denote different $E_c$ that determines $I_c$ . (b) Logarithmic plot of the $V(I)$ . The slope of the linear fit corresponds to the N-value. . . . .	18
3.8	Schematic diagram of the cantilever holder for the Hall probe. . . . .	19
3.9	The coordinates used for the inversion algorithm. . . . .	21
3.10	(Upper panel) Field profile of a homogenous superconducting film with a constant $J_c$ . (Lower panel) Schematic diagram of the current flow. The angle $\alpha$ is also indicated on both pictures. . . . .	22

3.11	(a) Diagram of the net magnetic field detected by the tilted Hall probe. The tilt is exaggerated for illustration. (b) Calculated field profile with constant $J_c$ including tilts of $3^\circ$ and $20^\circ$ . The inset on the left is the radial field profile and the inset on the right is an enlarged picture of the peak at the center of the sample. . . . .	23
3.12	Experimental data at the remanent state in (a) in $\text{LN}_2$ and at $T = 4$ K. . . . .	24
3.13	(a) Experimental data of the background and field profile at 64 K and 1 T. (b) Field profile data at 4 K and 3 T with a linear background. (c) Field profile after subtraction of the background. . . . .	24
3.14	Remanent field profile (top) and local $J_c$ map (bottom) of a 15-cm coated conductor measured in $\text{LN}_2$ . The areas denoted by the black arrows are macroscopic defects. The scanning parameters are: $s_x = s_y = 200$ $\mu\text{m}$ and $d = 15$ $\mu\text{m}$ . . . . .	25
3.15	Remanent field (top) and $J_c$ (bottom) profiles across half of the width of different YBCO films and tapes with rectangular geometry. The black dashed line denotes the sample edges. . . . .	26
3.16	Field profile (top) and $J_c$ (bottom) of sample YBCO-SS in the remanent state and with $\mu_0 H_{\text{app}} = 1$ T. The measurement was made at 4 K with stepwidths $s_x = s_y = 5$ $\mu\text{m}$ . The black dashed lines denote the sample edges. . . . .	26
3.17	Field dependence of $J_c$ of different YBCO films. The solid lines correspond to $J_c$ evaluated from magnetization loops at 77 K and the symbols were extracted from the local $J_c$ calculated from the Hall maps. . . . .	27
4.1	Annular bright field image of the (a) transverse lamella and (b) longitudinal lamella. Large CuO precipitates are present and the dashed yellow lines indicate the grain boundaries. The inset in (a) is a diffractogram obtained from a HRTEM image of a grain boundary showing a small misorientation of the two neighbouring grains of about $6^\circ$ . . . . .	30
4.2	Schematic diagram of the two bridge-configurations, L-bridge and T-bridge, patterned on the tape. The red arrows show the current directions. . . . .	31

4.3	(a) $J_c$ distribution of the YBCO films on miscut STO at vicinal angles of $5^\circ$ , $10^\circ$ , $15^\circ$ and $25^\circ$ . Some defects are indicated by the black arrows and the direction of the currents, $J_{c,L}$ and $J_{c,T}$ are shown on the film with $\theta_v = 25^\circ$ – the film with largest current anisotropy. (b) SEM images of the surface of the YBCO-mSTO films. (c) Dependence of $J_c$ and $\Gamma$ on the vicinal angle, $\theta_v$ . (d) Schematic diagram of the current flow. (e) Component of $J_c$ parallel to the $c$ -axis.	32
4.4	Remanent field profile (left) and the evaluated spatial- $J_c$ (right) of the unpatterned GdBCO-ISD tape. Notice the slight difference in the value between the transverse and longitudinal currents. The Hall mapping was done in LN <sub>2</sub> bath with a scanning stepwidth of 200 $\mu\text{m}$ and a Hall probe-sample distance of 50 $\mu\text{m}$ .	33
4.5	Schematic diagram of the MLF configuration of the L-bridge. The angle $\phi$ denotes the angle of the applied field from the direction normal to the tape surface, $\hat{n}$ .	34
4.6	(a) $J_c(\phi)$ and (b) N-value at $T = 77$ K and different applied fields for the L-bridge at MLF.	35
4.7	(a) $J_c(\phi)$ at 77 K and low fields. (b) Schematic diagram of $\vec{B}$ and $\vec{F}_L$ that influence the asymmetry and shift of the $ab$ -peak at low fields.	35
4.8	(a) $J_c(\phi)$ and (b) $N(\phi)$ at different temperatures and $\mu_0 H_{\text{app}} = 5$ T.	36
4.9	Geometry of the VLF configuration of the L-bridge.	37
4.10	Angle dependence of $J_{c,L}$ in VLF configurations at 77 K and different applied fields. (a) In-plane measurement obtained at $\theta = 90^\circ$ . (b) Angular scan in $\theta$ at $\phi = 0$ .	38
4.11	$\phi$ -dependence of $J_{c,L}$ different $\theta$ and $T = 64$ K, $\mu_0 H_{\text{app}} = 5$ T. (b) $\theta$ -dependence of $J_{c,L}$ at different $\phi$ , $T = 77$ K and $\mu_0 H_{\text{app}} = 3$ T.	38
4.12	Geometry of the L-bridge in VLF configuration showing the sample unit vectors $\hat{e}_1$ , $\hat{e}_2$ and $\hat{e}_3$ and the unit vector $\hat{e}_c$ parallel to the $c$ -axis of the L-bridge.	39
4.13	$F_L(\alpha_L)$ and $J_c(\alpha_L)$ at different $\phi$ , $T = 77$ K and $\mu_0 H_{\text{app}} = 0.5$ T. The Lorentz force roughly scales with $\alpha_L$ while $J_c$ does not.	40
4.14	$F_L(\alpha_L)$ at different $\phi$ and a $J_c$ -curve in MLF at $T = 77$ K and applied magnetic fields of 0.5 T, 1 T, 3 T and 5 T.	41
4.15	$F_L(\alpha_L)$ at different $\theta$ at $T = 64$ K and $\mu_0 H_{\text{app}} = 1$ T and 5 T.	42
4.16	Schematic diagram of the MLF configuration of the T-bridge. The angle $\phi$ denotes the angle of the applied field with $\hat{n}$ . By convention, $\vec{H}_{\text{app}} \parallel \hat{n}$ at $\phi = 0$ and $\vec{H}_{\text{app}} \parallel ab$ -planes at $\phi = 90^\circ$ .	42

4.17	(a) Angle dependence of $J_c$ of the T-bridge at MLF, at different fields and $T = 77$ K. (b) Normalized $J_c$ enlarged near the minimum at $H \parallel ab$ . . . . .	43
4.18	(a) Normalized $J_c(\phi)$ at $\mu_0 H_{app} = 2$ T and different temperatures for the T-bridge in MLF configuration. (b) Schematic diagram of the Lorentz force vector acting on the vortex string when $\vec{B} \parallel ab$ -planes ( $\phi = 90^\circ$ ). . . . .	44
4.19	Schematic diagram of the VLF configuration of the T-bridge. . . . .	45
4.20	(a) In-plane $J_c$ -anisotropy measurement at $T = 77$ K and different applied magnetic fields. (b) Normalized $J_{c,T}$ for a better comparison of the vortex channeling minima at $\phi = 90^\circ$ . . . . .	45
4.21	In-plane $J_c$ -anisotropy measurement of the T-bridge at $\mu_0 H_{app} = 2$ T and different temperatures. The data were normalized with respect to $J_c(\phi = 0)$ for a better comparison. . . . .	46
4.22	(a) $\theta$ -dependence of $J_{c,T}$ at $\phi = 0$ , $T = 77$ K and at different applied fields. (b) Normalized $J_{c,T}$ for a better comparison of the curves at different fields. . . . .	46
4.23	Geometry of the T-bridge in VLF configuration showing the sample unit vectors $\hat{e}_1$ , $\hat{e}_2$ and $\hat{e}_3$ and the unit vector $\hat{e}_c$ parallel to the $c$ -axis in the T-bridge. . . . .	47
4.24	$\phi$ -dependence of $J_c$ with $\mu_0 H_{app} = 5$ T and different $\theta$ at temperatures of (a) 77 K and (b) 64 K. . . . .	48
4.25	$J_c(\alpha_L)$ at $\mu_0 H_{app} = 5$ T, (a) $T = 64$ K and (b) $T = 77$ K and the corresponding $F_L(\alpha_L)$ at the same temperatures in (c) and (d). . .	49
4.26	$J_c(\phi)$ at $\mu_0 H_{app} = 0.5$ T, (a) $T = 85$ K and (b) $T = 77$ K. (c)-(d) are the corresponding $\alpha_T$ scaling of $J_c$ and (e)-(f) are the scaling of $F_L$ . . .	50
5.1	EBSD maps of the (c) YBCO-SS and (d) the YBCO Ni5W samples. The colored lines denote the GB misorientation angles with the following notation: Blue $\rightarrow < 1.5^\circ$ , green $\rightarrow > 3^\circ$ and yellow $\rightarrow 6-10^\circ$ . The scale from white to black correspond to the misorientation from the ideal cubic texture from 0 to $12^\circ$ . . . . .	53
5.2	(a) SEM image of a bare NiW template. The blue arrows denote the trenches between grains. (b) SEM image of the surface of YBCO-Ni5W. The red arrows point to smooth GBs and the yellow arrows denote the grooved GBs. Notice that the deposited YBCO layer has different porosity and density on each NiW grain. . . . .	54

- 5.3 (a) Higher magnification SEM image of the surfaces of (b) YBCO-SS and YBCO-NiW. In these pictures, the YBCO grain size and porosity are almost the same. . . . . 55
- 5.4 Remanent field profile of (a) YBCO-NiW and (b) YBCO-SS tape. The Hall probe-sample distance was approximately 4  $\mu\text{m}$  and the scanning stepwidth are 5 and 4  $\mu\text{m}$  in  $x$  and  $y$ -direction, respectively. The white dashed lines correspond to the positions of the linescans below each map. . . . . 55
- 5.5 (a) Remanent field profile at  $T = 4$  K of a 1.5 mm etched spot on YBCO-Ni9W. The Hall probe-sample distance,  $d$ , was 3  $\mu\text{m}$  and the stepwidths,  $s_x$  and  $s_y$  were 5  $\mu\text{m}$ . (b) Remanent field profile of a whole 10-mm-width YBCO-Ni5W in  $\text{LN}_2$ . The scanning parameters were  $d = 45$   $\mu\text{m}$  and  $s_x, s_y = 200$   $\mu\text{m}$ . On both images, the granular morphology of the field profile is depicted independent of the size of the scanning area and temperature of the measurement. . . . . 56
- 5.6 (a) Remanent field map of YBCO-STO at  $T = 4$  K. The Hall probe-sample distance was approximately 5  $\mu\text{m}$  and the scanning stepwidth are 5 and 7  $\mu\text{m}$  in  $x$  and  $y$ -direction, respectively. (b) Comparison of the remanent field profile of YBCO-SS and YBCO-STO at  $T = 4$  K and calculated curves with a constant  $J_c$  and if a field-dependent  $J_c$  is assumed. . . . . 57
- 5.7 (a) Line scans at different applied fields at  $T = 4$  K of YBCO-NiW. (a)-(b) Line scans of two different etched spots measured in decreasing field after ramping the magnetic field to 5 T. Each measurement from 4 T to the remanent state ( $\mu_0 H_{\text{app}} = 0$ ) was taken consecutively. (c) Line scan at the position  $x = 410$   $\mu\text{m}$  in figure 5.4b in decreasing field after applying a field of -2 T. The black dashed lines in all the images denote the edges of the sample. . . . . 58
- 5.8 (a) Line scans at different applied fields at  $T = 4$  K of YBCO-SS. The data presented were taken in decreasing field after ramping the magnetic field to 5 T. Each measurement from 4 T to the remanent state ( $H_{\text{app}} = 0$ ) was taken consecutively. The dashed lines denote the edges of the sample. (b) Normalized  $B(y)$  to show how the shape of the field profile evolves with field. The blue dashed curve corresponds to the theoretical field profile assuming a constant  $J_c$ . It is fitted to the data at  $\mu_0 H_{\text{app}} = 5$  T. . . . . 59
- 5.9  $J_c$  map at  $T = 4$  K in the (a) remanent state and (b)  $\mu H_{\text{app}} = 1$  T. The white dashed line correspond to the linescans in (c) and (d). . . 60

- 5.10 (a)  $J_c$  map at  $T = 4$  K of YBCO-Ni5W. (b) Backscatter electron image of the surface of the 400- $\mu\text{m}$  spot in YBCO-Ni5W. The colored lines correspond to the GBs traced from the EBSD map in figure 5.1b. The solid line correspond to smooth GB while the dashed lines are grooved. . . . . 61
- 5.11 (a)  $B(x, y)$  and (b)  $J_c(x, y)$  of a 150- $\mu\text{m}$  spot on YBCO-Ni5W at  $T = 4$  K. The colored lines denote the GBs and each color correspond to the following  $\theta_{\text{GB}}$ : dark blue  $\rightarrow \theta_{\text{GB}} < 1.5^\circ$ , yellow  $\rightarrow \theta_{\text{GB}} = 1.5 - 3^\circ$ , pink  $\rightarrow \theta_{\text{GB}} = 3 - 6^\circ$ , white  $\rightarrow \theta_{\text{GB}} = 6 - 10^\circ$ . The solid lines and the dashed lines represent smooth and grooved GBs, respectively. (c) EBSD maps of the same spot each corresponding to the misorientation relative to the 001, 010 and 100 fiber texture. (d) BSE image of the same spot. . . . . 62
- 5.12 (a) An EBSD linescan in YBCO-Ni5W. (b) Schematic diagram of the 100, 010 and 001 directions. (c) GB types formed in YBCO films. 63
- 5.13 (a)  $B(x, y)$  and (b)  $J_c(x, y)$  of a 400- $\mu\text{m}$  spot on YBCO-Ni5W at  $T = 4$  K. (c) BSE image of grain 1. (d) SEM picture of GB 2. EBSD linescan along the (c) line A and (f) line B marked in the  $J_c$  map in (b). . . . . 65
- 5.14 Field dependence of  $J_c$  at different temperatures for (a) YBCO-SS and (b) YBCO-Ni5W. The filled symbols correspond to  $H_{\text{app}} \parallel c$  and the hollow symbols correspond to  $H_{\text{app}} \parallel ab$ . . . . . 66
- 5.15 (a)  $J_c(H_{\text{app}})$  in increasing and decreasing field at  $T = 64$  K and in two field directions,  $H_{\text{app}} \parallel ab$  and  $H_{\text{app}} \parallel c$ . The error bars are calculated by obtaining three consecutive IV-curves at each field. No sample heating was observed during the measurement. (b)  $J_c(H_{\text{app}})$  at  $T = 64$  K at different angles the applied field to the  $c$ -axis. By convention,  $\phi = 90^\circ$  and  $\phi = 0$  corresponds to  $H_{\text{app}} \parallel ab$  and  $H_{\text{app}} \parallel c$ , respectively. . . . . 67
- 5.16 Angle dependence of  $J_c$  at different applied magnetic fields and temperatures of (a) 40 K, (b) 64 K and (c) 77 K. The black lines (black data points in the case of 64 K) indicate the self-field  $J_c$  ( $J_{c,\text{sf}}$ ) at each temperature. (d) Field dependence of  $J_c$  at 40 K. The colored lines correspond to the fields of the  $J_c(\phi)$  curves in (c). . . . . 68
- 5.17 VJ curves at  $T = 40$  K and fields of 0, 0.6 and 5 T when  $H_{\text{app}} \parallel ab$ . 69
- 5.18 Schematic diagram of the SHPM configuration for  $H_{\text{app}} \parallel ab$ . . . . . 69

- 5.19 Linescans across the center of a 400- $\mu\text{m}$  spot at 40 K after zero-field cooling. The applied magnetic field was ramped up to 3.0 T, taking a linescan at each magnetic fields. The stepwidth was 2  $\mu\text{m}$ . The Hall probe was moved at a constant distance across the diameter and the asymmetry at the two opposite ends is due to the inclination of the surface of the sample, which is about 2  $\mu\text{m}$  away from the Hall probe at one end and 10  $\mu\text{m}$  away on the other end. (b) The remanent field profile of the same spot when the field is applied parallel to the  $c$ -axis. (c) In-field linescans that correspond to the dashed white line in (b). The black arrows correspond to a NiW GB with  $\theta_{\text{GB}} = 9^\circ$  found in the EBSD image that divides two magnetic grains. . . . . 70
- 5.20 Comparison of the field profiles measured by SHPM when the field is applied parallel to the two main crystallographic direction in (a) remanent state and (b) with an applied field of 3 T. . . . . 71
- 5.21 The five plots of  $B - B_{\text{app}}(x)$  numbered between 1-5 are linescans across the center of the same circular spot on YBCO-Ni5W. After the sample was zero field cooled, linescans were obtained from -3 T to +5 T and back to -2 T. The peak of the in-field profiles is plotted as a function of the applied field. The sequence of the applied fields are denoted by the direction of the arrows. . . . . 72
- 5.22 Representation of an Abrikosov Josephson (AJ) vortex in a planar defect along the  $xy$ -plane. . . . . 74
- 5.23 (a) Schematic of current flow on YBCO-Ni5W. (b) Diagram of an AJ-vortex lying in the GB when  $H_{\text{app}} \parallel c$  and (c) when  $H_{\text{app}} \parallel ab$ . . . . . 76
- 5.24 Field dependence of  $J_c$  of YBCO-Ni5W in  $H_{\text{app}} \parallel ab$  and  $H_{\text{app}} \parallel c$  at temperatures of (a) 40 K, (b) 64 K and (c) 77 K. The symbols correspond to data while the solid lines are the fits from equations 5.6 and 5.9. . . . . 77
- 5.25 The red circles correspond to the calculated values of the penetration depth from the fitting parameters,  $B_s$  and  $J_o$ . The solid line denotes the fitted  $\lambda_{\text{exp}}(T)$  and the blue square symbols denote the predicted temperature dependence of  $\lambda$  for a  $d$ -wave superconductor. . . . . 78
- 5.26 (a)  $J_c$  as a function of  $H_{\text{eff}} = \varepsilon(\phi)$ . (b)  $\phi$ -dependence of  $J_c$ . Symbols show the data while the solid lines are calculation of  $J_c(\phi)$  according to Blatter scaling. . . . . 80
- 5.27 Experimental data of  $J_c(\phi)$  at 64 K and 1 T with the practical fit function. . . . . 80



- 5.28 Dependence of  $H_{\text{peak}}$  on the angle  $\phi$ . The data points are from experimental data while the lines are those predicted by Gurevitch model, Blatter scaling and practical fit for  $J_c(\phi)$ . . . . . 81
- 5.29 Maximum trapped magnetic field ( $B_{\text{peak}}$ ) obtained from in-field linescans across the YBCO-Ni5W for two field directions: (a)  $H_{\text{app}} \parallel c$  at  $T = 4$  K and (b)  $H_{\text{app}} \parallel ab$  at  $T = 40$  K. The insets show the actual linescans. . . . . 82
- 5.30 (a) Spatial distribution of  $J_c$  at  $T = 77$  K of three PLD-YBCO on Ni5W. The top image refers to pure YBCO, the middle is for YBCO with 5 mol%  $\text{Ba}_2\text{YNb}_{0.5}\text{Ta}_{0.5}\text{O}_6$  and the bottom for 5 mol%  $\text{BaHfO}_3$ . Field dependence of  $J_c$  at  $T = 40$  K when the applied field is (b) parallel to the  $c$ -axis and (c) parallel to the  $ab$ -planes. . . . . 83
- 5.31 SEM images of the cross-sections of YBCO-Ni5W and YBCO9+6BHO-Ni5W. The red and blue arrows indicate the  $\text{Y}_2\text{O}_3$  and pores, respectively. . . . . 83
- 5.32 Field dependence of  $J_c$  for  $H_{\text{app}} \parallel ab$  at temperatures of 40 K 64 K and 77 K. The symbols correspond to data while the solid lines are the fits to equations 5.6 and 5.9. . . . . 84
- 5.33  $\phi$ -dependence of  $J_c$  at 40 K, 64 K and 77 K. The solid lines denote the self-field  $J_c$  at each temperature. Hollow and filled symbolized correspond to -0.5 T and +0.5 T, respectively. . . . . 85
- 5.34 (a) TEM images from the cross-section of CSD-YBCO-Ni5W. The yellow dashed curves denote the meandering grain boundaries. The red arrows in the lower panel indicate  $\text{Y}_2\text{O}_3$  precipitates. (b) SEM image of the surface. (b) Higher magnification SEM images of PLD-YBCO-Ni5W and CSD-YBCO-Ni5W samples. . . . . 87
- 5.35 Remanent field profile and spatial  $J_c$ -maps of YBCO on (a)-(b) Ni5W and (c)-(d) Ni9W templates. The scanning parameters were  $s_x = s_y = 100 \mu\text{m}$ ,  $d = 35 \mu\text{m}$  and  $d = 15 \mu\text{m}$  for the Ni5W and Ni9W, respectively. . . . . 88
- 5.36 (a) Remanent field profile at 4 K of CSD-YBCO-NiW. The scanning parameters were  $s_x = s_y = 5 \mu\text{m}$  and  $d = 3 \mu\text{m}$ . The white dashed line corresponds to the position of the in-field linescans in (b) and (c) at  $T = 4$  K and 40 K, respectively. . . . . 88
- 5.37 Field dependence of  $J_c$  at (a)  $T = 77$  K, (b)  $T = 64$  K and (c)  $T = 40$  K. The insets in each figure are enlarged plots at lower fields. . . . . 89
- 5.38 Angle dependence of  $J_c$  at (a)  $T = 77$  K, (b)  $T = 64$  K and (c)  $T = 40$  K at different fields. . . . . 89

6.1	High-angle annular dark field (HAADF) image of the cross-section of YBCO-SS. $\text{Y}_2\text{O}_3$ nanoparticles and Y-124 intergrowths are denoted by the black and white arrows, respectively. . . . .	92
6.2	$J_c(\phi)$ in different applied magnetic fields at (a) $T = 77$ K and (b) $T = 40$ K. The direction of the $c$ -axis and the $ab$ -plane are at $0^\circ$ and $\phi = 90^\circ$ , respectively. . . . .	92
6.3	Angle-dependence of $J_c$ at $\mu_0 H_{\text{app}} = 5$ T and 77 K, 64 K, 55 K and 40 K normalized with respect to $J_c(\phi = 0)$ . The inset is an enlarged view around the $ab$ -peak for $T < 77$ K. (a) Dependence of the N-value on $\phi$ . The $N(\phi)$ for each temperature are plotted with an offset for clarity. . . . .	93
6.4	Angle-dependence of $J_c$ at $\mu_0 H_{\text{app}} = 0.2$ T and 77 K, 64 K, 55 K and 40 K normalized with respect to $J_c(\phi = 0)$ . The hollow symbols correspond to a field of +0.2 T and the solid ones are with -0.2 T. (a) Dependence of the N-value on $\phi$ . The $N(\phi)$ for each temperature are plotted with an offset for clarity. . . . .	94
6.5	(a) Bright field TEM image of the cross-section of the YBCO+BHO-SS tape showing the BHO nanorods with a splay around the $c$ -axis of the YBCO. (b) HAADF STEM Z-contrast showing the BHO nanorods and the Y-124 intergrowths. (c) EDX map with a planar view on the YBCO+BHO-SS sample showing the BHO nanorods with a typical diameter of $4 \pm 2$ nm. . . . .	95
6.6	$J_c(B, \phi)$ of YBCO-BHO-SS at (a) $T = 77$ K and (b) $T = 64$ K. . . . .	96
6.7	$J_c(\phi)$ and $N(\phi)$ of YBCO-BHO-SS in different applied magnetic fields at (a)-(b) $T = 77$ K and (c)-(d) $T = 64$ K. The direction parallel to the $c$ -axis and $ab$ -plane are at $\phi = 0^\circ$ and $\phi = 90^\circ$ , respectively. . . . .	97
6.8	(a) HAADF image of the cross-section of the YBCO+BYNTO sample. (b)-(d) Corresponding EDX maps confirming the elemental composition of the defects of $\text{Ba}_2\text{Y}(\text{Nb}/\text{Ta})\text{O}_6$ (BYNTO). . . . .	98
6.9	Normalized $J_c(\phi)$ of YBCO-BYNTO-SS in different applied magnetic fields at (a) $T = 77$ K, (b) $T = 64$ K, (c) $T = 55$ K and (d) $T = 40$ K. The plots are normalized for an easier comparison of the behavior of anisotropy at each field. The direction parallel to the $c$ -axis and $ab$ -plane is at $\phi = 0^\circ$ and $\phi = 90^\circ$ , respectively. . . . .	99
6.10	$\phi$ -dependence of $J_c$ at applied fields of (a) 1 T, (b) 3 T and (c) 5 T and different temperatures. $\phi$ -dependence of the N-value at (d) 1 T, (e) 3 T and (f) 5 T. The solid vertical line indicates the field direction $H_{\text{app}} \parallel ab$ ( $\phi = 90^\circ$ ). . . . .	100

- 6.11 (Upper panels) Field dependence of  $J_c$  in  $H_{\text{app}} \parallel ab$  of the pure and doped samples. The  $J_c$  was evaluated from magnetization measurements in the vector VSM. (Lower panels) Normalization of  $J_c$  with respect to the pure YBCO sample to illustrate the enhancement in  $J_c$ . . . . . 101
- 6.12 Angular dependence of  $J_c$  (upper panels) and normalized  $J_c$  of the doped samples with respect to the pure YBCO (lower panel) at (a)-(b) 77 K and (c)-(d) 64 K and applied fields of 2 T and 5 T. . . 103
- 6.13 Angle dependence of the N-value of the three PLD-grown samples at  $T = 64$  K and applied fields of (a) 2 T and (b) 5 T. The angle  $\phi_k$  marks the onset of the kinked vortex formation with respect to the direction of the  $ab$ -planes ( $\phi = 90^\circ$ ). . . . . 104
- 6.14 Angle dependence of the N-value of the three PLD-grown samples at  $T = 40$  K and applied fields of (a) 1 T and (b) 5 T. The angle  $\phi_T$  marks the onset of the pseudo-lock in state of the vortices parallel to the  $ab$ -planes ( $\phi = 90^\circ$ ). . . . . 104
- 6.15 Field dependence of the (a) onset of the kinked state at  $T = 64, 55$  K and (b) onset of the lock-in state at  $T = 40$  K of the pure and doped samples. . . . . 105
- 6.16 TEM image of the YBCO+5BHO-Ni5W tape showing the microstructural defects such as the BHO nanocolumns,  $Y_2O_3$  precipitates and Y-124 intergrowths. . . . . 105
- 6.17 TEM and EDX images of the YBCO+5BYNTO-Ni5W tape showing the microstructural defects such as the BYNTO nanocolumns and  $Y_2O_3$  precipitates. . . . . 106
- 6.18 Angular dependence of  $J_c$  of the (a) BHO- and (b) BYNTO-doped YBCO films on RABiTS Ni5W template. The measurement temperature was 40 K. The dashed horizontal line denote the self-field  $J_c$  at each temperature. . . . . 106
- 6.19 The upper panels correspond to the angular dependence of  $J_c$  of the three YBCO films with Ni5W template at (a) 77 K, (b) 64 K and (c) 40 K and applied field of 5 T. The lower panels are plots of the enhancement factor in  $J_c$  with respect to the pure YBCO. . . . . 107
- 6.20 Angular dependence of the N-value of the three samples at (a) 77 K, (b) 64 K and (c) 40 K and  $\mu_0 H_{\text{app}} = 5$  T. The vertical lines denote the onset of  $\phi_k$  and  $\phi_T$  in (b) and (c), respectively. . . . . 108

# List of tables

3.1	Summary of the coated conductors investigated. . . . .	13
5.1	Fitting parameters for fits of $J_c^G(B)$ and $J_c^{GB}(B)$ to data at 40 K, 64 K and 77 K. . . . .	77
5.2	Fitting parameters from $J_c^G(B)$ and $J_c^{GB}(B)$ to data of YBCO+5BYNTO-Ni5W at 40 K, 64 K and 77 K. . . . .	84
5.3	Fitting parameters from $J_c^G(B)$ and $J_c^{GB}(B)$ to data of YBCO+5BHO-Ni5W at 40 K, 64 K and 77 K. . . . .	85

# List of abbreviations and symbols

## Abbreviations

ABAD	alternating beam assisted deposition
AJ	Abrikosov-Josephson
APC	artificial pinning center
BHO	BaHfO <sub>3</sub>
BYNTO	BaYNb <sub>0.5</sub> Ta <sub>0.5</sub> O <sub>6</sub>
BSE	back scatter electron
CC	coated conductor
CSD	chemical solution deposition
EBSD	electron backscatter diffraction
EDX	energy dispersive x-ray spectroscopy
FF	force-free
GB	grain boundary
GdBCO	GdBa <sub>2</sub> Cu <sub>3</sub> O <sub>7-x</sub>
HAADF-STEM	high angle annular dark field scanning transmission electron microscopy
HAGB	high angle grain boundary
HTS	high temperature superconductor
IP	in-plane
ISD	inclined substrate deposition
L	longitudinal direction where current flows parallel to the <i>ab</i> -planes
LAGB	low angle grain boundary
MLF	maximum Lorentz force
mSTO	miscut SrTiO <sub>3</sub>
NOLD	non-Ohmic linear differential
PLD	pulsed laser deposition
RABiTS	rolling assisted biaxially textured substrate
REBCO	(RE=rare earth)Ba <sub>2</sub> Cu <sub>3</sub> O <sub>7-x</sub>

SEM	scanning electron microscopy
SHPM	scanning Hall probe microscopy
SS	stainless steel
STO	SrTiO <sub>3</sub>
T	transverse direction where the current flow is crossing the <i>ab</i> -planes
TEM	transmission electron microscopy
VLF	variable Lorentz force
VSM	vibrating sample magnetometer
YBCO	YBa <sub>2</sub> Cu <sub>3</sub> O <sub>7-x</sub>
YSZ	yttria stabilized zirconia

## Symbols

$\alpha$	angle of the discontinuity line with respect to the longer side in a current density distribution of a rectangular film
$\alpha_L$	angle of the applied field with respect to the <i>c</i> -axis in the L-bridge
$\alpha_T$	angle of the applied field with respect to the <i>c</i> -axis in the T-bridge
$\xi_c$	coherence length along the <i>c</i> -axis
$\xi_{ab}$	coherence length along the <i>ab</i> -planes
$\lambda_c$	penetration depth along the <i>c</i> -axis
$\lambda_{ab}$	penetration depth along the <i>ab</i> -planes
$\gamma$	anisotropy parameter
$\Gamma$	ratio of the planar current flowing in longitudinal and transverse directions
$\kappa$	Ginzburg-Landau parameter
$\Phi_o$	flux quantum
$\phi_k$	onset of kinked vortex state as the applied magnetic field is rotated towards the <i>ab</i> -planes
$\phi_T$	onset of pseudo-lock-in state as the applied magnetic field is rotated towards the <i>ab</i> -planes
$\Theta$	angle between the applied field and the current flow

---

$\theta_{\text{GB}}$	grain boundary misorientation angle
$\theta_c$	grain boundary misorientation angle that denotes the onset of exponential decrease of critical current
$\theta_v$	vicinal angle of an mSTO substrate, amount of tilt of the $c$ -axis of REBCO with respect to the direction normal to the film surface
$a$	spacing between vortices
$B$	local magnetic induction
$B_\phi$	matching field
$B_{c1}, H_{c1}$	lower critical field
$B_{c2}, H_{c2}$	upper critical field
$B_{\text{peak}}$	the peak of the magnetic field profile in SHPM
$B_s$	minimum field at which the pinning force on an AJ vortex is determined by shear flux pinning
$d$	distance of the Hall probe to sample surface in SHPM
$d_1, d_2$	discontinuity lines in the current density distribution of a rectangular film
$\hat{e}_c$	unit vector parallel to the $c$ -axis
$\hat{e}_1, \hat{e}_2, \hat{e}_3$	unit vectors of the sample coordinate system
$\hat{n}$	unit vector parallel to the direction normal to tape surface
$E$	electric field
$E_c$	electric field criterion
$F_L$	Lorentz force
$F_p$	pinning force density
$f_{\text{GB}}$	total pinning force on an AJ vortex parallel to a GB
$f_h$	component of pinning force on an AJ vortex due to inhomogeneities
$f_i$	effective pinning on an AJ vortex due to Abrikosov vortices in the grains
$H_{\text{app}}$	applied magnetic field
$H_c$	thermodynamic critical field
$H_{\text{peak}}$	applied magnetic field at which the peak in $J_c(B)$ occurs in transport measurement
$H_{\text{loc}}$	local magnetic field at the grain boundary
$H_{\text{edge}}$	return field induced by magnetic induction in each grain

$I$	current
$I_c$	critical current
$J$	current density
$J_c$	critical current density
$J_c^{\text{GB}}$	intergranular critical current density
$J_c^{\text{G}}$	intragranular critical current density
$J_{c,L}$	critical current density in longitudinal direction
$J_{c,T}$	critical current density in transverse direction
$J_{c,\text{sf}}$	self-field critical current density
$j_d$	depairing current density
$J_{\text{max}}$	maximum local current density
$l$	length of the vortex core parallel to a planar defect such as GB
$L$	length of inhomogeneity in a grain boundary
$N$	exponent of the power law transition in the $V(I)$ curve
$R$	radius of a defect
$S$	vortex creep rate
$s_x, s_y$	stepwidth in the SHPM measurement in the $x$ - and $y$ - direction
$t$	thickness of the superconductor layer
$T$	temperature
$T_c$	critical temperature
$V$	voltage
$u_o$	pinning energy per unit length
$u_c$	condensation energy density
$U_p$	pinning energy
$w, p$	fitting parameters of the practical fit functions for the angle-dependence of $J_c$





# Chapter 1

## Introduction

The research and development of superconducting materials for industrial applications has paved a long way since the discovery of superconductivity by Heike Kammerlingh Onnes 106 years ago. The main impetus for this continuing research is the remarkable property of superconductors to carry resistanceless current and expel magnetic field from its interior. These make them an inevitable material for generation of very high magnetic fields. Over 55 years ago, the first magnets made of alloys or intermetallic compounds such as NbTi and Nb<sub>3</sub>Sn were developed and are making up over 90% of industrial superconducting wires being produced nowadays. They are now used in scientific facilities such as accelerator magnets and nuclear magnetic resonance (NMR) systems and for medical purposes such as in magnetic resonance imaging (MRI) systems [32, 59].

The discovery of high-temperature superconductors (HTS) in 1987 has pushed the area for application further to electric power grid such as in fault current limiters, magnetic energy storage and power transmission cables because of their higher transition temperatures – above the temperature of liquid nitrogen. Magnets made of HTS wires are also being eyed to operate at lower temperatures down to 4.2 K due to their large critical current, which can surpass the highest possible magnetic field generated by magnets with NbTi and Nb<sub>3</sub>Sn wires. However, due to the ceramic nature of the cuprates, one of the biggest challenges is to produce them in a flexible form. The initial design for HTS wires is known as the first generation superconducting wires (1G-HTS) where cuprates of the BSCCO family (i.e. Bi<sub>2</sub>Sr<sub>2</sub>Ca<sub>1-x</sub>Cu<sub>x</sub>O<sub>2x+4+δ</sub>,  $x = 1, 2, 3$ ) are packed into a silver tube [33]. However, this approach is very expensive due to the large amount of silver needed and it is not ideal for large scale production. Therefore, the second-generation superconducting wires (2G-HTS) was conceptualized and what is now known as the coated conductors (CCs). They are made up of (RE)Ba<sub>2</sub>Cu<sub>3</sub>O<sub>7-δ</sub> (RE=rare earth) material coated on metallic tapes. With this approach, the amount of Silver is significantly reduced, making 2G-wires a cheaper option than its predecessor. However, the production of long-length CCs is still challenging due to two main problems. First, a granular morphology of the deposited layer limits the current-carrying capacity significantly. Therefore, the REBCO layer has to be deposited with a minimized granularity by confining the misorientation between two single crystalline grains to small angles.

The second problem is the anisotropy of the critical current to the orientation of the magnetic field with respect to the crystallographic axes. The lowest current over the whole angular orientation of field would be the limitation to the operating current. Therefore, one of the solution to this is adding APCs that cause directional enhancement to  $J_c$ . Otherwise, pinning centers that can contribute an isotropic enhancement in  $J_c$  are also preferable. Presently, there has already been a lot of progress to minimize granularity and reduce anisotropy with a payoff of having a complicated buffer layer architecture. The cost of producing CCs in long-lengths is still more expensive than Copper and also higher than NbTi and Nb<sub>3</sub>Sn. Therefore, aside from optimizing the material properties, a search for alternative conductor architecture and deposition technique is also important in order to achieve a competitive material not just in the aspect of current-carrying capacity but also in the cost of production as well.

In this thesis, different coated conductor architectures produced in lab scale and as industrial prototypes are studied. This includes transport and magnetic characterization of 2G-HTS wires ranging from low cost CCs with biaxially textured metallic templates to medium cost CCs with textured buffer layer. One of the main goals of this thesis is to show and explain how the seemingly fundamental problem of grain boundary limitation, which is already a big issue since 30 years still plays a significant limitation to the performance of the coated conductors produced at present especially the ones with the low cost design. The second goal is to assess the vortex pinning mechanisms in CCs with artificial pinning centers and in tapes with an interesting, tilted crystallographic structure. Understanding vortex pinning properties is the main key to further boost the performance of CCs at lower temperatures and higher magnetic fields.

## Outline of this thesis

This thesis is composed of three parts, the first part starts in chapter 2 where a brief background of the coated conductor technology is given as well as a short discussion about the REBCO compound and fundamental understanding of the vortex states. The second part includes experimental details in chapter 3 comprising of a brief description of the samples investigated and characterization techniques used. The third part presents the main results, which begins in chapter 4 with the interesting transport and magnetic properties of an alternative coated conductor design where the crystallographic axes of the REBCO layer are tilted with respect to the sample geometry. The impact of the granular morphology of the YBCO layer on the superconducting properties at low temperatures are explored especially for biaxially textured NiW templates in chapter 5. The dynamics of vortices and pinning properties of YBCO CCs with  $\text{BaHfO}_3$  and  $\text{Ba}_2\text{YNb}_{0.5}\text{Ta}_{0.5}\text{O}_6$  precipitates are investigated in chapter 6. The conclusions and a future outlook are given in chapter 7. Some sentences were taken verbatim from two published articles under this thesis [57, 58].



# Chapter 2

## Background

### 2.1 The coated conductors

The 2G-HTS wires or coated conductors (CCs) consist of four main components: a metallic substrate, buffer layers, a REBCO layer and protection layers/stabilizers. Early studies of CCs and thin films of YBCO on bi-crystal substrates have shown that the critical current density exponentially decreases with increasing grain boundary misorientation angle [18, 93], i.e.  $J_c(\theta_{GB}) = J_c(0) \exp\left(-\frac{\theta_{GB}}{\theta_c}\right)$ , where  $\theta_c$  is about  $4^\circ$ . High angle grain boundaries (HAGB), which are considered nowadays to have  $\theta_{GB}$  values greater than  $10^\circ$  [22, 46], are found to suppress the superconducting order parameter, hence the current transport is governed by the Josephson effect [12, 93]. For low angle grain boundaries (LAGB), that is for  $\theta_{GB} < 10^\circ$ , the GBs mainly consist of dislocation cores with strained regions [50].

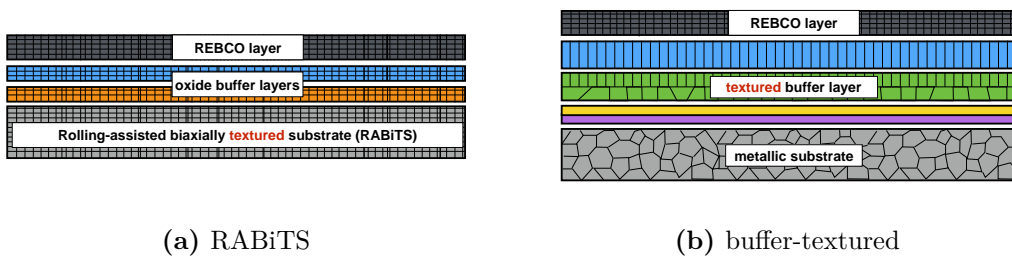


**Figure 2.1:** Diagram of two main coated conductor architectures [22].

Since it is important for the REBCO layer to have well-aligned grains and to avoid formation of HAGBs, there are two main processing routes that are widely used nowadays. They are shown by a diagram in figure 2.1. The first is by rolling assisted biaxially textured substrates (RABiTS), which are usually Ni alloys. As the name suggests, the biaxial texture is introduced by the metallic substrate itself and it is transferred to the buffer and to the REBCO layers. In the second route, the biaxial texture is induced by a buffer layer grown by ion beam assisted deposition (IBAD). Another technique known as inclined substrate deposition (ISD)

also introduces the texture through the buffer layer but the deposition is done on a metallic substrate inclined by a few degrees with respect to the incoming beam [3].

With the much improved texture of the REBCO layer in coated conductors, typical tapes produced nowadays have a self-field critical current density,  $J_{c, sf}$ , at 77 K of 1-3 MA/cm<sup>2</sup> or critical current,  $I_c$ , of 250-400 A for 4-mm width tapes. The limiting effects of grain boundaries are confined only to very low fields. Usually, the thickness of the superconducting layer is between 1-2  $\mu\text{m}$  and this is only about 1-2% of the total thickness of the tapes. So far, it was found that it is quite challenging to push  $I_c$  to a higher value by increasing the REBCO thickness because  $J_c$  is found to decrease as the thickness increases. This is because more defects and  $a$ -axis grains form that partially blocks the current transport [70]. Although recently there are successful results of obtaining relatively high  $I_c$  for thicknesses greater than 3  $\mu\text{m}$ . One of them is a DyBCO-based ISD-buffered CC with 1000 A/cm-width self-field  $I_c$  at 77 K [23].

Most of these coated conductors are optimized to operate at liquid nitrogen temperatures. However, as the temperature decreases, the limiting effect of grain boundaries spans a wider field range [31]. Therefore, if these CCs are to be operated at liquid Helium temperature, further studies must be done to gain insight on the significance of the grain boundary limitation at lower temperatures.

## 2.2 REBCO: A layered superconductor

Aside from granularity, which significantly affects  $J_c$ , the epitaxial growth of the REBCO compounds on metallic substrates has led to the manifestation of the anisotropy of  $J_c$  to the direction of the applied magnetic field. It is believed that the conduction of supercurrents occurs along the CuO<sub>2</sub> planes of RE-based cuprates and there is a weak coupling between these planes [11]. Therefore, the anisotropy can be characterized by effective masses  $m_a$ ,  $m_b$  and  $m_c$  according to the continuous anisotropic Ginzburg-Landau (GL) theory [16]. In REBCO,  $m_a$  and  $m_b$  are almost equal (will be denoted hereafter as  $m_{ab}$ ) and  $m_c$  is the largest. The anisotropy  $\gamma$  is defined according to the ratio of these two effective masses:  $\gamma = (m_c/m_{ab})^{1/2}$ . The characteristic lengths of superconductivity  $\xi$  and  $\lambda$ , which correspond to the coherence length and penetration depth, respectively, take two values at the two main directions and  $\gamma = \lambda_c/\lambda_{ab} = \xi_{ab}/\xi_c$ . In type II superconductors, the magnetic field penetrates the superconductor in the form of quantized vortices for  $B_{c1} < B_{app} < B_{c2}$ , where  $B_{c1}$  and  $B_{c2}$  are the lower and upper critical fields, respectively. These quantities varies with the angle of the applied field with respect to the  $c$ -axis,  $\theta$ :

$$B_{c1}(\theta) = \frac{\Phi_o}{4\pi\lambda_{ab}^2} \varepsilon(\theta) \ln \kappa(\theta) \quad (2.1)$$

$$B_{c2}(\theta) = \frac{\Phi_o}{2\pi\xi_{ab}^2} \varepsilon(\theta) \quad (2.2)$$

where  $\varepsilon^2(\theta) = (\cos^2 \theta + \frac{1}{\gamma^2} \sin^2 \theta)$ ,  $\Phi_0$  is the flux quantum and  $\kappa_i = \lambda_i/\xi_i$  is the GL parameter and the subscript  $i$  correspond to  $ab$  or  $c$ -axis directions. The radius of a vortex line oriented parallel to the  $c$ -axis is equal to the length scale  $\xi_{ab}$  and forms into an elliptical shape as the field is oriented towards the  $ab$ -planes. Both  $\lambda_i$  and  $\xi_i$  are temperature-dependent quantities given approximately as:

$$\xi_i(T) = \xi_i(0) \left(1 - \frac{T}{T_c}\right)^{-1/2} \quad (2.3) \quad \lambda_i(T) = \lambda_i(0) \left[1 - \left(\frac{T}{T_c}\right)^p\right]^{-1/2} \quad (2.4)$$

where  $T_c$  is the critical temperature and  $p$  has a value of  $4/3$  for a d-wave superconductor [76]. For YBCO,  $\xi_{ab}(0)$  and  $\lambda_{ab}(0)$  are about 1.5 nm and 150 nm, respectively and the value for  $\gamma$  is usually 5-7 [60]. The superconducting transition temperature,  $T_c$ , is typically 90-93 K [11].

For an ideal superconductor without any defects, an applied current inducing a Lorentz force would push the vortices into motion and cause dissipation. This is where the presence of defects, which are unavoidable in real samples, comes as an advantage. They lower the energy of vortex lines and tend to keep them trapped or "pinned" in their potential wells. However, for defects to be effective pinning centers, their size must be of the order of the coherence length of the vortex and the density must be low enough so as not to deteriorate the general current-carrying property of the superconductor. There are a lot of defects present in a REBCO film that can function as pinning centers, such as twin boundaries, threading dislocations, voids, oxygen vacancies, grain boundaries, anti-phase boundaries and precipitates [33].

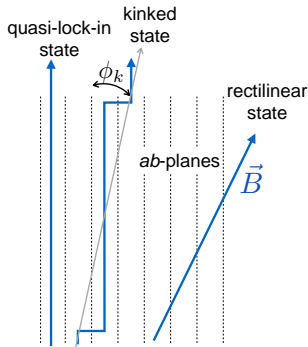


**Figure 2.2:** Schematic diagram of vortex states as the angle of the applied magnetic field is rotated towards the  $ab$ -plane.

M. Tachiki and S. Takahashi [89] have identified the layered structure of cuprates as intrinsic pinning centers when the vortices are oriented parallel to the  $ab$ -planes. Since cuprates such as the REBCO compounds have alternating weak and strong superconducting layers, the vortex energy is lowered at the weakly superconducting layers and thus, vortices are effectively pinned. Due to the periodic potential of the layered structure of REBCO, the vortices undergo transitions as their orientation is varied with respect to the  $ab$ -planes. According to G. Blatter, et al. [5], the vortices undergo a lock-in transition at a very narrow angular range around the  $ab$ -plane since it is more favorable for them to align parallel to these planes. As the field



is oriented away from the  $ab$  direction, the vortices form a kinked structure and transform into a rectilinear state as the field is oriented towards the direction of the  $c$ -axis. A schematic diagram of the vortex state in a layered superconductor is shown in figure 2.2.

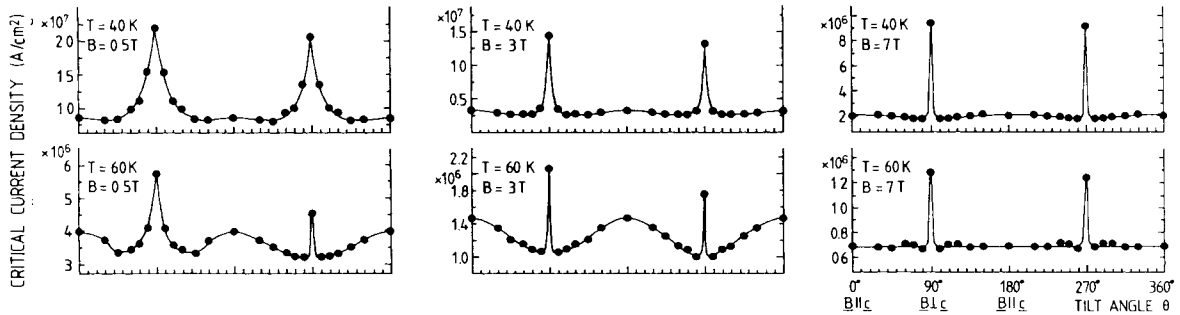


**Figure 2.3:** Angle-dependence of  $J_c$  measured by B. Roas et al. at different temperatures and applied field [81].

An example of an angle-dependence of  $J_c$  of a YBCO film is shown in figure 2.3 [81]. In maximum Lorentz force configuration, the pinning force is equal to the Lorentz force. Therefore,  $J_c$  can be directly related to pinning. The features of the angle-dependence of  $J_c$  consists of a peak parallel to the  $ab$ -planes due to intrinsic pinning and another peak parallel to the  $c$ -axis, which is attributed to defects oriented in this direction such as twin boundaries in this case. Until this day, the prospect of enhancing the pinning properties to increase  $J_c$  and alter its anisotropy with fields is widely utilized. One of the biggest breakthroughs in this area is the introduction of correlated pinning centers to reduce the anisotropy and increase  $J_c$  at a specific direction of field. In the beginning this is done by particle irradiation [13] until it was demonstrated that the addition of epitaxial secondary phase of  $\text{BaZrO}_3$  can also form fine-sized correlated defects suitable in pinning vortices [64]. In the present, a lot of other oxide phases are being incorporated in the REBCO matrix such as  $\text{BaMO}_3$  ( $M=\text{Hf},\text{Ti}$ ), niobates and tantalates. The formation of isotropic defects that will cause enhancement in  $J_c$  over the whole angular range is also more preferable. However, the efficiency of these pinning centers at different fields and lower temperatures remains to be understood especially if more than one kind of pinning center interact with the vortices and form different vortex states.

# Chapter 3

## Experimental Details

### 3.1 Sample preparation

Various coated conductor architectures with different deposition conditions were investigated in this thesis. Each deposition process and choice of template lead to different microstructures and grain boundary properties. A brief description of the fabrication process will be discussed in the following sections.

#### 3.1.1 ISD-MgO buffered tape

$\text{GdBa}_2\text{Cu}_3\text{O}_7$  (GdBCO)-based CCs were produced by THEVA GmbH. The GdBCO layer was deposited by evaporating stoichiometric and granular GdBCO material by electron beam [80]. A reel-to-reel process was developed to deposit HTS material on a MgO-buffered Hastelloy C276 substrate [78]. What makes this tape interesting is the resulting crystallographic orientation of the deposited superconducting layer due to the deposition conditions of the buffer layer. As shown by the schematic diagram in figure 3.1, the substrate is tilted by an angle  $\alpha$ , usually in the range of  $25^\circ - 30^\circ$ , with respect to the substrate normal such that the deposition of the MgO is at this angle [3], hence it is called inclined substrate deposition (ISD) technique. Through the tilted configuration, the deposited MgO buffer layer forms facets on the surface being orthogonal to the direction of the incoming vapor [23]. The surface of the facets is parallel to the (200) plane of the MgO. Then, a thin MgO layer was deposited with perpendicular incidence ( $\alpha = 0$ ) that serves as a cap layer between the tilted MgO and the superconductor layer [79]. The GdBCO is then deposited with untilted configuration ( $\alpha = 0$ ). Henceforth, this tape will be referred to as GdBCO-ISD. A schematic diagram of the tape architecture and corresponding TEM images are shown in figure 3.2.

Because of the tilted crystallographic orientation and faceting of the MgO buffer layer, the  $c$ -axis of the GdBCO tends to grow perpendicular to the surface of the facets (figure 3.2a) [1]. In the GdBCO tapes used in this work, the facet of the

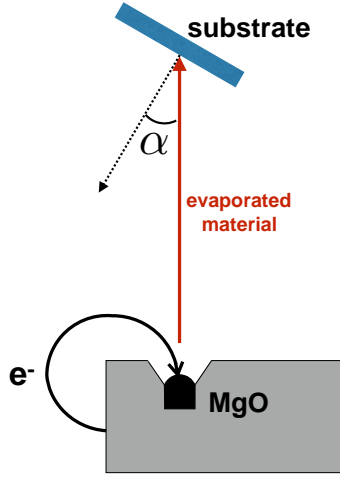
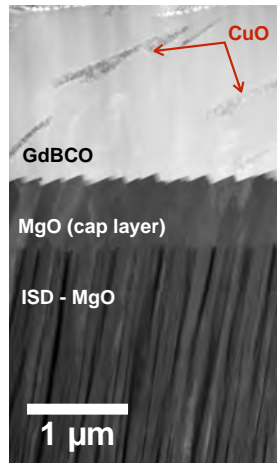
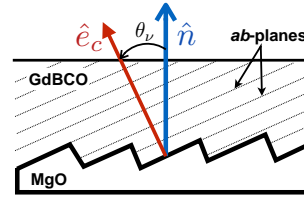


**Figure 3.1:** Schematic diagram of the ISD setup.



(a)



(b)

**Figure 3.2:** (a) TEM image of the longitudinal cross-section of GdBCO-ISD showing the buffer layers and the GdBCO layer. (b) Schematic diagram of the GdBCO layer showing the vectors  $\hat{n}$  and  $\hat{e}_c$  that corresponds to the direction normal to the tape surface and  $c$ -axis, respectively and the angle  $\theta_v = 24^\circ$  that denotes the tilt of the  $c$ -axis with respect to  $\hat{n}$ .

MgO buffer layer was found to be tilted by about  $24^\circ$  with respect to the plane of the tape. Thus, the  $ab$ -plane of the GdBCO layer was tilted by about  $24^\circ$  as well.

### 3.1.2 PLD-YBCO tapes

YBCO films grown by pulsed laser deposition (PLD) are lab-scale CCs fabricated at the Leibniz Institut für Festkörper und Werkstofforschung Dresden (IFW Dresden). The PLD technique is a type of physical vapor deposition in which a high power laser, such as the KrF excimer laser (COHERENT LPXpro 305,  $\lambda = 248$  nm) used

in the setup, hits a stoichiometric target, ablates its surface, forms a plasma plume and allows deposition of the stoichiometric material on a substrate exposed to the plume [11] (see schematic diagram in figure 3.3).

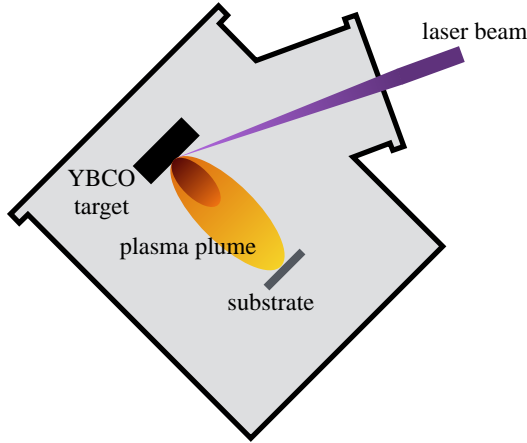


**Figure 3.3:** Schematic diagram of the PLD setup [40].

A single crystalline  $\text{SrTiO}_3$  and two types of metallic substrates were used for the PLD of YBCO. For the metallic substrates, one was a stainless steel (SS) with oxide buffer layers composed of an Yttria stabilized Zirconia (YSZ) deposited by alternating beam assisted deposition (ABAD) developed by Bruker GmbH and PLD- $\text{CeO}_2$ . The ABAD deposition of YSZ provides the biaxial texture transferred to the YBCO layer [92]. It is a variation of the IBAD-template mentioned in section 2.1. The second substrate is a rolling-assisted biaxially textured (RABiT) Ni-W alloy. The RABiT template has chemically deposited oxide buffer layers composed of  $\text{La}_2\text{Zr}_2\text{O}_7$  and  $\text{CeO}_2$ . Two kinds of Ni-W templates were used with different W content, one with 5at% and another with 9at%. The higher the amount of W, the lower the magnetization of the Ni-W alloy. The magnetic moment of a Ni-5at%W is about two orders of magnitude higher than the Ni-9at%W at 77 K [35]. All the PLD-YBCO films on metallic substrate have a silver protection layer. Schematic diagrams of the tape architectures are shown in figure 3.4. The growth mechanism of the YBCO layer is columnar, thus, the orientation of the  $c$ -axis and  $ab$ -planes are approximately perpendicular and parallel to the tape surface, respectively. The grain boundary formed are also planar throughout the layer thickness.

On the other hand, the YBCO layer on STO is directly deposited without intermediate buffer layer. Some films, which will be referred to as YBCO-mSTO, were prepared on a single crystalline (001) STO with an intentional cut off the 001 plane towards the 100 plane. The angle subtended by the cut is what is referred to as the vicinal angle,  $\theta_v$ . The growth of the YBCO layer in this type of functional substrate is in a step-flow growth mode [39]. The  $c$ -axis of YBCO is oriented perpendicular to the surface of the steps and therefore leads to the tilted geometry with respect to the surface of the films. Vicinal angles of 0, 5°, 10°, 15° and 25° were used.

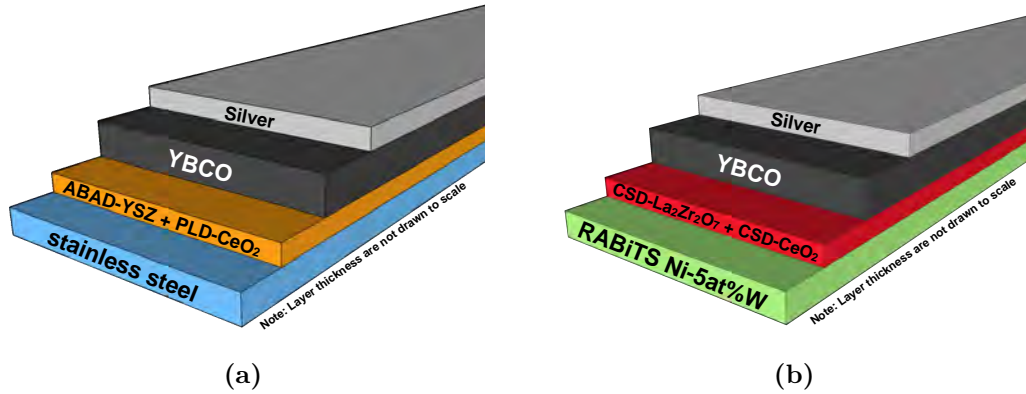


**Figure 3.4:** Architecture of (a) YBCO on ABAD-YSZ/SS tape and (b) YBCO on RABiTS-Ni-5at%W tape.

PLD-YBCO films with doping of X mol% BaHfO<sub>3</sub> (BHO, X=5,6) and 5 mol% BaYNb<sub>0.5</sub>Ta<sub>0.5</sub>O<sub>6</sub> (BYNTO) were also prepared in order to explore the effects of the secondary phases formed by these compounds in the YBCO matrix on vortex pinning and enhancement of  $J_c$ .

### 3.1.3 CSD-YBCO tapes

The tape with YBCO layer grown by chemical solution deposition (CSD) was produced by Deutsche Nanoschicht GmbH. The metallic substrate used are RABiTS Ni-W alloy with CSD-grown oxide buffer layers composed of La<sub>2</sub>Zr<sub>2</sub>O<sub>7</sub> and CeO<sub>2</sub> which are the same as the RABiTS template used with PLD. The W content of the NiW is either 5at% or 9at%. The CSD process mainly consists of preparation of the precursor solution of metallo-organic salts of Y, Ba and Cu (trifluoroacetates, TFA) with the right stoichiometric content to form YBa<sub>2</sub>Cu<sub>3</sub>O<sub>7- $\delta$</sub>  [8]. The deposition of the precursor solution on the substrate used slot die coating. Subsequent pyrolysis and annealing was done to dry the film and crystallize the YBCO with the right composition. The growth of the YBCO layer is laminar in CSD-route in contrast to the columnar growth in PLD.

A summary of the coated conductors investigated in this study is presented in table 3.1.

**Table 3.1:** Summary of the coated conductors investigated.

Sample Name	Nanocomposite addition	Superconductor deposition method	Buffer layers	Substrate	superconductor layer thickness ( $\mu\text{m}$ )
GdBCO-ISD	–	co-evaporation	MgO, ISD-MgO	Hastelloy C-276	2
YBCO-SS	–	PLD	PLD-CeO <sub>2</sub> + ABAD-YSZ	stainless steel	1.3
YBCO+BHO-SS	6 mol% BaHfO <sub>3</sub>	PLD	PLD-CeO <sub>2</sub> + ABAD-YSZ	stainless steel	1.2
YBCO+BYNTO-SS	5 mol% Ba <sub>2</sub> YNb <sub>0.5</sub> Ta <sub>0.5</sub> O <sub>6</sub>	PLD	PLD-CeO <sub>2</sub> + ABAD-YSZ	stainless steel	1.55
YBCO-Ni5W	–	PLD	270 nm-CSD-LZO + 30 nm CSD-CeO <sub>2</sub>	Ni-5at%W	1.7
YBCO-Ni9W	–	PLD	270 nm-CSD-LZO + 30 nm PLD-CeO <sub>2</sub>	Ni-9at%W	1.5
YBCO+BHO-Ni5W	6 mol% BaHfO <sub>3</sub>	PLD	270 nm-CSD-LZO + 30 nm CSD-CeO <sub>2</sub>	Ni-5at%W	1.7
YBCO+5BYNTO-Ni5W	5 mol% Ba <sub>2</sub> YNb <sub>0.5</sub> Ta <sub>0.5</sub> O <sub>6</sub>	PLD	270 nm-CSD-LZO + 30 nm CSD-CeO <sub>2</sub>	Ni-5at%W	1.6

Sample Name	Nanocomposite addition	Superconductor deposition method	Buffer layers	Substrate	superconductor layer thickness ( $\mu\text{m}$ )
YBCO+15BYNTTO Ni5W	15 mol% $\text{Ba}_2\text{YNb}_{0.5}\text{Ta}_{0.5}\text{O}_6$	PLD	270 nm-CSD-LZO + 30 nm CSD-CeO <sub>2</sub>	Ni-5at%W	1.6
YBCO-STO	-	PLD	-	SrTiO <sub>3</sub> (STO)	1
YBCO-mSTO	-	PLD	-	SrTiO <sub>3</sub> (STO) with different $\theta_v$	1-1.5
CSD-YBCO- Ni5W	-	CSD	270 nm-CSD-LZO + 30 nm CSD-CeO <sub>2</sub>	Ni-5at%W	1.5
CSD-YBCO- Ni9W	-	CSD	270 nm-CSD-LZO + 30 nm CSD-CeO <sub>2</sub>	Ni-9at%W	1.5

## 3.2 Angle-resolved $J_c$ measurements

### 3.2.1 Transport $J_c$

#### Cryostat and temperature regulation

The transport  $J_c$  measurement of the coated conductors was done in a Helium gas-flow cryostat equipped with a 6 T split-coil superconducting magnet. The sample rod was placed in a variable temperature insert (VTI) and the temperature can be stabilized from 4.2 to 300 K. The temperature variation was within  $\pm 0.06$  K. The  $V(I)$  curves were obtained using the four-probe method where the current was applied step-wise while the voltage was acquired. The CCs can be mounted on two different types of sample rod depending on the desired angular configuration of the magnetic field with respect to the sample surface.

#### Sample rods

The two sample rods available for the angle-dependent  $J_c$  measurement are both equipped with a stepper motor that controls the rotation of the whole rod about its axis, denoted by the angle  $\phi$  (see figure 3.5). With the horizontal field generated by the superconducting split-coil magnet, it is easy to realize maximum Lorentz force (MLF) configuration, where the applied field is maintained to be perpendicular to the direction of the current flow throughout the angular rotation. Both of the rods are capable of this rotation. The second rod, which will be referred to as the "two-axis rod" (figure 3.5) is equipped with an additional goniometer that allows rotation of the sample stage about an axis perpendicular to the rod and parallel to the sample surface (figure 3.5b). With the second rotation axis denoted by  $\theta$ , the angle between the applied magnetic field and current can be varied and thus, variable Lorentz force (VLF) configuration can be obtained.

Pressed indium was used for the current contacts in the single axis sample rod and silver paste for the voltage contacts. Tapes with typical width of 4-12 mm and length of 20-27 mm can be mounted and current up to 150 A can be applied.

The size of the tape that can be loaded in the two-axis rod has a maximum of 10 mm  $\times$  10 mm. The sample space is limited due to the additional gears for the horizontal rotation of the stage [82]. The current contacts and voltage contacts were all done using silver paste and the applied current was limited to 5 A.

For both of the rods, the angle  $\phi$  was checked using a Hall probe mounted in the sample stage. The rotation about the angle  $\phi$  has a precision of  $0.2^\circ$ . For the second angular rotation,  $\theta$ , in the two-axis rod, no Hall probe was attached to monitor the orientation of the field during the measurement. A calibration with a Hall probe was done prior to the measurement to determine the orientation of the



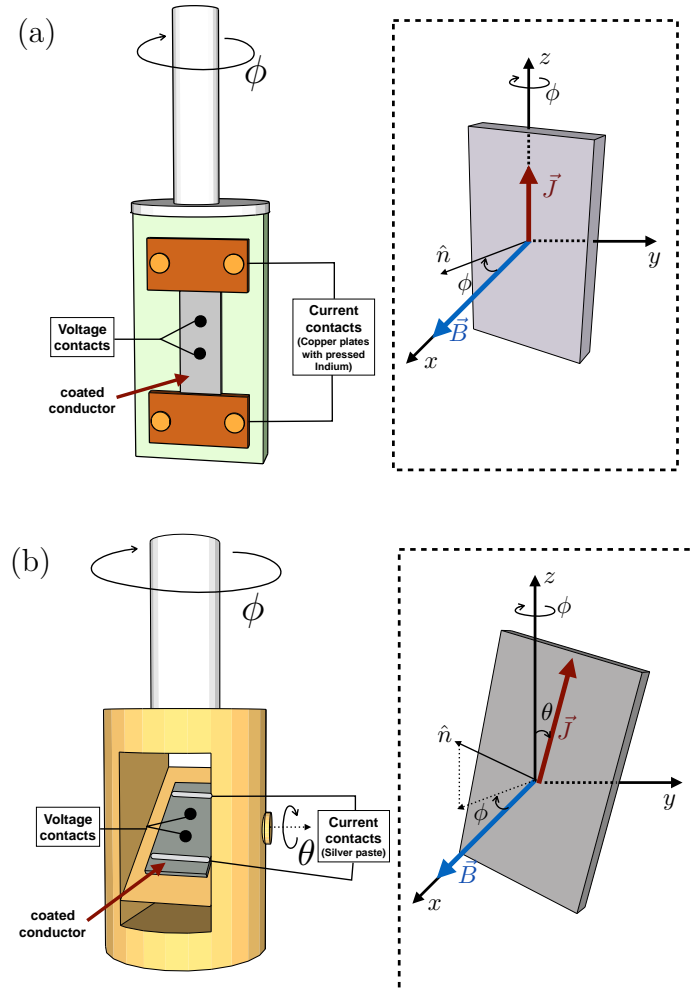


**Figure 3.5:** Sketch of the two sample rods used for the angle-resolved transport  $J_c$  measurements. (a) Single axis rod and (b) two axis rod.

field with respect to the sample stage. Therefore, with the additional uncertainty introduced by the backlash in the gears when the direction of rotation is reversed,  $\theta$  has a precision of about  $1^\circ$ .

The present state-of-the-art coated conductors have a typical self-field critical current  $I_{c,sf}$ , of 250-400 A at 77 K. Therefore, measuring  $I_c$  of full width conductors becomes a challenge especially at lower temperature ( $< 77$  K) due to the limitation of the available current supplies as well as Ohmic heating. To reduce the needed current, a bridge was patterned on the tapes and the method will be discussed in the next section.

### Micro-bridge Patterning

All the CCs used in this study have a silver protection layer of a few micrometers deposited on top of the superconducting layer. Two main methods were used to pattern a microbridge. The PLD-YBCO tapes fabricated in IFW Dresden were provided with laser-structured bridges done in Karlsruhe Institute of Technology. The other samples were patterned by chemical wet etching. A lacquer was used as mask to the etchants. The silver and YBCO layer were removed by Lugol's iodine solution and 1% nitric acid, respectively. Images of a laser-structured and chemically etched bridge are shown in figure 3.6.

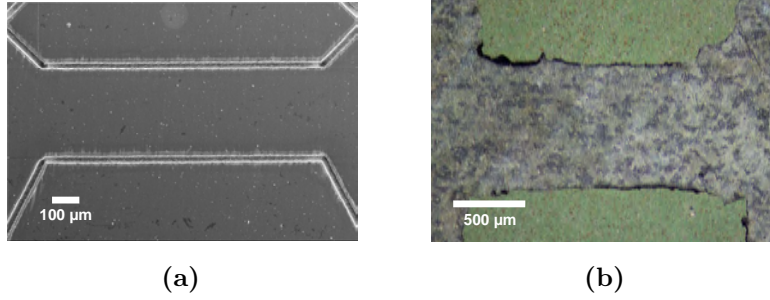


**Figure 3.6:** (a) SEM image of a laser-structured bridge. (b) Optical image of a chemically etched bridge.

### Evaluation of the critical current and N-value

All the experimental  $V(I)$ -curves has a transition that is well-described by the EJ power-law relation:

$$E(J) = E_c \left( \frac{J}{J_c} \right)^N \quad (3.1)$$

The critical current,  $I_c$ , was evaluated with an electric field criterion,  $E_c$ , of  $1 \mu\text{V}/\text{cm}$ .

A typical  $V(I)$  data is shown in figure 3.7a. The usual background noise in the voltage measurement was about 30 nV. As an example, the distance between the voltage contacts is 2 mm. Thus,  $I_c$  is the current at  $V_c = 0.2 \mu\text{V}$  indicated by the arrow in figure 3.7a.

The N-value, which is the exponent of  $J_c$  in the EJ-relation may be determined in two different ways. It can directly be obtained from the fit of the power-law and it can also be evaluated from the slope in the linear part of the logarithmic plot of  $V(I)$  as shown in figure 3.7b. The values of N from both methods are

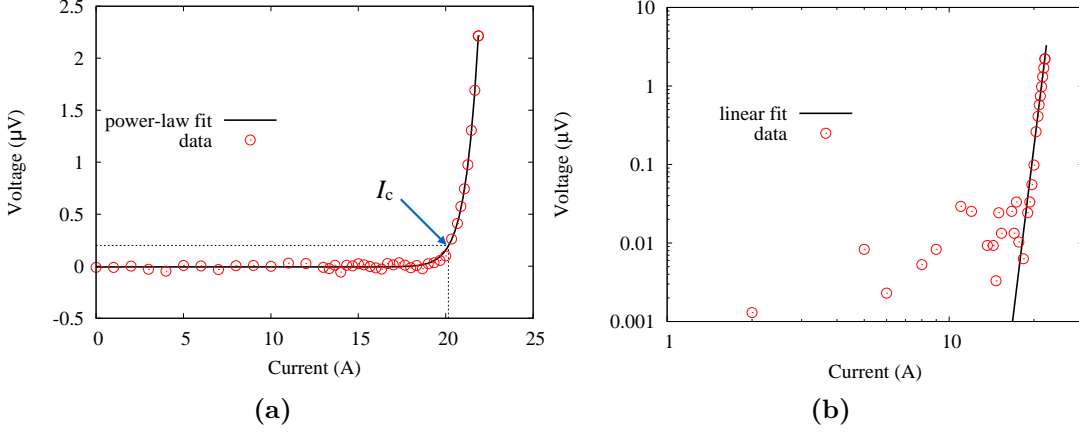


**Figure 3.7:** (a) Typical  $V(I)$  curve obtained from the transport measurement. The lines denote different  $E_c$  that determines  $I_c$ . (b) Logarithmic plot of the  $V(I)$ . The slope of the linear fit corresponds to the N-value.

not significantly different (about 0.3% difference from each other), therefore, the N-value was taken directly from the fit of the power-law for convenience.

### 3.2.2 Magnetic measurement of $J_c$

A few set of data of the angular dependence of  $J_c$  was measured by a vector vibrating sample magnetometer (VSM). The VSM is equipped with two sets of Mallinson coils and the component of the magnetic moment parallel and perpendicular to the applied field is measured.  $J_c(\phi)$  is evaluated from the width of the hysteresis loop and the net magnetic moment is evaluated as:  $m_{\text{net}} = \sqrt{\Delta m_{\parallel}^2 + \Delta m_{\perp}^2}$ , where  $m_{\parallel}$  and  $m_{\perp}$  are the irreversible magnetic moments parallel and perpendicular to the field, respectively. In a fully-penetrated state,  $J_c$  can be estimated for a rectangular-shaped sample using the Bean model as:

$$J_c = \frac{m_{\text{net}}}{V} \frac{4}{b \left(1 - \frac{b}{3a}\right)} \quad (3.2)$$

where  $V$  is the volume of the superconductor and  $a$  and  $b$  are the length and width, respectively, where  $a \geq b$ . An algorithm that includes a self-field correction was used to calculate  $J_c(B)$  [96].

The use of VSM becomes advantageous for measurements at low temperatures since there is no need for current contacts, sample heating is eliminated and the measurements are not limited by the applied current. However, the evaluation of the actual  $J_c$  can become tricky because of the currents closing the loop at

the ends of the sample that are subjected to variable Lorentz force (VLF). The VLF-contribution adds to the discrepancy between the evaluated  $J_c$  and the actual  $J_c$  measured from transport measurements. Hengstberger, et al. [48], have shown that this can be solved by the proper sample length that reduces the sensitivity of the VSM signal to the VLF currents. However, this is not feasible for some lab-scale samples with limited size. Aside from that, the calculation of  $J_c$  is impossible for the field orientation parallel to the  $ab$ -planes and to some angular range around it because the evaluation is only valid for a fully-penetrated state. The penetration field,  $H^*$ , is inversely proportional to the cosine of the angle  $\theta$ . Therefore, the VSM was used only to a few sets of data for a qualitative description of the angle-dependence of  $J_c$ .

### 3.3 Scanning Hall probe microscopy

Scanning Hall probe microscopy (SHPM) was used to directly image the magnetic properties of CCs. By moving a Hall probe in a reasonable proximity to the sample surface the local magnetic signal can be mapped. This yields information on the spatial characteristics of the superconducting layer such as defects and inhomogeneities.

#### 3.3.1 The cantilever

In the method of SHPM, a small distance of the Hall probe to the sample surface is important to enhance the resolution of the local magnetic field and will therefore improve the sensitivity of the measurement to local inhomogeneities. The Hall scanning set-up in the laboratory has previously utilized a holder for the Hall sensor with fixed Hall probe to sample distance,  $d$ , of about 200  $\mu\text{m}$  [34]. To enable a smaller distance to the sample surface, a holder with a cantilever was made. A schematic diagram of this holder is illustrated in figure 3.8.

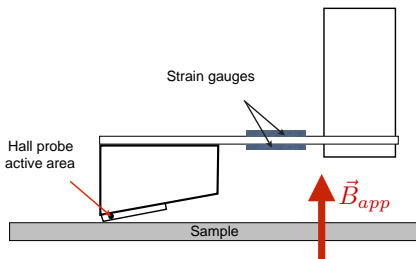


**Figure 3.8:** Schematic diagram of the cantilever holder for the Hall probe.

The cantilever was made of a carbon sheet and the Hall probe was placed on the other end of the support. The Hall probe was inclined by a few degrees to protect the active area when it comes in contact to the sample. Two strain gauges

serving as two resistors in a wheatstone bridge circuit were attached to the opposite sides of the carbon sheet. When the edge of the Hall probe comes in contact to the surface, the cantilever is bent or in strain changing the resistance of the two strain gauges and causing a non-zero voltage on the wheatstone bridge. This setup makes it possible to determine the onset of contact between the Hall probe and the sample surface (contact-mode). From this point, the distance to the surface can be adjusted more precisely.

### 3.3.2 SHPM in LN<sub>2</sub> bath

In one of the two setups for SHPM, the sample and the Hall probe are immersed in a LN<sub>2</sub> bath that provides a stable temperature of 77.2 K. Tapes with lengths of up to 22 cm can fit the scanning area. The position of the Hall probe is controlled by a stepper motor and the smallest step size possible in  $x$ ,  $y$  and  $z$  directions is 10  $\mu\text{m}$ . The Hall probe used in this system is a HHP-VC model from Arepoc with  $50 \times 50 \mu\text{m}^2$  active area and this limits the meaningful step size of the measurements to 50  $\mu\text{m}$ . According to the Hall probe specifications [2], the active area is 250  $\mu\text{m}$  from the corner edge. With the inclination of the designed holder of about  $3^\circ \pm 0.2^\circ$ , the distance,  $d$ , of the active area to the sample surface is approximately  $13 \pm 1 \mu\text{m}$  when the edge of the Hall probe is in contact to the sample surface. Scanning the sample in contact mode was possible by monitoring the change in voltage from the wheatstone bridge circuit and it gives additional advantage for long tapes since it assures a roughly constant distance  $d$ . Non-contact scans were made by making reference to the contact distance and adjusting  $d$  with an increment of 10  $\mu\text{m}$ . The control of the stepper motor, acquisition of Hall voltage and wheatstone bridge voltage are all done through a graphical user interface (GUI) programmed using C++.

For the process of magnetizing the tapes, a rectangular SmCo permanent magnet was used. This magnet generates a field of about 300 mT at a distance of 1 mm from the center of its surface to around 450 mT near its surface. This field was enough to introduce a fully penetrated state into the coated conductors at 77 K.

### 3.3.3 High-resolution SHPM

Another Hall scanning setup was used that was mounted in a He gas flow cryostat with variable temperature insert that allows control of temperature from 3 K to 300 K. The cryostat is equipped with a superconducting magnet that can generate magnetic fields up to 8 T. The Hall probe installed is a Magcam CSHP-400 with a  $400 \times 400 \text{ nm}^2$  active area and thus enables scans with higher resolution compared to the setup in LN<sub>2</sub>. The  $x$ ,  $y$  and  $z$  positions are controlled by piezo positioner and the scanning step width in  $x$  and  $y$  is limited by the distance of the Hall probe and sample surface, which is about 1  $\mu\text{m}$ . The maximum scanning area possible is  $3 \times$

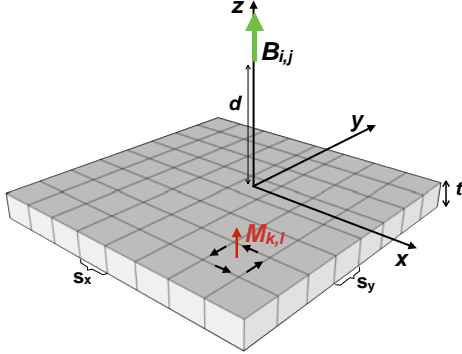


**Figure 3.9:** The coordinates used for the inversion algorithm.

3 mm<sup>2</sup>. Note that the positioners are not calibrated so there is about 10% and 40% differences between the actual dimension in the  $x$  and  $y$  directions, respectively.

Acquisition of Hall and strain gauge voltages, control of the magnet power supply, piezo positioners and temperature were all done through a GUI programmed using Python [45].

### 3.3.4 Spatial $J_c$ evaluation

The critical current density  $J_c$  was evaluated using an algorithm that inverts the Biot-Savart law using the information on the local magnetic field  $B$  obtained from the Hall scan measurements [49].

The method divides the whole scanning area into cubic volume elements with a constant  $M$  and with direction normal to the sample surface (see figure 3.9). This corresponds to a discretized integral equation:

$$B(\vec{r}) = \mu_0 M(\vec{r}) + \frac{\mu_0}{4\pi} \int \int dx' dy' \frac{M(x', y')(z - z')}{[(x - x')^2 + (y - y')^2 + (z - z')^2]^{3/2}} \Bigg|_{d+t}^d \quad (3.3)$$

$$B_{i,j} = \sum_{k=1}^{n_x} \sum_{l=1}^{n_y} K_{i,j,k,l} M_{k,l} \quad (3.4)$$

where  $t$  and  $d$  are the thickness of the superconducting layer and distance of the Hall probe to the sample surface, respectively.

The critical current density  $J_c$  is simply evaluated as the curl of the magnetization obtained after inversion of equation 3.4. This algorithm works well for very thin samples where  $J_c$  is assumed to flow only along the  $xy$ -plane and the second term in 3.3 vanishes for infinitely thick samples ( $z - z' \rightarrow \infty$ ).

In order to minimize the error in the magnetization profile obtained by inverting 3.4, it was found that the inversion procedure is well-conditioned if the  $d$  and the scanning stepwidths  $s_x$  and  $s_y$  satisfies the following condition:

$$s_x, s_y \geq d + t \quad (3.5)$$

Thus, for all the measurements, it was assured that this condition was satisfied.

### 3.3.5 Application to coated conductors

Since the thickness of the superconducting layer of CCs is much less than their lateral dimension, their geometry is that of a thin film. In the fully-penetrated state, the magnetic field profile,  $B(x, y)$ , can be predicted by using the assumption of the Bean model where  $J_c = \text{constant}$  and  $B_z(x, y)$  is calculated using Biot-Savart law with a sheet current density,  $\vec{J} = J_x \hat{x} + J_y \hat{y}$  [7]. The calculated  $B_z(x, y)$  and a schematic diagram of current flow is shown in figure 3.10.

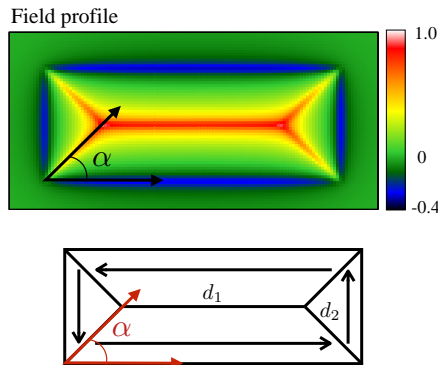


**Figure 3.10:** (Upper panel) Field profile of a homogeneous superconducting film with a constant  $J_c$ . (Lower panel) Schematic diagram of the current flow. The angle  $\alpha$  is also indicated on both pictures.

For a rectangular-shaped sample, the field profile has a roof-like structure. In the corresponding  $J_c(x, y)$ , closed loops of current flow around the entire superconducting area. Therefore, two types of discontinuity lines are formed. First is the zero- $J_c$  horizontal line ( $d_1$ ) at the center that corresponds to currents that flow in opposite directions and the second is where the currents change direction ( $d_2$ ). For an isotropic planar current, the angle  $\alpha$  of  $d_2$  with respect to the sample edges is  $45^\circ$ , as shown in figure 3.10.

#### Tilt effects of the Hall probe

As mentioned in section 3.3.1, the cantilever was designed such that the Hall probe has a maximum tilt of about  $3^\circ \pm 0.2^\circ$ . Therefore, the total magnetic field detected by the active area of the Hall probe must be a sum of the components of the radial

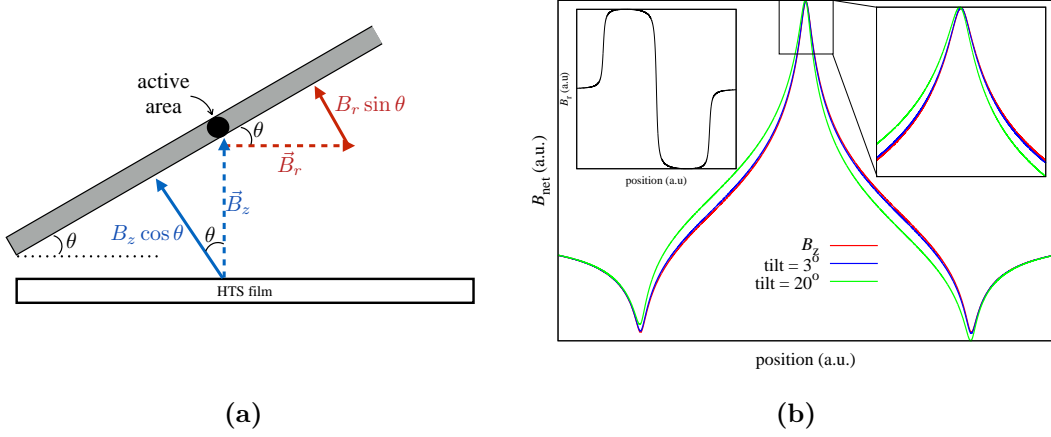


**Figure 3.11:** (a) Diagram of the net magnetic field detected by the tilted Hall probe. The tilt is exaggerated for illustration. (b) Calculated field profile with constant  $J_c$  including tilts of  $3^\circ$  and  $20^\circ$ . The inset on the left is the radial field profile and the inset on the right is an enlarged picture of the peak at the center of the sample.

field,  $B_r$ , and the out-of-plane field,  $B_z$ , as illustrated by the diagram in figure 3.11a. Therefore, the measured magnetic field is expressed as:  $B_{net} = B_z \cos \theta + B_r \sin \theta$  where  $\theta$  is the inclination of the active area of the Hall probe with respect to the surface of the film.  $B_z$  and  $B_r$  are calculated by solving Biot-Savart law assuming an infinite strip with a constant  $J_c$ . Results of the net field profile assuming  $\theta$  of  $3^\circ$  and  $20^\circ$  are presented in figure 3.11b. Notice that the radial component of field causes an asymmetry to the profile. However, a tilt of  $3^\circ$  does not cause a significant difference. Therefore, the effects of the tilt of the Hall probe is considered to be negligible in all the analyzed data.

### Magnetic background subtraction

Stainless steel and NiW are both magnetic materials. In the case of NiW, a higher amount of W leads to a smaller magnetic moment. The alloy with 9at%W has a magnetization of about  $0.25 \text{ Am}^2/\text{kg}$  at  $T = 77 \text{ K}$  and is around two orders of magnitude smaller than the one with 5at% W [35]. However, most of the CCs studied in this thesis are with Ni-5at%W. Therefore it is important to address the magnetic background introduced by the substrate.

In the remanent state, no visible alteration in the shape of the field profile is observed in both the SHPM in  $\text{LN}_2$ -bath and in the He gas-flow cryostat as shown in figure 3.12. Only a constant offset that is introduced both by the substrate and mostly of the Hall probe. Such constant background is subtracted prior to the evaluation of  $J_c$ .



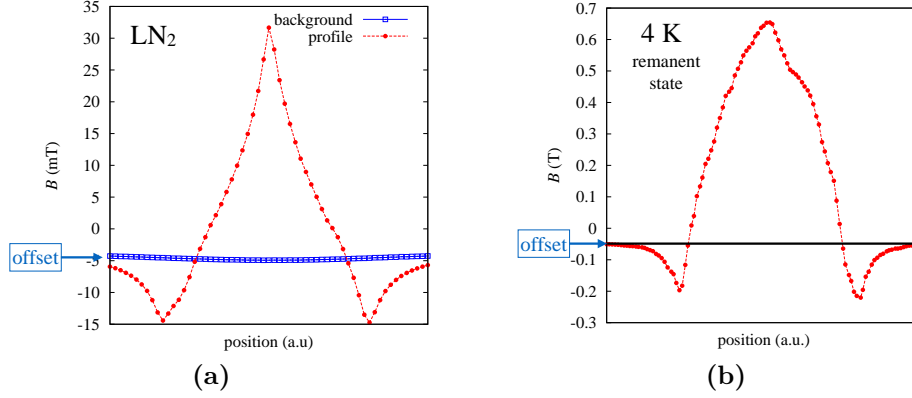


**Figure 3.12:** Experimental data at the remanent state in (a) in LN<sub>2</sub> and at  $T = 4$  K.

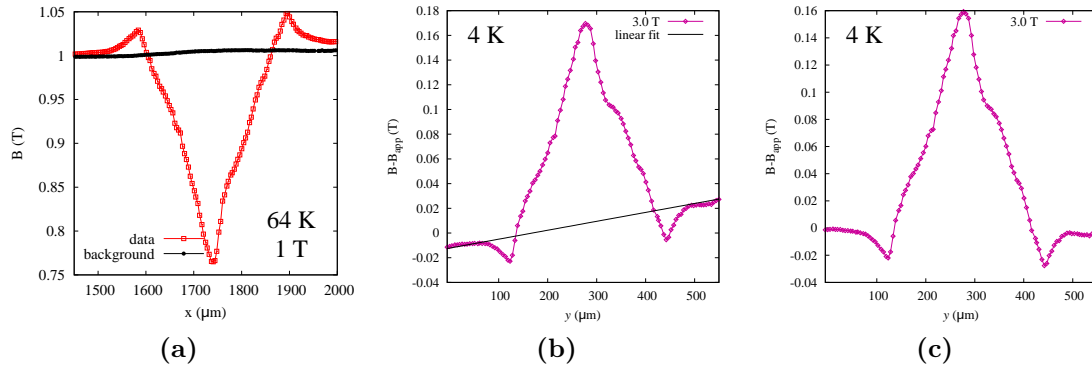


**Figure 3.13:** (a) Experimental data of the background and field profile at 64 K and 1 T. (b) Field profile data at 4 K and 3 T with a linear background. (c) Field profile after subtraction of the background.

On the other hand, once the field profiles are measured with an applied magnetic field, an asymmetry between the offsets at the two edges of the sample is observed and is shown in figure 3.13a. The asymmetry can be well described by a linear function and its slope increases as the applied field increases. Therefore, a linear background is subtracted from all the experimental data under an applied field as illustrated in figure 3.13b-c.

### Identifying defects

Through the measurement of the magnetic field profile and consequent evaluation of the spatial distribution of  $J_c$ , SHPM has been a powerful tool in identifying defects in CCs. Figure 3.14 shows a 15-cm piece of a coated conductor with macroscopic defects (denoted by the black arrows) that are introduced either as a physical damage during handling and/or transport or during the deposition of

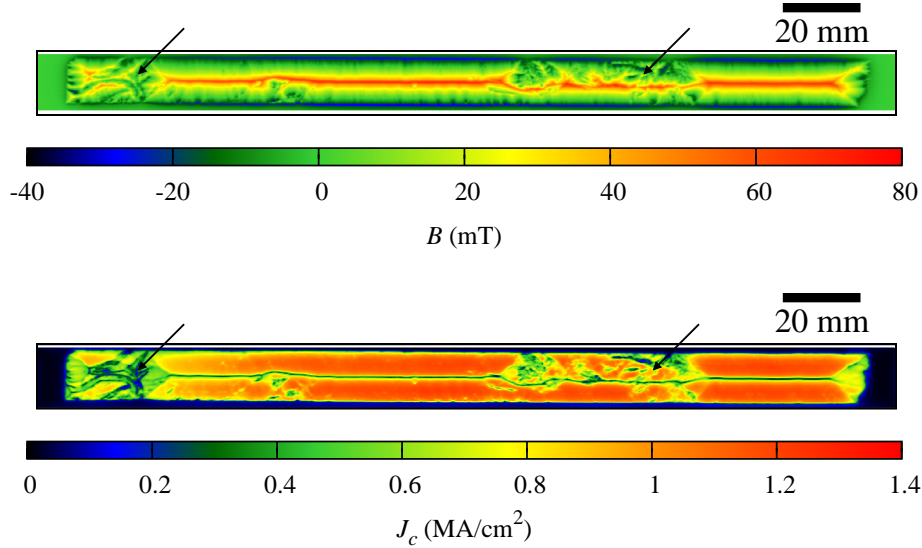


**Figure 3.14:** Remanent field profile (top) and local  $J_c$  map (bottom) of a 15-cm coated conductor measured in LN<sub>2</sub>. The areas denoted by the black arrows are macroscopic defects. The scanning parameters are:  $s_x = s_y = 200 \mu\text{m}$  and  $d = 15 \mu\text{m}$ .

the superconducting layer. For the industrial prototypes studied in this thesis, the areas with high and homogenous  $J_c$  were selected for transport measurements.

### Local dependence of $J_c$ in the low-field limit

In addition to identifying defects, the high spatial resolution of the SHPM has also revealed additional information about the critical current density of the coated conductors. The general shape of the field profile deviates from the prediction of the Bean model. The calculated  $B(x)$  plotted as the dot-dashed curve in figure 3.15 refers to a thin strip with a constant current density,  $J = J_c$  [7]. Compared to the calculated curve, all experimental data in the remanent state at  $T = 77 \text{ K}$  have a broader peak. The peak at the center is not as sharp as the predicted one. This behavior may be related to the non-linear flux diffusion during magnetic relaxation, which is usually characterized by the power law relation:  $E(J) = E_c(J/J_c)^N$ , where  $E$  is the electric field,  $J$  is the current density and  $N$  depends on the homogeneity of the superconducting layer and the present pinning centers [83]. At the center of the sample,  $E$  and  $J$  goes to zero due to the zero magnetix flux as the area enclosed by the circulating current becomes infinitesimally small. The reduction of  $J$  nearby the center then depends on the exponent  $N > 1$ , in the flux creep regime.

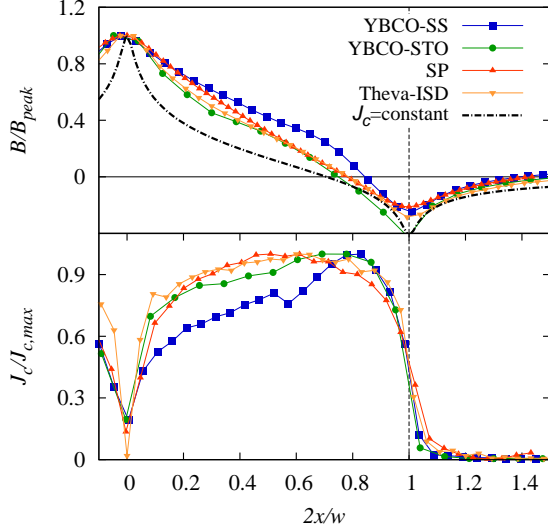


**Figure 3.15:** Remanent field (top) and  $J_c$  (bottom) profiles across half of the width of different YBCO films and tapes with rectangular geometry. The black dashed line denotes the sample edges.

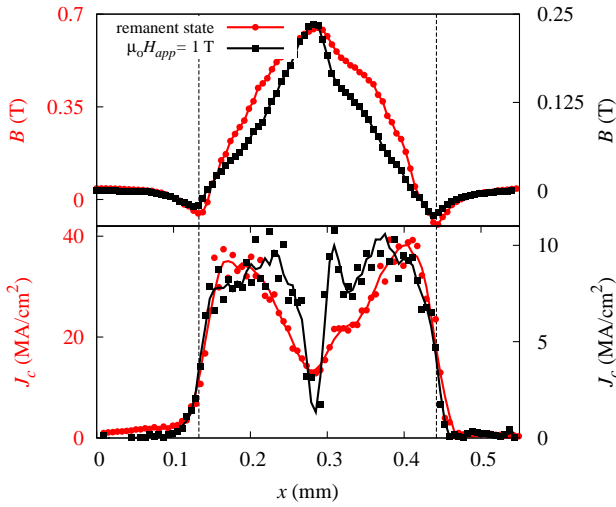


**Figure 3.16:** Field profile (top) and  $J_c$  (bottom) of sample YBCO-SS in the remanent state and with  $\mu_0 H_{app} = 1$  T. The measurement was made at 4 K with step-widths  $s_x = s_y = 5$   $\mu\text{m}$ . The black dashed lines denote the sample edges.

Away from the center,  $B(x)$  remains above the predicted curve and this behavior translates to a monotonic decrease of  $J$  towards the center. This directly corresponds to a dependence of the local  $J(x, y)$  on the local magnetic induction,  $B(x, y)$ . For instance, it is clearly observed in the YBCO-STO film that the maximum  $J(x)$  (lower panel) coincides with the position where  $B = 0$  in the upper panel of figure 3.15 and it continuously decreases towards the center as  $B$  approaches its maximum. The same behavior in the spatial variation of  $J$  in the remanent state is observed as well in a disk-shaped film with a higher resolution ( $s_x = 5$   $\mu\text{m}$ ) and closer distance of the Hall probe to the sample surface ( $d = 3$   $\mu\text{m}$ ) at  $T = 5$  K shown by the red curve in figure 3.16. As the field increases, the dependence of  $J_c$  on  $B$  is expected to be weaker which is indeed the case for the curve with  $\mu_0 H_{app} = 1$  T (black curve in figure 3.16). The field profile is steeper and the evaluated  $J(x)$  is flatter.

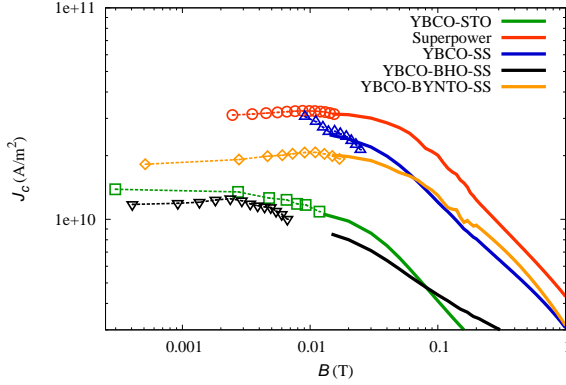


**Figure 3.17:** Field dependence of  $J_c$  of different YBCO films. The solid lines correspond to  $J_c$  evaluated from magnetization loops at 77 K and the symbols were extracted from the local  $J_c$  calculated from the Hall maps.

Figure 3.17 shows the  $J_c(B)$ -dependence of different samples at  $T = 77$  K. The solid lines were obtained from magnetization measurements using a VSM with the applied field parallel to the  $c$ -axis of YBCO [96]. The symbols correspond to data points extracted from the  $J$  maps along a line across the widths of the rectangular samples. The data points of  $J$  were taken between the position where the local field  $B(x, y)$  becomes zero and the center excluding the data very near the center where  $J$  decreases faster due to the sharp decrease of  $E$ . Since the field profiles refer to the fully-penetrated state, the values of  $J$  are equivalent to the critical current density,  $J_c$ , in the critical state model. Good agreement is obtained between the SHPM data and the magnetic  $J_c$  obtained from magnetization loops. As pointed out earlier, the maximum current density,  $J_{\max}$ , coincides with the position where  $B=0$  (see figure 3.15) for YBCO-STO. At this local point, the value of  $J_c$  is  $1.2 \text{ MA/cm}^2$  while the self-field  $J_c$  is  $1.06 \text{ MA/cm}^2$ . On the other hand, the  $J_{\max}$  of the CCs occurs at  $B \neq 0$ . This translates to a peak in the  $J_c(B)$ -dependence. The appearance of such a peak was also observed in magnetization [72] and transport measurements [36] and is attributed to the granularity of the YBCO layer on metallic substrates. The peak is expected to be very small at 77 K and close to  $B = 0$ , especially if the grain size is small ( $< 1 \mu\text{m}$ ), which is indeed the case for the investigated tapes. Since the evaluation of  $J(x, y)$  from  $B(x, y)$  allows access to values of  $J_c$  when  $B$  is locally zero, we were able to observe this effect.  $J_c$  is obtained for fields well below the self-field, a field range which is not accessible by magnetization nor transport measurements [58].

### 3.4 Microstructural analysis

Additional microstructural analysis was used in this thesis, such as scanning electron microscopy (SEM), electron backscatter diffraction mapping (EBSD) and transmission electron microscopy (TEM). The SEM and EBSD analyses were done at IFW Dresden and the TEM measurements were obtained in the electron microscopy for materials science laboratory at University of Antwerp, Belgium and the electron

microscopy laboratory at TU Wien. Since structural studies is beyond the focus of this thesis, only a brief discussion will be devoted on them in this section.

The SEM was used for imaging surface features of the YBCO layer using a JEOL-JSM-6510 SEM at an acceleration voltage of 20 kV. Spatial analysis of the crystal orientation is done by utilizing EBSD patterns that were indexed using a cubic cuprate phase. The details about the analysis are discussed in reference [71]. TEM was used to determine the microstructural defects in the films together with high angle annular dark field scanning transmission electron microscopy (HAADF-STEM) and energy dispersive X-ray spectroscopy (EDX).

# Chapter 4

## REBCO films with tilted $c$ -axis

In this chapter, properties of REBCO films with tilted  $c$ -axis with respect to the substrate surface were studied both by scanning Hall probe microscopy and transport  $J_c$  measurements. The geometry of the superconducting layer in these samples is unique. Unlike the “conventional” films and tapes where the  $ab$ -planes and  $c$ -axis are usually parallel and perpendicular to substrate surface, respectively, the main directions of the crystal structure in ISD-buffered films are tilted with respect to the tape surface as discussed in section 3.1.1.

In earlier studies, single-crystalline SrTiO<sub>3</sub> (STO) with different miscut angles were used to induce the tilted  $c$ -axis of the superconducting layer. Investigations were performed in these films to elucidate the structure and pinning mechanism of the flux-line lattice in layered superconductors such as YBCO [20]. The design of the tilted  $c$ -axis growth is now transferred to coated conductor technology using an inclined substrate deposition of the buffer layer on a metallic template. The ISD-buffered CCs have promising performance since  $J_c$  does not decrease with increasing thickness because the growth of  $a$ -axis grains is avoided. Therefore, the critical current,  $I_c$ , can be raised to a higher value with a present record of 1000 A/cm-width as a self-field  $I_c$  at 77 K [23].

In the succeeding sections, a discussion about the anisotropic planar current flow in films with tilted  $c$ -axis will be presented first using SHPM followed by an extensive investigation of the angle-resolved  $J_c$  measurements on ISD-buffered CCs (GdBCO-ISD). Some of the discussions were taken verbatim from the published paper on the anisotropy of critical current density in these tapes [57].

### 4.1 Microstructure

#### 4.1.1 YBCO on miscut SrTiO<sub>3</sub> substrate

The growth of the YBCO crystal structure on miscut single crystalline STO has a step-flow growth mode [39]. The orientation of the  $c$ -axis of the YBCO layer grown on top of the mSTO substrate by PLD is oriented perpendicular to the surface of

the steps. As discussed in section 3.1.2, the inclination angle of the  $c$ -axis with respect to the direction normal to the surface of the film is roughly the same as the vicinal angle of the substrate.

Although actual TEM images are not available for the PLD-YBCO-mSTO films in this study, results of PLD-YBCO on a conventional (without miscut) [001]-STO substrate typically indicate the formation of  $Y_2O_3$  nanoparticles of about 2-200 nm in size.

#### 4.1.2 GdBCO on ISD-buffered coated conductor

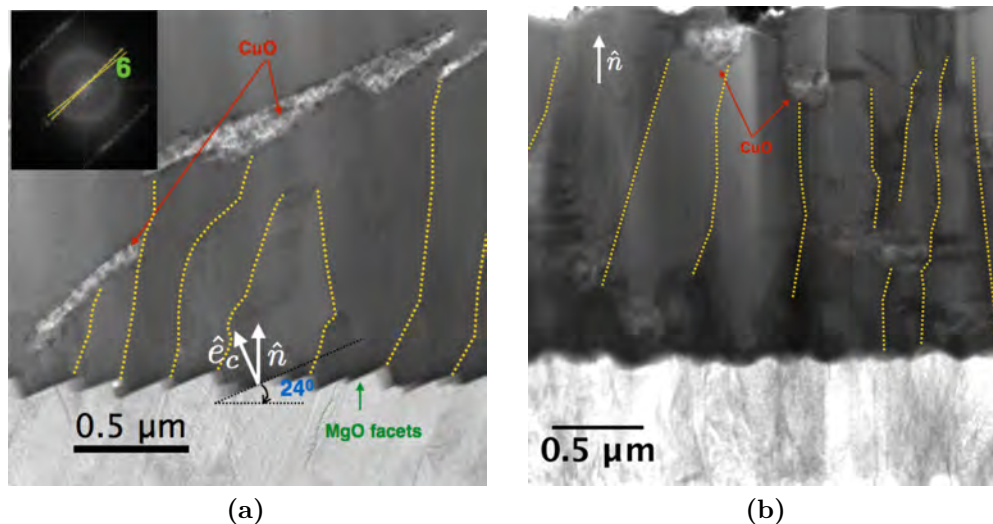


**Figure 4.1:** Annular bright field image of the (a) transverse lamella and (b) longitudinal lamella. Large CuO precipitates are present and the dashed yellow lines indicate the grain boundaries. The inset in (a) is a diffractogram obtained from a HRTEM image of a grain boundary showing a small misorientation of the two neighbouring grains of about  $6^\circ$ .

Lamellae of the GdBCO-ISD sample for TEM investigations were cut in longitudinal and transverse direction. Results are presented in figure 4.1. The  $c$ -axis of the GdBCO layer is confirmed to be tilted by about  $24^\circ$  with respect to the direction normal to the surface. The misorientation of the MgO columns is directly transferred to the GdBCO layer forming grain sizes from 200 nm to 900 nm. The grain boundary misorientation angles are small ( $< 10^\circ$ ) as shown by a diffractogram in the inset of figure 4.1a. These inclined GBs are a characteristic of ISD-CCs and were also found in  $DyBa_2Cu_3O_{7-\delta}$  tapes grown by the same technique [23]. The GBs in the longitudinal lamella are planar and normal in average as shown in figure 4.1b.

A high density of stacking faults, which were characterized by double CuO chain intergrowths, was found in a HRTEM image of the sample. Large CuO precipitates

were also observed in the GdBCO layer of both lamellae. The composition of these precipitates was confirmed by EDX. They are roughly cylindrical with their axis perpendicular to the tape direction and tilted by about  $10^\circ$ - $20^\circ$  from the  $ab$ -planes (figure 4.1a-b). The formation of  $a$ -axis grains that leads to HAGBs is also avoided in this sample.

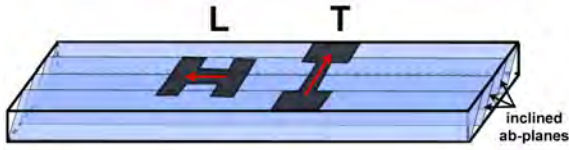


**Figure 4.2:** Schematic diagram of the two bridge-configurations, L-bridge and T-bridge, patterned on the tape. The red arrows show the current directions.

Because of the reduced symmetry by the tilted crystal structure, two configurations of bridges were patterned from the tape and are illustrated in figure 4.2. The first one was parallel to the longitudinal direction in which the current flows along the  $ab$ -planes. It will be referred to as L-bridge. The second was in transverse direction, called T-bridge, in which the current crosses the  $ab$ -planes. Wet chemical etching as described in section 3.2.1, was performed to narrow the width of the bridges down to  $350\ \mu\text{m}$  for the L-bridge and  $180\ \mu\text{m}$  for the T-bridge. The angle-resolved transport  $J_c$  of both bridges were measured in maximum Lorentz force (MLF) and variable Lorentz force (VLF) configurations. The VLF measurement was conducted with the two-axis rod discussed in section 3.2.1.

## 4.2 Magnetic field profiles

The spatial distribution of  $J_c$  of the YBCO-mSTO samples with  $\theta_v = 5^\circ, 10^\circ, 15^\circ, 25^\circ$  are shown in figure 4.3a. The thickness of the YBCO layer in these films is about  $1\ \mu\text{m}$ .  $J_{c,L}$  and  $J_{c,T}$  denote the currents flowing parallel and transverse (having a component along the  $c$ -axis) to the  $ab$ -plane, respectively as illustrated by a schematic diagram in figure 4.3d. In the YBCO-mSTO film with  $\theta_v = 25^\circ$ , the planar anisotropy  $\Gamma = J_{c,L}/J_{c,T}$  is the largest. As expected,  $J_{c,T}$  is smaller than  $J_{c,L}$  due to the partial flow of the current through the more weakly superconducting layers between the  $ab$ -planes. As a consequence of the  $J_c$ -anisotropy, the orientation of the  $d_2$ -line in  $J_c(x, y)$  deviates from  $45^\circ$  as discussed in section 3.3.5, and follows the relation  $\tan \alpha = J_{c,L}/J_{c,T}$ , where  $\alpha$  is the angle between the sample edge and the  $d_2$ -line [84]. Similar to previous results reported for vicinal films of pure YBCO [10, 19, 75],  $\Gamma$  at  $T=77\ \text{K}$  is small up to  $\theta_v = 10^\circ$  and remains below 2 up to  $25^\circ$  as shown by the circles in figure 4.3c. However, it is also observed that both  $J_{c,L}$  and  $J_{c,T}$  of YBCO-mSTO films decrease as the vicinal angle of the substrate increases. The overall decrease of  $J_c$  can be attributed to an increasing density of microstructural defects such as pores found by scanning electron microscopy (SEM) images of the surfaces of the films (figure 4.3b).



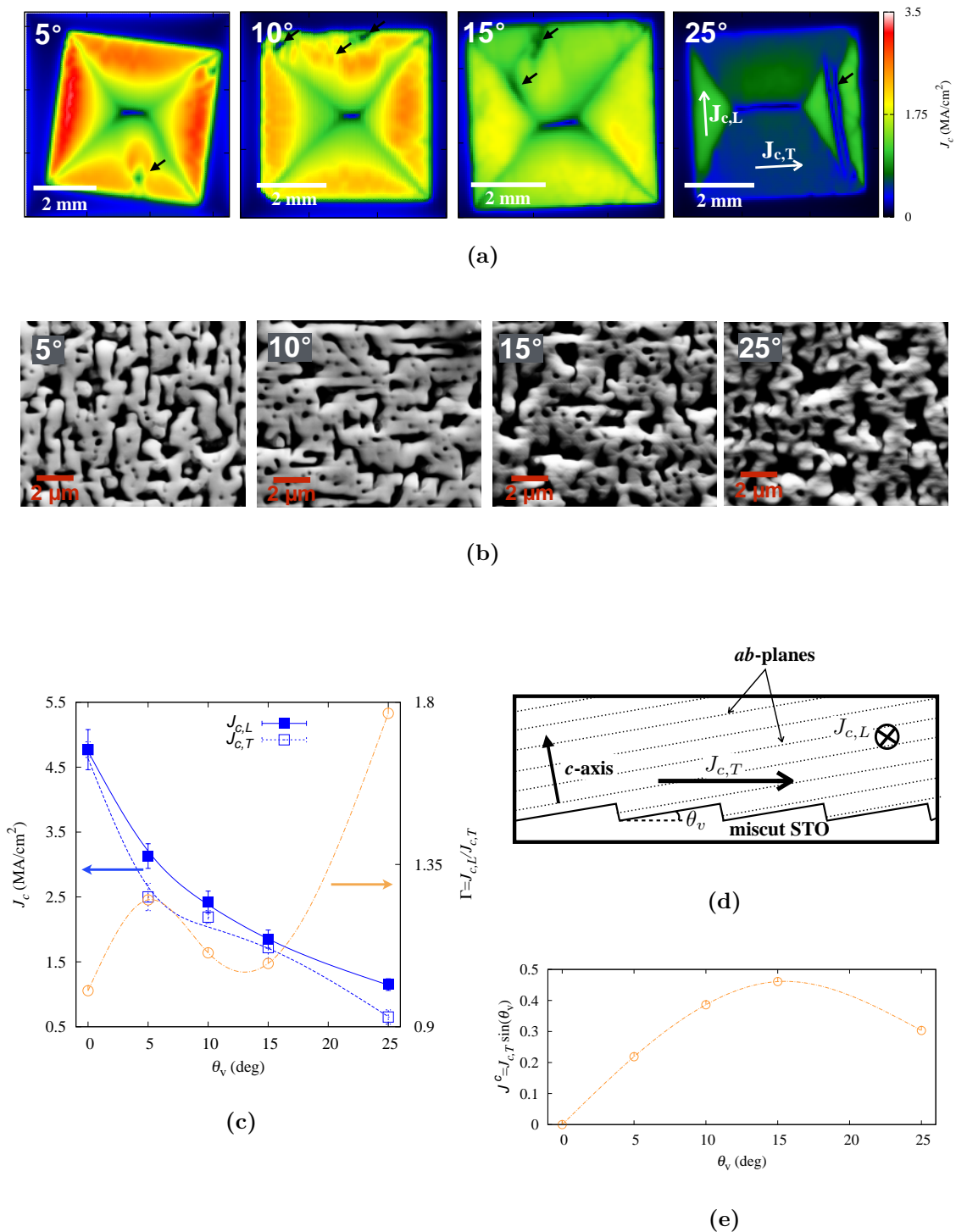


**Figure 4.3:** (a)  $J_c$  distribution of the YBCO films on miscut STO at vicinal angles of  $5^\circ$ ,  $10^\circ$ ,  $15^\circ$  and  $25^\circ$ . Some defects are indicated by the black arrows and the direction of the currents,  $J_{c,L}$  and  $J_{c,T}$  are shown on the film with  $\theta_v = 25^\circ$  – the film with largest current anisotropy. (b) SEM images of the surface of the YBCO-mSTO films. (c) Dependence of  $J_c$  and  $\Gamma$  on the vicinal angle,  $\theta_v$ . (d) Schematic diagram of the current flow. (e) Component of  $J_c$  parallel to the  $c$ -axis.

The component of  $J_{c,T}$  flowing parallel to the  $c$ -axis, can be expressed as  $J^c = J_{c,T} \sin(\theta_v)$ . In the  $J_c(\theta_v)$  dependence in figure 4.3e, a maximum in  $J^c$  occurs at  $\theta_v = 15^\circ$  with a value of around  $0.45 \text{ MA/cm}^2$ . This can be taken as the lower limit of the  $c$ -axis current,  $J_c^c$  in our case. It is not likely that  $J_{c,T}$  is limited by the current flowing parallel to the  $c$ -axis below  $15^\circ$  due to geometrical reasons while the decrease of  $J_c$  at  $25^\circ$  may be due to the presence of additional defects obstructing the transverse current flow. Note that the derived values of  $J^c$ , i.e. the lower limit of  $J_c^c$ , is up to two orders of magnitude higher than the self-field  $J_c^c$  value of about  $4 \text{ kA/cm}^2$  reported by Y. Jia et al. [52] who have measured  $J_c^c$  along the  $c$ -axis by transport measurements [58].

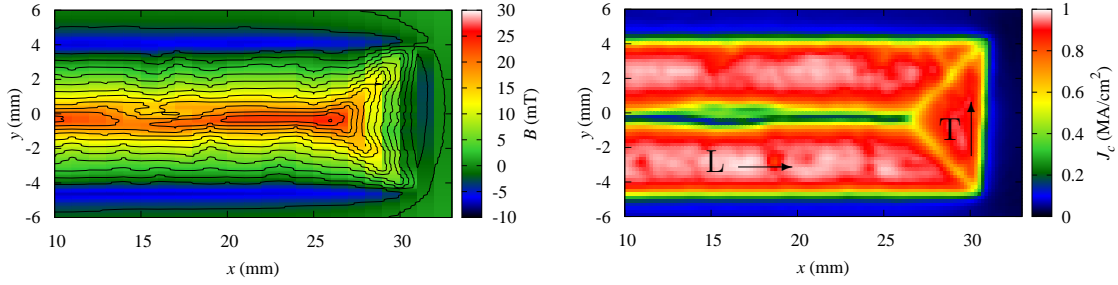


**Figure 4.4:** Remanent field profile (left) and the evaluated spatial- $J_c$  (right) of the unpatterned GdBCO-ISD tape. Notice the slight difference in the value between the transverse and longitudinal currents. The Hall mapping was done in LN<sub>2</sub> bath with a scanning stepwidth of  $200 \mu\text{m}$  and a Hall probe-sample distance of  $50 \mu\text{m}$ .

On the other hand, figure 4.4 shows the remanent field profile and the evaluated  $J_c$ -map of a piece of the GdBCO-ISD tape with a  $2 \mu\text{m}$ -thick GdBCO layer. Both the  $B(x, y)$  and  $J_c(x, y)$  show that the superconducting layer is deposited homogeneously along the length with minimal defects at the transverse edges. Along the longitudinal direction of the tape, the average  $J_{c,L}$  is  $0.96 \pm 0.01 \text{ MA/cm}^2$  and is slightly larger than the average  $J_{c,T}$  along the transverse direction with a value of  $0.89 \pm 0.01 \text{ MA/cm}^2$ . This translates to an anisotropy of only about 1.3 which is smaller compared to  $\Gamma = 1.8$  of the  $25^\circ$  miscut YBCO-mSTO, although the average tilt of the  $c$ -axis of the GdBCO-ISD sample is about  $24^\circ$  which is comparable to the film with  $25^\circ$  miscut substrate. The difference in the values of  $\Gamma$  is also depicted clearly in the  $J_c$ -maps in figures 4.3a and 4.4. The GdBCO layer was deposited by co-evaporation and the defects formed in the superconducting matrix include inclined grain boundaries and large CuO precipitates, which are roughly cylindrical and tilted  $10 - 20^\circ$  from the  $ab$ -planes [57]. On the other hand, the YBCO-mSTO films have  $\text{Y}_2\text{O}_3$  nanoprecipitates. In previous studies conducted on pure YBCO films on miscut STO, anti-phase boundaries (APBs) oriented normal to the surface were found and they caused additional pinning especially in applied fields and caused

an enhancement in  $J_{c,L}$  but not in  $J_{c,T}$  [53]. The different structure of secondary phases, defects and the absence of correlated pinning centers perpendicular to the substrate surface in the GdBCO-ISD tape therefore lead to smaller planar current anisotropy compared to the YBCO-mSTO films.

## 4.3 Angular dependence of $J_c$ in longitudinal current direction

### 4.3.1 $J_{c,L}$ at maximum Lorentz force

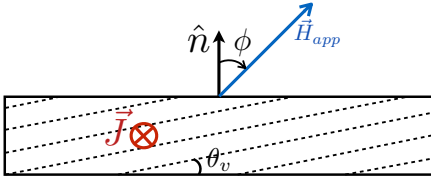


**Figure 4.5:** Schematic diagram of the MLF configuration of the L-bridge. The angle  $\phi$  denotes the angle of the applied field from the direction normal to the tape surface,  $\hat{n}$ .

A 400  $\mu\text{m}$ -width L-bridge was patterned for the angle-resolved  $J_c$  measurement in MLF configuration. The self-field  $J_c$  at  $T=77$  K is 1.1 MA/cm<sup>2</sup>. The 12% difference from the  $J_{c,L}$  calculated from the inversion of the Hall map in section 4.2 is expected if the electric field criterion and the temperature of the measurement is considered. The electric field during SHPM is much lower than the criterion for the transport measurement and temperature of the LN<sub>2</sub> bath is about 0.2 K higher than the stabilized temperature in transport measurement.

Figure 4.5 shows the schematic diagram of the MLF configuration in the L-bridge. The angle  $\phi$  denotes the orientation of the applied field,  $H_{\text{app}}$ , with respect to  $\hat{n}$ . Based on this convention,  $\phi = 90^\circ$  when  $H_{\text{app}}$  is parallel to the tape surface and  $\phi = 90 - \theta_v$  when it is parallel to the  $ab$ -plane. Therefore, for  $\theta_v = 24^\circ$ , a large peak at  $\phi = 66^\circ$  is observed in figure 4.6a. This peak is related to the intrinsic pinning by the tilted  $ab$ -planes and additional pinning contribution from the stacking faults parallel to the these planes. Hereafter, this peak will be referred to as the  $ab$ -peak. The presence of a peak in the direction of  $\hat{n}$  is induced by growth-related defects parallel to this direction. The angular dependence of  $J_c$  has a direct correlation to the behavior of  $N(\phi)$  in figure 4.6b. Since the IV-curves are well described by a power law dependence, the exponent  $N$  can be related to the potential barrier  $U_p$  that inhibits the motion of vortices in the flux creep regime [63].  $J_c(\phi)$  and  $N(\phi)$  are directly correlated with each other, the peaks are centered on the same angular positions on both plots, although the asymmetric  $ab$ -peaks in  $J_c(\phi)$  appear to be symmetric in the  $N(\phi)$ , which is especially visible in the 5 T curve.

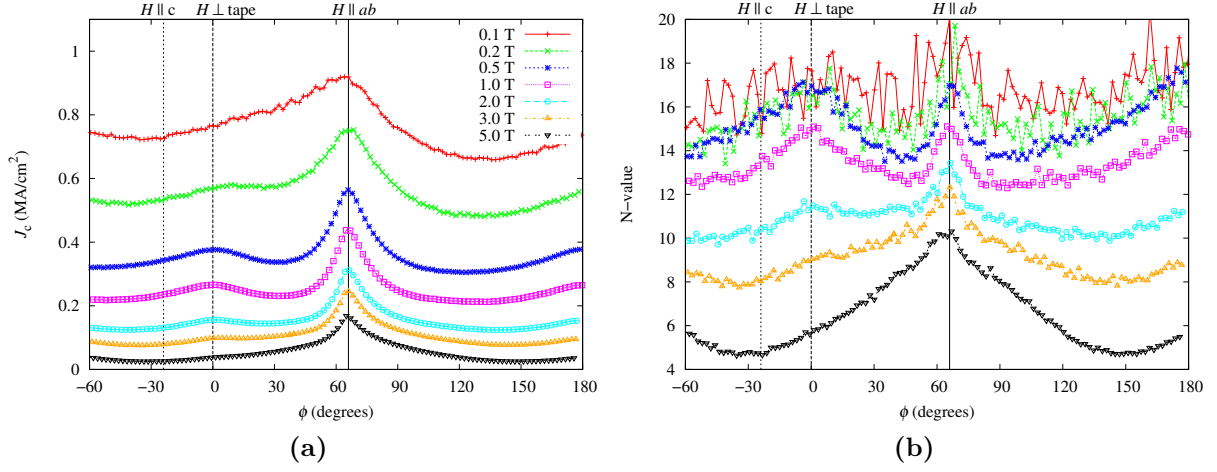


**Figure 4.6:** (a)  $J_c(\phi)$  and (b) N-value at  $T = 77$  K and different applied fields for the L-bridge at MLF.

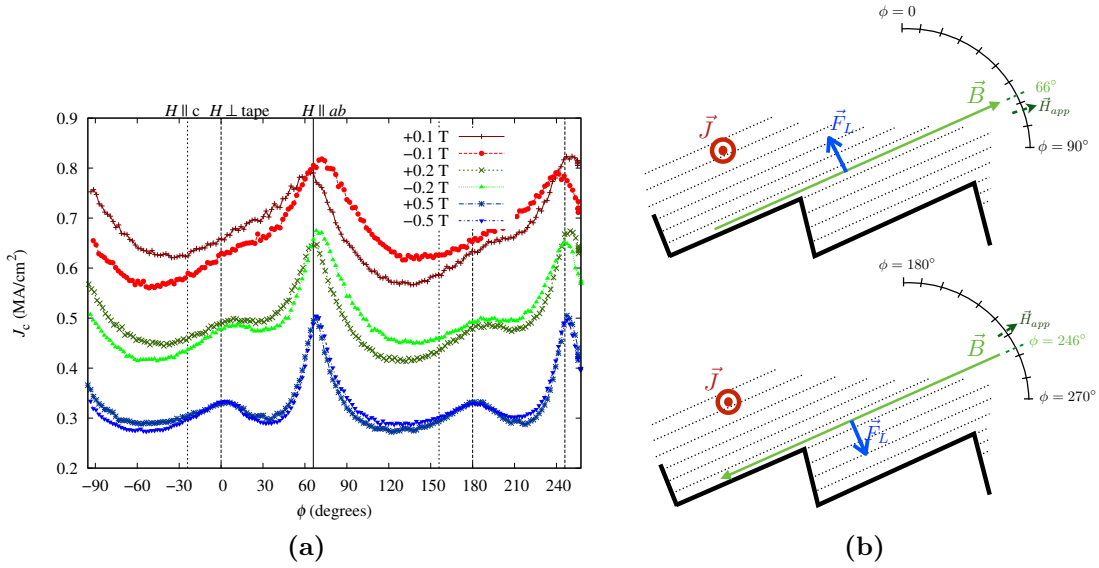


**Figure 4.7:** (a)  $J_c(\phi)$  at 77 K and low fields. (b) Schematic diagram of  $\vec{B}$  and  $\vec{F}_L$  that influence the asymmetry and shift of the  $ab$ -peak at low fields.

For 0.5 T and below, a slight shift of the  $ab$ -peak and difference in height between  $\phi = 66^\circ$  and  $\phi = 246^\circ$  are observed as shown in figure 4.7a.  $J_c(\phi)$  is highly asymmetric around  $H \parallel ab$ , which led to a periodicity of  $360^\circ$  instead of the usual  $180^\circ$  for conventional tapes. Upon reversing the direction of  $\vec{H}_{app}$ , which effectively reverses the direction of the Lorentz force,  $F_L$ , the whole behavior of  $J_c(\phi)$  flips indicating the influence of the direction of  $F_L$ . As shown by the schematic diagram in figure 4.7b, the shift of the peak at  $\phi = 66^\circ$  (top of figure 4.7b) is probably due to a slight misalignment between  $\vec{H}_{app}$  and local field  $B$ . Since the tendency

of a vortex is to align with the  $ab$ -plane, the direction of  $\vec{F}_L$  becomes in favor for the vortex to remain aligned with the  $ab$ -plane even if of  $\vec{H}_{app}$  was already tilted. The higher peak in the same position also indicate the entry of the vortices from the superconductor-MgO interface which introduces additional surface pinning compared to the exit of vortices depicted in the other direction ( $\phi = 246^\circ$ ). The misalignment between  $\vec{H}_{app}$  and  $B$  was already predicted and reported before for films with tilted geometry [65,95] as well as the effect of surface pinning on the  $J_c$ -anisotropy at low fields [44].

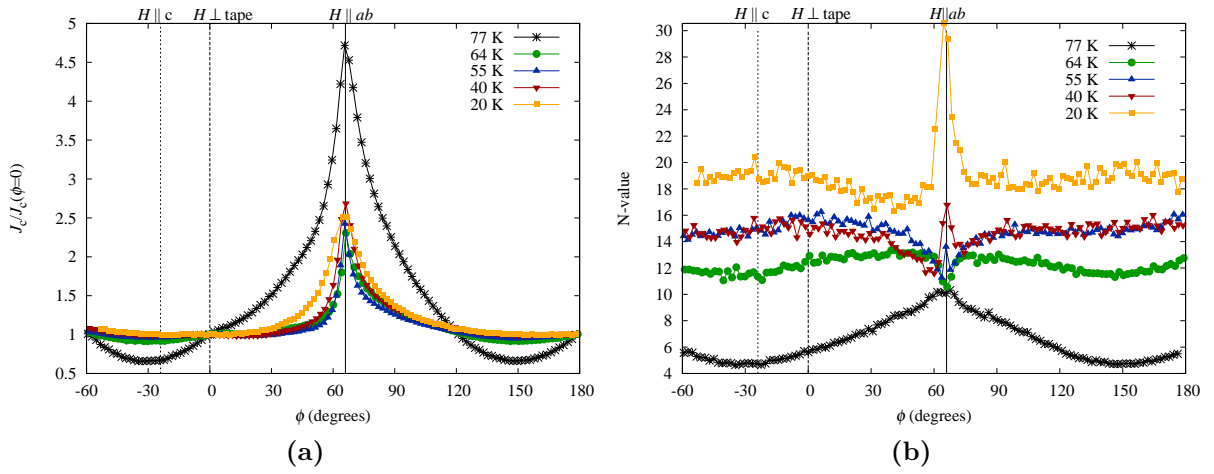


**Figure 4.8:** (a)  $J_c(\phi)$  and (b)  $N(\phi)$  at different temperatures and  $\mu_0 H_{app} = 5$  T.

The asymmetry of the  $ab$ -peak persists in the  $J_c$ -anisotropy as the applied field is increased.  $J_c(\phi)$  is presented for  $\mu_0 H_{app} = 5$  T at different temperatures from 20 K to 77 K in figure 4.8a. As the applied field increases, the reproducibility of the  $J_c(\phi)$  curve upon the reversal of the field and rotation improves. This means that the effects of the surface barrier and the misalignment between  $\vec{H}_{app}$  and  $\vec{B}$  become negligible.

With the data normalized to  $J_c(\phi = 0)$  in figure 4.8a, the anisotropy at 77 K is observed to be biggest and leads to a higher and broader peak. This is probably an effect of the lower irreversibility field for  $H_{app} \parallel c$  at 77 K, which increases the ratio of  $J_c$  between the  $ab$ -plane and  $c$ -axis directions. As the temperature decreases, i.e. 64 K and below, the  $ab$ -peak becomes sharper and the anisotropies are similar down to 20 K.

In the corresponding plot of  $N(\phi)$  (figure 4.8b), an inverse correlation of the  $N$ -value and  $J_c$  is observed at 64 K and 55 K. The appearance of a dip at  $\phi = 66^\circ$ , which corresponds to the direction of the  $ab$ -planes, signifies the occurrence of the kinked vortex state. Since  $N \propto U_p$ , the formation of the kinks lowers the vortex energy and is manifested as a decrease in the  $N$ -value. As the temperature decreases ( $T=40$  and 20 K), a peak begins to appear that indicate a pseudo-lock-in state at which a longer segment of a vortex aligns with the  $ab$ -planes. Since energy is

gained when the vortices lock in the planes, the N-value is increased accordingly. Another interesting feature of the  $J_c$ -anisotropy is the persisting asymmetry of the  $ab$ -peak where  $J_c$  in the range of  $66^\circ < \phi < 90^\circ$  is higher than in the range  $42^\circ < \phi < 66^\circ$ . This behavior is observed as well in ISD-buffered tapes with thicker GdBCO layer. However, the specific mechanism that leads to this asymmetry remains to be identified.

### 4.3.2 $J_{c,L}$ at variable Lorentz force

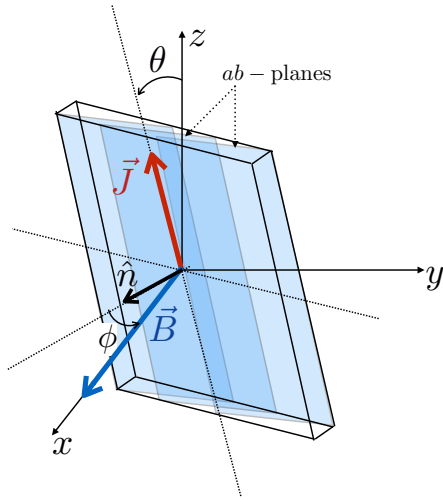
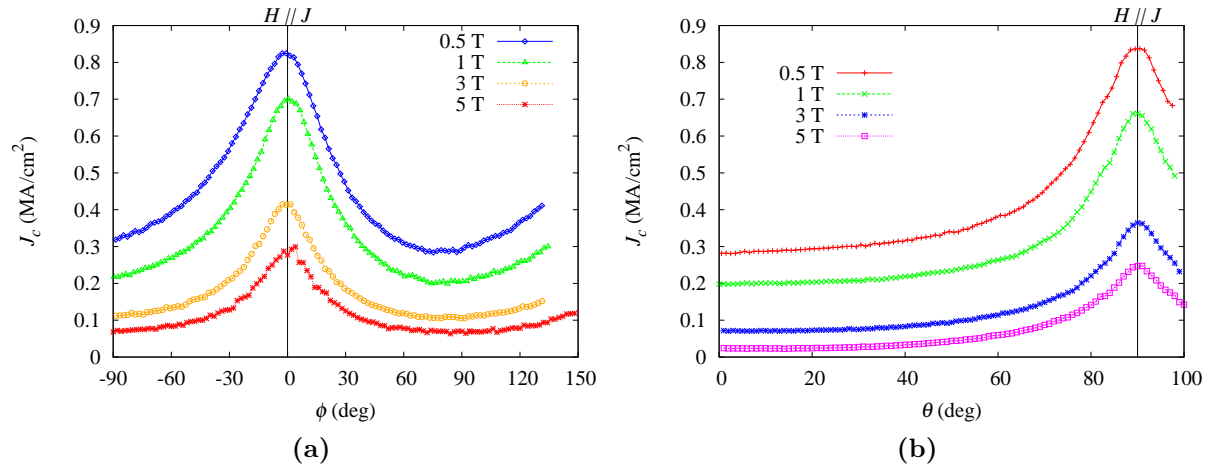


**Figure 4.9:** Geometry of the VLF configuration of the L-bridge.

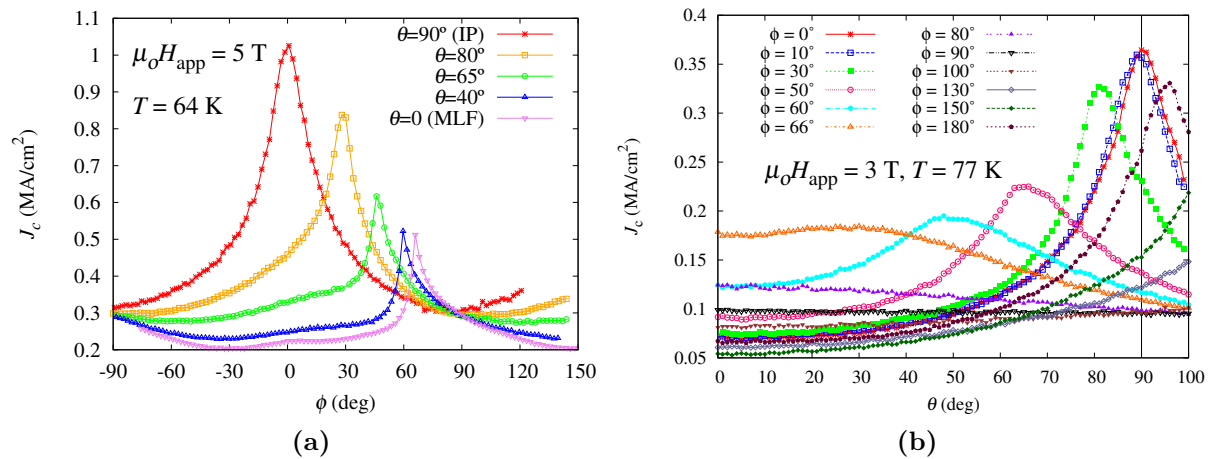
In view of applications of CCs, it is also interesting to investigate the  $J_c$ -anisotropy in VLF since a large  $J_c$  may be achieved if the "force-free" (FF) geometry could be realized. The FF-orientation is characterized by a formal zero Lorentz force by having parallel  $\vec{H}_{\text{app}}$  and macroscopic  $\vec{J}$  [66]. The most common VLF measurement is the in-plane (IP) configuration where the applied field is maintained parallel to the tape over the entire angular scan. By convention of the measurement geometry shown in figure 4.9, IP configuration is attained at  $\theta = 90^\circ$  while an angular rotation in  $\phi$  is done. The FF orientation in an IP scan is at  $\phi = 0$ . Force-free is also obtained in another configuration if  $\phi$  is fixed at zero and rotation is done in  $\theta$ . The FF direction in this case is at  $\theta = 90^\circ$ .

Figure 4.10 shows the IP scan and the  $\theta$  scan at  $\phi = 0$  at 77 K and different applied magnetic fields. The peaks in plots both correspond to the FF peak where  $\vec{H}_{\text{app}}$  is parallel to the macroscopic flow of  $\vec{J}$ . Some theoretical calculations predict that the vortices undergo a helical deformation in the FF configuration and the instability of the helical state is what limits the critical current [15, 73]. Otherwise, the GBs may do so in the absence of  $F_L$ .

When a  $\phi$ -scan is done at different  $\theta$  such as in the plot shown in figure 4.11b, the peak shifts from  $\phi = 0$  in the IP-configuration towards  $\phi = 66^\circ$  in the MLF configuration. Except for the IP scan, the peaks observed are due to pinning parallel



**Figure 4.10:** Angle dependence of  $J_{c,L}$  in VLF configurations at 77 K and different applied fields. (a) In-plane measurement obtained at  $\theta = 90^\circ$ . (b) Angular scan in  $\theta$  at  $\phi = 0$ .



**Figure 4.11:**  $\phi$ -dependence of  $J_{c,L}$  different  $\theta$  and  $T = 64$  K,  $\mu_0 H_{app} = 5$  T. (b)  $\theta$ -dependence of  $J_{c,L}$  at different  $\phi$ ,  $T = 77$  K and  $\mu_0 H_{app} = 3$  T.

to the  $ab$ -plane which shifts in the angular position since the angle between the  $ab$ -plane and the applied field varies as both  $\phi$  and  $\theta$  were changed. To further illustrate this, consider the geometry illustrated in figure 4.12 where the unit vectors  $\hat{e}_1$ ,  $\hat{e}_2$  and  $\hat{e}_3$  are assigned for the sample coordinate.

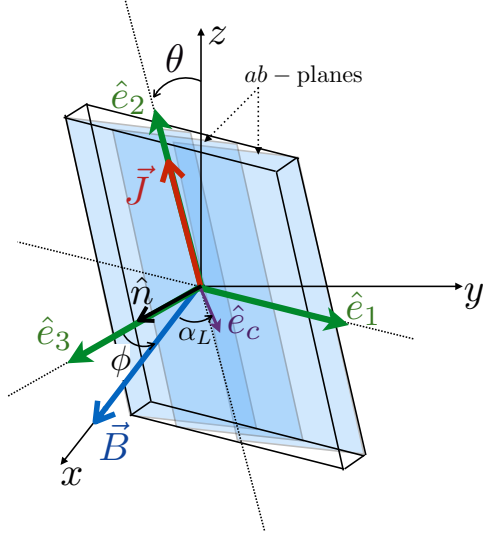


**Figure 4.12:** Geometry of the L-bridge in VLF configuration showing the sample unit vectors  $\hat{e}_1$ ,  $\hat{e}_2$  and  $\hat{e}_3$  and the unit vector  $\hat{e}_c$  parallel to the  $c$ -axis of the L-bridge.

The unit vectors  $\hat{e}_1$ ,  $\hat{e}_2$  and  $\hat{e}_3$  can be parametrized by rotations on  $\phi$  and  $\theta$  about the fixed  $xyz$ -coordinates of the sample space and are expressed as:

$$\hat{e}_1 = \begin{pmatrix} -\sin \phi \\ \cos \phi \\ 0 \end{pmatrix} \quad \hat{e}_2 = \begin{pmatrix} \cos \phi \sin \theta \\ \sin \phi \sin \theta \\ \cos \theta \end{pmatrix} \quad \hat{e}_3 = \begin{pmatrix} \cos \phi \cos \theta \\ \sin \phi \cos \theta \\ -\sin \theta \end{pmatrix} \quad (4.1)$$

The unit vector  $\hat{e}_c$ , parallel to the  $c$ -axis can be expressed as:

$$\hat{e}_c = \hat{e}_3 \cos \theta_v - \hat{e}_1 \sin \theta_v \quad (4.2)$$

If the field is parallel to the  $ab$ -plane, the scalar product of  $\hat{e}_c$  and  $\vec{B}_{\text{app}}$  must be zero, i.e.  $\hat{e}_c \cdot \vec{B}_{\text{app}} = 0$ , where  $\vec{B}_{\text{app}} = B_{\text{app}} \hat{x}$ .

Therefore, the angular position where the  $ab$ -peak is expected to appear upon rotation by either  $\phi$  or  $\theta$  is expressed as:

$$\frac{\cos \theta_v \cos \theta}{\sin \theta_v} = \tan \phi \quad (4.3)$$



The shift of the peak in the  $\theta$  scan at different  $\phi$  shown in figure 4.11 also agrees with equation 4.3.

In order to determine the factors that limit  $J_c$  that leads to a quite complex  $J_c$ -anisotropy behavior of the L-bridge, measurements in VLF configuration are presented as a function of the angle between the applied field and the  $c$ -axis which will be denoted by  $\alpha_L$ . V. Mishev et al. [68] obtained a remarkable scaling of  $J_c$  in iron-pnictide films. They have shown that scaling with  $\alpha_L$  is an effective method to determine the pinning dimensionality since it eliminates other factors such as the density of the vortices that is inherent to scaling with the applied magnetic field. Extracting information related to the geometry of the dominant pinning centers in GdBCO-ISD film can only be obtained with the VLF measurements.

An expression for  $\alpha_L$  is derived from the parametrized expressions for  $\hat{e}_1$ ,  $\hat{e}_2$  and  $\hat{e}_3$  as done by V. Mishev, et al. [68]. By expanding the scalar product of  $\hat{e}_c$  and  $\vec{B}$ ,  $\alpha_L$  is derived as:

$$B_{\text{app}} \cos \alpha_L = B_{\text{app}} (\cos \theta_v \cos \phi \cos \theta + \sin \theta_v \sin \phi) \quad (4.4)$$

$$\alpha_L = \arccos(\cos \theta_v \cos \phi \cos \theta + \sin \theta_v \sin \phi) \quad (4.5)$$

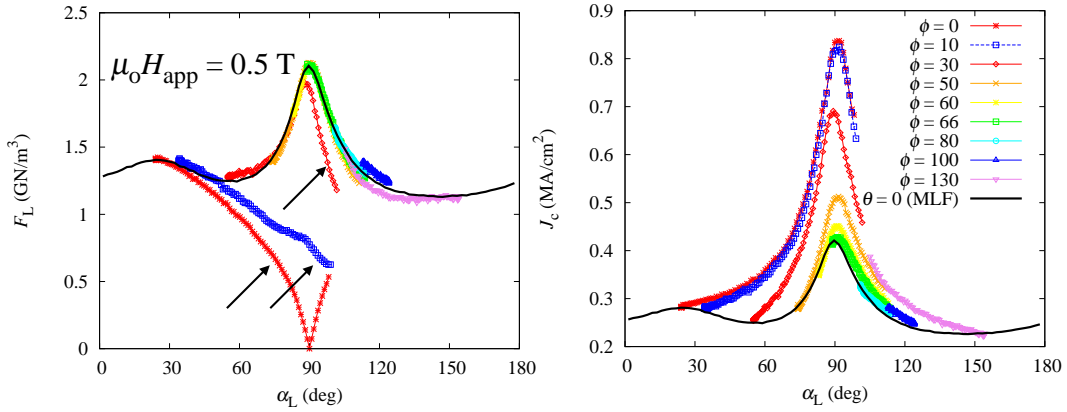


**Figure 4.13:**  $F_L(\alpha_L)$  and  $J_c(\alpha_L)$  at different  $\phi$ ,  $T = 77$  K and  $\mu_0 H_{\text{app}} = 0.5$  T. The Lorentz force roughly scales with  $\alpha_L$  while  $J_c$  does not.

$J_c$  does not scale with  $\alpha_L$  in the data of GdBCO-ISD in figure 4.13. Instead,  $F_L$  does roughly scale except for  $\phi = 0^\circ$ ,  $10^\circ$  and  $30^\circ$  as shown in figure 4.13.  $F_L(\phi, \theta)$  is derived from the cross-product of  $\vec{J}$  and  $\vec{B}_{\text{app}}$ :

$$F_p = F_L = |\vec{J}_c \times \vec{B}_{\text{app}}| = J_c B_{\text{app}} \sin \Theta \quad (4.6)$$

$$F_L(\phi, \theta) = J_c B_{\text{app}} \sin[\arccos(\cos \phi \sin \theta)] \quad (4.7)$$

In VLF measurements the reduction of  $F_L$  contributes to the gradual increase of  $J_c$  as the force-free orientation ( $F_L = 0$ ) is approached. This is already discussed earlier in the IP scans where a peak centered at  $\phi = 0$  is attributed to a FF configuration.

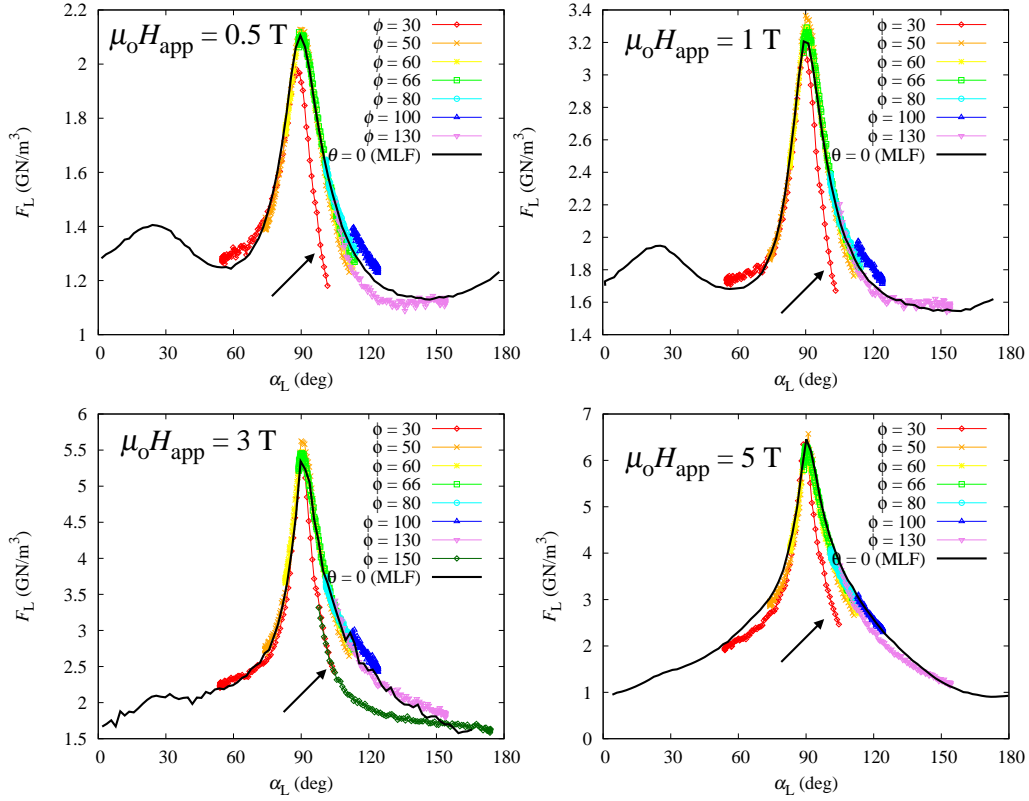


**Figure 4.14:**  $F_L(\alpha_L)$  at different  $\phi$  and a  $J_c$ -curve in MLF at  $T = 77$  K and applied magnetic fields of 0.5 T, 1 T, 3 T and 5 T.

Additional plots at different applied fields in figure 4.14 depict that the  $F_L(\alpha_L)$  curves at different  $\phi$  converge to the MLF curve except for  $\phi < 30^\circ$  and its supplementary angles ( $\phi \geq 150^\circ$ ). The  $F_L(\alpha_L)$  at different  $\theta$  also collapse in a limited angular range at  $\alpha_L = [90^\circ : 115^\circ]$  as shown in figure 4.15. Hence, the calculated  $F_L$  can be interpreted as equivalent to the pinning force density,  $F_p$ . Scaling with  $\alpha_L$  presents data as a function of the crystallographic orientation while the direction of pinning force varies at different  $\theta$  and  $\phi$ . The convergence of the experimental curves to the MLF curve at different  $\theta$  and  $\phi$  indicates that an isotropic pinning landscape dominates the pinning mechanism. This is also consistent to the prediction of the critical state model.

The deviations from the scaling of  $F_L$  of the IP scan ( $\phi = 0^\circ$ ) and  $\phi = 10^\circ$  are a consequence of the reduction of the angle between  $\vec{B}_{app}$  and  $\vec{J}$ , denoted by  $\Theta$  in equation 4.7. On the other hand, the deviation from the scaling of the  $\phi = 30^\circ$  in the range of  $\alpha_L > 90^\circ$  in figure 4.14 and  $\alpha_L < 90^\circ$  in figure 4.15 manifest a different pinning mechanism, which may probably be a depiction of vortex channeling at a

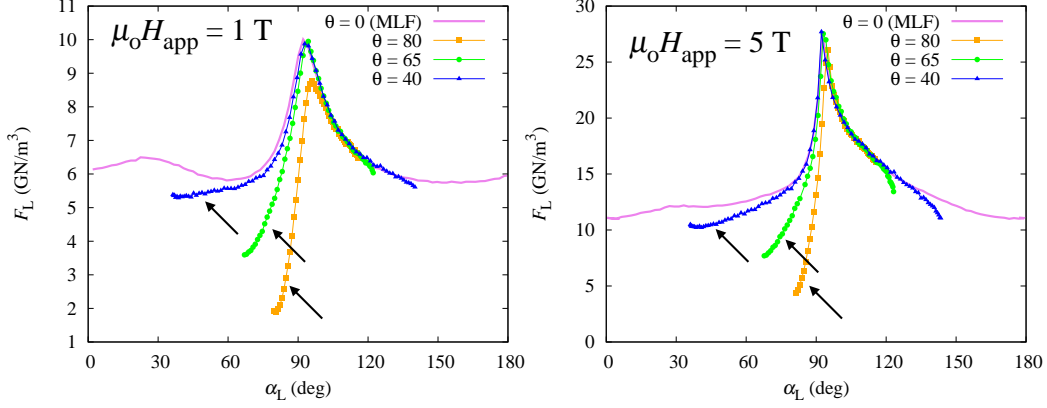


**Figure 4.15:**  $F_L(\alpha_L)$  at different  $\theta$  at  $T = 64$  K and  $\mu_0 H_{\text{app}} = 1$  T and 5 T.

certain orientation of  $F_p$  or may probably be caused by a different pinning landscape related to the inherent asymmetry of the  $ab$ -peak caused by the tilted geometry.

## 4.4 Angular dependence of $J_c$ in transverse current direction

In this section, the angular dependence of  $J_c$  of the GdBCO-ISD sample in the transverse direction will be discussed. In these measurements, the tilted growth of the  $c$ -axis and  $ab$ -planes with respect to the substrate surface causes additional effects in the  $J_c$  anisotropy connected to the dynamics of vortices in the GdBCO as a layered superconductor.

### 4.4.1 $J_{c,T}$ at maximum Lorentz force

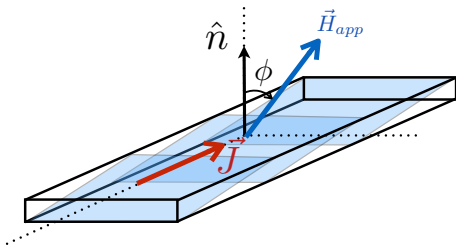


**Figure 4.16:** Schematic diagram of the MLF configuration of the T-bridge. The angle  $\phi$  denotes the angle of the applied field with  $\hat{n}$ . By convention,  $\vec{H}_{\text{app}} \parallel \hat{n}$  at  $\phi = 0$  and  $\vec{H}_{\text{app}} \parallel ab$ -planes at  $\phi = 90^\circ$ .

To start with, a schematic diagram of the MLF configuration of the T-bridge is shown in figure 4.16. Recall that the T-bridge was patterned such that the currents

flow transverse to the  $ab$ -planes. With this convention, the angle when  $\vec{H}_{app} \parallel ab$  is at  $\phi = 90^\circ$ .

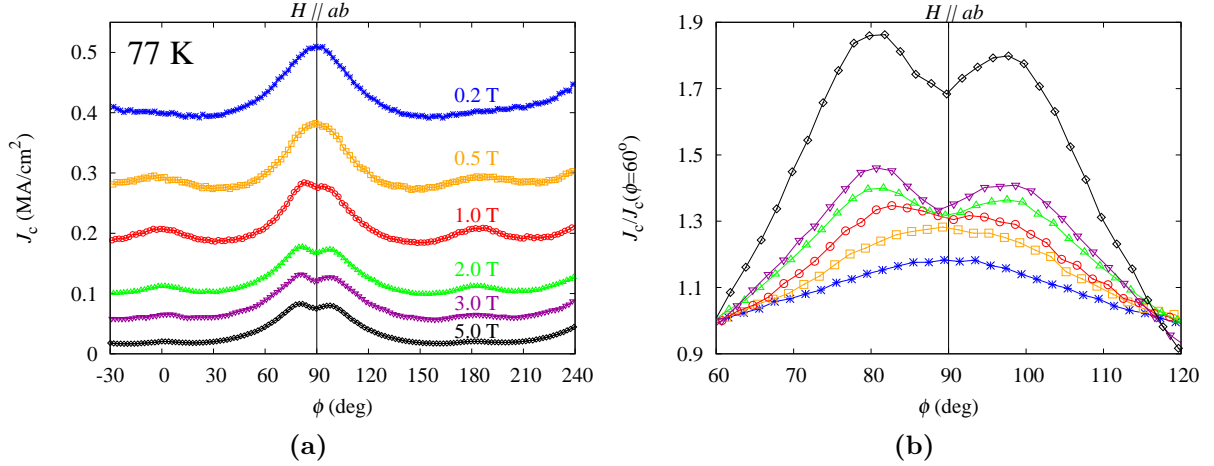


**Figure 4.17:** (a) Angle dependence of  $J_c$  of the T-bridge at MLF, at different fields and  $T = 77$  K. (b) Normalized  $J_c$  enlarged near the minimum at  $H \parallel ab$ .

The  $\phi$  dependence of  $J_c$  at 77 K and different applied magnetic fields is shown in figure 4.17. The  $\hat{n}$ -peak ( $\phi = 0, 180^\circ$ ) is also found and is consistent to the behaviour observed in the L-bridge (figure 4.6a), which is attributed to enhanced pinning by correlated defects parallel to this direction. As the orientation of  $\vec{H}_{app}$  becomes parallel to the  $ab$ -plane ( $\phi = 90^\circ$ ), a minimum ( $\phi=90^\circ$ ) appears and the formation of a peak resulting from intrinsic pinning is suppressed. This particular appearance of a minimum parallel to the  $ab$ -planes is a manifestation of vortex channeling. This phenomenon is also reported in YBCO films on vicinal substrate by J. Durrell et al [20]. If the vortices form a kinked state at a certain angular range towards the  $ab$ -planes, the component of the Lorentz force parallel to the planes,  $F_{L\parallel ab}$ , serves as the driving force that induces motion of vortex strings and results in a decrease in  $J_c$  as shown by the diagram in figure 4.18b. However, in the previous reports on YBCO films on vicinal STO substrate [20], there is no vortex channeling minimum reported above  $\theta_v > 10^\circ$ . In these results, the minimum appears only at temperatures below 50 K for vicinal angles of  $2 - 10^\circ$ . Another study done on IBAD-MgO tape with tilt angles of  $4-10^\circ$  found no channeling minimum [65].

In the GdBCO-ISD tape, the channeling minimum was observed up to temperatures as high as 77 K. Since the tilt of the crystallographic axes of GdBCO in this CC is more than twice larger than those reported in vicinal films, the component of the Lorentz force parallel to the  $ab$ -planes,  $F_{L\parallel ab}$ , is also larger and enough to overcome the suppression due to defects and shear forces. In addition to this, TEM analysis has shown that the GdBCO layer of this tape has a different microstructure and the correlated defects constitutes only of slightly tilted grain boundaries and stacking faults parallel to the  $ab$ -plane. In contrast to previous reports on YBCO-mSTO films, where anti-phase boundaries (APBs) normal to the

tape surface are commonly formed which are additional defects that inhibit the motion of vortex strings along the  $ab$ -plane. It was actually shown that a decrease in the density of the APBs in vicinal YBCO films enhanced vortex channeling [21]. The absence of a correlated defect that may enhance  $J_{c,L}$  and impede the vortex channeling is also consistent to the observed low anisotropy of the in-plane  $J_c$  observed in the current density map in section 4.2.

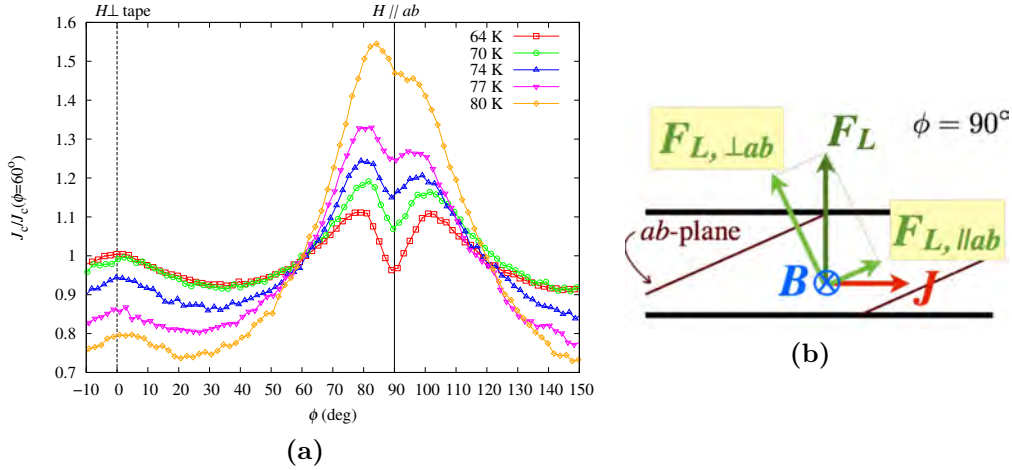


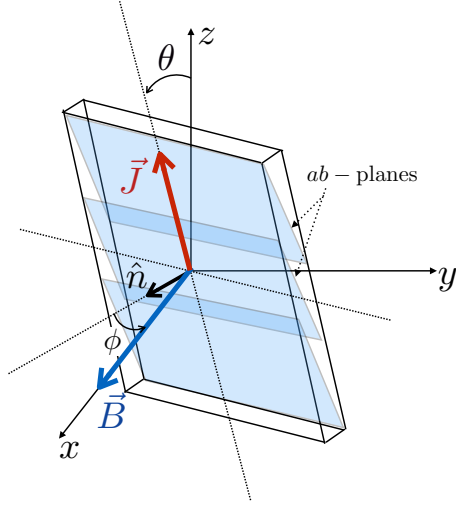
**Figure 4.18:** (a) Normalized  $J_c(\phi)$  at  $\mu_0 H_{app} = 2$  T and different temperatures for the T-bridge in MLF configuration. (b) Schematic diagram of the Lorentz force vector acting on the vortex string when  $\vec{B} \parallel ab$ -planes ( $\phi = 90^\circ$ ).

A very small trace of vortex channeling was observed at 80 K and it disappeared at higher temperatures (figure 4.18a). This result agrees with the idea that rectilinear vortex state persists above a certain temperature  $T_{cr}$  with a reported value of 80 K for YBCO [4, 27]. The channeling minimum also does not appear at low fields such as below 1.0 T at 77 K in figure 4.17a. Thus, the Lorentz force required for flux cutting is still larger than the force required to de-pin a vortex line. Note that the grain boundaries and other isotropic pinning center may pin a segment of the vortex line inhibiting flux cutting. Therefore, below 1 T at  $T = 77$  K, the limiting mechanism for  $J_c$  near  $H \parallel ab$  is governed by pinning in the defects.

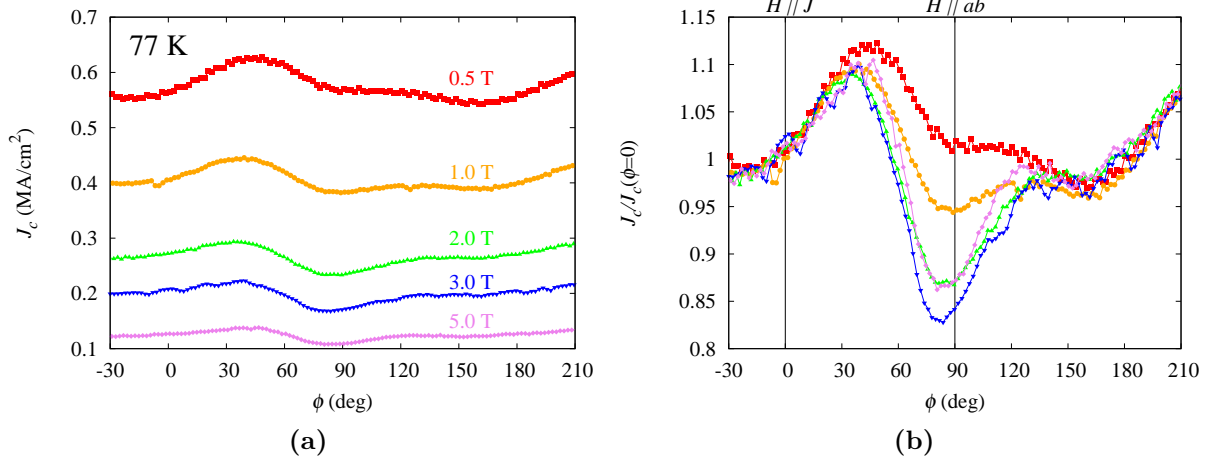
#### 4.4.2 $J_{c,T}$ at variable Lorentz force

Figure 4.19 illustrates the geometry of the VLF measurements of the T-bridge. Similar to the in-plane (IP) configuration of the L-bridge, the applied field is rotated around the plane of the substrate at  $\theta = 90^\circ$ . The force-free configuration, i.e.  $\vec{H}_{app} \parallel \vec{J}$ , is obtained when  $\theta = 90^\circ$  and  $\phi = 0$ .

Figure 4.20 shows the in-plane measurement at 77 K at different applied magnetic fields. In comparison to the IP scans of the L-bridge, the T-bridge has lower anisotropy. The vortex channeling minimum is again observed around  $\phi = 90^\circ$  for



**Figure 4.19:** Schematic diagram of the VLF configuration of the T-bridge.



**Figure 4.20:** (a) In-plane  $J_c$ -anisotropy measurement at  $T = 77$  K and different applied magnetic fields. (b) Normalized  $J_{c,T}$  for a better comparison of the vortex channeling minima at  $\phi = 90^\circ$ .

the same reason as in the MLF configuration. This minima disappears at lower fields and occurs only at 80 K and below. As shown in figure 4.21, only a broad peak appears around  $\phi = 60^\circ$  at  $T=85$  K and  $T = 77$  K with  $\mu_o H_{app} = 0.5$  T in figure 4.20 since under these temperature and field conditions, the vortices are in their rectilinear state, thus channeling does not occur.

Another interesting behavior observed in the IP measurements of the T-bridge is the absence of a FF-peak which was expected at  $\phi=0$  in contrast to the prominent FF-peak observed in a similar IP measurements of the L-bridge discussed in section 4.3.2.

The FF maximum is also not observed in another VLF-configuration with an angular scan of  $\theta$  at fixed  $\phi$ . A data set at  $\phi = 0$ ,  $T = 77$  K and different fields is

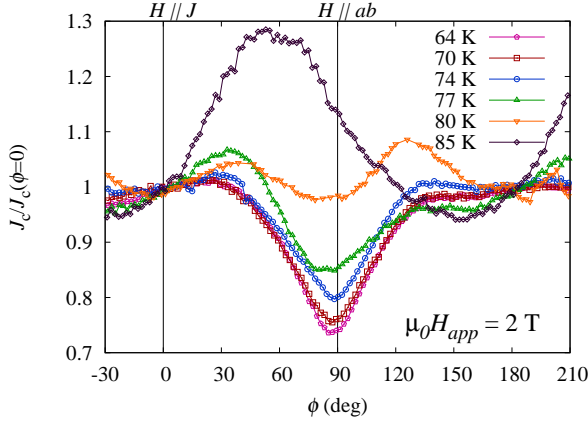


**Figure 4.21:** In-plane  $J_c$ -anisotropy measurement of the T-bridge at  $\mu_0 H_{app} = 2\text{T}$  and different temperatures. The data were normalized with respect to  $J_c(\phi = 0)$  for a better comparison.

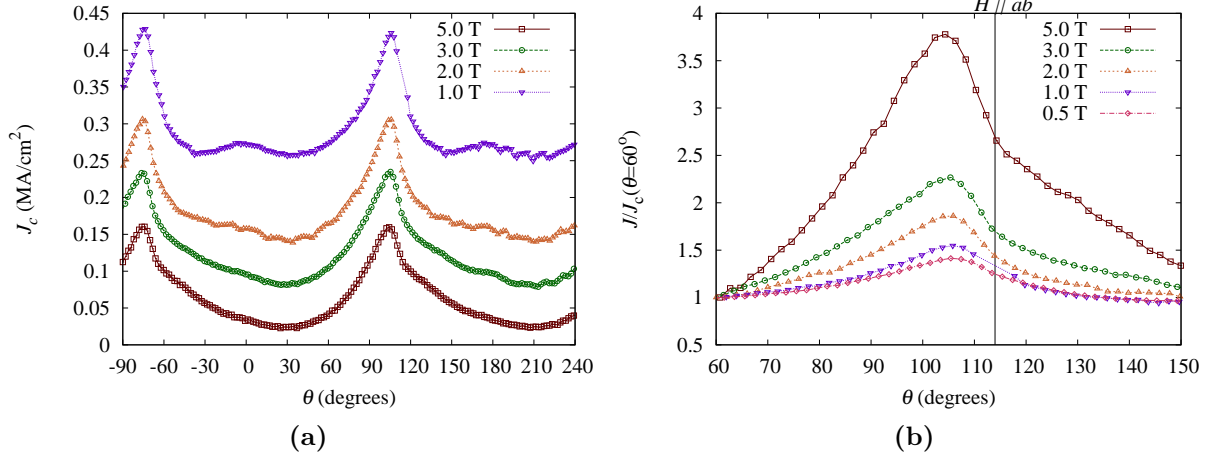


**Figure 4.22:** (a)  $\theta$ -dependence of  $J_{c,T}$  at  $\phi = 0$ ,  $T = 77\text{ K}$  and at different applied fields. (b) Normalized  $J_{c,T}$  for a better comparison of the curves at different fields.

presented in figure 4.22. A monotonous behavior around  $\theta = 90^\circ$  occurs instead of a FF-peak.

The manifestation of vortex channeling in this configuration is the rapid decrease of  $J_c$  before the kink at  $\theta = 114^\circ$ . It is found to be best visible at 5 T and decreases in prominence at lower fields. Again, vortex channeling suppressed the  $ab$ -peak expected at  $\theta = 114^\circ$ . Thus at 5 T, a peak at  $\theta = 105^\circ$  was visible and shifts to higher  $\theta$  as the kink disappears at lower fields. In contrast to results on vicinal YBCO films reported by J. Durrell et al. [20], where a sharp minimum is visible at the angle where the vortices lie in the  $ab$ -planes, vortex channeling manifests only as a kink in our data. The vortex channeling minimum is smeared out in our samples because of the grain-to-grain misalignment of the  $ab$ -planes. The same indication of vortex channeling suppression was also reported in MOCVD/IBAD tapes with meandering GBs [95].

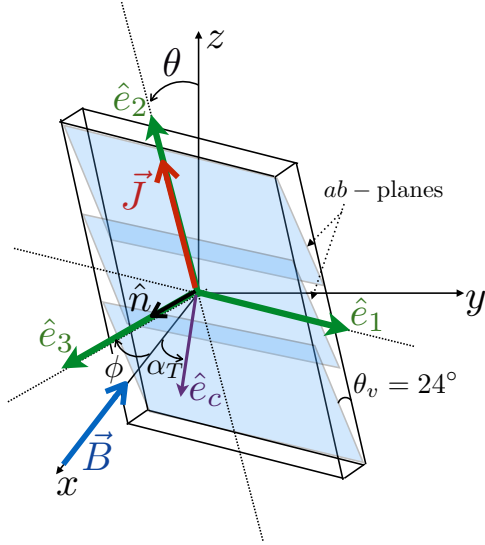


**Figure 4.23:** Geometry of the T-bridge in VLF configuration showing the sample unit vectors  $\hat{e}_1$ ,  $\hat{e}_2$  and  $\hat{e}_3$  and the unit vector  $\hat{e}_c$  parallel to the  $c$ -axis in the T-bridge.

Going back to the mechanism that leads to the the absence of an actual peak due to the FF configuration, one can consider scaling the angle-dependent measurements according to the angle of  $\vec{H}_{app}$  and the crystallographic  $c$ -axis which is denoted by  $\alpha_T$  (see figure 4.23). The expression for  $\alpha_T$  is derived similarly as  $\alpha_L$ . In the geometry of the T-bridge,  $\hat{e}_c$  is now expressed as:

$$\hat{e}_c = \hat{e}_2 \sin \theta_v + \hat{e}_3 \cos \theta_v \quad (4.8)$$

Therefore, the angle  $\alpha_T$  can be written as:

$$\alpha_T = \cos^{-1}[\cos \phi \cos(\theta_v - \theta)] \quad (4.9)$$

where  $\theta_v$  is the tilt angle of the crystallographic axes.

Figure 4.24 shows  $J_{c,T}(\phi)$  at different  $\theta$ ,  $\mu_0 H_{app} = 5$  T and  $T = 77$  K, 64 K at which vortex channeling appears. As  $\theta$  increases, the anisotropy of  $J_c$  decreases and the minima also broadens. To analyze this data, scaling with  $\alpha_T$  was implemented similar to  $J_{c,L}$  in section 4.3.2. Both  $J_c(\alpha_T)$  and  $F_L(\alpha_T)$  are presented in figure 4.25

Scaling is obtained in the  $J_c(\alpha_T)$  around the vortex channeling minimum. The reasonable scaling of the  $J_c$  values in this angular range implies that the vortex channeling minimum is, as expected, independent of the out-of-plane component of the Lorentz force,  $F_{L\perp ab}$ , which changes with  $\theta$  [68] and is only limited by the parallel component,  $F_{L\parallel ab}$ , which is independent of  $\theta$  at fixed  $\alpha_T$ .



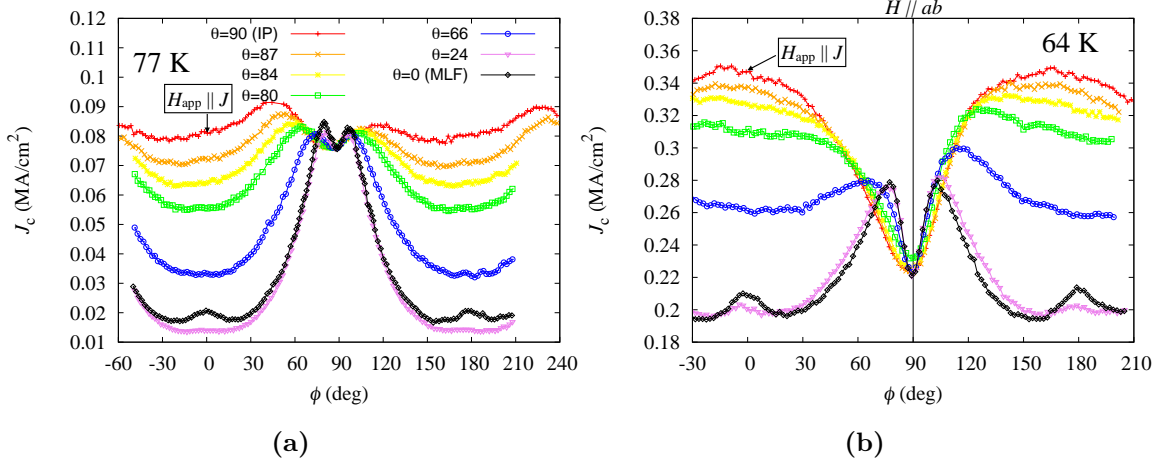


**Figure 4.24:**  $\phi$ -dependence of  $J_c$  with  $\mu_0 H_{\text{app}} = 5$  T and different  $\theta$  at temperatures of (a) 77 K and (b) 64 K.

By plotting  $J_c(\alpha_T)$  and  $F_L(\alpha_T)$ , the apparent absence of a FF peak in the  $J_c(\phi, \theta = 90^\circ)$  can be more clearly understood as an effect when the rapidly changing  $J_c$  around the direction of the  $ab$ -planes dominates the behavior owing to the anisotropy of  $J_c$ . At 64 K, the monotonic decrease of  $F_L$  in figure 4.25c corresponds to a monotonic increase in  $J_c$  in figure 4.25a.

Two regimes in  $\alpha_T$  can then be distinguished that characterize what type of vortex mechanism is limiting  $J_c$ . This information can only be accessed by VLF measurements of the transverse geometry. First,  $J_c$  in the range of  $\alpha_T$  around  $H \parallel ab$  ( $\alpha_T = 90^\circ$ ) is limited by vortex channeling. The onset angle of field with respect to the  $ab$ -plane,  $\alpha_k$ , at which the kinked vortex state starts to form can then be determined to be about  $11.7^\circ$ . This agrees to the predicted onset of the kinked state of about  $11^\circ$  [20]. Beyond  $\alpha_k$  ( $\alpha_T < 78^\circ$  and  $\alpha_T > 102^\circ$ ), rectilinear vortices form where  $J_c$  is limited by vortex pinning in the defects. This is also the regime where the scaling of  $F_L$  is expected in accordance to the critical state model. However, due to the dominance of the  $\sin \Theta$  term, a rapid decrease of  $F_L$  in some range of  $\alpha_T$  is observed as  $\theta$  approaches the IP configuration.

The sets of VLF measurements without a vortex channeling minimum such as at 85 K and 77 K with  $\mu_0 H_{\text{app}} = 0.5$  T are shown in figure 4.26. Similar to the behavior of the L-bridge,  $F_L$  scales with  $\alpha_T$  instead of  $J_{c,T}$ , but only within a certain range around the  $H \parallel ab$  direction ( $\alpha_T = 90^\circ$ ). A FF-peak in the IP scan is not apparent again as a consequence of  $J_c$  anisotropy when the field is rotated close to the  $ab$ -planes. However, a peak forms at  $\phi = 50^\circ$ , which shifts towards  $\phi = 90^\circ$  as  $\theta$  decreases. In the corresponding plot of  $F_L(\alpha_T)$  (figure 4.26e-4.26f), the peak is not exactly parallel to the  $ab$ -planes indicating that maximum pinning is not achieved exactly in the direction of the  $ab$ -planes. Such asymmetry around  $\alpha_T = 90^\circ$  may be related to the asymmetric  $ab$ -peak in the  $J_c(\phi)$  at MLF configuration of the

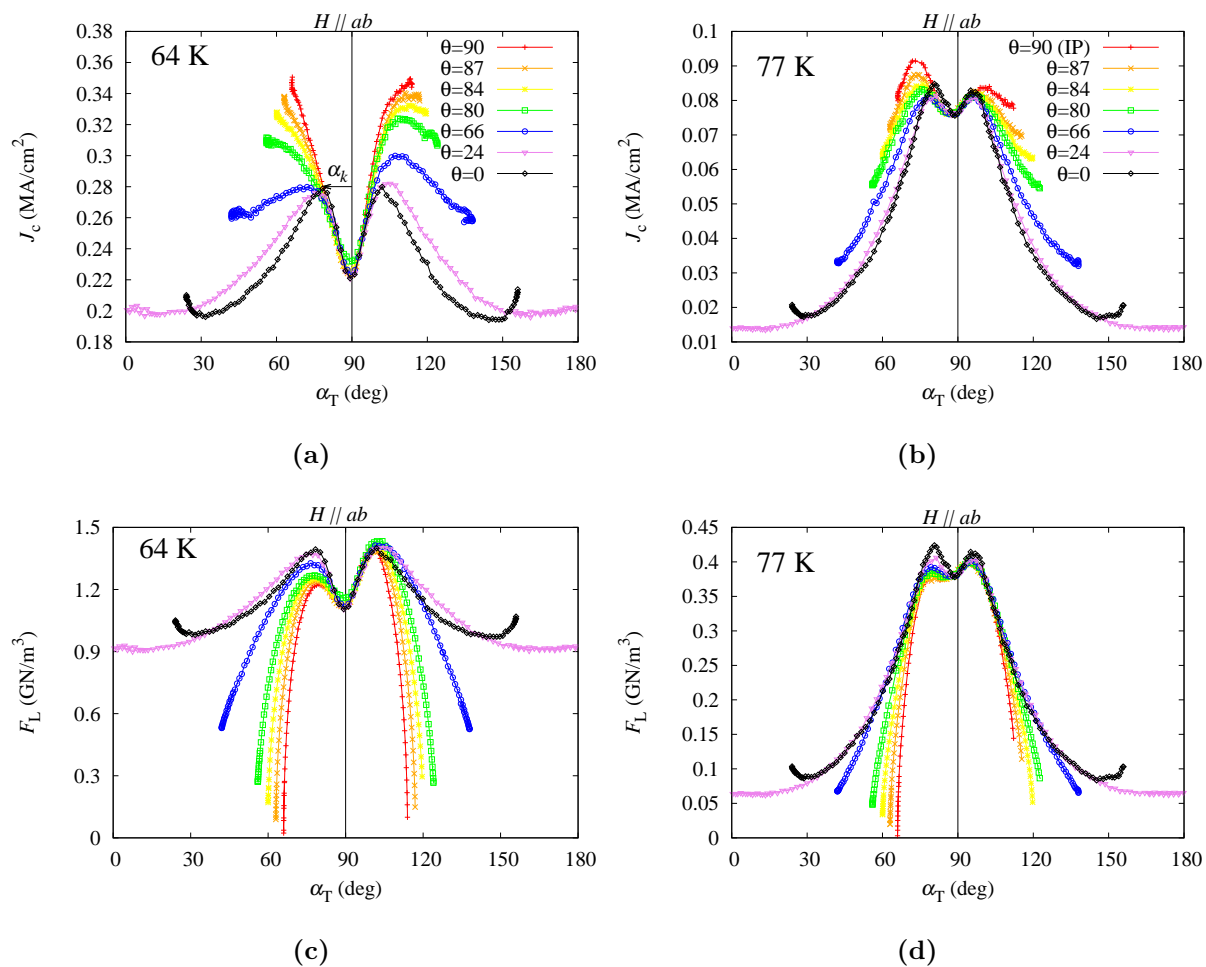


**Figure 4.25:**  $J_c(\alpha_L)$  at  $\mu_o H_{app} = 5$  T, (a)  $T = 64$  K and (b)  $T = 77$  K and the corresponding  $F_L(\alpha_L)$  at the same temperatures in (c) and (d).

L-bridge, however, further studies must still be done such as identifying additional tilted defects that may have caused the asymmetry.

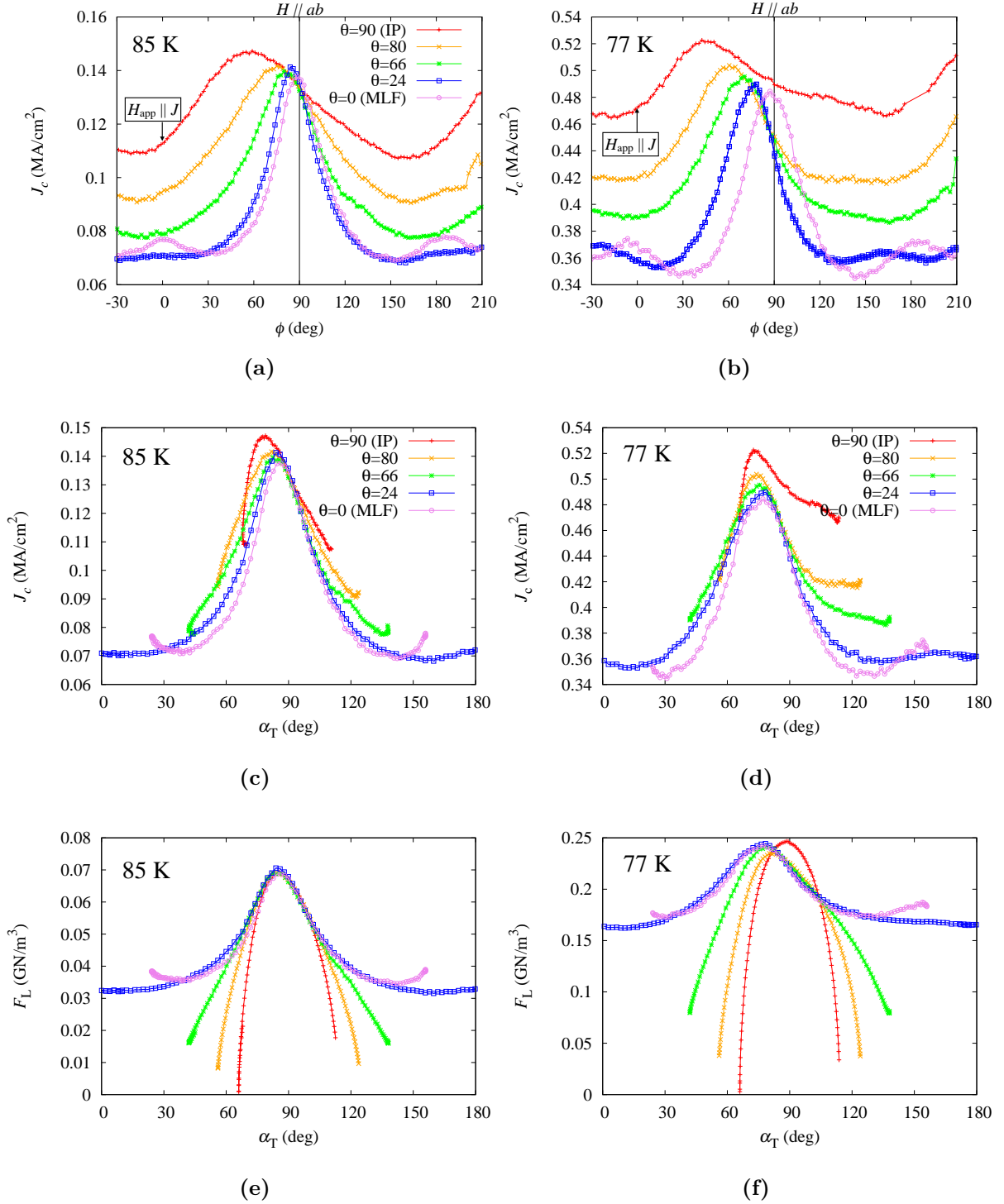


**Figure 4.26:**  $J_c(\phi)$  at  $\mu_0 H_{app} = 0.5$  T, (a)  $T = 85$  K and (b)  $T = 77$  K. (c)-(d) are the corresponding  $\alpha_T$  scaling of  $J_c$  and (e)-(f) are the scaling of  $F_L$ .

## 4.5 Summary

In this chapter, the angle-resolved measurements of the critical current density in GdBCO coated conductor deposited on ISD-MgO-buffered templates revealed an interesting anisotropic behaviour both on longitudinal and transverse current directions.  $J_c(\phi)$  curves in the longitudinal direction showed broken symmetry around the  $ab$ -peak. At lower fields, the asymmetry is influenced by different surface texture at the GdBCO surface and the faceted GdBCO-MgO interface. The inclined GBs were not found to enhance pinning even if their orientation is parallel to the applied field.

Vortex channeling, which is characterized by a suppression of the  $ab$ -peak and appears as a minimum in angle-resolved  $J_c$ , was found in the transverse current direction at temperatures as high as 77 K. It was observed to be field-dependent. Its occurrence at 77 K and high fields, which was not reported so far, is a consequence of the large tilt of the crystallographic axes of the deposited superconducting layer by this ISD technique and absence of defects that would impede the vortex motion at the specific field orientation as discussed. The appearance of the channeling minimum makes  $J_c$  less anisotropic in the T-bridge than in the L-bridge. The competing effect of the Lorentz force and the crystallographic anisotropy of GdBCO on  $J_c$  at VLF is prominent in this CC due to its large crystallographic tilt and leads to an absence of an actual peak in the force-free orientation. The suppression of a vortex channeling minimum at lower fields and at VLF configuration may also be a consequence of this competing effect in addition to the grain to grain misorientation of the  $ab$ -planes.

Overall,  $J_c$  of the GdBCO-ISD CC is limited mainly by the dynamics of vortices and there is no indication of grain boundary limitation at least in the field and temperature range of the measurements. Despite the complicated  $J_c$  anisotropy due to the tilted growth of the crystallographic axes, this coated conductor architecture has a good potential for large scale production since  $J_c$  does not decrease with increasing thickness, at least up to 7  $\mu\text{m}$  according to reference [23]. The composition of the layers is also not complicated since the buffer layer is only made up of MgO and the co-evaporation technique is also a cheaper deposition process. One important contribution of this thesis is that it has shown how vortex dynamics controls the anisotropy of  $J_c$  at every possible field orientation. However, further studies is still needed such as investigation on CCs with thicker GdBCO layer and/or addition of artificial pinning centers.



# Chapter 5

## Effects of the granular morphology of coated conductors

Coated conductors are basically granular REBCO materials deposited on a metallic substrate which are engineered to have a preferential growth direction. Grain boundaries and grain misorientations are inherent attributes of CCs and are kept to a minimum in order to avoid their detrimental effects to their current carrying capacity as discussed in section 2.1. In this chapter, the effects of the granularity of the YBCO layer on metallic templates especially on RABiTS NiW are investigated and its impact on the global  $J_c$  both through transport and magnetic measurements will be discussed.

### 5.1 PLD-YBCO on metallic substrate

#### 5.1.1 Microstructure

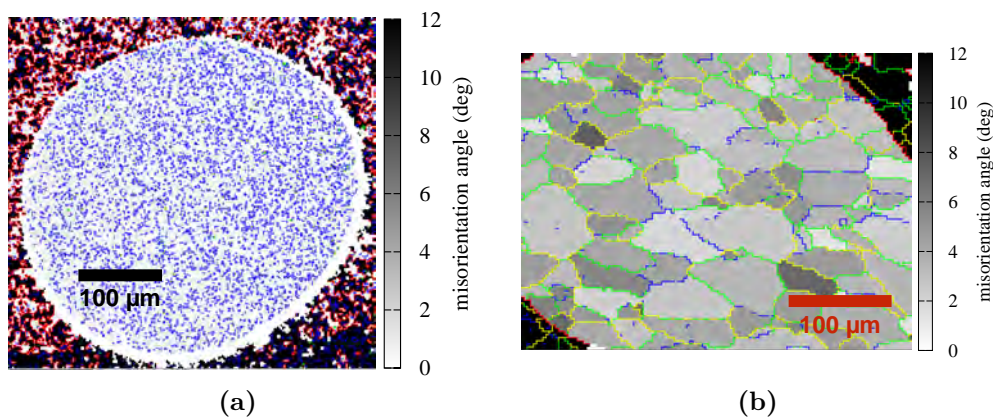


**Figure 5.1:** EBSD maps of the (c) YBCO-SS and (d) the YBCO Ni5W samples. The colored lines denote the GB misorientation angles with the following notation: Blue  $\rightarrow <1.5^\circ$ , green  $\rightarrow >3^\circ$  and yellow  $\rightarrow 6-10^\circ$ . The scale from white to black correspond to the misorientation from the ideal cubic texture from 0 to  $12^\circ$ .

The YBCO layer fabricated by PLD on stainless steel (YBCO-SS) adapts its texture from the ABAD-YSZ buffer layer and the typical grain size of the deposited YBCO is less than  $1\ \mu\text{m}$ . As shown in the EBSD map in figure 5.1a, the GB angles of YBCO-SS are less than  $1.5^\circ$  and it has a sharp cubic texture. On the other hand, the YBCO layer on a NiW template conforms to the texture of the NiW substrate with grain sizes between  $20\text{--}80\ \mu\text{m}$ . The GB angles reaches up to  $10^\circ$ . It is also observed that the degree of misorientation of the crystal structure of the YBCO to the ideal cubic texture is non-uniform and varies from one grain to another. This is revealed by the different grain contrasts in the EBSD map in figure 5.1b.

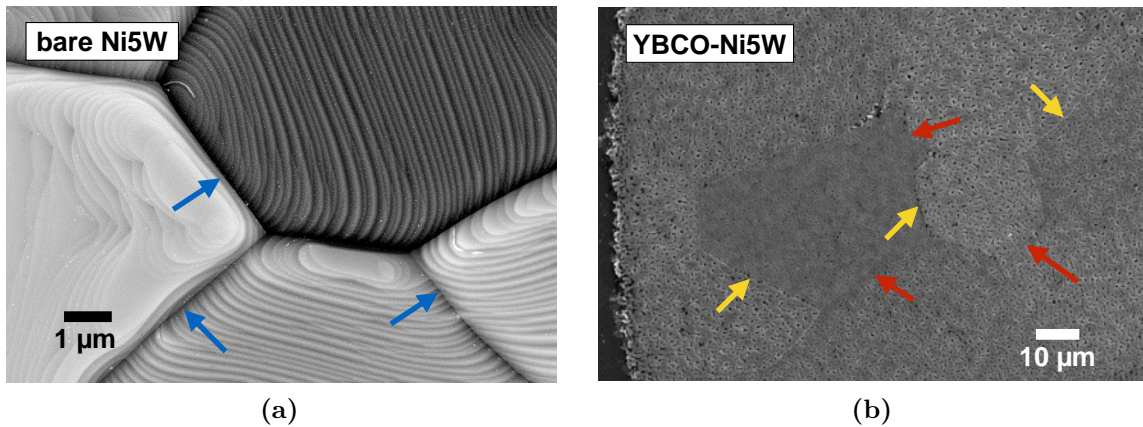


**Figure 5.2:** (a) SEM image of a bare NiW template. The blue arrows denote the trenches between grains. (b) SEM image of the surface of YBCO-Ni5W. The red arrows point to smooth GBs and the yellow arrows denote the grooved GBs. Notice that the deposited YBCO layer has different porosity and density on each NiW grain.

The variation of the crystallographic orientation of YBCO in each grain can be attributed to the characteristics of the underlying RABiT substrate. An SEM image of a bare NiW is shown in figure 5.2a. The picture shows that each grain in the NiW template has step-like structure similar to the faceted surface observed in miscut STO substrate and ISD-buffered metallic template as discussed in chapter 4. The direction of the facetation differs in each grain. Therefore, the deposited YBCO layer on top grows with varying tilted crystallographic axes, which is reflected in the misorientation observed in the EBSD maps. The misorientations are only limited to less than  $10^\circ$ . In the SEM image of the surface of YBCO-Ni5W in figure 5.2b, the GBs also appear either as smooth (denoted by the red arrows) or grooved (indicated by the yellow arrows) as a consequence of the trenches between two grains observed in the bare NiW. The local tilt of the  $c$ -axis in each grain also leads to a varying density of the deposited YBCO where one grain can become more porous than the other. The variation of porosity of YBCO layer with vicinal angle was also observed in YBCO-mSTO films discussed in section 4.1.1.

Higher magnification images shown in figure 5.3 illustrate that both YBCO-SS and YBCO-Ni5W have the same shape of YBCO grains and both YBCO layers are

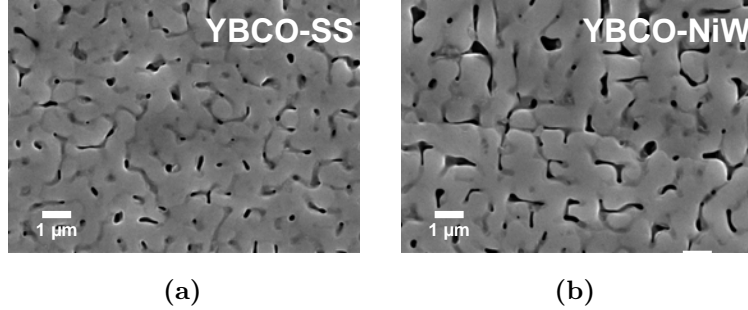


**Figure 5.3:** (a) Higher magnification SEM image of the surfaces of (b) YBCO-SS and YBCO-NiW. In these pictures, the YBCO grain size and porosity are almost the same.

porous. The grain boundaries on top of a NiW grain have  $\theta_{GB} \leq 3^\circ$  [71]. With the columnar growth mode of YBCO by PLD, the grain boundaries formed are usually planar and maintain almost the same width through its thickness [22, 50].

### 5.1.2 Magnetic field profiles

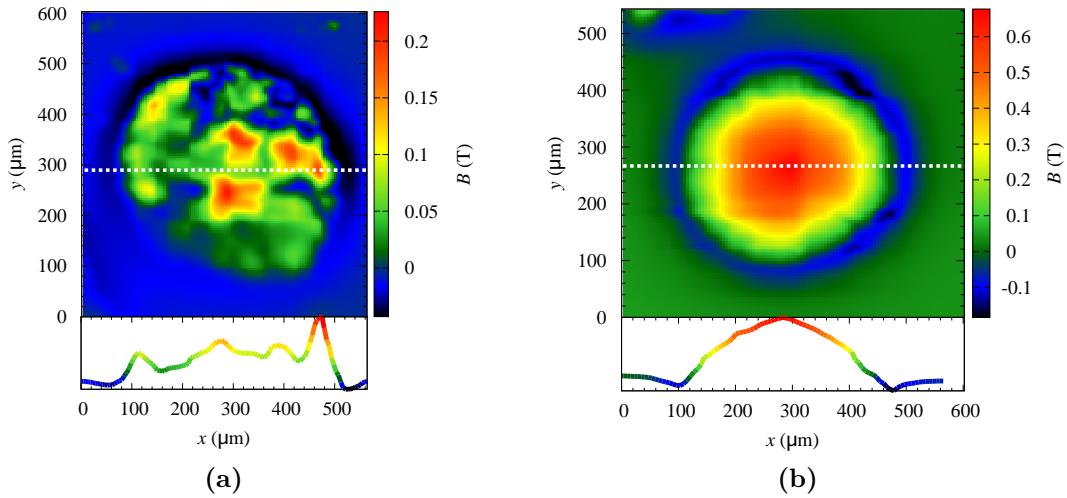


**Figure 5.4:** Remanent field profile of (a) YBCO-NiW and (b) YBCO-SS tape. The Hall probe-sample distance was approximately  $4 \mu\text{m}$  and the scanning stepwidth are 5 and  $4 \mu\text{m}$  in  $x$  and  $y$ -direction, respectively. The white dashed lines correspond to the positions of the linescans below each map.

As already apparent in the EBSD images of the two YBCO tapes in figure 5.1, the large granular structure of YBCO-NiW adapted from its RABiTS template must have particular effects on its magnetic and transport properties. To start with the magnetic properties, figure 5.4 shows the remanent field profiles at 4 K of the  $\approx 400 \mu\text{m}$  spot patterned by photolithography and wet chemical etching on



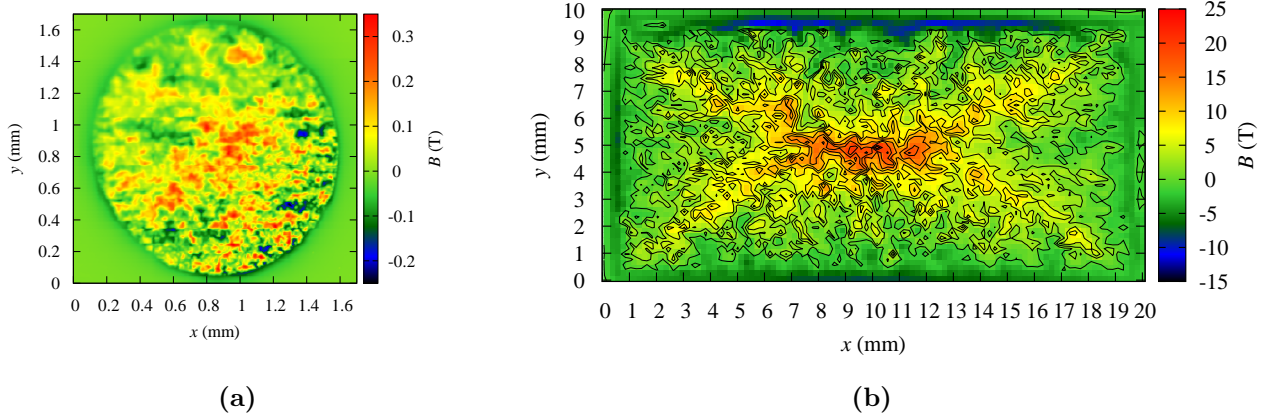


**Figure 5.5:** (a) Remanent field profile at  $T = 4$  K of a 1.5 mm etched spot on YBCO-Ni9W. The Hall probe-sample distance,  $d$ , was  $3 \mu\text{m}$  and the stepwidths,  $s_x$  and  $s_y$  were  $5 \mu\text{m}$ . (b) Remanent field profile of a whole 10-mm-width YBCO-Ni5W in  $\text{LN}_2$ . The scanning parameters were  $d = 45 \mu\text{m}$  and  $s_x, s_y = 200 \mu\text{m}$ . On both images, the granular morphology of the field profile is depicted independent of the size of the scanning area and temperature of the measurement.

each of the tape. Both tapes have YBCO layer thickness of about  $1.5 \mu\text{m}$ . Due to a small bending of the metallic templates, it is hard to keep a constant distance between the Hall probe and the sample surface. Thus, slight asymmetry is observed between the two opposite ends of the field profile. The trapped field in YBCO-NiW is formed into clusters with widths of up to  $120 \mu\text{m}$ , which correspond to groups of grains that favors local current flow. The strength of the signal of each magnetic grain varies and some parts of the spot outside the large clusters have very small to almost zero field. This implies that the underlying microstructure of each YBCO grain on the NiW template can be correlated to the variation in the local magnetic signal and formation of magnetic grain. Note that the granularity in the field map is observed in all PLD-grown tapes on NiW such as in the 1.5-mm etched YBCO spot with a Ni9at%W (YBCO-Ni9W) and in a 10-mm-width tape measured in  $\text{LN}_2$ -bath in figure 5.5.

On the other hand, the field profile of YBCO-SS in figure 5.4b is more homogenous compared to YBCO-NiW. In parallel with the structure of the deposited YBCO layer, this tape has better and more uniform cubic texture than YBCO-NiW, the grain size of YBCO is less than  $1 \mu\text{m}$  and  $\theta_{\text{GB}} \leq 1.5^\circ$ . Granularity is not resolved in the Hall mapping, possibly because the resolution of the measurement is above the grain size of YBCO. Nevertheless, the shape of the field profile is more homogenous and comparable to a YBCO-STO sample as shown in figure 5.6. The peak of the trapped field reaches  $0.67 \text{ T}$ , which is more than three times larger than the local  $B_{\text{max}}$  of YBCO-NiW that is about  $0.20 \text{ T}$ . A slight asymmetry and dent near the center signify local inhomogeneities such as microcracks, local nonstoichiometry, precipitates, etc. However, the general shape of the field profiles

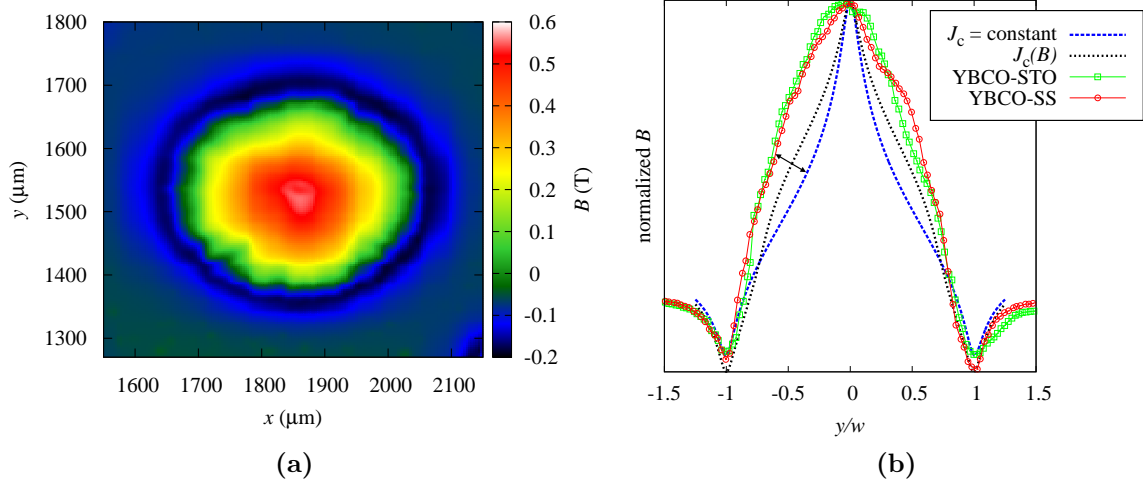


**Figure 5.6:** (a) Remanent field map of YBCO-STO at  $T = 4$  K. The Hall probe-sample distance was approximately  $5 \mu\text{m}$  and the scanning stepwidth are  $5$  and  $7 \mu\text{m}$  in  $x$  and  $y$ -direction, respectively. (b) Comparison of the remanent field profile of YBCO-SS and YBCO-STO at  $T = 4$  K and calculated curves with a constant  $J_c$  and if a field-dependent  $J_c$  is assumed.

still deviate from the one that can be calculated assuming a homogenous thin film with constant  $J_c$  as shown by the dashed blue curve in figure 5.6b. A field dependent  $J_c$  in the form of  $J_c(B) = J_0 \left(1 + \frac{B}{B_0}\right)^\beta$  was fitted to the experimental data of  $J_c(B)$  of a similar sample at  $5$  K and a self-consistent curve was recalculated and plotted as the dashed black line in the figure. Incorporating local field dependence of  $J_c$  indeed demonstrate broadening of the peak. However, the broadness of the shape of the experimental curves of YBCO-SS and YBCO-STO are still not replicated especially at the center where the absence of a steep peak may be due to another mechanism related to the non-linear flux diffusion as discussed in section 3.3.5.

Linescans of YBCO-NiW in different applied magnetic fields at  $T = 4$  K are presented in figure 5.7. The granularity in the profiles remains up to the largest field of  $4$  T. At  $0.3$  T and above, the peak in each cluster decreases with increasing field as expected for a superconductor under applied magnetic field since this corresponds to a decrease in  $J_c$  with field. However, an interesting behavior is observed below  $0.3$  T. The peaks of some clusters do not follow the monotonic decrease in the profiles between the remanent state and  $0.2$  T. This will be further tackled in later discussions.

As for the YBCO-SS in figure 5.8a, the profile with a peak at the center of the width is retained and the asymmetry and dent (denoted by the black arrows) are visible at all fields. The decrease of  $B_{\text{peak}}$  is consistent with the expected decrease of  $J_c$  with increasing  $H_{\text{app}}$ . When all the experimental data are normalized, as shown in figure 5.8b, the broadness of the peak at the remanent state and  $0.2$  T decreases as the field increases. This is a demonstration that indeed the field

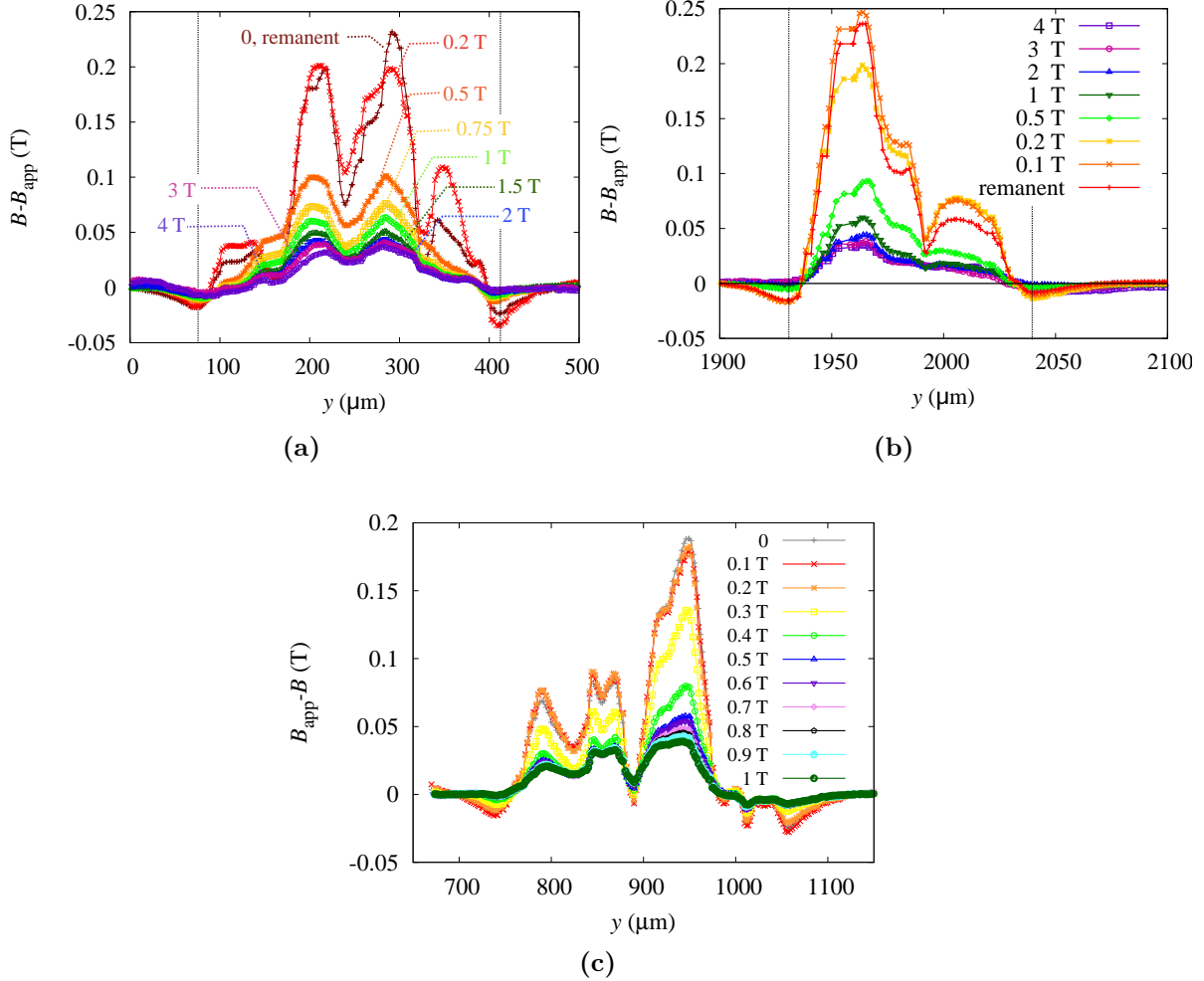


**Figure 5.7:** (a) Line scans at different applied fields at  $T = 4$  K of YBCO-NiW. (a)-(b) Line scans of two different etched spots measured in decreasing field after ramping the magnetic field to 5 T. Each measurement from 4 T to the remanent state ( $\mu_0 H_{\text{app}} = 0$ ) was taken consecutively. (c) Line scan at the position  $x = 410$   $\mu\text{m}$  in figure 5.4b in decreasing field after applying a field of -2 T. The black dashed lines in all the images denote the edges of the sample.

dependence of  $J_c$  alters the shape of the profile at low fields while the peak becomes less broad as the field increases because the  $J_c(B)$ -dependence is weaker at higher fields. A theoretical field profile assuming a constant  $J_c$  (dashed blue curve in figure 5.8b) is fitted to the experimental data at 5 T. The local position around a defect (denoted by the red arrow) deviates from the theoretical curve as well as the peak at the center. The deviation from the center is probably an effect of non-linear flux diffusion which depends on the rate of decrease of  $E$  towards the center of the sample as discussed in section 3.3.5.

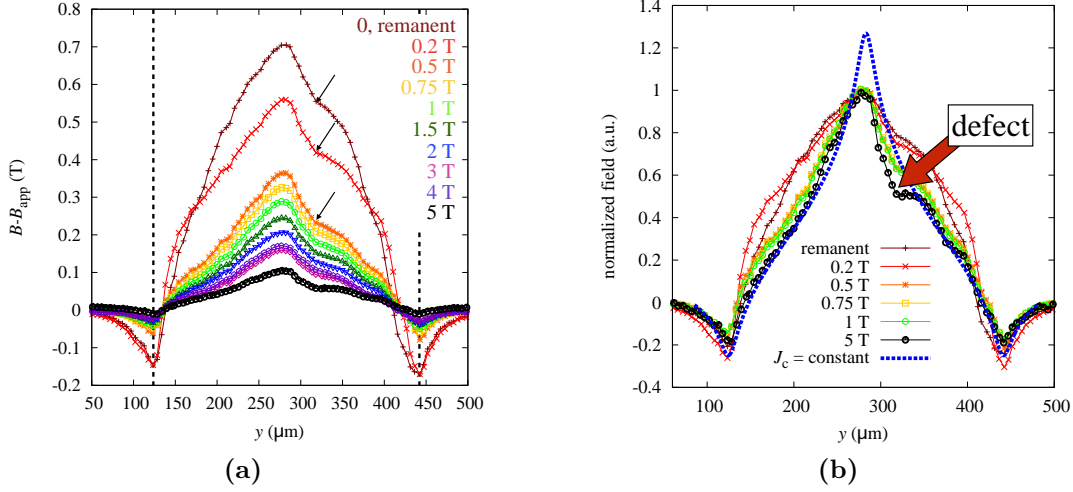


**Figure 5.8:** (a) Line scans at different applied fields at  $T = 4$  K of YBCO-SS. The data presented were taken in decreasing field after ramping the magnetic field to 5 T. Each measurement from 4 T to the remanent state ( $H_{\text{app}} = 0$ ) was taken consecutively. The dashed lines denote the edges of the sample. (b) Normalized  $B(y)$  to show how the shape of the field profile evolves with field. The blue dashed curve corresponds to the theoretical field profile assuming a constant  $J_c$ . It is fitted to the data at  $\mu_0 H_{\text{app}} = 5$  T.

### 5.1.3 Spatial dependence of $J_c$

The spatial distribution of  $J_c$  of YBCO-SS that was calculated using the inversion procedure [49] discussed in section 3.3.4 is shown in figure 5.9. As expected from the shape of the field profile, the evaluated current flow circulates homogeneously around the center. The minimum of  $J_c(x, y)$  at the center is due to the decreasing  $E$  as the area enclosed by the circulating currents becomes infinitesimally small. The broad peak of the remanent field curve causes the monotonic decrease of the current from the edges towards the center of the sample as an influence of the dependence of the local  $J_c$  to the local  $B$  and  $E$ . This behavior relaxes at higher field such as at 1 T shown in figure 5.9b, where a more flat  $J_c$  distribution and a narrower minimum at the center are observed (figure 5.9ba and 5.9d).

For the YBCO-Ni5W, the granular field profile is caused by an inhomogeneous  $J_c(x, y)$  and percolative current flow as shown in figure 5.10a. The maximum local  $J_c$  of YBCO-Ni5W is about 26 MA/cm<sup>2</sup> while that of the YBCO-SS is 44 MA/cm<sup>2</sup>. With the aim of determining the correlation between the superconducting properties of the YBCO layer with the microstructure which was adapted from the underlying NiW template, a comparison between the EBSD mapping and SHPM images was conducted.

To account for the distortions of the EBSD scans and Hall maps, an SEM image of the etched spots was first overlapped and aligned with the field map. This

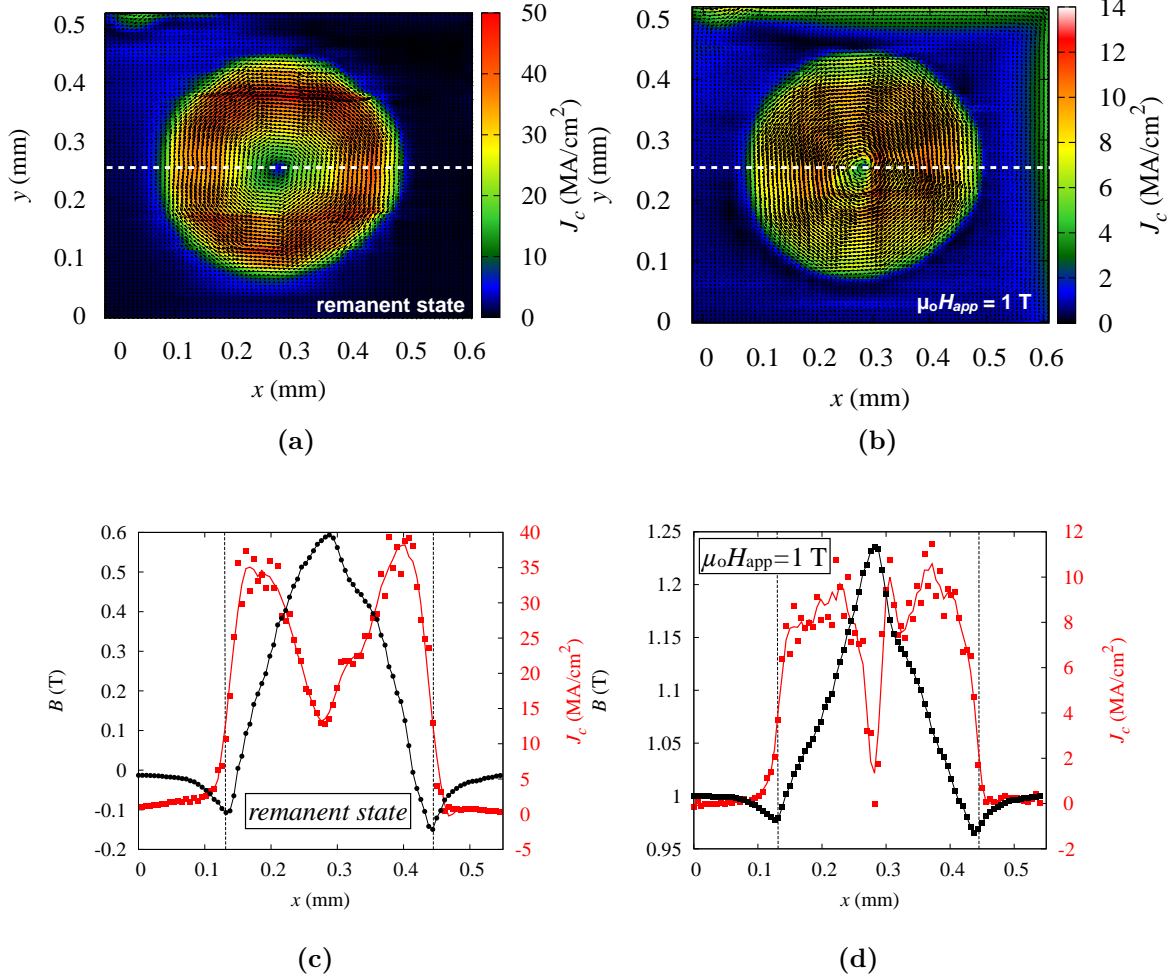
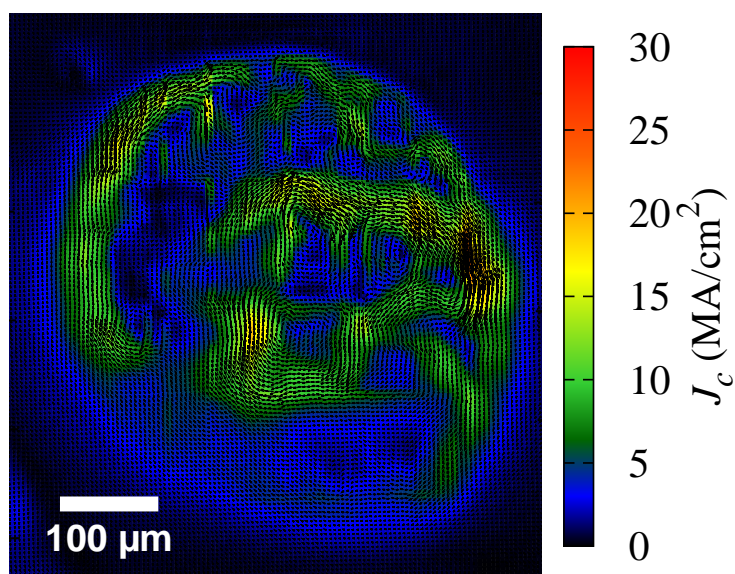


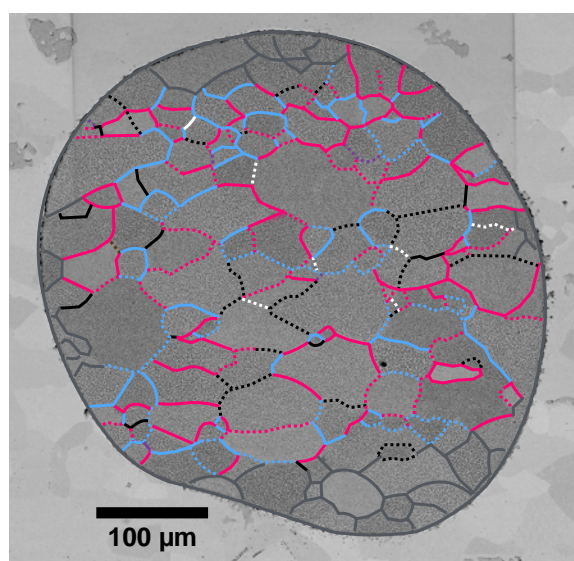
**Figure 5.9:**  $J_c$  map at  $T = 4$  K in the (a) remanent state and (b)  $\mu_0 H_{\text{app}} = 1$  T. The white dashed line correspond to the linescans in (c) and (d).

procedure corrects the rotation and aspect ratio of  $B(x, y)$  with respect to the real geometry provided by SEM. Then, the GBs evaluated from the EBSD maps were traced on the SEM image of the same spot (see figure 5.10b) and is consequently overlapped to the field and  $J_c$  maps. The conducted analysis may still have a small spatial misalignment between the EBSD and the field maps since only the apparently best correlation between the field profile, SEM and EBSD images was chosen. However, a possible rotation of up to  $10^\circ$  and positional variation of  $\pm 5\mu\text{m}$  does not change the general correlation between the local  $B$ , GBs and the shape of the clusters of grains in the EBSD images. These comparisons enable the analysis of local properties with  $B(x, y)$ ,  $J(x, y)$  and EBSD.

Images of the  $B(x, y)$  and  $J_c(x, y)$  at  $T = 4$  K with overlapped  $\vec{J}$ -vector field and GBs of a  $150\text{-}\mu\text{m}$  spot on YBCO-Ni5W are shown in the upper panel of figure 5.11.



(a)



(b)

**Figure 5.10:** (a)  $J_c$  map at  $T = 4$  K of YBCO-Ni5W. (b) Backscatter electron image of the surface of the 400- $\mu\text{m}$  spot in YBCO-Ni5W. The colored lines correspond to the GBs traced from the EBSD map in figure 5.1b. The solid line correspond to smooth GB while the dashed lines are grooved.

Each line color in the figures pertains to a specific range of  $\theta_{\text{GB}}$  and the smooth and grooved grain boundaries are drawn as solid and dashed lines, respectively.

There are two main magnetic grain clusters that are visible in the  $B(x, y)$  and they are marked by the blue arrows and numbered 1 and 2. The division between the clusters have GBs composing of a HAGB (red), a  $> 6^\circ$  smooth and a grooved

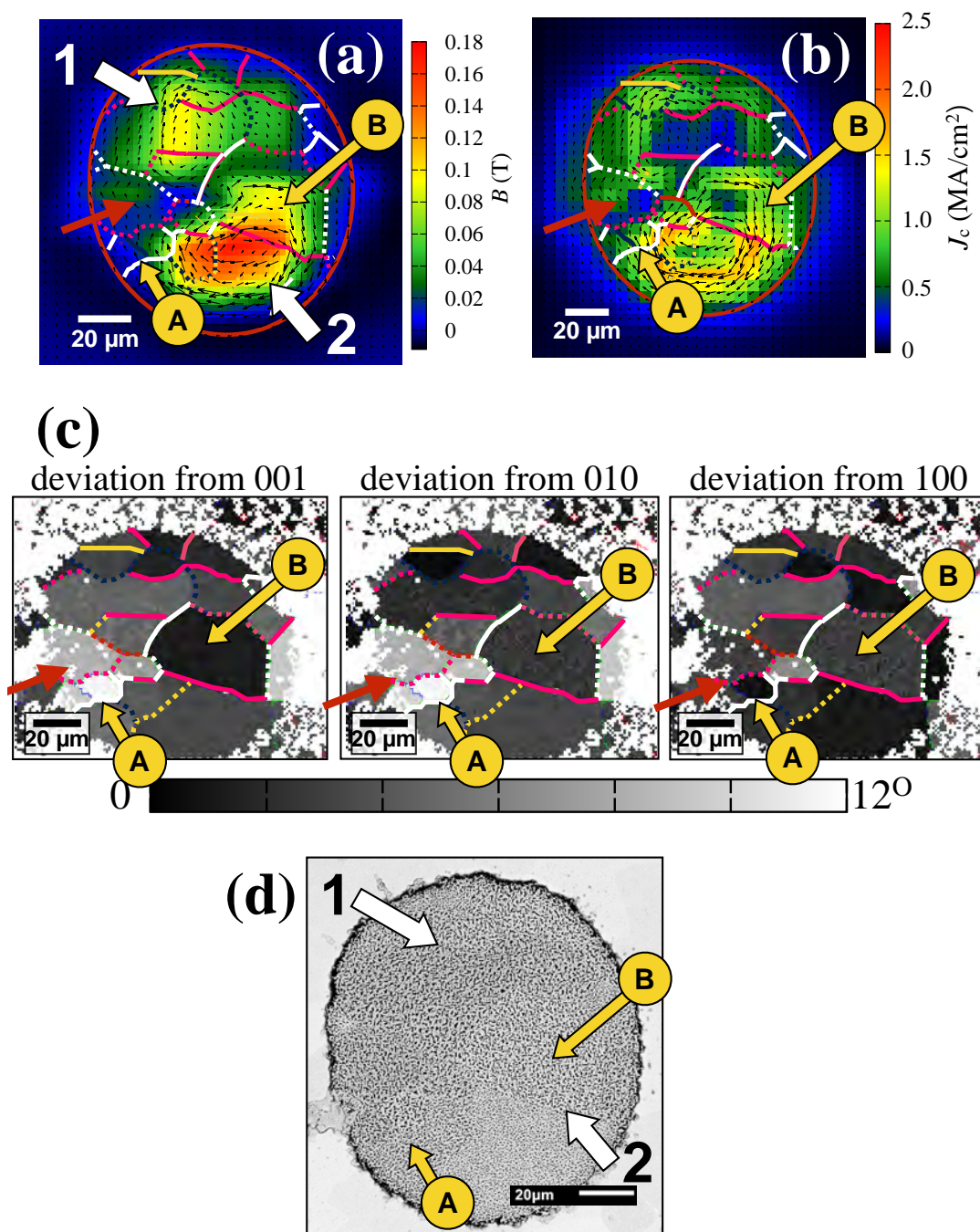


**Figure 5.11:** (a)  $B(x, y)$  and (b)  $J_c(x, y)$  of a 150- $\mu\text{m}$  spot on YBCO-Ni<sub>5</sub>W at  $T = 4$  K. The colored lines denote the GBs and each color correspond to the following  $\theta_{\text{GB}}$ : dark blue  $\rightarrow \theta_{\text{GB}} < 1.5^\circ$ , yellow  $\rightarrow \theta_{\text{GB}} = 1.5 - 3^\circ$ , pink  $\rightarrow \theta_{\text{GB}} = 3 - 6^\circ$ , white  $\rightarrow \theta_{\text{GB}} = 6 - 10^\circ$ . The solid lines and the dashed lines represent smooth and grooved GBs, respectively. (c) EBSD maps of the same spot each corresponding to the misorientation relative to the 001, 010 and 100 fiber texture. (d) BSE image of the same spot.

GBs (white lines) and  $5^\circ$  grooved GBs (dashed pink line). However, aside from the clustering of the grains, an area indicated by the red arrow has a small local magnetic signal and  $J_c$ . One must be careful in interpreting the  $J_c(x, y)$  of YBCO-NiW. As discussed in section 3.3.5,  $J_c$  approaches zero towards the center of a homogenous sample due to decreasing area enclosed by circulating currents. This minimum corresponds to a peak in  $B(x, y)$ . The other areas with reduced  $J_c$  are correlated with the reduction of the slope in the field profile and can be considered as a reasonable representation of local  $J_c$ .

According to the local orientation mapping in the lower panel of figure 5.11, the area with the largest misorientation from a cubic texture corresponds to the area with lower  $B$  and  $J_c$  denoted by the red arrow. Each of the panels of the EBSD images correspond to deviation from three directions: the rolling (100), transverse (010) and orthogonal (001) directions of the substrate (see schematic diagram in figure 5.12a). Using the separated misorientations from each direction, the relative orientation of two adjacent grains can be deduced and the type of GB can also be determined.

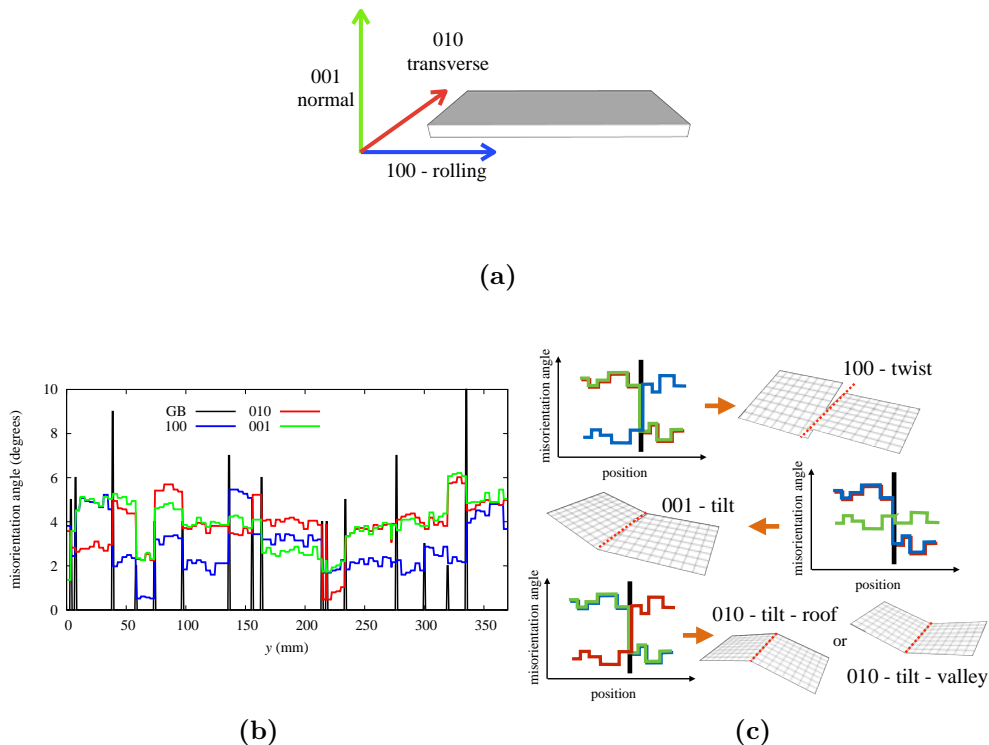


**Figure 5.12:** (a) An EBSD linescan in YBCO-Ni5W. (b) Schematic diagram of the 100, 010 and 001 directions. (c) GB types formed in YBCO films.

To elaborate this, consider a linescan taken across an EBSD map of the YBCO-Ni5W. The GBs are indicated by the black solid lines and the misorientation angle from the 001, 010 and 100 directions are indicated by the green, red and blue lines,



respectively. Based on the EBSD linescans, some grains have two directions with correlated misalignment. If this occurs, the axis of rotation for the misalignment is about the third uncorrelated axis. As an example, consider the uppermost panel of figure 5.12c, if the 010 and 001 directions of two adjacent grains are correlated, the axis of rotation of both the grains is about the 100 direction and the type of GB is a 100-twist type. Similar analysis is done for the other possible correlations as illustrated in figure 5.12c. In some cases, all the three directions, i.e. 100, 010 and 001, are all misoriented and a GB can be a combination of two types. The diagrams presented in figure 5.12c are the simplest systems that can be deduced from the results of EBSD linescans and are the ones relevant in CCs. The behavior of the current density of each type of GB was investigated by Held et al. [47] on bicrystal samples. They found that the most detrimental to  $J_c$  is the 001-tilt boundaries compared to the 010-tilt and 100-twist boundaries.

Going back to the EBSD maps in figure 5.11, the area marked by the red arrow has correlated misorientation along 001 and 010, this means that this area has a local crystallographic tilt of about  $8^\circ$ , similar to vicinal films, which has caused the low magnetic field signal and  $J_c$ . Despite the formation of two main magnetic clusters being divided by GBs with misorientations of at least  $5^\circ$ , there are additional interesting behaviors that deviate from expectation. An example of this is the GB marked by arrow A, which has  $\theta_{GB} > 6^\circ$  but does not block the current flow as shown by the  $\vec{J}$ -vector field. Based on the EBSD map, the boundary is a 100-twist type and it is not grooved as illustrated in the backscatter electron (BSE) image in figure 5.11d. There are also local areas within the clusters that have reduced  $J_c$  such as the grain indicated by arrow B. The local orientation map shows that such grain actually has good texture with misorientation of only about  $2^\circ$ . However, the BSE image (figure 5.11d) of the grain illustrates that it has a more porous YBCO layer compared to the surrounding grains. Larger pores are also formed in the grains of the upper magnetic cluster (#1) that has evidently smaller  $J_c$  compared to the lower magnetic cluster (#2).

Similar correlation between the magnetic field,  $J_c$  and EBSD map is observed in the larger 400- $\mu\text{m}$  spot despite the more complicated analysis due to its larger area. An enlarged part of this spot is presented in figure 5.13a-b. Most of the GBs that affects the current percolation has at least  $\theta_{GB} = 6^\circ$ . The boundaries are mostly either blocking the current flow, where the  $\vec{J}$ -vector are directed almost parallel to the GB, or reduce the current flowing to the adjacent grain. An example of this is GB 3 marked in figure 5.13b, which has a  $9^\circ$  misorientation angle as shown by the EBSD linescan in 5.13f. However, it is still not always the case that GBs of at least  $6^\circ$  obstruct the current flow. Some of them, especially those that are not grooved, does not block the current. The physical characteristics of the deposited YBCO layer and relative misorientation with respect to the adjacent grain seem to have more significant effects. A grooved GB, marked with #2 in figure 5.13a and shown in the SEM image in figure 5.13d is clearly dividing two magnetic grain clusters. Another grain, marked with #1 in figure 5.13c has a more porous YBCO layer

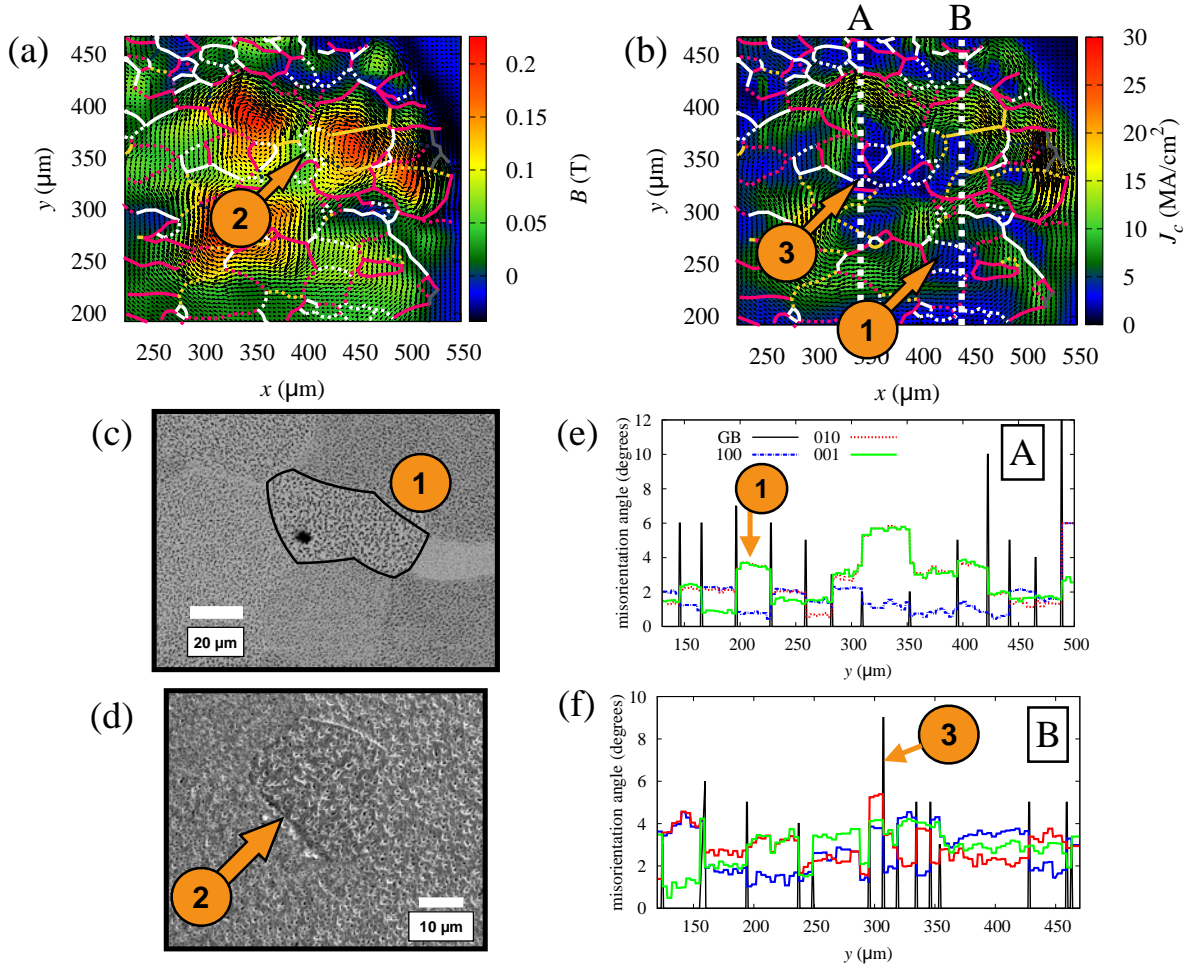


**Figure 5.13:** (a)  $B(x, y)$  and (b)  $J_c(x, y)$  of a 400- $\mu\text{m}$  spot on YBCO-Ni5W at  $T = 4$  K. (c) BSE image of grain 1. (d) SEM picture of GB 2. EBSD linescan along the (c) line A and (f) line B marked in the  $J_c$  map in (b).

relative to the surrounding grains, thus it has lower  $J_c$  as shown in figure 5.13b. It also has a tilted crystal structure determined by the EBSD linescan in figure 5.13e.

By conducting simultaneous analysis of the superconducting properties through magnetic field profiles and local orientation mapping, a few important results about YBCO-Ni5W coated conductors is attained. First is the big influence of the underlying texture of the NiW template to the structural and superconducting properties of the YBCO layer. This leads to a granular magnetic field profile and percolative current flow. The formation of magnetic grains depends on the GB misorientation angle and relative misorientation of adjacent grains. Some GBs with at least  $\theta_{\text{GB}}$  of  $6^\circ$  affects the current flow. This value is slightly larger than the critical angle,  $\theta_c$  found by Verelbeyi, et al. [93] by transport measurements of bicrystal films. Their value of  $\theta_c$  is  $4^\circ$  and was obtained experimentally as the onset of exponential dependence of  $J_c$  with  $\theta_{\text{GB}}$ . Feldmann et al. [30], found the same  $\theta_c$  in PLD-YBCO films on RABiTS Ni substrate through a combined

magneto-optical imaging and local orientation mapping. They have shown that with an applied field of 60 mT and temperature of 15 K, magnetic flux starts to penetrate in the weak linked region with  $\theta_{GB}$  of at least  $4^\circ$ . However, the limitation by the  $6^\circ$ -boundaries does not always happen in the case of the YBCO-Ni5W. The formation of grooves and trenches on boundaries also inhibit the current flow. In addition, local inhomogeneity in  $J_c$  is also present due to local vicinity within each NiW grain.

### 5.1.4 Transport $J_c$

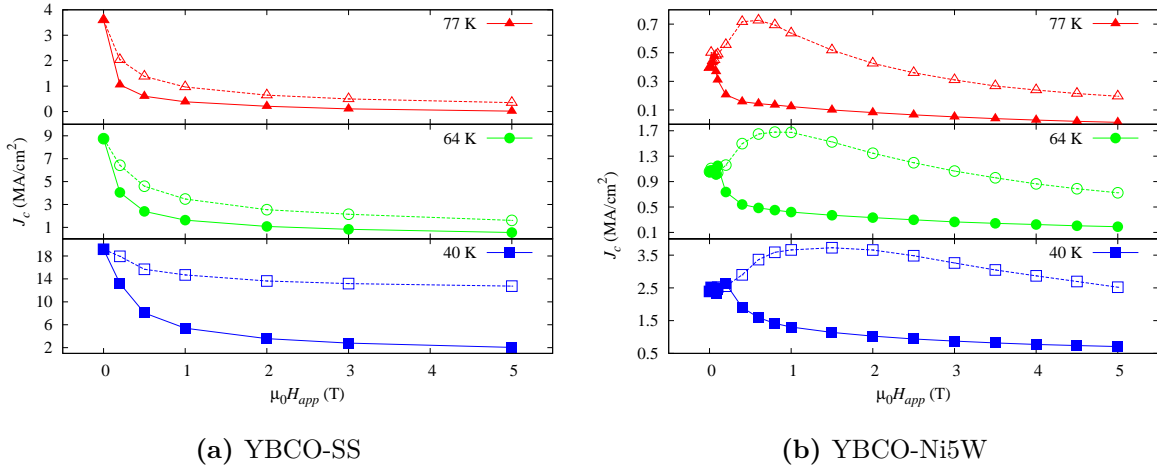


**Figure 5.14:** Field dependence of  $J_c$  at different temperatures for (a) YBCO-SS and (b) YBCO-Ni5W. The filled symbols correspond to  $H_{app} \parallel c$  and the hollow symbols correspond to  $H_{app} \parallel ab$ .

Figure 5.14 shows the field dependence of  $J_c$  of YBCO-SS and YBCO-Ni5W at temperatures of 40 K, 64 K and 77 K measured by transport measurement. Both tapes have laser-structured bridges with a width of about  $300 \mu\text{m}$ . The YBCO-SS has a monotonically decreasing  $J_c$  with increasing field, when the applied field is parallel to both the  $ab$ -planes and the  $c$ -axis. This behavior is expected and widely observed on different YBCO samples with pure composition [17]. On the other hand, the YBCO-Ni5W has a peculiar behavior that leads to two different  $J_c(H_{app})$ -dependences for  $H_{app} \parallel ab$  and  $H_{app} \parallel c$ . For  $H_{app} \parallel c$ ,  $J_c$  starts with a stochastic behavior at low fields, which increases in field range as the temperature decreases (see figure 5.14b). At  $T = 40 \text{ K}$ , the stochastic range extends up to 0.2 T followed by the usual monotonic decrease as the field is increased. For  $H_{app} \parallel ab$ , the stochastic behavior at low-fields is followed by an increase of  $J_c$  up to some applied field,  $\mu_0 H_{peak}$ , and then followed by a monotonic decrease at high fields. The peak becomes broader and shifts to larger fields as the temperature decreases. Note that the YBCO-SS has about 9 times larger self-field  $J_c$  than the YBCO-Ni5W.

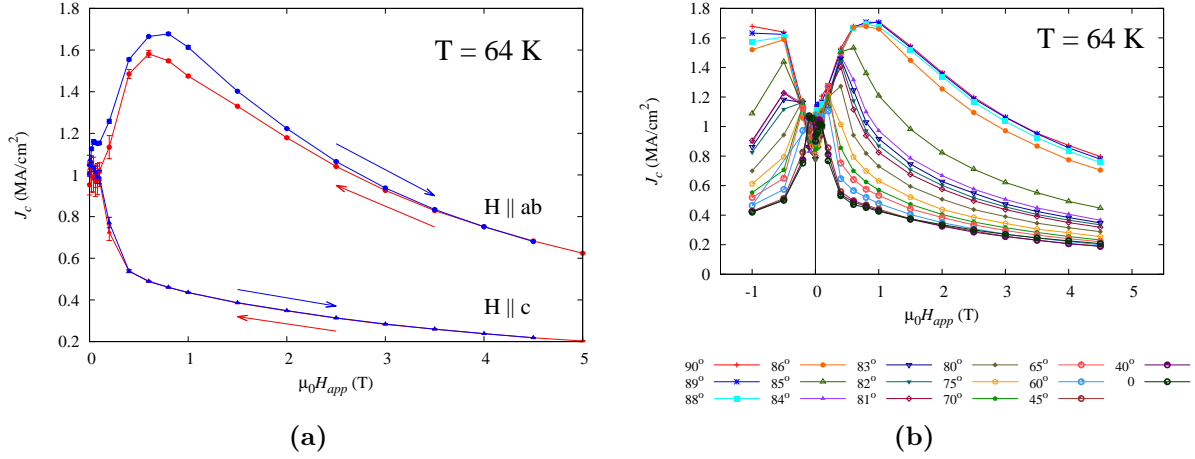


**Figure 5.15:** (a)  $J_c(H_{\text{app}})$  in increasing and decreasing field at  $T = 64$  K and in two field directions,  $H_{\text{app}} \parallel ab$  and  $H_{\text{app}} \parallel c$ . The error bars are calculated by obtaining three consecutive IV-curves at each field. No sample heating was observed during the measurement. (b)  $J_c(H_{\text{app}})$  at  $T = 64$  K at different angles the applied field to the  $c$ -axis. By convention,  $\phi = 90^\circ$  and  $\phi = 0$  corresponds to  $H_{\text{app}} \parallel ab$  and  $H_{\text{app}} \parallel c$ , respectively.

As shown in figure 5.15a, the peak in  $J_c(H_{\text{app}})$  when the field is parallel to the  $ab$ -planes appears both in the increasing (blue curve) and decreasing field (red curve) after the sample is zero field cooled. A hysteresis is also observed around  $H_{\text{peak}}$  and the scatter in  $J_c$  is larger at smaller fields, i.e. in the range where the stochastic behavior is observed. When the applied field is tilted away from the  $ab$ -planes (figure 5.15b), the peak becomes narrower and shifts to smaller fields until it disappears near the direction of the  $c$ -axis.

Plots of the angle-dependence of  $J_c$  at different applied fields and temperatures of 77 K, 64 K and 40 K are shown in figure 5.16. At 77 K,  $J_c$  is  $\phi$ -independent and the  $ab$ -peak is truncated within an angular range  $\Delta\phi_{\text{GB}}$ . As the field is increased, the usual anisotropy in  $J_c$  is observed. At the lowest measurement temperature of 40 K, the  $J_c(\phi)$  curve at  $\mu_0 H_{\text{app}} = 0.2$  T is almost  $\phi$ -independent over the whole angular range and fluctuates around the value of  $J_{c,\text{sf}}$ . Note that 0.2 T is within the range when  $J_c$  has the stochastic behavior in its magnetic field dependence, indicated by the corresponding red vertical line in figure 5.16d. 0.5 T is within the field range when  $J_c$  is increasing and that's where a finite  $\Delta\phi_{\text{GB}}$  is observed in  $J_c(\phi)$ . For applied fields of 1 T and above, the angle dependence of  $J_c$  has its usual anisotropic behavior.

It is noteworthy to mention that all the experimental VJ-curves at each angle, field and temperature are well-described by a power law. Data at  $T = 40$  K and applied fields of 0, 0.6 T and 5 T are shown on figure 5.17 for  $H_{\text{app}} \parallel ab$ . Various publications have reported a non-Ohmic linear differential (NOLD) behavior in the VJ-curves due to viscous flux flow of vortices along the GBs [31, 55]. However, in

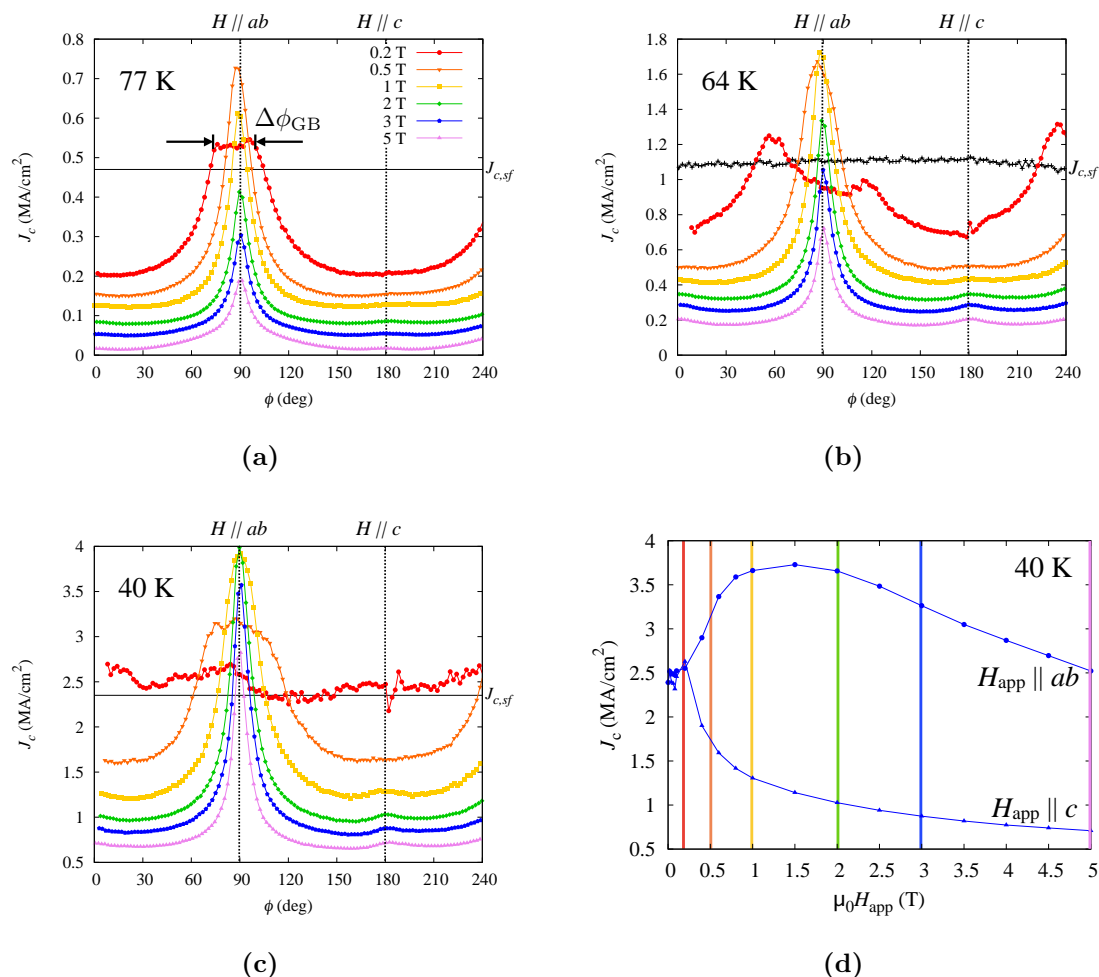


**Figure 5.16:** Angle dependence of  $J_c$  at different applied magnetic fields and temperatures of (a) 40 K, (b) 64 K and (c) 77 K. The black lines (black data points in the case of 64 K) indicate the self-field  $J_c$  ( $J_{c,sf}$ ) at each temperature. (d) Field dependence of  $J_c$  at 40 K. The colored lines correspond to the fields of the  $J_c(\phi)$  curves in (c).

the present set of data, such NOLD behavior is not observed indicating a probable dominance of the flux creep in parts of the grains. Alternatively, this may be an average result from all the percolative flow of the current through the network of GBs.

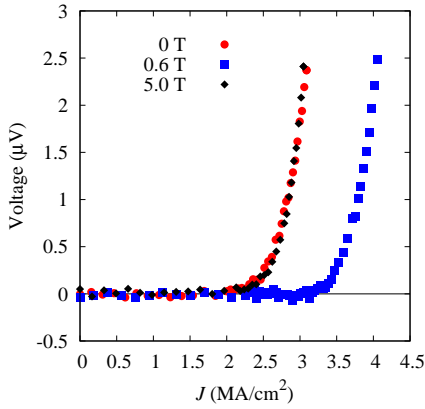


**Figure 5.17:** VJ curves at  $T = 40$  K and fields of 0, 0.6 and 5 T when  $H_{\text{app}} \parallel ab$ .

### 5.1.5 Magnetic field profiles in the direction of $H_{\text{app}} \parallel ab$

The peculiar behaviors in the field dependence and anisotropy of  $J_c$  in YBCO-Ni5W, which are absent in the YBCO-SS, are effects of its strong granularity manifested in the magnetic field mapping. To further examine the occurrence of the peak in  $J_c(H_{\text{app}})$  in the direction of the  $ab$ -planes, magnetic field profiles were measured using the SHPM with the field applied nearly parallel to the surface of the substrate.

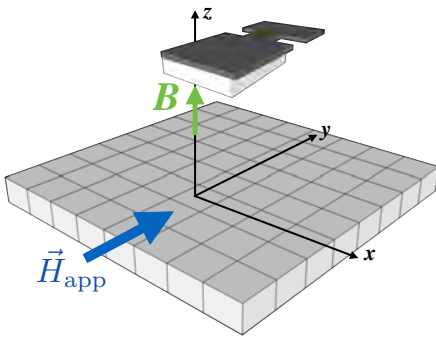


**Figure 5.18:** Schematic diagram of the SHPM configuration for  $H_{\text{app}} \parallel ab$ .

Figure 5.18 illustrates a schematic diagram of the configuration of the SHPM measurement. The sample rod was placed inside a He gas flow cryostat with a split-coil 6 T magnet. In principle, the magnetic field is applied approximately parallel to the substrate surface while the field detected by the Hall probe is along the  $z$ -axis. In a real system, it is almost impossible and not desirable to achieve the configuration where the applied field is parallel to the  $ab$ -planes or to the substrate surface because the NiW tape has an intrinsic bending. There is an estimated tilt of about  $3^\circ$  between the applied field and the sample surface. This value was obtained by taking the  $z$ -position where the Hall probe is in contact to the sample surface on two opposite ends of the measured area. The small tilt becomes an advantage for the measurement because it allowed a finite value of penetration field for this configuration. The value of  $H^*$  for thin films varies according to the angle between the applied field and the direction normal to the sample,  $\theta$ , as

$H^* \approx J_c d / \cos \theta$ . Therefore, for a typical value of  $J_{c,\text{sf}}$  at 40 K of 2.5 MA/cm<sup>2</sup> (this value was taken from the transport measurement), one can expect  $H^{*\perp}$  to be about 0.9 T. In the trapped field profile with  $H_{\text{app}} \parallel c$ , typical values of the local field along the boundaries is about 20-40 mT (refer to figure 5.20a), this corresponds to a penetration field when  $H_{\text{app}}$  is 3° away from the surface of the tape as:  $H_{\text{peak}} / \cos(87^\circ) \approx 0.4 - 0.8$  T which is well within the range of the expected value from transport measurement.

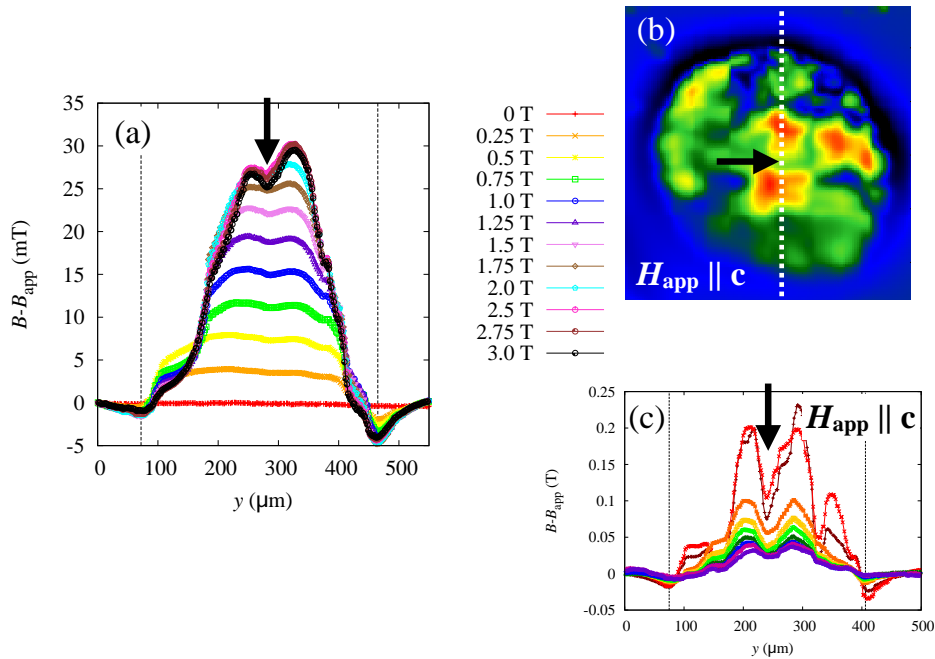


**Figure 5.19:** Linescans across the center of a 400- $\mu\text{m}$  spot at 40 K after zero-field cooling. The applied magnetic field was ramped up to 3.0 T, taking a linescan at each magnetic fields. The stepwidth was 2  $\mu\text{m}$ . The Hall probe was moved at a constant distance across the diameter and the asymmetry at the two opposite ends is due to the inclination of the surface of the sample, which is about 2  $\mu\text{m}$  away from the Hall probe at one end and 10  $\mu\text{m}$  away on the other end. (b) The remanent field profile of the same spot when the field is applied parallel to the  $c$ -axis. (c) In-field linescans that correspond to the dashed white line in (b). The black arrows correspond to a NiW GB with  $\theta_{\text{GB}} = 9^\circ$  found in the EBSD image that divides two magnetic grains.

In figure 5.19a, a linescan across the center of the 400- $\mu\text{m}$  spot at 40 K and different  $\mu_0 H_{\text{app}}$  is presented after zero-field cooling. It can be observed that as the field increases from zero to 0.5 T, a plateau-like profile forms. At 0.75 T and above, two peaks and a boundary at the center of the profile becomes visible. This boundary corresponds to the NiW GB with  $\theta_{\text{GB}} = 9^\circ$  that divides two magnetic grains. At 2.0 T and above, the field profile is fully formed and  $B$  starts to decrease.

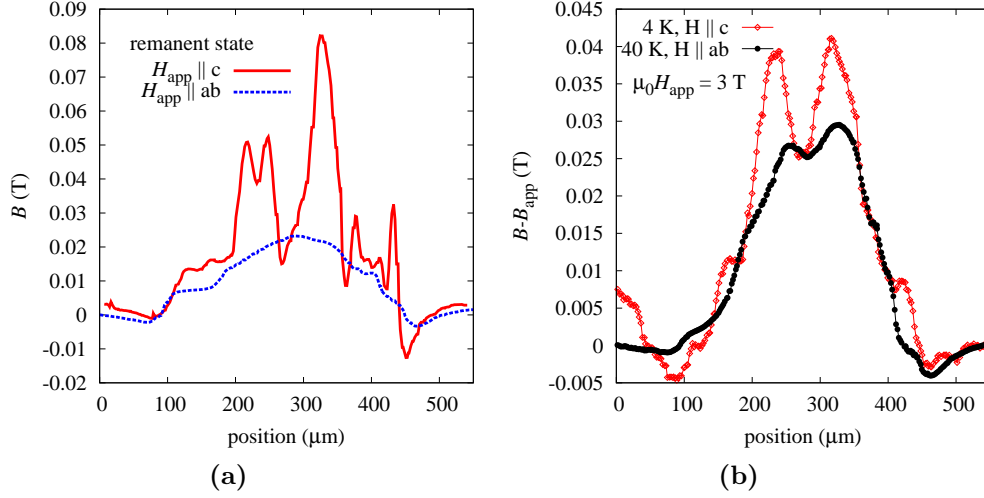


**Figure 5.20:** Comparison of the field profiles measured by SHPM when the field is applied parallel to the two main crystallographic direction in (a) remanent state and (b) with an applied field of 3 T.

Comparisons of the field profiles when  $H_{\text{app}} \parallel ab$  and  $H_{\text{app}} \parallel c$  are shown in figure 5.20. The linescans were taken at approximately similar positions denoted by the white dashed line in figure 5.19b. The distance between the Hall probe and the sample surface of the measurements was about 4  $\mu\text{m}$ . The profile with  $H_{\text{app}} \parallel c$  is strikingly more granular than with  $H_{\text{app}} \parallel ab$ . The dip at the center of the remanent field for  $H_{\text{app}} \parallel ab$  (figure 5.20a), which corresponds to the  $9^\circ$  boundary does not appear. Although this may signify that the applied field of 3 T prior to the measurement of the remanent field is not enough to fully penetrate and reverse the field profile of a magnetic cluster. As observed in figure 5.20a, a magnetic grain at  $H_{\text{app}} \parallel c$  has a peak value of 0.085 T which corresponds to an  $H^*$  of 1.6 T and  $2H^*$  of 3.2 T. The previously estimated  $H^*$  of 0.9 T corresponds to  $J_c$  which is limited by the GBs and this is consistent to the appearance of a dip at the center of the field profile (figure 5.19a) starting at 0.75 T. Nevertheless, even by comparing the profiles with an applied field of 3 T (figure 5.20b), the linescan with  $H_{\text{app}} \parallel c$  is evidently more granular.<sup>1</sup> The difference in the degree of granularity between the two field directions is quite unexpected if one considers that the intragranular current is larger than the intergranular current at least in the remanent state where  $J_c$  is limited by the GB in both directions.

Linescans taken subsequently from -3 T to +5 T and back to -2 T (marked by the arrows) after applying a magnetic field of -5 T are shown in figure 5.21. The value of the peak in each profile is plotted as a function of the applied field and is presented by the blue curve in the largest panel of figure 5.21. The profile with

<sup>1</sup>The compared data in figure 5.20b refer to different temperatures due to unavailability of the linescan at 3 T and 40 K for  $H_{\text{app}} \parallel c$ . However, the granular morphology is not expected to be different between 4 K and 40 K as confirmed by other set of experimental data.



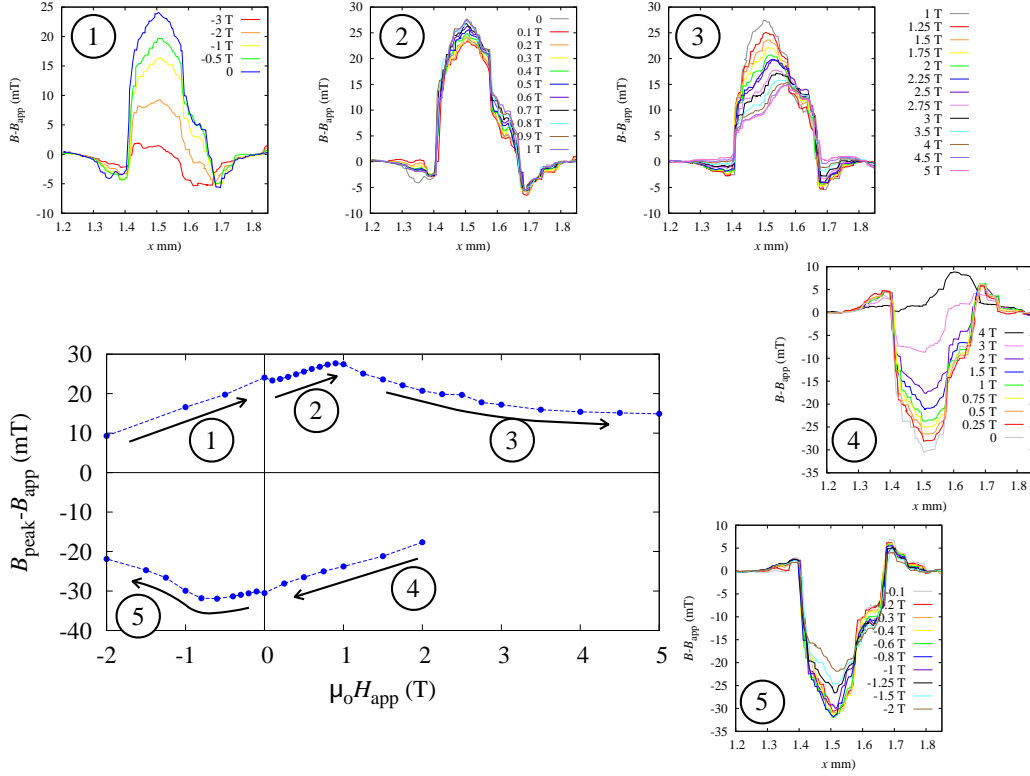


**Figure 5.21:** The five plots of  $B - B_{app}(x)$  numbered between 1-5 are linescans across the center of the same circular spot on YBCO-Ni5W. After the sample was zero field cooled, linescans were obtained from -3 T to +5 T and back to -2 T. The peak of the in-field profiles is plotted as a function of the applied field. The sequence of the applied fields are denoted by the direction of the arrows.

$\mu_0 H_{app} = -3$  T (panel 1) is not in a fully-reversed state yet as well as the profiles of 3 T and 4 T in panel 4. Therefore,  $B_{peak}$  of these curves is omitted in the plot of  $B_{peak}(H_{app})$ .

One interesting feature of these sequence of  $B(x)$  curves is the increasing  $B_{peak}$  from zero to 0.9 T in panel 2 and from zero to -0.8 T in panel 5 while a monotonic decrease of  $B_{peak}$  with field is observed in decreasing field.

The increasing  $B_{peak}$  in the increasing field segment has a direct correlation with the peak observed in the  $J_c(H_{app})$ -dependence from transport measurements. Both occur at a similar range in  $H_{app}$  i.e. zero to 1 T. Note that the samples used in SHPM and in the transport measurements are not from the same piece but were prepared with similar deposition conditions on the same substrate. Therefore, the non-monotonic behavior of  $J_c(H_{app})$  is indeed related to the granularity in YBCO-Ni5W. A possible mechanism in relation to vortices will be discussed in the next section.

These SHPM measurements with field applied roughly parallel to the  $ab$ -planes are done for the first time. It is demonstrated that a difference can be observed between the granularity of the field profile when  $H_{\text{app}}$  is oriented parallel to the  $c$ -axis or to the  $ab$ -planes. The evolution of the profiles with field were also found to have an interesting behavior. However, the mechanism governing such peculiar behaviors is beyond the scope of this thesis and further studies must still be done in order to gain more insight on this type of SHPM measurement configuration.

### 5.1.6 Non-monotonic $J_c(B)$ behavior

The occurrence of a peak in  $J_c(H_{\text{app}})$  has already been observed and reported in various publications. One of them is in a system with columnar pinning centers (CPC). When the applied field is oriented parallel to the CPCs, the peak in  $J_c$  occurs at the matching field,  $B_\Phi$ , where the density of the pinning centers is equal to the density of the vortices such that each columnar defect has one pinned vortex [13]. Therefore, matching field effects must be temperature independent. However, this is not the case in the observed data and the pinning centers parallel to the  $ab$ -planes are either the  $ab$ -planes or stacking faults, which have large density and would lead to very high matching fields, larger than the  $H_{\text{app}}$  where the peak occurs in the data.

A peak on the decreasing field branch of the irreversible magnetization was observed by A. Palau, et. al. [72] and has been explained according to the electromagnetic granularity of HTS films on metallic templates. The local magnetic field,  $H_{\text{loc}}$ , at the GBs is expressed as a vector sum of the applied field,  $H_{\text{app}}$ , and the return field induced by the magnetic induction in each individual grain,  $H_{\text{edge}}$ , such that:  $H_{\text{loc}} = H_{\text{app}} + H_{\text{edge}}$ . On the decreasing field branch of the magnetization loops,  $H_{\text{app}}$  and  $H_{\text{edge}}$  have opposite directions. Therefore, the appearance of the peak is due to an approximately zero net field at the GBs when the return field from the trapped flux in the grains and the applied fields are approximately equal. This leads to a maximum of  $J_c^{\text{GB}}$  at non-zero  $H_{\text{app}}$ . This was also observed in transport measurements by A. Gapud, et al. [36]. However, in the case of the data observed in the YBCO-Ni5W, the peak in  $J_c(H_{\text{app}})$  in transport measurements occurs both when the field is increased and decreased and does not depend on the history of the applied field. Therefore, the model by A. Palau does not explain the experimental data.

A plausible mechanism for the behavior of the PLD-grown YBCO on RABiTS NiW is according to a model proposed by A. Gurevitch and L. Cooley [37]. The observed non-monotonic behavior in  $J_c(B)$  is explained as a consequence of magnetic interaction between Abrikosov (A) vortices and vortices residing in planar defects. Such planar defects must not necessarily block the current flow and cause decoupling of grains. A network of low angle grain boundaries ( $\theta_{\text{GB}} < 10^\circ$  [22]) is a perfect example for this system since LAGBs consist of an array of dislocation cores and

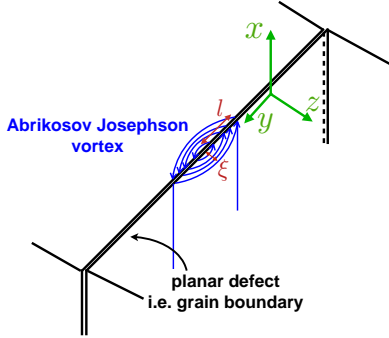


**Figure 5.22:** Representation of an Abrikosov Josephson (AJ) vortex in a planar defect along the  $xy$ -plane.

strained superconducting channels that leads to suppression of the superconducting order parameter [28]. However, the dislocation cores do not overlap in the boundary yet unlike Josephson junctions. The weak link nature of LAGBs causes a distortion of the circulating current of a vortex lying in the boundary. Using the non-local Josephson equations which accounts for a local variation of the phase  $\varphi$  across a weak link, A. Gurevich [37,38] has derived the field distribution when an Abrikosov vortex interacts with a planar defect.

Consider a LAGB lying on the  $xy$ -plane as shown in figure 5.22. When a vortex is localized in it, the characteristic length of the vortex core parallel to the  $y$ -axis has some length  $l$  while it takes the length  $\xi$  in the  $z$ -direction such that  $l > \xi$ . This vortex structure is referred to as Abrikosov-Josephson (AJ) vortex. AJ vortices are pinned more weakly than the A vortices due to their larger dimension parallel to the planar defect.

Implementing the Gurevich model on the planar GBs in PLD-grown samples, the pinning force on an AJ vortex parallel to the plane of the defect (along the  $xy$ -plane in figure 5.22) can be written as a sum of two contributions:

$$f_{\text{GB}} = f_{\text{h}} + f_{\text{i}} \quad (5.1)$$

where  $f_{\text{h}}$  refers to pinning due to the inhomogeneities in the GB and  $f_{\text{i}}$  refers to effective pinning due to the interaction of the AJ vortices with the A vortices inside the grains.

The contribution  $f_{\text{h}}$  is derived by A. Gurevitch by considering the energy gain in the AJ vortex core as it is moved from an inhomogeneity of length  $L$  and is expressed as:

$$f_{\text{h}} = \left( \frac{\Phi_0}{4\pi\lambda} \right)^2 \frac{\alpha L}{\mu_0(L^2 + l^2)} \quad (5.2)$$

where  $\alpha$  characterizes the degree of inhomogeneity of current density in the GB ( $j_c$ ), i.e.  $\alpha \cong \delta j_c / \langle j_c \rangle$ . The contribution from  $f_i$  is determined from the minimum gradient of the A vortex energy along the defect.

$$f_i = \frac{\Phi_o \langle \delta H^2 \rangle^{1/2}}{4\pi a} \quad (5.3)$$

where  $a$  is the spacing between A vortices,  $a = (\Phi_o/B)^{1/2}$ , and  $\langle \delta H^2 \rangle$  is the mean dispersion relation of the quasi-periodic fluctuation of the local field in the flux line structure and was derived by P. Pincus, et al. [74] as  $\langle \delta H^2 \rangle = \Phi_o^2 / (16\mu_o^2 \pi^3 \lambda^4)$ . Therefore,  $f_i$  is finally expressed as:

$$f_i = \frac{\Phi_o}{4\mu_o \pi^2 \lambda^2} \left( \frac{B}{\pi \Phi_o} \right)^{1/2} \quad (5.4)$$

By equations 5.1, 5.2 and 5.4, the total pinning force on an AJ vortex parallel to the GB is:

$$f_{\text{GB}} = \frac{\Phi_o^2}{16\pi^2 \mu_o \lambda^2} \left( \frac{\alpha L}{L^2 + l^2} + \sqrt{\frac{B}{\pi \Phi_o}} \right) \quad (5.5)$$

By taking the derived pinning force on an AJ vortex in equation 5.5 to be equal to the Lorentz force per unit length,  $f_L$ , the critical current density of the GB,  $J_c^{\text{GB}}$ , is expressed as  $f_L = G f_{\text{GB}} = J_c^{\text{GB}} \Phi_o$ , where  $G$  is a constant depending on the relative orientation of the magnetic flux to the current flow. For simplicity we can take  $G=1$ , therefore,  $J_c^{\text{GB}}$  is written as:

$$J_c^{\text{GB}} = J_o \left( 1 + \sqrt{\frac{B}{B_s}} \right) \quad (5.6)$$

where:

$$J_o = \frac{\alpha \Phi_o L}{\mu_o (4\pi \lambda)^2 (L^2 + l^2)} \quad (5.7)$$

$$B_s = \frac{\pi\Phi_o\alpha^2L^2}{(L^2 + l^2)^2} \quad (5.8)$$

Equation 5.6 convey that the second term, which represents the increase in  $J_c$  with  $B$  can occur due to the interaction of the A vortices in the grains and AJ vortices along the GB.

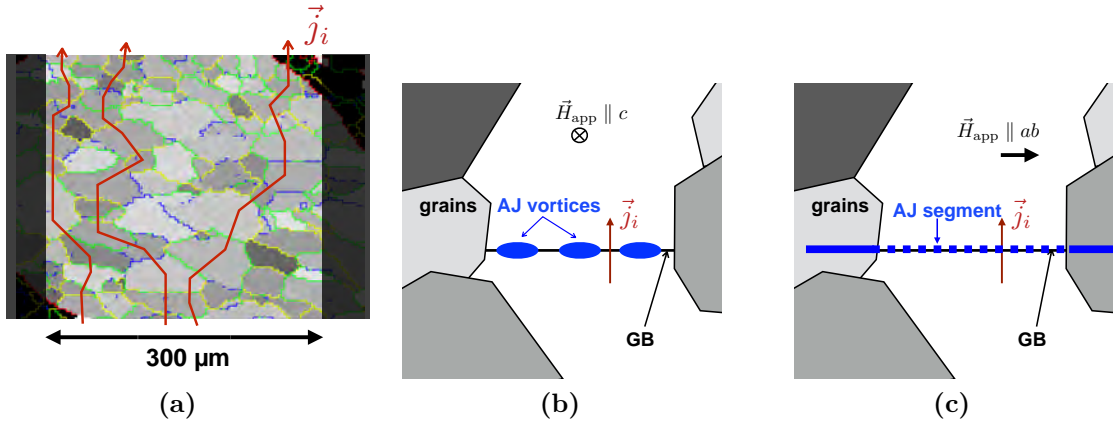


**Figure 5.23:** (a) Schematic of current flow on YBCO-Ni5W. (b) Diagram of an AJ-vortex lying in the GB when  $H_{\text{app}} \parallel c$  and (c) when  $H_{\text{app}} \parallel ab$ .

The non-monotonic behavior of  $J_c(B)$  that is explained by the Gurevich model was reported by Kim et al. [54] and Cai et al. [9] in bi-crystal samples and Cantoni et al. [10] in YBCO films on vicinal STO substrate with a network of anti-phase boundaries. Their samples are relatively simple systems where it is easy to visualize how the field would be oriented with respect to the current flow, the planar defect and the crystallographic orientation of YBCO. In all of these reports, the applied field is oriented perpendicular to the macroscopic surface of the films. However, the morphology of YBCO-Ni5W is much more complicated. Pulsed laser deposition of YBCO leads to formation of planar GBs across the whole layer thickness and irregularly shaped grains if viewed from the top of its surface. Recall that according to the result of the spatial distribution of  $J_c$  and local orientation mapping in section 5.1.3, the magnetic grains enclose GBs with misorientation angles less than  $6^\circ$ , or even higher. In transport measurements, narrowing the width of the bridge down to  $300 \mu\text{m}$  (see figure 5.23a) causes a higher probability that the current passes only through a single to a few GBs. The whole length of the penetrating flux at  $B \parallel c$  or part of its length towards the  $B \parallel ab$  direction may lie along a GB that becomes a channel for weakly pinned segments of an AJ vortex. This would therefore limit  $J_c$  within a particular range of  $H_{\text{app}}$ .

The non-monotonic dependence of  $J_c(B)$  measured by transport measurements can be divided into two regions: The first region occurs below  $H_{\text{peak}}$  where  $J_c$  is limited by the GBs considering the dynamics of the AJ vortices confined in the

GBs. The region above  $H_{\text{peak}}$  corresponds to  $J_c$  limitation by vortex pinning in the grains.

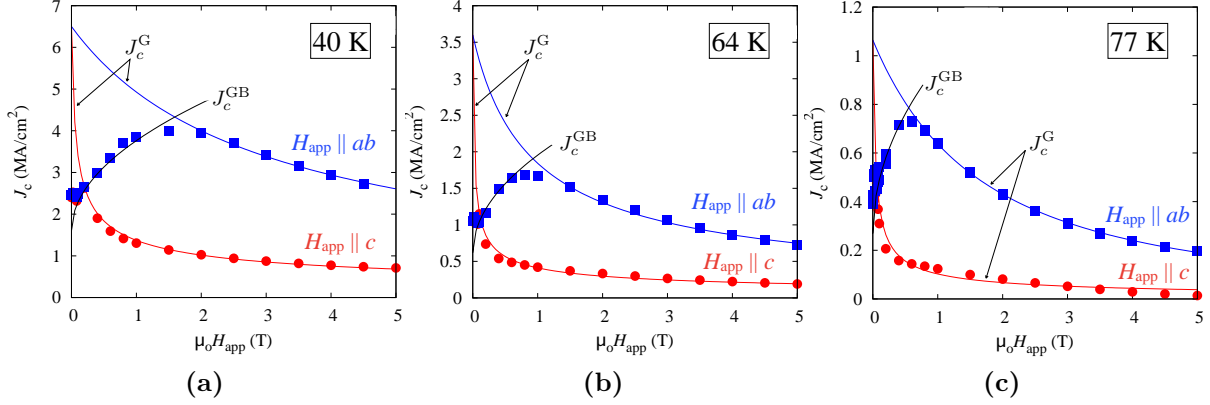


**Figure 5.24:** Field dependence of  $J_c$  of YBCO-Ni5W in  $H_{\text{app}} \parallel ab$  and  $H_{\text{app}} \parallel c$  at temperatures of (a) 40 K, (b) 64 K and (c) 77 K. The symbols correspond to data while the solid lines are the fits from equations 5.6 and 5.9.

Therefore, equation 5.6 is fitted to the range where an increase in  $J_c$  is observed. The Anderson-Kim model for the field dependence of  $J_c$ :

$$J_c(B) = J_c(0) \left(1 + \frac{B}{B_o}\right)^a \quad (5.9)$$

is fitted above  $H_{\text{peak}}$ . The data together with the fitting curves are shown in figure 5.24. The fitting parameters are given in table 5.1.

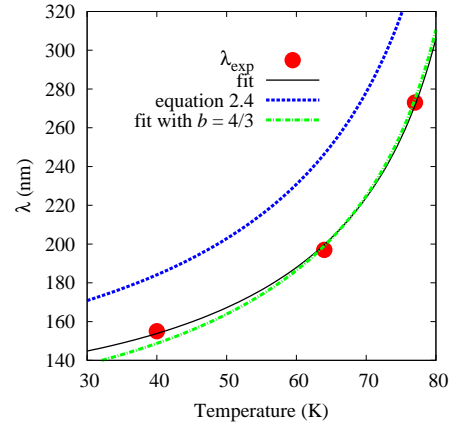
**Table 5.1:** Fitting parameters for fits of  $J_c^G(B)$  and  $J_c^{\text{GB}}(B)$  to data at 40 K, 64 K and 77 K.

T (K)	$B_s$ (T)	$J_o$ (A/m <sup>2</sup> )	$J_c(0)$ (A/m <sup>2</sup> )	$B_o[   c,    ab]$ , (T)	$\beta[   c,    ab]$
40	0.56	$1.602 \times 10^{10}$	$6.5 \times 10^{10}$	0.030, 2.6151	-0.44, -0.85
64	0.21	$0.62 \times 10^{10}$	$3.6 \times 10^{10}$	0.01, 0.68	-0.47, -0.74
77	0.15	$0.27 \times 10^{10}$	$1.06 \times 10^{10}$	0.024, 2.76	-0.623, -1.66

The parameters  $B_s$  and  $J_o$  in equations 5.8 and 5.7 are both dependent on the characteristics of the GB. A. Gurevitch has interpreted  $B_s$  as the minimum field at which  $f_{\text{GB}}$  is determined by shear flux pinning. On the other hand, the parameter  $J_o$  is defined in this work as the current density at  $B = 0$  if the mechanism is purely determined by AJ flux lines penetrating along the GB. However, the values of  $J_o$  do not exactly coincide with  $J_c(H_{\text{app}} = 0)$  in the experimental data as shown in

figure 5.14b. At very low fields, a stochastic variation in  $J_c$  is observed, which is probably due to strong percolation of currents since more grains are basically “decoupled” in this field range. The values of  $\beta$ , which is the exponent of the field term in equation 5.9 are similar to the values obtained by C. Senatore, et al. [85] for different coated conductors.

**Figure 5.25:** The red circles correspond to the calculated values of the penetration depth from the fitting parameters,  $B_s$  and  $J_c$ . The solid line denotes the fitted  $\lambda_{\text{exp}}(T)$  and the blue square symbols denote the predicted temperature dependence of  $\lambda$  for a  $d$ -wave superconductor.



Using equations 5.8 and 5.7, experimental values of the penetration depth  $\lambda_{\text{exp}}$  can be calculated. The values at 40 K, 64 K and 77 K are 155 nm, 197 nm and 273 nm, respectively and are plotted in figure 5.25. A temperature dependent function given by

$$\lambda_{\text{exp}}(T) = \lambda_{\text{exp}}(0) \left[ 1 - \left( \frac{T}{T_c} \right)^b \right]^{-\frac{1}{2}} \quad (5.10)$$

is fitted to the experimental data. With  $T_c = 90.5$  K, the fitting parameters  $\lambda_{\text{exp}}(0)$  and  $b$  are 133 nm and 1.7, respectively. For a  $d$ -wave superconductor,  $b$  takes a value of  $4/3$  [76]. Assuming  $\lambda(0) = 150$  nm [60], a predicted curve is shown as the blue-dashed plot in figure 5.25. If the parameter  $b$  is fixed to  $4/3$ , the fit to the experimental data returns  $\lambda_{\text{exp}}(0) = 121$  nm and is plotted as the green dot-dashed curve in the figure. The value of  $\lambda(0)$  is generally a quantity that is difficult to determine. It is usually extrapolated from experimental data obtained by muon spin resonance ( $\mu\text{SR}$ ) and radio frequency oscillator methods. Its value ranges from 135 [97] - 155 nm [77, 90]. Therefore, the experimental values determined from the fitting parameters are within an acceptable range for YBCO.

Since the appearance of a peak in  $J_c(B)$  of YBCO-Ni5W at  $H_{\text{app}} \parallel ab$  shows a transition from a GB-limited regime to grain-limited regime, one can interpret  $H_{\text{peak}}$  to correspond to the point at which  $J_c^{\text{G}}$  is approximately equal to  $J_c^{\text{GB}}$ . Therefore, an expression for  $H_{\text{peak}}$  can be derived as:

$$J_c^G \sim J_o \left( 1 + \sqrt{\frac{H_{\text{peak}}}{H_s}} \right) \quad (5.11)$$

$$H_{\text{peak}} \propto H_s \left( \frac{J_c^G}{J_o} - 1 \right)^2 \rightarrow H_s \left( \frac{J_c^G(\phi)}{J_o} - 1 \right)^2 \quad (5.12)$$

As follows from equation 5.12,  $H_{\text{peak}}$  is proportional to  $J_c^G$ . Since  $J_c^G$  is anisotropic with respect to the direction of  $\vec{H}_{\text{app}}$ , it is expected that  $H_{\text{peak}}$  shifts towards smaller field as the direction of the  $c$ -axis is approached. This is indeed the case in the experimental data in figure 5.15b. The increasing segment of  $J_c(B)$  merges into one curve while the onset of the intra-grain dominated field range decreases rapidly as  $\phi \rightarrow 0^\circ$ . This means that  $B_s$  and  $J_o$  are constant even if the direction of  $H_{\text{app}}$  is varied around the GB. The parameters characterizing the inhomogeneities such as  $\alpha$  and  $L$  may be constant as well. Therefore, in the simplest case, we can take the shift of  $H_{\text{peak}}$  to be solely influenced by the anisotropy of  $J_c^G$ .

The function  $H_{\text{peak}}(\phi)$  proposed in equation 5.12 can be compared to experimental data from figure 5.15b if an anisotropic  $J_c^G(\phi)$  is assumed. As an initial approximation, Blatter's anisotropic scaling approach [6] is used such that  $J_c^G$  is written as:

$$J_c^G = J_c(\varepsilon(\phi)H) \propto J_c^G(B=0)\varepsilon(\phi)^{-m} \quad (5.13)$$

where  $\varepsilon(\phi) = \sqrt{\cos^2 \phi + \gamma^{-2} \sin^2 \phi}$ ,  $\gamma$  is the anisotropy parameter and  $m$  is the slope of  $J_c$  as a function of the effective field,  $H_{\text{eff}} = \varepsilon(\phi)H$ . The plot of  $J_c(H_{\text{eff}})$  and the corresponding  $J_c(\phi)$  with the Blatter scaling for the data set at  $T = 64$  K of YBCO-Ni5W is presented in figure 5.26.

However, Blatter's scaling approach does not take into account correlated defects, especially those that are parallel to the  $ab$ -plane that cause sharper  $ab$ -peaks and larger  $J_c$  anisotropy, i.e.  $J_c(\phi = 90^\circ)/J_c(\phi = 0^\circ)$ . Thus, a practical fit function for  $J_c(\phi)$  is implemented in order to account for the  $ab$ -peak that is typical for CCs with intrinsic pinning and stacking faults parallel to the  $ab$ -planes. Based on the method by N. Long [51, 62],  $J_c(\phi)$  can be described as:

$$J_c(\phi) = J_{c, H_{\text{app}} \parallel c} \varepsilon_p(w, \phi) \quad (5.14)$$

The angle-dependent parameter  $\varepsilon_p(w, \phi)$  is written as:



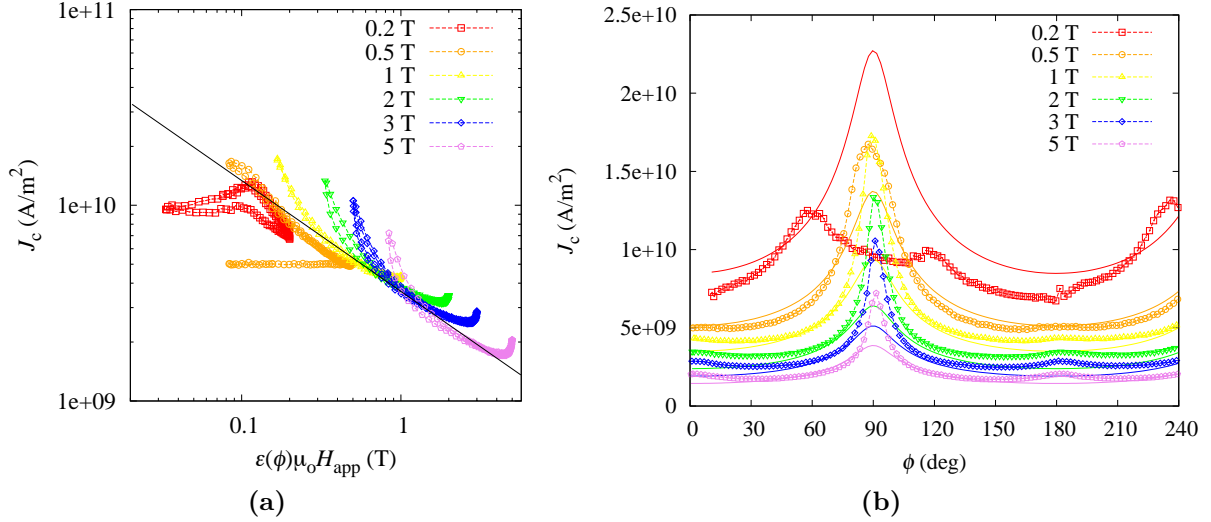


**Figure 5.26:** (a)  $J_c$  as a function of  $H_{\text{eff}} = \varepsilon(\phi)$ . (b)  $\phi$ -dependence of  $J_c$ . Symbols show the data while the solid lines are calculation of  $J_c(\phi)$  according to Blatter scaling.

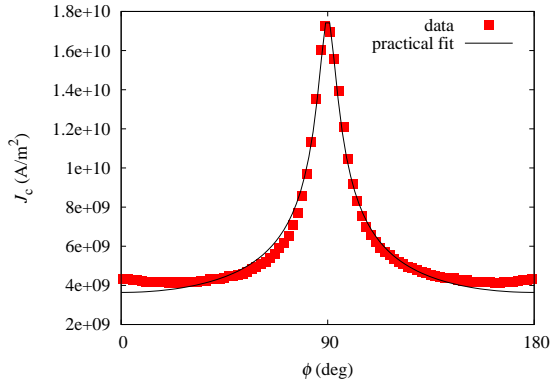


**Figure 5.27:** Experimental data of  $J_c(\phi)$  at 64 K and 1 T with the practical fit function.

$$\varepsilon_p(w, \phi) = (\cos^2 \phi + w^2 \sin^2 \phi)^{-\frac{1}{p}} \quad (5.15)$$

where  $w$  and  $p$  are fitting parameters.

Figure 5.27 shows the result of fitting the experimental data at 64 K and 1 T with equation 5.14. After obtaining  $w$  and  $p$ ,  $J_c^G(\phi)$  is then expressed as:  $J_c^G(B=0)\varepsilon_p(w, \phi)$ .

The result of  $H_{\text{peak}}(\phi)$  and the experimental data at 64 K are shown in figure 5.28a. A prediction from the Gurevitch model is also shown as the blue curve. According to A. Gurevitch, the increase in  $J_c(B)$  occurs as long as  $H_{c1} \ll H_{\text{app}} < H_d$ , where  $H_d$  refers to the field at which the AJ vortices overlap:

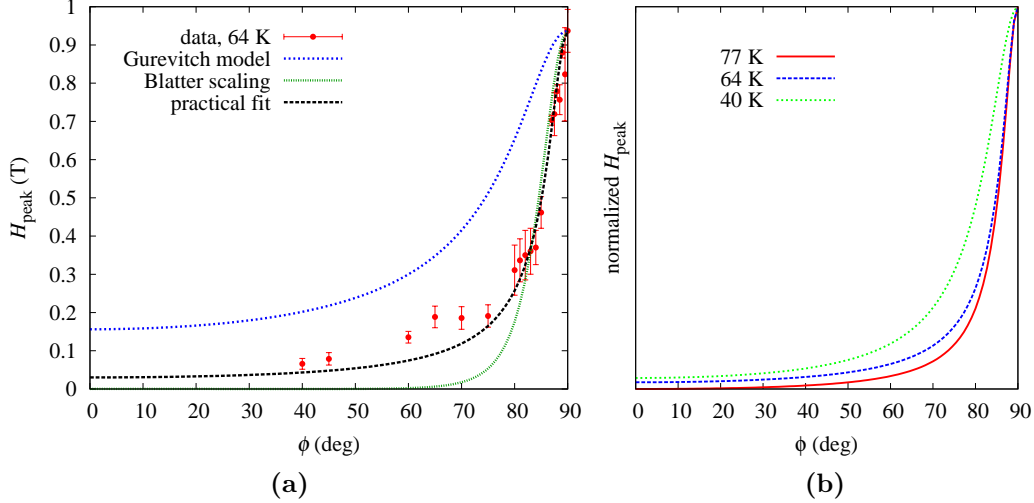


**Figure 5.28:** Dependence of  $H_{\text{peak}}$  on the angle  $\phi$ . The data points are from experimental data while the lines are those predicted by Gurevitch model, Blatter scaling and practical fit for  $J_c(\phi)$ .

$$H_d \sim \frac{\Phi_o}{l^2} \sim \left( \frac{j_c}{j_d} \right)^2 H_{c2}. \quad (5.16)$$

where  $j_c$  and  $j_d$  are the GB current density and depairing current density, respectively. Cantoni et al. [10] has pointed out that  $B_{\text{peak}}$  in  $J_c(B)$  must agree with the value of  $H_d$  as in the case of their data. Therefore, the angular-dependence of  $H_d$  would be dominated by the anisotropy of  $H_{c2}$ . However, as shown in figure 5.28, such a dependence deviates from the steep decrease of  $H_{\text{peak}}$  near the direction of the  $ab$ -planes. On the other hand, the practical fit for  $J_c(\phi)$  leads to a better agreement to the experimental data than the Blatter scaling approach as shown in the figure because the sharpness of the  $ab$ -peak is better accounted by equation 5.15. The temperature dependence of the peak, which shifts to lower fields as  $T$  increases, also agrees to the predicted curve using the practical fit function in figure 5.29b. This work does not aim to validate and discuss the physical meaning of the fitting parameters in the practical fit function given by equation 5.15, but one important implication of these results is that the good agreement between the data and the behavior of  $H_{\text{peak}}(\phi)$  according to the practical fit function demonstrates that the appearance of the peak in  $J_c(B)$  is a consequence of the transition between the GB-limited regime, where the increasing  $J_c$  is governed by the dynamics of flux lines in the GBs and the grain-limited regime where the limitation to  $J_c$  is due to the vortices in the grains. The peak in  $J_c(B)$  shifts to higher fields as  $H_{\text{app}}$  approaches the direction of the  $ab$ -planes because  $J_c^{\text{G}}$  decreases more slowly with increasing field than in the direction of  $H_{\text{app}} \parallel c$ . This is also manifested in the

behavior of the peak in the trapped magnetic field with increasing applied field with increasing applied field extracted from the field profiles obtained by SHPM as shown in figure 5.29.

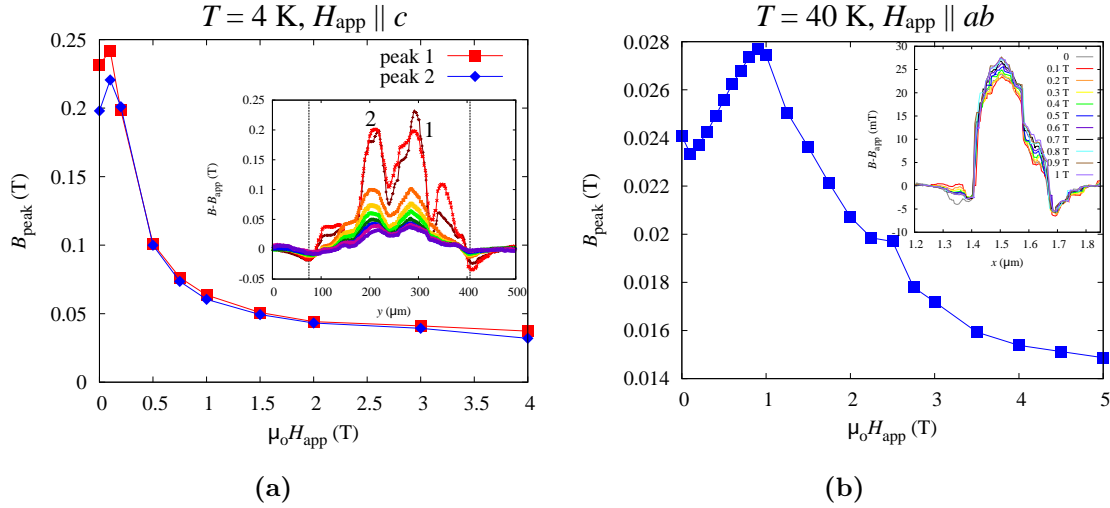


**Figure 5.29:** Maximum trapped magnetic field ( $B_{\text{peak}}$ ) obtained from in-field linescans across the YBCO-Ni5W for two field directions: (a)  $H_{\text{app}} \parallel c$  at  $T = 4$  K and (b)  $H_{\text{app}} \parallel ab$  at  $T = 40$  K. The insets show the actual linescans.

Figure 5.29a shows that even at a lower temperature of 4 K, the onset of the rapid decrease of  $B_{\text{peak}}$  occurs at a lower field in the  $H_{\text{app}} \parallel c$  configuration compared to the measurements with  $H_{\text{app}} \parallel ab$ . In figure 5.29b an increase in  $B_{\text{peak}}$  is observed below 1 T before the decrease in  $B_{\text{peak}}$  begins.

## 5.2 PLD-YBCO with secondary phases

The addition of secondary phases to form artificial pinning centers has been a common practice to enhance  $J_c$  especially in applied fields. In addition to the enhancement in pinning, it is also found in the spatial  $J_c$  distribution of YBCO-Ni5W, YBCO+BHO-Ni5W and YBCO+BYNTO-Ni5W presented in figure 5.30a that the electromagnetic granularity is also influenced by BHO and BYNTO doping. The inhomogeneity in  $J_c(x, y)$  is reduced in the doped samples. In the corresponding field dependence of the transport  $J_c$  (figure 5.30b-5.30c), the peak when  $H_{\text{app}} \parallel ab$  is also found at smaller fields in the BYNTO-doped sample and is almost absent in the BHO-doped tape. The transport data presented are from a 300  $\mu\text{m}$ -wide bridge patterned on the samples used for the  $J_c$  maps shown in figure 5.30a.  $J_{c, \text{sf}}$  of the YBCO+BHO-Ni5W is two times larger than in the pure and BYNTO-doped tapes and  $J_c$  remains highest up to 5 T in both main orientations. Possible effects of BHO and BYNTO additions on pinning will be discussed in the next chapter.

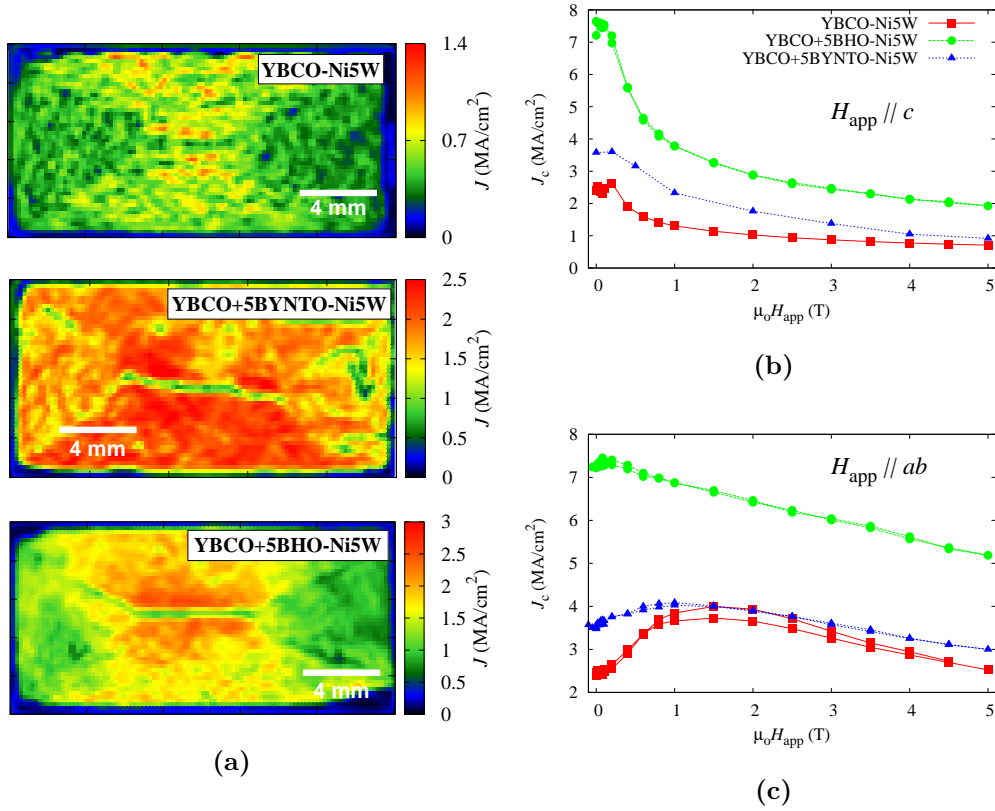


**Figure 5.30:** (a) Spatial distribution of  $J_c$  at  $T = 77$  K of three PLD-YBCO on Ni5W. The top image refers to pure YBCO, the middle is for YBCO with 5 mol%  $\text{Ba}_2\text{YNb}_{0.5}\text{Ta}_{0.5}\text{O}_6$  and the bottom for 5 mol%  $\text{BaHfO}_3$ . Field dependence of  $J_c$  at  $T = 40$  K when the applied field is (b) parallel to the  $c$ -axis and (c) parallel to the  $ab$ -planes.

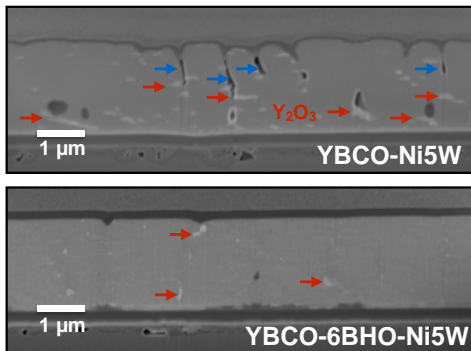


**Figure 5.31:** SEM images of the cross-sections of YBCO-Ni5W and YBCO9+6BHO-Ni5W. The red and blue arrows indicate the  $\text{Y}_2\text{O}_3$  and pores, respectively.

Exploring the possibility of doping the YBCO layer to enhance the GB properties to increase the global critical current density has been explored in the past [50]. However, for the case of BYNTO and BHO doping, the mechanism of how these secondary phases affect the microstructure and the GB properties is still an ongoing study and is beyond the scope of this thesis. What is known so far by comparing the SEM images of the cross-section of a pure and BHO doped samples is that

a doped film has refined  $\text{Y}_2\text{O}_3$  nanoparticles, smoother surface and less pores as shown in figure 5.31 [86]. The improved microstructure in the BHO-doped films is consistent to the higher  $J_c$  and less granular magnetic field profile found by transport and SHPM.

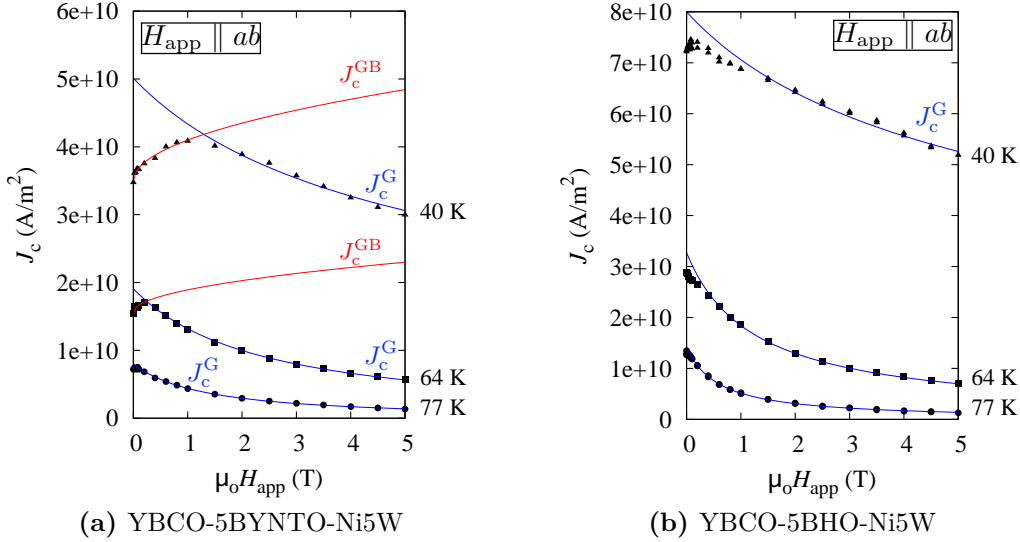


**Figure 5.32:** Field dependence of  $J_c$  for  $H_{\text{app}} \parallel ab$  at temperatures of 40 K, 64 K and 77 K. The symbols correspond to data while the solid lines are the fits to equations 5.6 and 5.9.

$J_c^{\text{GB}}$  predicted by A. Gurevitch (equation 5.6) was fitted to the increasing  $J_c$  segment of the YBCO+BYNTO-Ni5W sample. The penetration depth  $\lambda$ , which is a material-dependent property determined by the density of superconducting charged carriers, was taken from YBCO-Ni5W and the factor  $\mathcal{F} = \frac{\Phi_0 \alpha L}{16\pi^2 \mu_0 (L^2 + l^2)}$  was extracted from the fit instead of taking  $J_0$  directly as a fitting parameter. Due to an almost absent peak in the YBCO+BHO-Ni5W sample and at 77 K of the BYNTO-doped tape, only equation 5.9 is fitted to the experimental data. The fitting parameters of YBCO+BYNTO-Ni5W and YBCO+BHO-Ni5W are given in table 5.2 and 5.3, respectively. The values of the field exponent,  $\beta$ , are consistent with typical values obtained from various CCs [85].

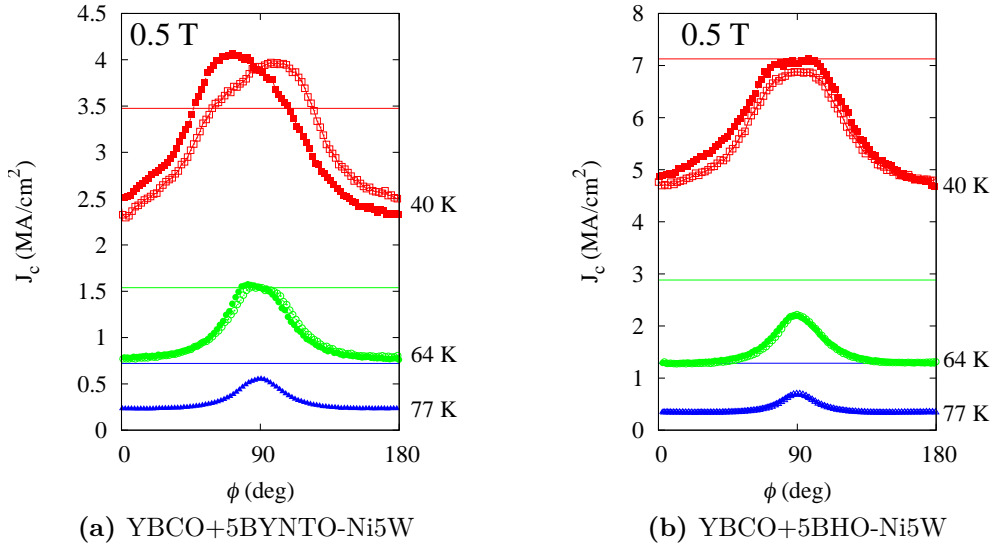
**Table 5.2:** Fitting parameters from  $J_c^{\text{G}}(B)$  and  $J_c^{\text{GB}}(B)$  to data of YBCO+5BYNTO-Ni5W at 40 K, 64 K and 77 K.

T (K)	$B_s$ (T)	$J_0$ (A/m <sup>2</sup> )	$J_c(0)$ (A/m <sup>2</sup> )	$B_0[\parallel ab]$ , (T)	$\beta[\parallel ab]$
40	33.7	$3.5 \times 10^{10}$	$5.0 \times 10^{10}$	3.0	-0.5
64	22.42	$1.6 \times 10^{10}$	$1.9 \times 10^{10}$	2.6	-1.1
77	-	-	$0.8 \times 10^{10}$	1.6	-1.3

**Table 5.3:** Fitting parameters from  $J_c^G(B)$  and  $J_c^{GB}(B)$  to data of YBCO+5BHO-Ni5W at 40 K, 64 K and 77 K.

T (K)	$J_c(0)$ (A/m <sup>2</sup> )	$B_o[   ab],$ (T)	$\beta[   ab]$
40	$8.0 \times 10^{10}$	2.8	-0.4
64	$3.2 \times 10^{10}$	1.1	-0.9
77	$1.4 \times 10^{10}$	0.6	-1.0

For the BYNTO-doped sample, the values of  $B_s$  and  $\mathcal{F}$  are higher compared to those acquired from the pure YBCO (see table 5.1). The value of  $\mathcal{F}$  for pure YBCO is  $3.85 \times 10^{-4}$  A,  $2.41 \times 10^{-4}$  A and  $2.01 \times 10^{-4}$  A for 40 K, 64 K and 77 K, respectively. From equation 5.8,  $B_s$  is proportional to the square of  $\alpha$  – a quantity that refers to the degree of inhomogeneity of the GB and can only have a maximum value of 1, which would correspond to a homogeneous boundary. Therefore, the higher value of  $B_s$  in YBCO+BYNTO-Ni5W is consistent to the improvement of its granular properties observed from Hall mapping and the reduction of the  $B_{peak}$  as well. The stochastic behavior of  $J_c$  at low fields is not visible in the doped-samples, so  $J_o$  from YBCO+5BYNTO-Ni5W sample is approximately equal to the self-field  $J_c$  at each temperature and this is an additional indication of an improved connection between grains.

**Figure 5.33:**  $\phi$ -dependence of  $J_c$  at 40 K, 64 K and 77 K. The solid lines denote the self-field  $J_c$  at each temperature. Hollow and filled symbol correspond to -0.5 T and +0.5 T, respectively.

The angular-dependence of  $J_c$  of the BYNTO- and BHO-doped films is shown in figure 5.33 with an applied field of 0.5 T at 40 K, 64 K and 77 K. Similar to YBCO-Ni5W, a field-independent  $J_c$  forms near  $\phi = 90^\circ$  which indicates that  $J_c$

is limited by the dynamics of AJ vortices in the GBs. At 40 K, a reversal in the shape of the  $ab$ -peak is observed in YBCO+5BYNTO-Ni5W sample and a decrease in the peak height in YBCO+5BHO-Ni5W when the direction of the applied field is reversed. This may indicate that surface pinning effect also comes into play in the net pinning force on the AJ vortices.

### 5.3 CSD-YBCO on RABiTS NiW

Coated conductors with YBCO layer grown by chemical solution deposition (CSD) technique are interesting because the structure of the GBs is different from the PLD-grown films. In addition to this, an all-CSD route can become more cost-effective compared to deposition techniques that need vacuum system like PLD. A TEM image from the cross-section of the CSD-YBCO-Ni5W sample is shown on figure 5.34a. The GBs are found to meander through the thickness of the YBCO layer. The texture of the underlying NiW is not necessarily transferred directly to the YBCO layer on top as shown by the difference in contrast between one grain of the YBCO layer and the NiW grain directly beneath it (upper panel of figure 5.34a). Correspondingly, there is no noticeable trace of the NiW grain on the surface of the CSD-YBCO film as shown in the SEM image in figure 5.34b. Recall that the YBCO-Ni5W sample has visible grooves and boundaries on its surface as a direct consequence of the underlying morphology of the NiW template (figure 5.2b). These features are not observed in the CSD-grown tape. In addition, high magnification SEM image of CSD-YBCO film shows a more loosely packed YBCO layer with higher density but smaller pores compared with PLD-YBCO as illustrated in figure 5.34c.

#### 5.3.1 Magnetic field profile

The remanent field profiles and current distributions in LN<sub>2</sub>-bath of CSD-YBCO on Ni5W and Ni9W templates are shown in figure 5.35. The YBCO layer is inhomogeneous but not as granular as the profiles of PLD-YBCO. Planar anisotropy in  $J_c$  of the CSD-YBCO-Ni9W tape is observed where  $J_c$  in the rolling direction (longitudinal, L) is larger than in the transverse (T) direction. This indicates that the YBCO grain grows longer in the L direction rendering a shorter length in the T direction, which is expected due to a laminar growth mode of chemical solution deposition.

The inhomogeneity in the field profile is further seen in the higher resolution Hall mappings at 4 K shown in figure 5.36. Traces of granularity appear as peaks in the linescans in figure 5.36b-c with an envelope of a global  $J_c$ -profile. The same shape of  $B(y)$  is observed up to 4 T and temperatures of 4 K and 40 K.

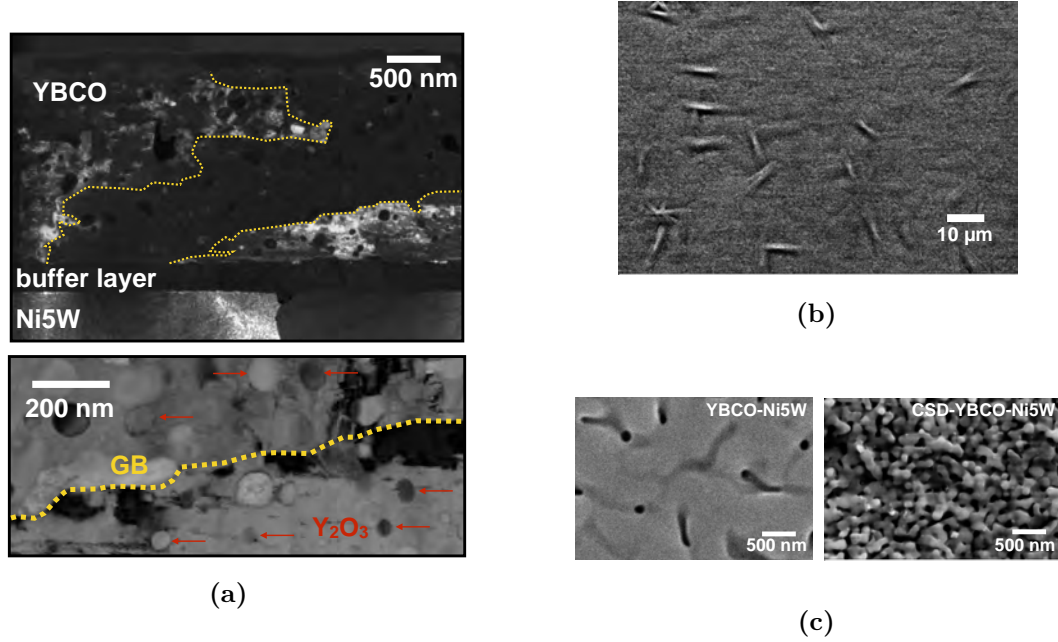


**Figure 5.34:** (a) TEM images from the cross-section of CSD-YBCO-Ni5W. The yellow dashed curves denote the meandering grain boundaries. The red arrows in the lower panel indicate Y<sub>2</sub>O<sub>3</sub> precipitates. (b) SEM image of the surface. (b) Higher magnification SEM images of PLD-YBCO-Ni5W and CSD-YBCO-Ni5W samples.

### 5.3.2 Transport $J_c$

The field dependence of  $J_c$  obtained by transport measurement at temperatures of 77 K, 64 K and 40 K are shown in figure 5.37. The width of the bridge patterned on the tape is about 230 μm. The peak in  $J_c(B)$  for  $H_{\text{app}} \parallel ab$  found in the PLD-grown tape (section 5.1.4) also appears in the CSD-grown sample but it is shifted to very low fields, i.e. 0.12 T at 40 K, and further to lower field as the temperature increases as shown by the insets in figure 5.37a-5.37b. The field-independent range is also absent and a monotonic decrease in  $J_c$  is observed in the  $H_{\text{app}} \parallel c$  direction.

In agreement with the behavior of  $J_c(H_{\text{app}})$ , the angle-dependence of  $J_c$  in MLF presented in figure 5.38 therefore shows the usual  $J_c$ -anisotropy having a large peak parallel to the  $ab$ -planes which is caused by enhanced pinning either by the stacking faults at 77 K or intrinsic pinning as the temperature decreases to 64 K and 40 K. The small peak in  $J_c(H_{\text{app}})$  at 40 K therefore causes  $J_c$  to be slightly larger in a small range in  $\phi$  around  $H \parallel ab$  for  $H_{\text{app}} = 0.2$  T than at self-field, but the flat,  $\phi$ -independent  $J_c$  observed in PLD-grown tapes is suppressed.

The reduced granularity such as the non-monotonic  $J_c(B)$  and the  $\phi$ -independent  $J_c$  in the CSD-grown tape is consistent with its less granular morphology observed in the magnetic field and  $J_c$  distributions. Unlike PLD-grown tapes where the



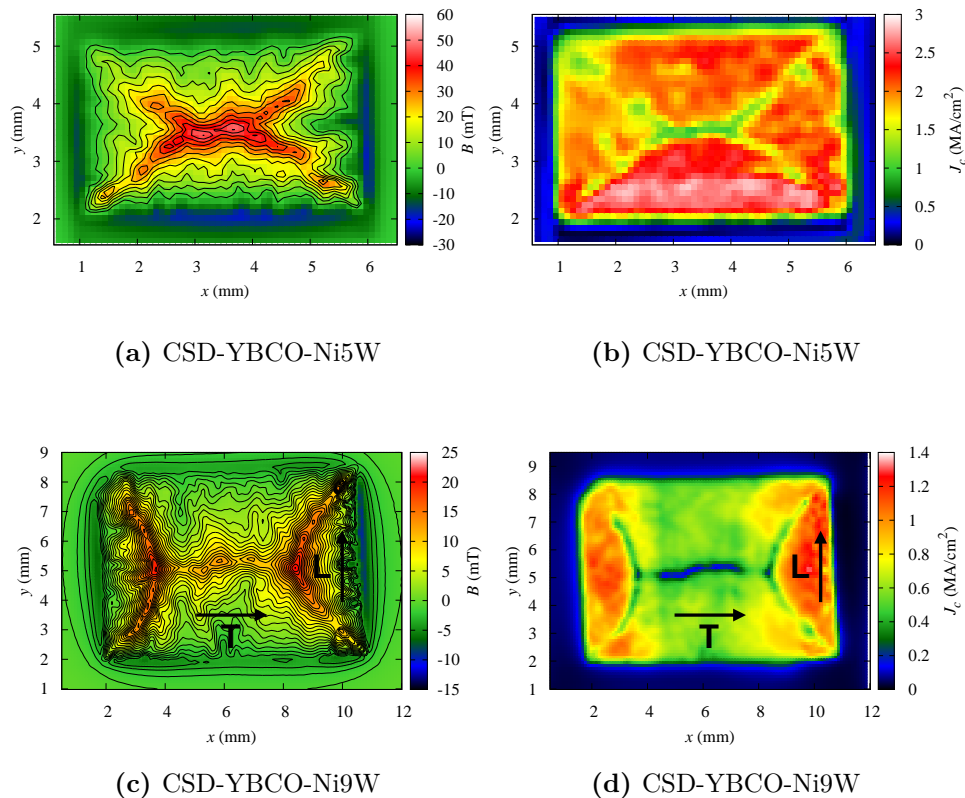


**Figure 5.35:** Remanent field profile and spatial  $J_c$ -maps of YBCO on (a)-(b) Ni5W and (c)-(d) Ni9W templates. The scanning parameters were  $s_x = s_y = 100 \mu\text{m}$ ,  $d = 35 \mu\text{m}$  and  $d = 15 \mu\text{m}$  for the Ni5W and Ni9W, respectively.

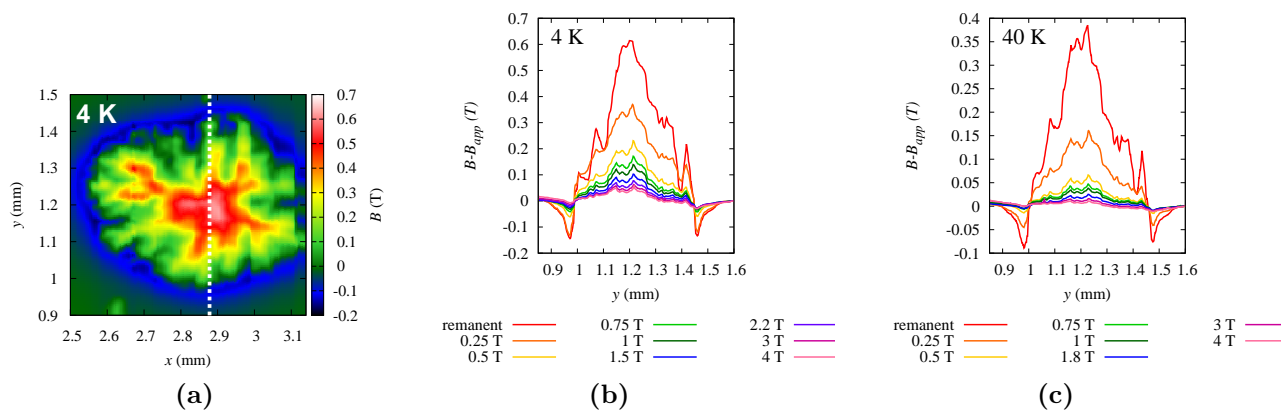


**Figure 5.36:** (a) Remanent field profile at 4 K of CSD-YBCO-NiW. The scanning parameters were  $s_x = s_y = 5 \mu\text{m}$  and  $d = 3 \mu\text{m}$ . The white dashed line corresponds to the position of the in-field linescans in (b) and (c) at  $T = 4 \text{ K}$  and  $40 \text{ K}$ , respectively.

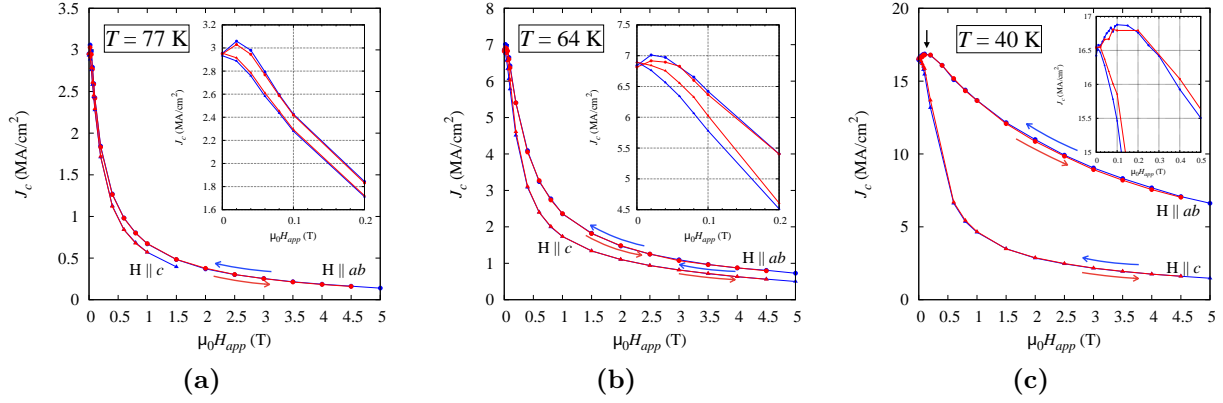


**Figure 5.37:** Field dependence of  $J_c$  at (a)  $T=77$  K, (b)  $T=64$  K and (c)  $T=40$  K. The insets in each figure are enlarged plots at lower fields.

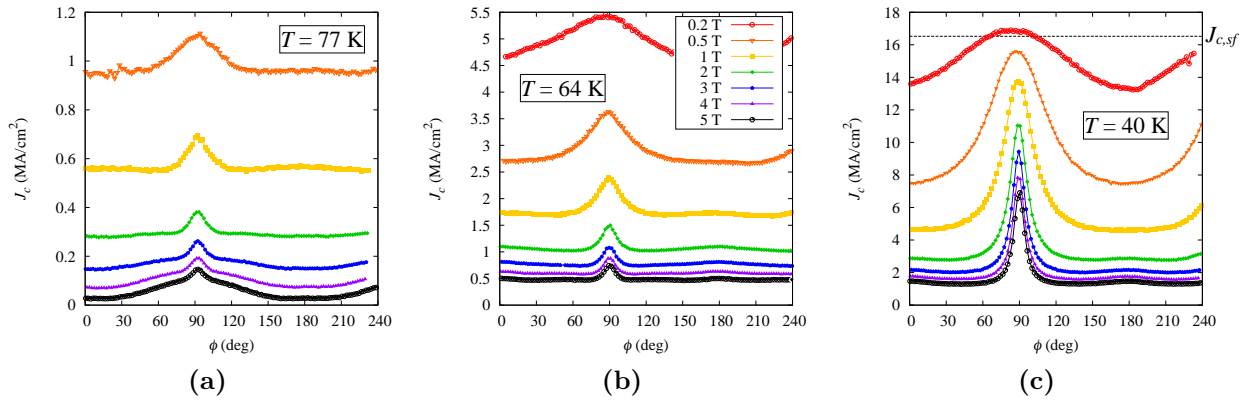


**Figure 5.38:** Angle dependence of  $J_c$  at (a)  $T=77$  K, (b)  $T=64$  K and (c)  $T=40$  K at different fields.

GBs are planar and the texture of the NiW grain is directly transferred to the YBCO layer, the meandering GBs in the CSD-grown tape effectively enhance the connectivity between grains. As shown in the SEM images in figure 5.34, the boundaries between misaligned grains that appears as grooved GBs are not visible in the CSD-tapes. Both of the results in the magnetic field mapping and transport  $J_c$  measurements signify that current transport is enhanced through the meandering of the grain boundaries in the CSD-grown tapes.

## 5.4 Summary

In this chapter, the influence of the granular morphology of the YBCO layer on metallic substrates was discussed. One of the most important results in this chapter is obtained from pulsed laser deposited YBCO on RABiTS NiW, which has turned out to have a more prominent granularity than PLD-YBCO on ABAD-YSZ-buffered stainless steel, as inferred from SHPM images. The granular texture of the NiW template, which is directly transferred to the YBCO layer by PLD, was found to result in a very inhomogeneous current. Some GBs with misorientation angle of at least  $6^\circ$  obstruct the current flow. However, this is not always the case. The morphology of the boundaries causes also significant effect on current percolation. Grooved boundaries formed above the trenches between NiW grains inhibit current flow as well. Varying porosity of the YBCO layer on top of each NiW grain also causes a local variation in  $J_c$ .

The granular behavior observed in the field maps has a direct influence on the corresponding transport properties. A transition from grain-boundary limited regime to grain-limited regime was observed in the field-dependence of  $J_c$ . It was shown for the first time, that the mechanism governed by the dynamics of the Abrikosov-Josephson vortices in the GB is effective up to a few Tesla at 40 K and likely to even larger fields at lower temperatures.

By the addition of BHO and BYNTO phases and by taking the CSD route for the growth of the YBCO layer, the granularity is less and  $J_c$  is improved. These are promising solutions to suppress the detrimental effects of the granular morphology to the performance of REBCO coated conductors on RABiTS template. Although further studies are still needed especially on the effects of the secondary phases in the PLD-route of YBCO on NiW substrate.

# Chapter 6

## $J_c$ -enhancement by artificial pinning centers

One of the most important objectives for the viability of coated conductors for applications is to further enhance its critical current especially at high magnetic fields and at lower operating temperatures ( $< 77$  K). This can be achieved by addition of secondary phases in the superconducting matrix that form artificial pinning centers (APCs). Aside from the enhancement of  $J_c$ , another advantage of APCs is that they can also alter/decrease the  $J_c$  anisotropy at high applied fields.

Through the years, various compounds have been incorporated and engineered as APCs using different growth methods. In this chapter, a closer focus will be devoted to the effects of  $\text{BaHfO}_3$  (BHO) and  $\text{Ba}_2\text{Y}(\text{Nb}/\text{Ta})\text{O}_6$  (BYNTO) nanoparticles in the YBCO matrix deposited by PLD on metallic substrates. The mentioned compounds form as correlated APCs in the PLD route. The YBCO tapes were fabricated at the IFW-Dresden. Details of the material preparation were given in section 3.1.2.

As already discussed in chapter 5, the granular morphology of the YBCO-Ni5W has drastic effects on its current carrying properties whether at self-field or in applied fields. On the other hand, the YBCO-SS has a wider range in field and temperature where the critical current is limited mostly by vortex pinning within its superconducting grains. Therefore, it is easiest to begin the discussion of the contributions of the BHO and BYNTO nanoparticles in YBCO-SS. At the later part of the chapter, their significance in YBCO-Ni5W will also be discussed.

### 6.1 Pure YBCO on SS

The typical microstructure of the YBCO-SS is presented in the TEM image in figure 6.1. The superconducting matrix includes  $\text{Y}_2\text{O}_3$  nanoparticles (denoted by black arrows) elongated parallel to the  $ab$ -plane with a diameter ranging from 11-60 nm and a thickness of 2.5-10 nm (parallel to the  $c$ -axis). Stacking faults in the

form of extra CuO layer (YBa<sub>2</sub>Cu<sub>4</sub>O<sub>7- $\delta$</sub> , Y-124 intergrowths) are also present and are indicated by the white arrows in the figure.

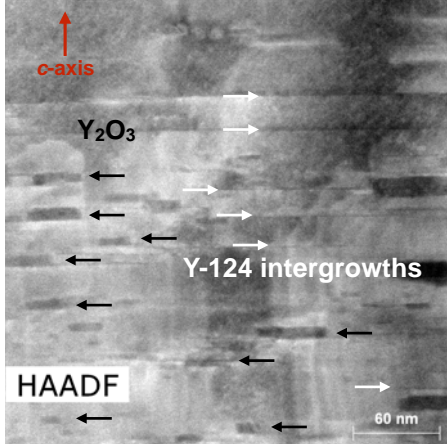


**Figure 6.1:** High-angle annular dark field (HAADF) image of the cross-section of YBCO-SS. Y<sub>2</sub>O<sub>3</sub> nanoparticles and Y-124 intergrowths are denoted by the black and white arrows, respectively.

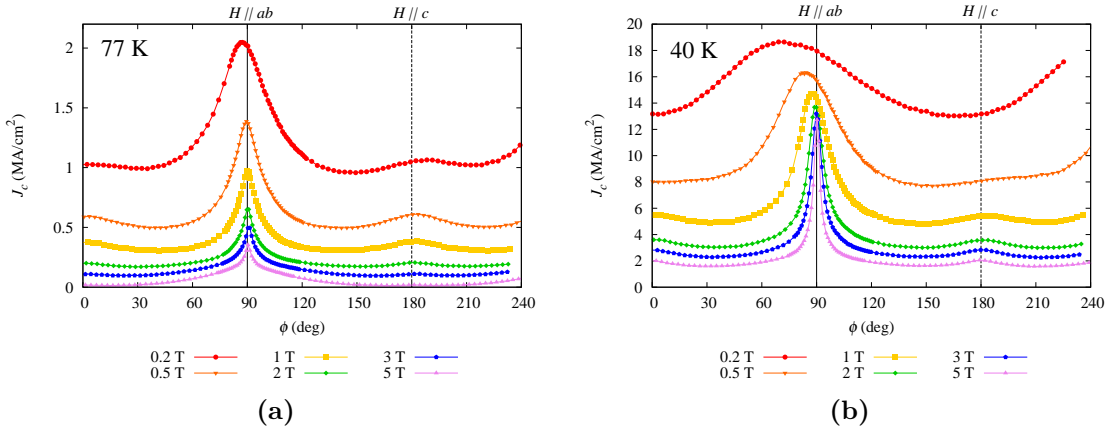


**Figure 6.2:**  $J_c(\phi)$  in different applied magnetic fields at (a)  $T = 77$  K and (b)  $T = 40$  K. The direction of the  $c$ -axis and the  $ab$ -plane are at  $0^\circ$  and  $\phi = 90^\circ$ , respectively.

The angular dependence of  $J_c$  in the MLF configuration is shown in figure 6.2 at two temperatures: 77 K and 40 K. As expected for YBCO with a pure composition, a large peak appears parallel to the direction of the  $ab$ -planes ( $\phi = 90^\circ$ ). This peak becomes sharper as the field is increased. The small peak parallel to the  $c$ -axis ( $\phi = 0^\circ$ ) may be attributed to pinning by the grain boundaries since no other pinning centers parallel to this direction were found so far in TEM. The  $ab$ -peak shifts away from the  $ab$ -planes as the field decreases. This will be discussed later.

A plot of the angle dependence of  $J_c$  normalized with respect to  $J_c(\phi = 0^\circ)$ , at the highest applied field of 5 T and different temperatures is shown in figure 6.3a. Notice that the curve at 77 K has the largest anisotropy such that  $J_c$  at  $\phi = 90^\circ$  is 20 times larger than at  $\phi = 0^\circ$ . The anisotropy suddenly decreases at  $T = 64$  K and gradually increases again as the temperature is further decreased.

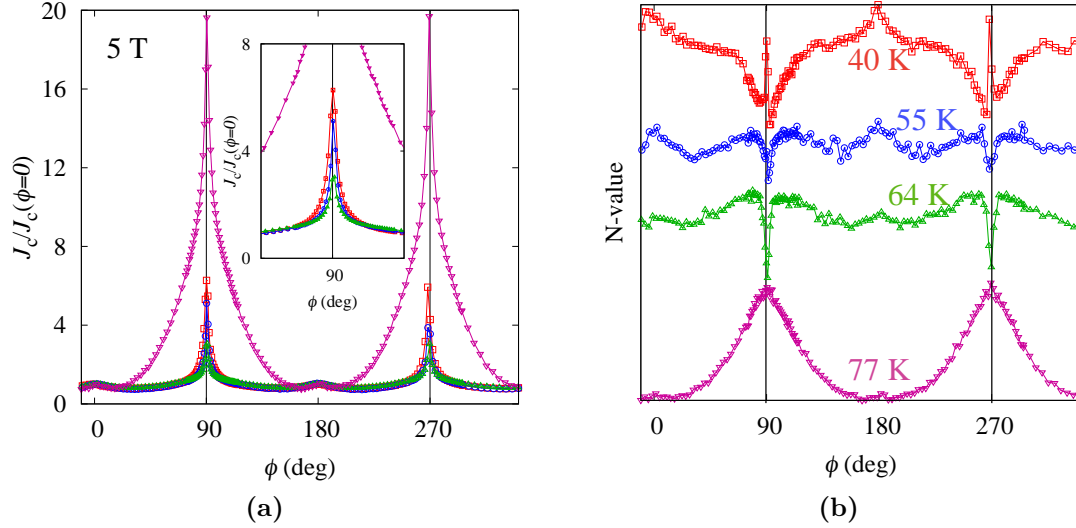


**Figure 6.3:** Angle-dependence of  $J_c$  at  $\mu_0 H_{\text{app}} = 5$  T and 77 K, 64 K, 55 K and 40 K normalized with respect to  $J_c(\phi = 0)$ . The inset is an enlarged view around the  $ab$ -peak for  $T < 77$  K. (a) Dependence of the N-value on  $\phi$ . The  $N(\phi)$  for each temperature are plotted with an offset for clarity.

The large anisotropy at 77 K is influenced by a low irreversibility field in the direction of the  $c$ -axis at this temperature, which is typically about 7 T [42] that leads to a large difference in the values of  $J_c$  for  $H_{\text{app}} \parallel ab$  and  $H_{\text{app}} \parallel c$  at 5 T. The corresponding angle-dependence of the N-value in figure 6.3b has a direct correlation with  $J_c(\phi)$  wherein a broad peak around the  $ab$ -plane forms. Since all the experimental IV-curves are well-described by a power law, the N-value can be interpreted to be proportional to the energy barrier of the pinning structure,  $U_o$ , within the flux creep regime. Hence, a broad peak in the  $N(\phi)$  centered at  $\phi = 90^\circ$  signifies that a gain in the pinning energy is obtained towards this direction. As the temperature is decreased to 64 K and 55 K, a minimum right at  $\phi = 90^\circ$  and  $270^\circ$  forms. Similar to the analysis by L. Civale et al. [14], the inverse correlation of  $J_c$  and N-value at lower temperature is considered as an indication of the dominance of intrinsic pinning. The pinning energy per unit length,  $u_o$ , of a defect or an APC is directly proportional to the condensation energy density,  $u_c \sim H_c^2/2\mu_o$  and the cross-section of the vortex core (for  $\xi \leq R$ ) in the defect [13] and can be expressed as:

$$u_o \sim u_c V = \frac{H_c^2}{2\mu_o} \pi \xi^2 \quad (6.1)$$

which results in optimum pinning when  $\xi \cong R$ , where  $R$  is the radius of the defect. Therefore, at 77 K, the larger  $Y_2O_3$  precipitates that are elongated parallel to the  $ab$ -planes are more effective pinning centers as  $\xi_{ab}$  and  $\xi_c$  are approximately

4 nm and 0.7 nm, respectively. At 64 K,  $\xi_{ab}$  and  $\xi_c$  reduces to 2.8 nm and 0.5 nm, respectively, assuming  $\xi_{ab}(0) = 1.4$  nm and the temperature dependence given by equation 2.3. This makes the weakly superconducting layers of YBCO with spacing of about 1.2 nm more efficient for pinning below 77 K. However, since YBCO is a layered superconductor, the vortices transform to a kinked state as the angle between the field and the  $ab$ -planes is small. Such a formation of vortex kinks lowers the pinning energy and results in the observed minimum in the  $N(\phi)$  for  $H_{\text{app}} \parallel ab$ . At 40 K, the pseudo-lock in state is manifested by the appearance of a sharp peak right at the direction of the  $ab$ -planes. Note that  $J_c(\phi)$  and  $N(\phi)$  of GdBCO-ISD has the same behavior at the same field and temperatures (refer to figure 4.8b in chapter 4). This implies that the observed properties influenced by the dynamics of vortices in a layered superconductor is consistent with different coated conductors whether with tilted crystallographic axes or other architecture since these are consequences of the layered crystal structure of YBCO. A peak parallel to the  $c$ -axis in the  $N(\phi)$  curve, which corresponds to a small peak in  $J_c(\phi)$  in the same direction, becomes more visible as the temperature decreases.

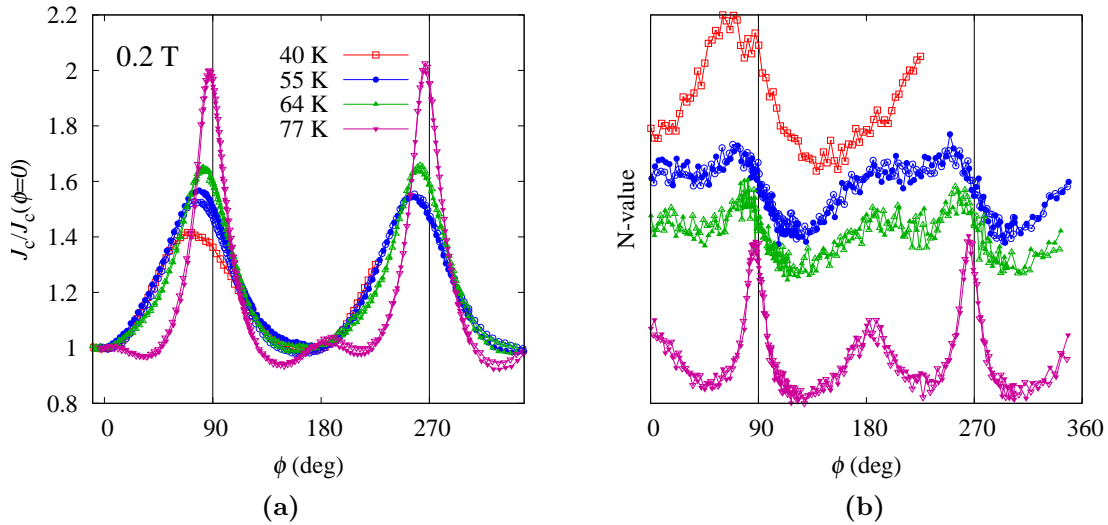


**Figure 6.4:** Angle-dependence of  $J_c$  at  $\mu_0 H_{\text{app}} = 0.2$  T and 77 K, 64 K, 55 K and 40 K normalized with respect to  $J_c(\phi = 0)$ . The hollow symbols correspond to a field of +0.2 T and the solid ones are with -0.2 T. (a) Dependence of the N-value on  $\phi$ . The  $N(\phi)$  for each temperature are plotted with an offset for clarity.

At a lower applied field of 0.2 T (figure 6.4a), the  $ab$ -peak tends to be broader relative to the curve at 5 T and shifts away from  $\phi = 90^\circ$  and  $\phi = 270^\circ$  as the temperature decreases. A shift of the  $ab$ -peak has already been reported to occur at low fields and low temperatures and was explained by the misalignment between the magnetic induction,  $B$ , that dictates the direction of the vortices and the applied field,  $H_{\text{app}}$  [5, 88]. Usually, this can be confirmed if the direction of the shift is flipped when the Lorentz force is reversed by either reversing the direction of the applied field or the applied current, as discussed in section 4.3.1. However,

in the case of the YBCO-SS, the  $ab$ -peak is found to remain at the same side of the  $ab$ -plane even if the direction of the applied field is reversed, as shown by the hollow and solid symbols in figure 6.4a. The two curves with +0.2 T and -0.2 T exactly overlap. The shifting  $ab$ -peak in  $J_c(\phi)$  has exactly the same positions as in the  $N(\phi)$  as shown in figure 6.4b. This means that the occurrence of the peak at low fields is because of vortices locking in a certain angular orientation such that a corresponding gain in the pinning energy is reflected in the  $N(\phi)$ . Notice that the height of the two  $ab$ -peaks is the same, which indicates that the two interfaces have the same surface pinning effects. Therefore, the quality of the surface is the same for the Ag-YBCO interface and YBCO-buffer layer interface which is also confirmed in the TEM images.

## 6.2 YBCO with BaHfO<sub>3</sub> addition

Recent works have shown that BHO nanoinclusions have a good potential to further improve  $J_c$  of REBCO films at high fields either as nanorods in the PLD route [67] or as isotropic nanoparticles grown by the CSD method [24]. The compound BaMO<sub>3</sub> with M=Hf does not decrease  $T_c$  significantly [41] as other transition metal do. Thus, it is a promising option as an APC.

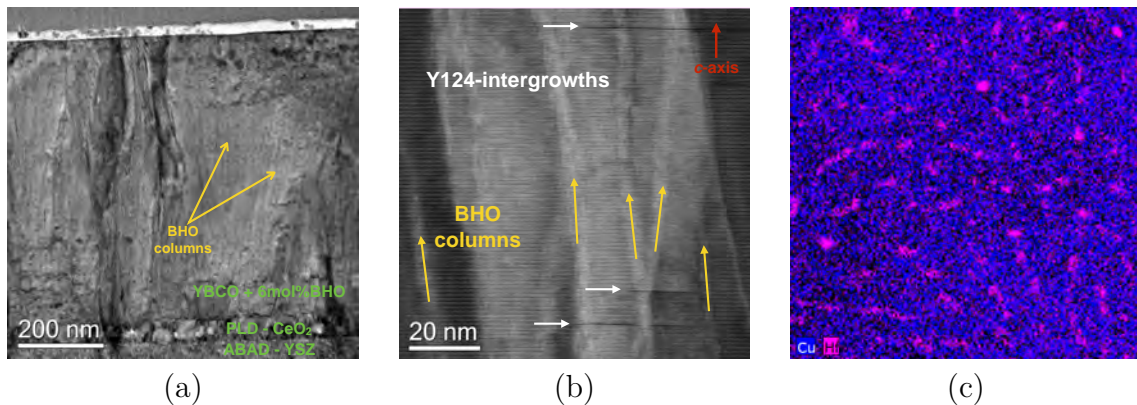


**Figure 6.5:** (a) Bright field TEM image of the cross-section of the YBCO+BHO-SS tape showing the BHO nanorods with a splay around the  $c$ -axis of the YBCO. (b) HAADF STEM Z-contrast showing the BHO nanorods and the Y-124 intergrowths. (c) EDX map with a planar view on the YBCO+BHO-SS sample showing the BHO nanorods with a typical diameter of  $4 \pm 2$  nm.

Figure 6.5 shows the cross-section of YBCO+BHO-SS. The BHO grows as columns roughly parallel to the  $c$ -axis of the YBCO with a splay of up to  $20^\circ$  around the  $c$ -axis. Note that the orientation of the columnar growth of BHO nanoinclusions greatly depends on the deposition temperature and growth rate during PLD. However, a detailed investigation on this topic is beyond the scope of this thesis. It is known so far that as the deposition rate increases, the lesser



is the splay of the BHO nanocolumns around the  $c$ -axis while a higher deposition temperature causes the formation of larger BHO nanoplates parallel to the  $ab$ -plane [87]. As shown by a TEM image in figure 6.5, some BHO rods have length extending throughout the thickness of the YBCO layer with a typical diameter of  $4 \pm 2$  nm. Y-124 intergrowths are also present in the YBCO matrix as shown in figure 6.5b. The formation of  $Y_2O_3$  nanoparticles is greatly suppressed compared to YBCO-SS.

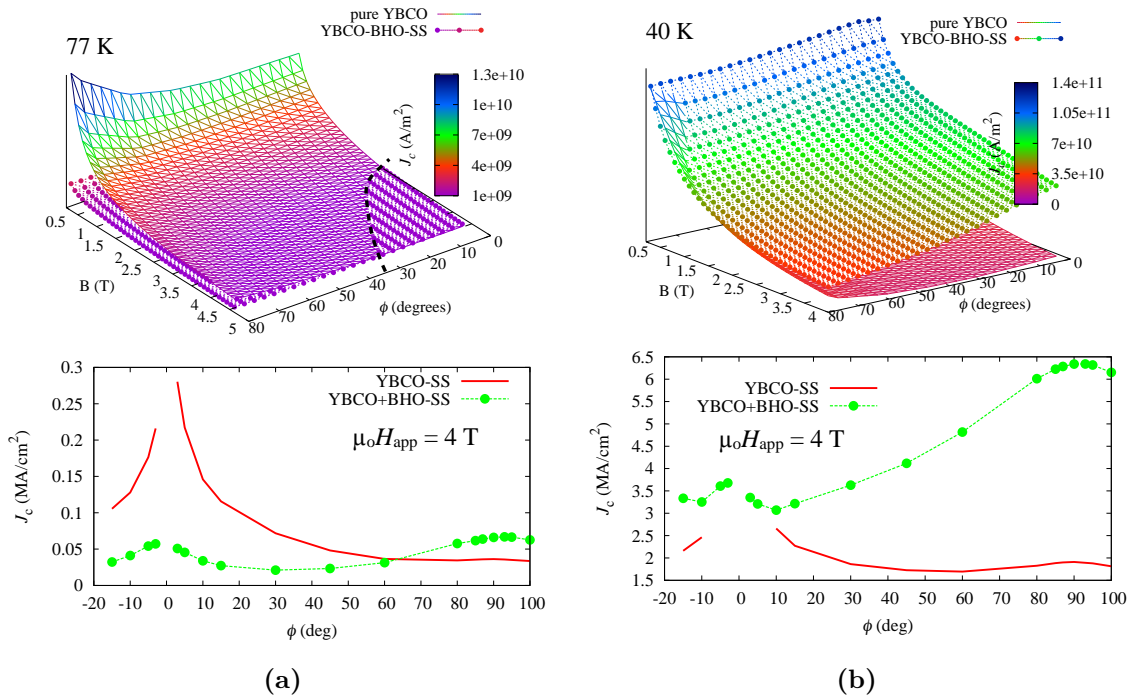


**Figure 6.6:**  $J_c(B, \phi)$  of YBCO-BHO-SS at (a)  $T = 77$  K and (b)  $T = 64$  K.

The corresponding  $J_c(\phi, B)$  of the same sample in figure 6.5 is shown in figure 6.6. The  $J_c$  was evaluated from magnetization loops obtained by a vector VSM. Due to the presence of splayed BHO nanocolumns roughly parallel to the  $c$ -axis, a peak around  $J_c(\phi = 0^\circ)$  is observed at 77 K, which exceeds that of the pure YBCO at higher fields as depicted in figure 6.6a. At a lower temperature of 40 K (figure 6.6b), the enhancement in  $J_c$  compared to the YBCO-SS spans a wide angular and field range. The  $J_c$  of YBCO+BHO-SS is up to three times that of the YBCO-SS at  $H_{app} \parallel c$ .

The angular dependence of the transport  $J_c$  of another BHO-doped sample prepared with a slightly higher deposition rate is presented in figure 6.7. Despite a possible difference in the microstructure of this sample such as formation of BHO plates parallel to the  $ab$ -plane, a consistent enhancement in  $J_c$  similar to the results in magnetization measurements, is observed. At 77 K (figure 6.7a) and 5 T, two peaks appear, one is the  $ab$ -peak at  $\phi = 90^\circ$  and another broad peak centered at

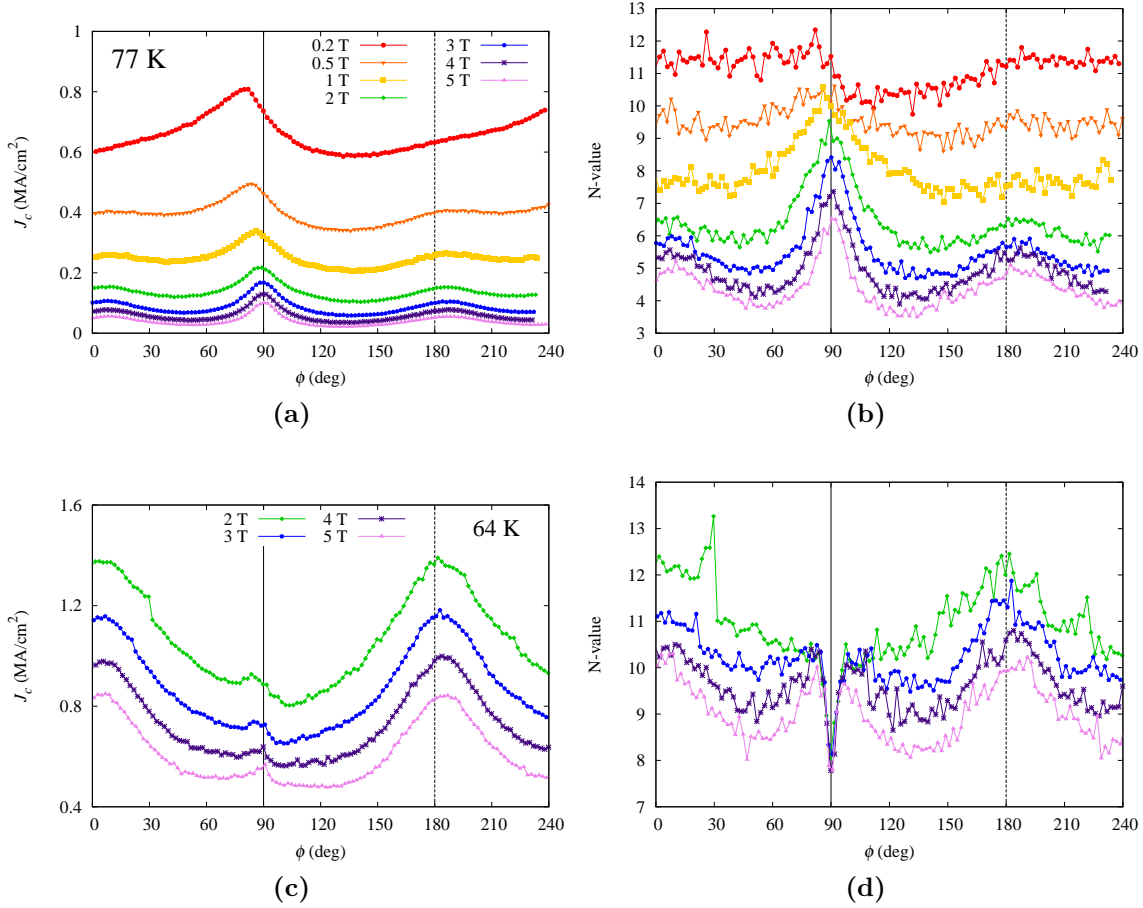


**Figure 6.7:**  $J_c(\phi)$  and  $N(\phi)$  of YBCO-BHO-SS in different applied magnetic fields at (a)-(b)  $T = 77$  K and (c)-(d)  $T = 64$  K. The direction parallel to the  $c$ -axis and  $ab$ -plane are at  $\phi = 0^\circ$  and  $\phi = 90^\circ$ , respectively.

$\phi = 0$ . The corresponding  $N(\phi)$  has two peaks as well, which has a direct correlation to the  $J_c(\phi)$ . As the  $H_{app}$  decreases, the prominence of the  $c$ -axis peak, both in  $J_c(\phi)$  and  $N(\phi)$ , decreases. The shift of the  $ab$ -peak away from  $\phi = 90^\circ$  also occurs in this sample as observed in the YBCO-SS.

At a lower temperature of 64 K (figure 6.7c), the  $c$ -axis peak appears larger and broader while the  $ab$ -peak is suppressed. With an average diameter of the nanorod of about 4 nm, it is evident that a larger gain in pinning energy is obtained at 64 K since  $2\xi_{ab}$  at this temperature is approximately 5.8 nm, whereas at 77 K,  $2\xi_{ab} \approx 8.8$  nm. Therefore, the BHO nanorods smaller than 4 nm that are also present, are less effective at 77 K. Despite the appearance of a suppressed  $ab$ -peak in  $J_c(\phi)$ , a sharp minimum is still present in  $N(\phi)$  (figure 6.7d). Therefore, in contrast to the previous claim that the existence of correlated pinning centers parallel to the  $c$ -axis destroys intrinsic pinning in the  $ab$ -plane [13], such persisting minimum in  $N(\phi)$  indicates that intrinsic pinning is not disrupted by the CPCs. The pinning energy

away from the  $ab$ -planes is elevated due to the existence of the BHO nanorods serving as strong pinning center at higher fields. Note that a valley in the  $N(\phi)$  occurs at intermediate angles of  $30^\circ - 60^\circ$  and  $120^\circ - 150^\circ$ , which is consistent to the decrease of the pinning efficiency of the nanorods as the applied field is tilted away from them.

### 6.3 YBCO with $\text{Ba}_2\text{YNb}_{0.5}\text{Ta}_{0.5}\text{O}_6$ addition

Double perovskite tantalate ( $\text{Ba}_2\text{RETaO}_6$ ) [43] and niobate ( $\text{Ba}_2\text{RENbO}_6$ ) [25, 29] are compounds that has also been shown to form pinning centers with good potential to enhance  $J_c$  of REBCO films. Ta and Nb are less likely to substitute Y in YBCO. Therefore, they do not effectively “poison” the superconducting matrix by reducing  $T_c$ . Various studies have shown that a combination of the columnar formation of niobate and tantalate to form mixed double perovskite structures in the YBCO layer can lead to a complex  $J_c$  anisotropy. Nevertheless, they enhance the current density especially at high fields [26, 69].

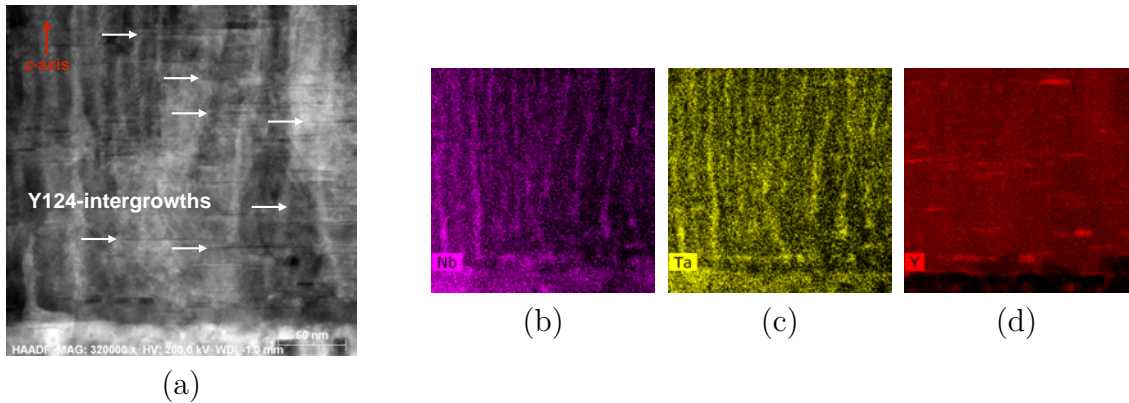


**Figure 6.8:** (a) HAADF image of the cross-section of the YBCO+BYNTO sample. (b)-(d) Corresponding EDX maps confirming the elemental composition of the defects of  $\text{Ba}_2\text{Y}(\text{Nb}/\text{Ta})\text{O}_6$  (BYNTO).

The BYNTO forms as rods with lengths roughly parallel to the  $c$ -axis and plates parallel to the  $ab$ -plane as shown in the TEM and EDX images in figure 6.8. Elongated  $\text{Y}_2\text{O}_3$  nanoparticles parallel to the  $ab$ -planes are also present. Compared with BHO nanocolumns, the BYNTO nanorods are shorter in length and larger in diameter. The columns have lengths of about 100-200 nm, diameter of  $8 \pm 3$  nm and an average distance of 24 nm.

The angle-dependence of  $J_c$  of the YBCO+BYNTO-SS sample is presented in figure 6.9. It shows a more complex anisotropy at different fields and temperatures compared with YBCO-SS and YBCO+BHO-SS in the previous sections. The plots are normalized by the value of  $J_c$  at  $\phi = 45^\circ$  at each field for a better comparison. At 77 K (figure 6.9a), the usual  $ab$ -peak is observed at 5 T and the anisotropy

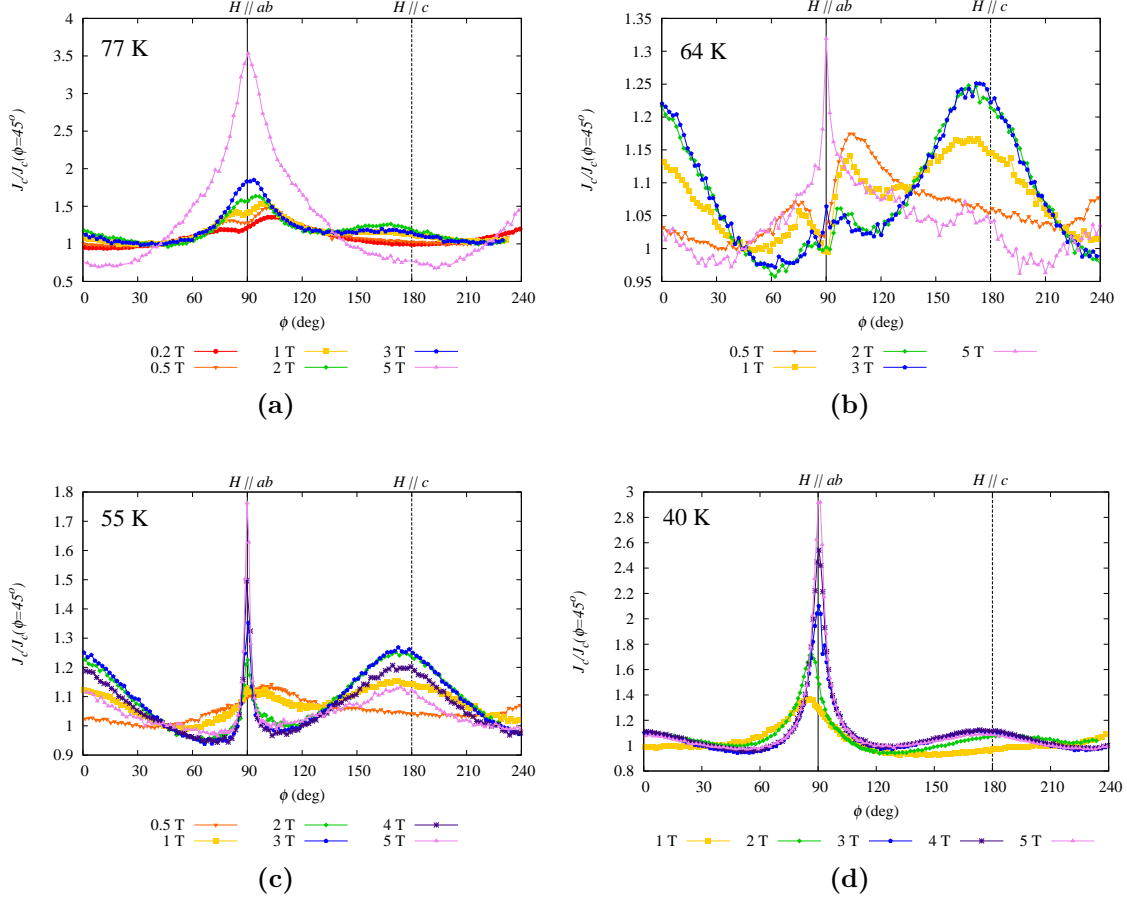


**Figure 6.9:** Normalized  $J_c(\phi)$  of YBCO-BYNT0-SS in different applied magnetic fields at (a)  $T = 77$  K, (b)  $T = 64$  K, (c)  $T = 55$  K and (d)  $T = 40$  K. The plots are normalized for an easier comparison of the behavior of anisotropy at each field. The direction parallel to the  $c$ -axis and  $ab$ -plane is at  $\phi = 0^\circ$  and  $\phi = 90^\circ$ , respectively.

is also the largest compared to lower fields. The anisotropy decreases rapidly as the field is decreased and a dip at  $H \parallel ab$  develops together with a broad peak around the  $c$ -axis. The same behavior is observed at 64 K (figure 6.9b), although the anisotropy of  $J_c$  is smaller compared to 77 K. The formation of the dip at  $H_{app} \parallel ab$  occurs at a higher field of 3 T and the  $c$ -axis peak appears to be the largest between 1 T and 3 T. At 55 K (figure 6.9c) the dip no longer appears and a sharp  $ab$ -peak forms instead. A broad  $c$ -axis peak appears at 5 T, which increases in prominence at 3 T and starts to decrease again as  $H_{app}$  decreases. At 40 K, a similar behavior than in YBCO-SS is obtained but with a smaller anisotropy. With the average distance of the BYNT0 nanocolumns, found in the TEM image to be about 24 nm, the matching field  $B_\phi = \phi/a^2$ , where  $a$  is the spacing between the pinning centers, is roughly estimated as 3.5 T. Therefore, it is not surprising that the prominence of the  $c$ -axis peak is largest at 3 T at all temperatures because above  $B_\phi$ , the number of vortices is larger than the number of CPCs and there

is a larger probability of vortex cutting and joining than in applied fields below  $B_\Phi$ . The size of the BYNTO nanoprecipitates is larger making them more efficient pinning centers at higher temperatures.

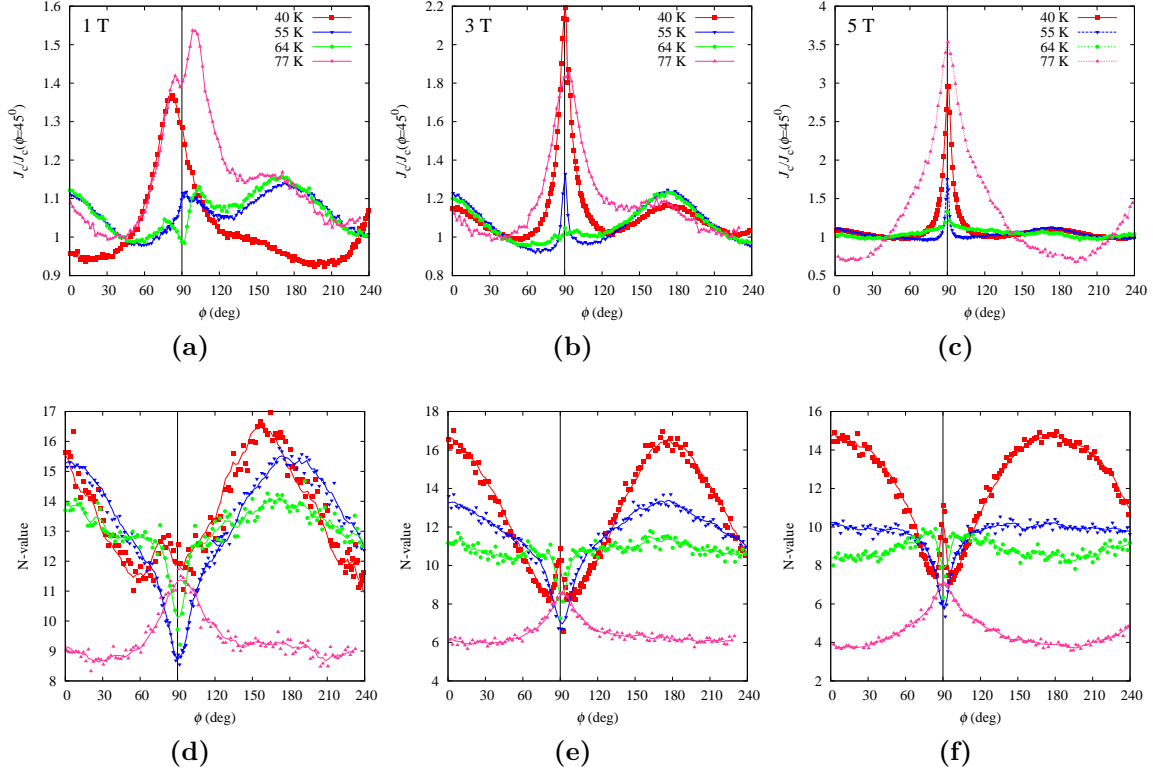


**Figure 6.10:**  $\phi$ -dependence of  $J_c$  at applied fields of (a) 1 T, (b) 3 T and (c) 5 T and different temperatures.  $\phi$ -dependence of the N-value at (d) 1 T, (e) 3 T and (f) 5 T. The solid vertical line indicates the field direction  $H_{\text{app}} \parallel ab$  ( $\phi = 90^\circ$ ).

Analyzing the angle-dependence of the N-value, figure 6.10 shows that despite the observed formation of the dip in  $H_{\text{app}} \parallel ab$  and the asymmetry of  $J_c(\phi)$  around the direction of the  $ab$ -planes, the behavior of  $N(\phi)$  still shows consistency to the pure YBCO. The  $N(\phi)$  curves have a broad peak around  $\phi = 90^\circ$  at 77 K, a minimum at 64 K and 55 K that indicates formation of kinked vortex state and a sharp peak at 40 K corresponding to the pseudo-lock in state.

However, a few more interesting details are observed that indicate how the BYNTO nanostructures affect the dynamics of vortices and thus,  $J_c$ . In YBCO-SS and YBCO-BHO-SS, a peak in  $N(\phi)$  is observed that corresponds to a peak in  $J_c(\phi)$  for the field parallel to the  $c$ -axis while a valley forms at intermediate angles indicating an increase in the pinning energy only when the vortices are directed parallel to the correlated defects such as the BHO nanorods in YBCO+BHO-SS and GBs in YBCO-SS. This is also the case for the intrinsic pinning at 40 K where a pseudo-lock in state occurs. However, for YBCO+BYNTO-SS,  $N(\phi)$  at 40 K (red curves in figure 6.10d-6.10f) has a broad peak centered at  $\phi = 180^\circ$  indicating that

the contribution of BYNTO nanocolumns to pinning spans a wider angular range than the BHO nanorods and GBs in pure YBCO. The more disperse formation and shorter lengths of BYNTO nanorods promote pinning of segments of vortices even if the field is tilted away from the  $c$ -axis.

In an applied field of 5 T, the peak in the  $N(\phi)$  centered at  $180^\circ$  becomes flat at 55 K, then forms a valley at 64 K and 77 K. Since the  $N$ -value is inversely proportional to the creep rate,  $S = -\partial \ln J / \partial \ln t \propto k_B T / U_o$  [63], the formation of a valley suggest an increase in the creep rate which is also induced by additional thermal activation at higher temperatures.

### 6.4 Comparison of the APCs in PLD-YBCO on SS

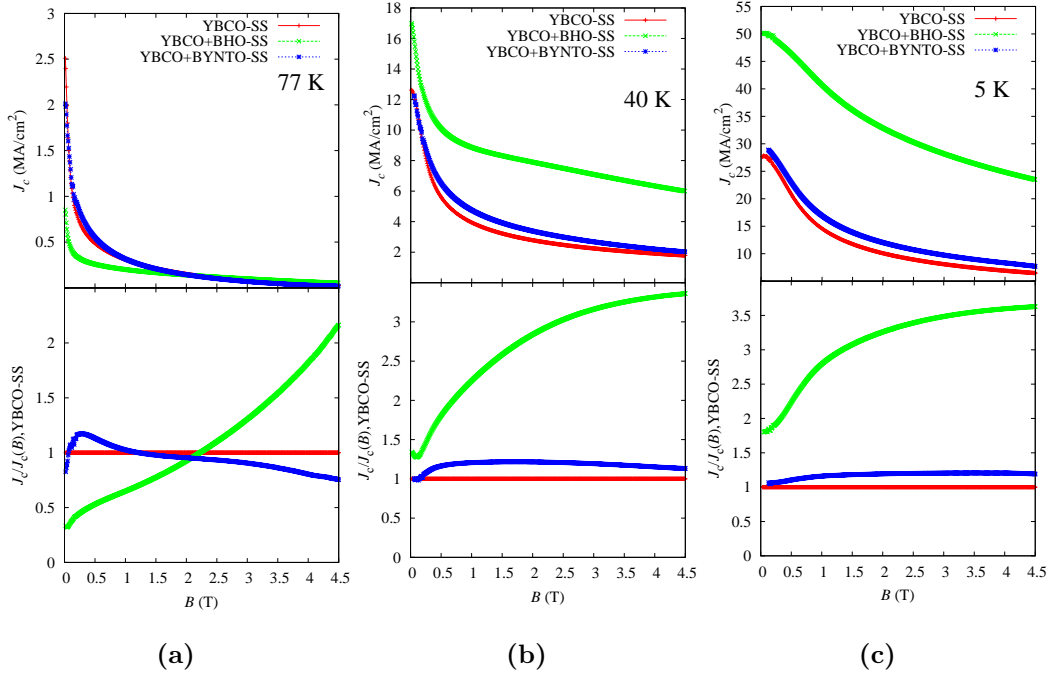


**Figure 6.11:** (Upper panels) Field dependence of  $J_c$  in  $H_{\text{app}} \parallel ab$  of the pure and doped samples. The  $J_c$  was evaluated from magnetization measurements in the vector VSM. (Lower panels) Normalization of  $J_c$  with respect to the pure YBCO sample to illustrate the enhancement in  $J_c$ .

To summarize the effects of incorporating BHO and BYNTO nanocolumns on vortex pinning and the enhancement of the in-field  $J_c$ , the field dependence of the current density for  $H_{\text{app}} \parallel c$  of the three tapes: YBCO-SS, YBCO+BHO-SS and YBCO+BYNTO-SS is shown in the upper panels of figure 6.11. The lower panels are normalized plots of the current density with respect to the pure YBCO to illustrate the enhancement factor in  $J_c$  of the BHO and BYNTO-doped tapes.

At 77 K, the BHO-doped tape begins with a lower self-field  $J_c$  compared to the pure YBCO and BYNTO-doped sample. Above 2.2 T, its  $J_c$  begins to become higher than that of the pure YBCO and has the largest value at 40 K and 5 K in the whole measurement field range. Its  $J_c$  is up to 3.5 times higher than in the pure YBCO at 5 K. On the other hand, the YBCO+BYNTO-SS tape shows a minimal enhancement of only up to 30% relative to the pure YBCO. It is an important result to show that the BHO nanocolumns of diameter  $4 \pm 2$  nm, still effectively pin vortices and has consistently introduced enhancement in  $J_c$  down to 5 K. However, it is interesting to note that the enhancement in  $J_c$  introduced by the BHO nanoprecipitates is larger than the enhancement in  $J_c$  caused by the BYNTO phase despite a similar columnar nature. Therefore, further studies must still be done to elucidate the differences such as in the aspect of strain induced by the BHO nanorods and BYNTO nanorods. A. Llordes et al. [61] found that the nano-scale strain around nanoprecipitates also contribute to pinning.

On the other hand, the BYNTO-doped sample can have the lowest  $J_c$  anisotropy of the three samples especially at intermediate fields such as at 2 T (figure 6.12a and 6.12c). At angles close to the  $ab$ -plane ( $\phi = 90^\circ$ ),  $J_c$  of YBCO+BHO-SS and YBCO+BYNTO-SS ceases to be larger than in pure YBCO, which is obviously due to the suppression of the  $ab$ -peak in the doped samples.

Comparing the angular dependence of the N-value of the pure and doped tapes, figure 6.13 shows that the onset of the formation of kinked vortices near the  $ab$ -planes, denoted by the angle  $\phi_k$ , is the same for all the three tapes. It is approximately  $8.0^\circ \pm 1.5^\circ$  and  $6.0^\circ \pm 1.0^\circ$  for 2 T and 5 T, respectively. This value is slightly lower than the  $\phi_k$  obtained as the onset of vortex channeling in GdBCO-ISD in section 4.4.2, which is  $11.7^\circ$  but it is well within the range of other experimental data [14, 94]. It is interesting that despite the presence of the nanocolumns in the doped samples that are oriented perpendicular to the  $ab$ -planes, the angular range where the kinked vortices form does not change since there is no observable broadening of the minimum.

Similar behavior is observed on the lock-in angle,  $\phi_T$ , which indicates the onset of the pseudo-lock in state of the vortices parallel to the  $ab$ -planes in figure 6.14. The value of  $\phi_T$  is approximately the same for the pure and BYNTO-doped sample (40 K transport measurements is not available for the BHO-doped) and is  $12.2 \pm 0.2^\circ$  and  $4.5 \pm 0.5^\circ$  for 1 T and 5 T, respectively. These values are larger than the theoretical prediction of  $0.1^\circ$ - $1^\circ$  [5], but is so far consistent to the experimental data in YBCO films [94] and iron-based superconductors [91]. The value of  $\phi_T$  is expected to vary with field as:  $[(T_c - T)/H]^{1/2}$  [56]. Although compared to the results presented by M. Weigand et al. [94] where an increase in  $\phi_T$  is observed in BaZrO<sub>3</sub>+Y<sub>2</sub>O<sub>3</sub>-doped YBCO,  $\phi_T$  does not change with the BYNTO addition, similar to  $\phi_k$ , and only the height of the peak is changed, which is largest in the pure YBCO. Figure 6.15 shows the field-dependence of  $\phi_k$  and  $\phi_T$  of the pure and doped samples. The decrease of the onsets is consistent to the theoretical predictions. There is no quantitative comparison of the behavior of these angles with field and temperature reported so

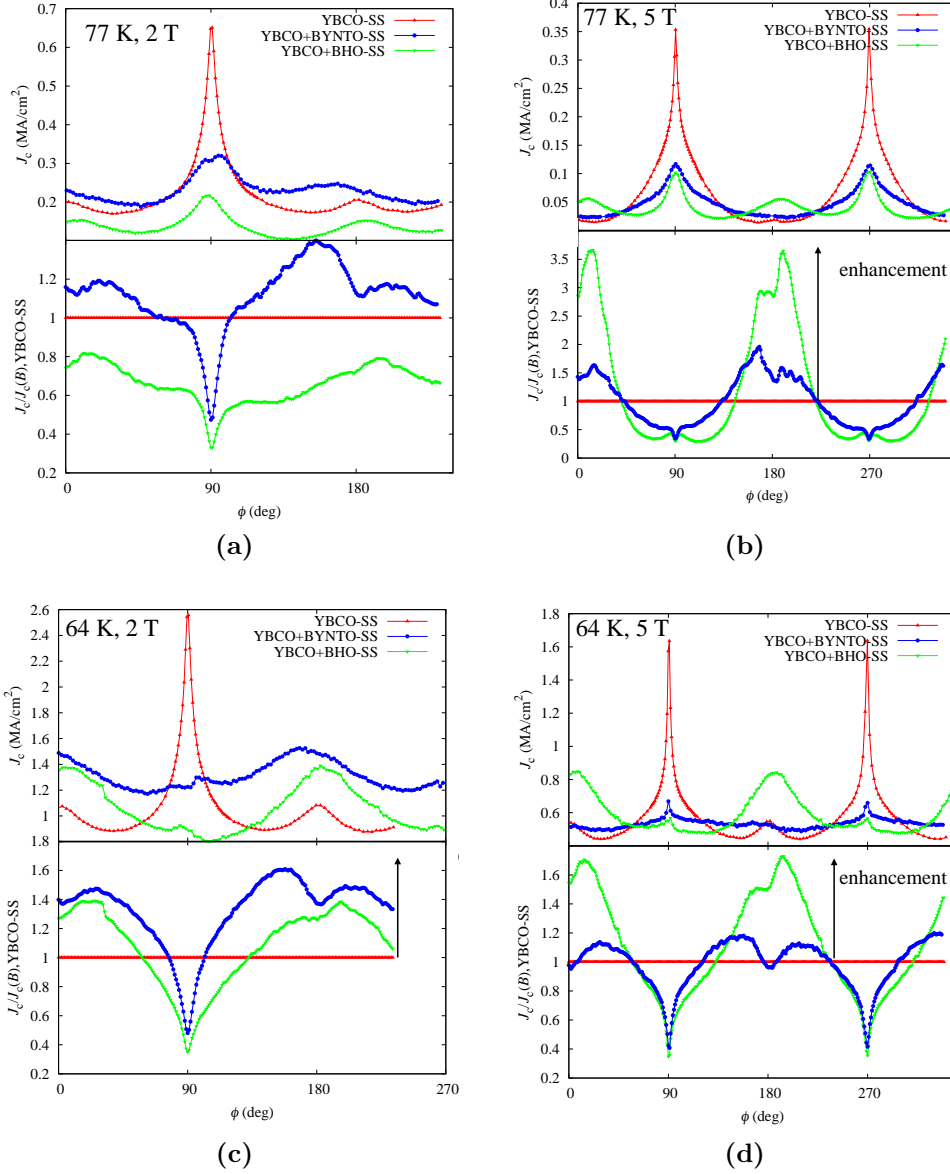


**Figure 6.12:** Angular dependence of  $J_c$  (upper panels) and normalized  $J_c$  of the doped samples with respect to the pure YBCO (lower panel) at (a)-(b) 77 K and (c)-(d) 64 K and applied fields of 2 T and 5 T.

far for YBCO films, while an  $H^{-3/4}$  dependence of  $\phi_k$  is reported by C. Tarantini, et al. in iron based superconductors [91].

The YBCO-SS sample has relatively larger N-values over the whole angular range compared to the other two samples. This indicates that the creep rate,  $S \propto 1/N$ , is higher in the doped samples. Such an increase in  $S$  can be ascribed to the presence of the columnar defects that can promote faster creep since vortices have high probability of hopping as they interact with the nearest defects. At 64 K



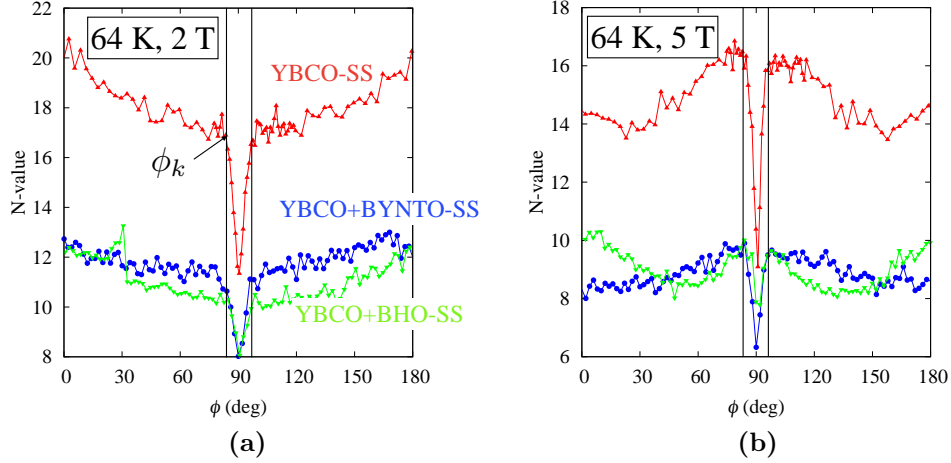


**Figure 6.13:** Angle dependence of the N-value of the three PLD-grown samples at  $T = 64$  K and applied fields of (a) 2 T and (b) 5 T. The angle  $\phi_k$  marks the onset of the kinked vortex formation with respect to the direction of the  $ab$ -planes ( $\phi = 90^\circ$ ).

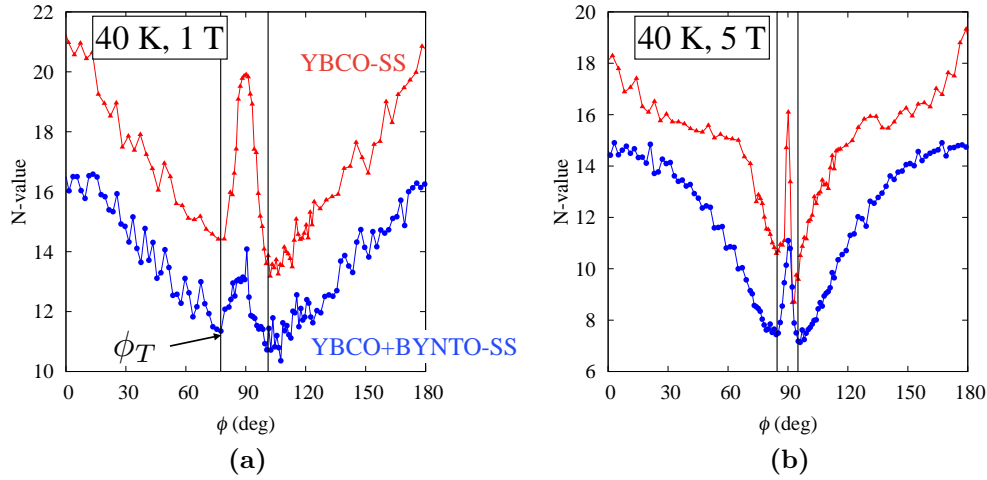


**Figure 6.14:** Angle dependence of the N-value of the three PLD-grown samples at  $T = 40$  K and applied fields of (a) 1 T and (b) 5 T. The angle  $\phi_T$  marks the onset of the pseudo-lock in state of the vortices parallel to the  $ab$ -planes ( $\phi = 90^\circ$ ).

and 5 T in figure 6.13b, compared with the BYNTO-doped sample, the BHO-doped film shows an increase in the N-value (decrease in  $S$ ) towards  $\phi = 0^\circ$  and  $180^\circ$  indicating that the vortices align more effectively with the longer BHO nanocolumns than in the BYNTO nanorods. Such increase of N has a corresponding increase in the angle-dependence of  $J_c$  parallel to the BHO nanocolumns compared to the minimal increase with BYNTO nanorods. Such promotion of creep due to shorter and splayed columns of BYNTO is the reason why the resulting increase in  $J_c$  relative to the pure YBCO is less than the enhancement induced by the BHO nanocolumns.

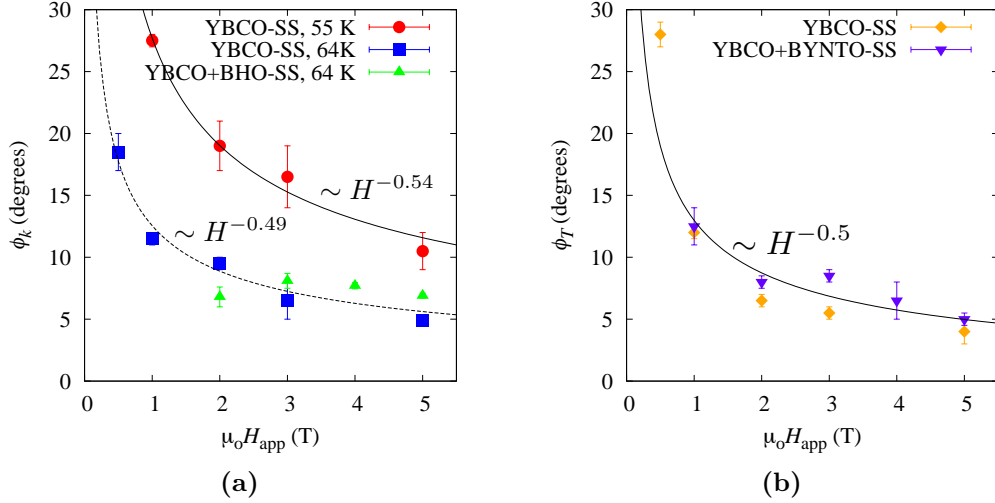


**Figure 6.15:** Field dependence of the (a) onset of the kinked state at  $T = 64, 55$  K and (b) onset of the lock-in state at  $T = 40$  K of the pure and doped samples.

## 6.5 APCs in PLD-YBCO with RABiTS NiW

As discussed in chapter 5, pulsed laser deposited YBCO films on RABiTS NiW have a defined range at low fields wherein the critical current is limited by the grain boundaries and the transition to a grain limited regime at higher fields depends upon the properties of the boundaries. By the addition of BHO and BYNTO phases, the granularity of the films are found to become less than the pure YBCO and thus the range of field governed by GB limitation is shifted to lower fields and temperatures. Therefore, at higher fields where  $J_c$  is limited by vortex pinning, the influence of the BHO and BYNTO doping must be discernible.

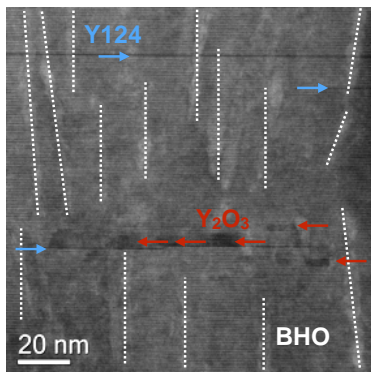


**Figure 6.16:** TEM image of the YBCO+5BHO-Ni5W tape showing the microstructural defects such as the BHO nanocolumns,  $Y_2O_3$  precipitates and Y-124 intergrowths.

Figures 6.16 and 6.17 shows the TEM images of the cross-section of the BHO-doped and BYNTO-doped YBCO films on Ni5W. Similar to the films on ABAD-YSZ/SS template, nanocolumns are also formed from the BHO precipitates that are oriented roughly parallel to the  $c$ -axis with an average diameter of  $3.8 \pm 1.2$  nm and lengths from 50 nm to 100 nm. On the other hand, the BYNTO nanoprecipitates

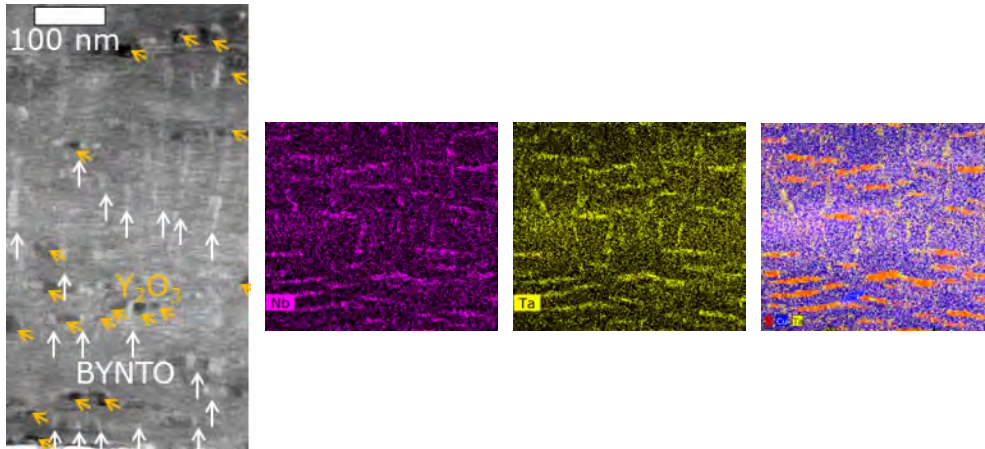


**Figure 6.17:** TEM and EDX images of the YBCO+5BYNTO-Ni5W tape showing the microstructural defects such as the BYNTO nanocolumns and  $Y_2O_3$  precipitates.

form a hybrid structure of columns parallel to the  $c$ -axis and nanoplates parallel to the  $ab$ -planes as shown by the EDX images in figure 6.17. The BYNTO columns have a typical diameter of  $10.0 \pm 2$  nm and lengths of up to 150 nm.

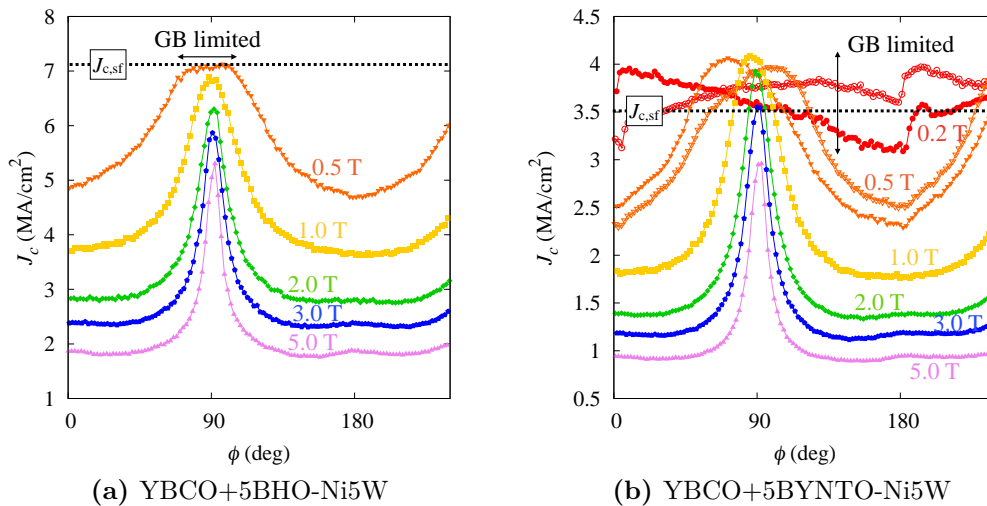


**Figure 6.18:** Angular dependence of  $J_c$  of the (a) BHO- and (b) BYNTO-doped YBCO films on RABiTS Ni5W template. The measurement temperature was 40 K. The dashed horizontal line denote the self-field  $J_c$  at each temperature.

The angular dependence of the current density of the doped YBCO tapes at  $T = 40$  K are presented in figure 6.18. The anisotropy of the two samples is quite similar to the one of the pure YBCO especially at high fields. At lower fields such as 0.5 T for the YBCO+5BHO-Ni5W, a  $\phi$ -independent range around  $\phi = 90^\circ$  is observed which is an indication of grain boundary limitation as discussed in section

5.1.6. In the BYNTO-doped sample,  $J_c$  at 0.2 T remains close to the self-field  $J_c$  (similar to the pure YBCO) over the whole angular range. The direction of the Lorentz force (open and solid symbols) reverses the angle dependence of  $J_c$  at 0.5 T and 0.2 T about  $\phi = 90^\circ$  signifying that surface pinning influences the total pinning force on the AJ vortices as well.

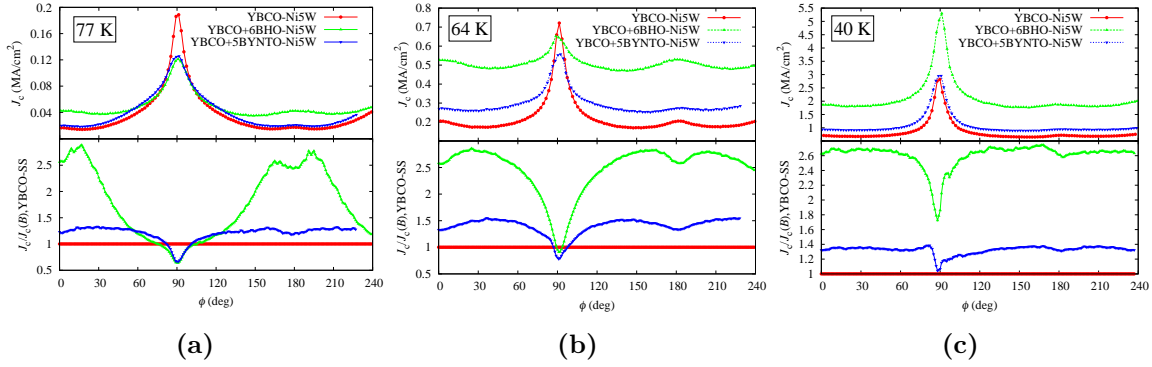


**Figure 6.19:** The upper panels correspond to the angular dependence of  $J_c$  of the three YBCO films with Ni5W template at (a) 77 K, (b) 64 K and (c) 40 K and applied field of 5 T. The lower panels are plots of the enhancement factor in  $J_c$  with respect to the pure YBCO.

Therefore, to gain insight on how much  $J_c$  can be enhanced by additional pinning caused by the BHO and BYNTO nanorods, a comparison of  $J_c$  of the pure and doped samples at the highest applied field of 5 T is presented in figure 6.19 at 77 K, 64 K and 40 K. At this field,  $J_c$  of the three samples must be dominated by the intragrain  $J_c$  according to the field dependence discussed in section 5.2. Similar to the behavior of BHO and BYNTO doped tapes on PLD-YBCO films on ABAD-YSZ/SS, the BHO nanocolumns cause the largest enhancement in  $J_c$  (up to 2.6 times) while the BYNTO nanorods can only induce an enhancement of up to 50%. The anisotropy of the critical current is found to be reduced in the doped samples. Unlike in the films on SS template, the formation of a dip parallel to the  $ab$ -planes (in BYNTO sample) does not occur and the  $c$ -axis peak of the BHO-doped YBCO on NiW is not as significantly broad and large as in YBCO+BHO-SS.

The corresponding  $\phi$ -dependence of the N-value at 5 T is shown in figure 6.20. At 77 K, a direct correlation of  $J_c(\phi)$  and  $N(\phi)$  is observed where a peak parallel to the  $ab$ -planes appear. At 64 K (figure 6.20b), a small dip in the direction of  $\phi = 90^\circ$  is observable in the doped samples that indicates the formation of kinked vortices. Consistent to the results on YBCO-SS tapes,  $\phi_k$  is about  $7 \pm 2^\circ$  at the same field and temperature. Such dip is not visible in the pure YBCO film. However, the N-value of the YBCO-Ni5W is smaller in general than the N-value of YBCO-SS at the same conditions. On the other hand, the appearance of a peak at 40 K is visible in all the three tapes which refers to the pseudo-lock in state along the  $ab$ -plane with an onset of  $6.4 \pm 1.7^\circ$ .

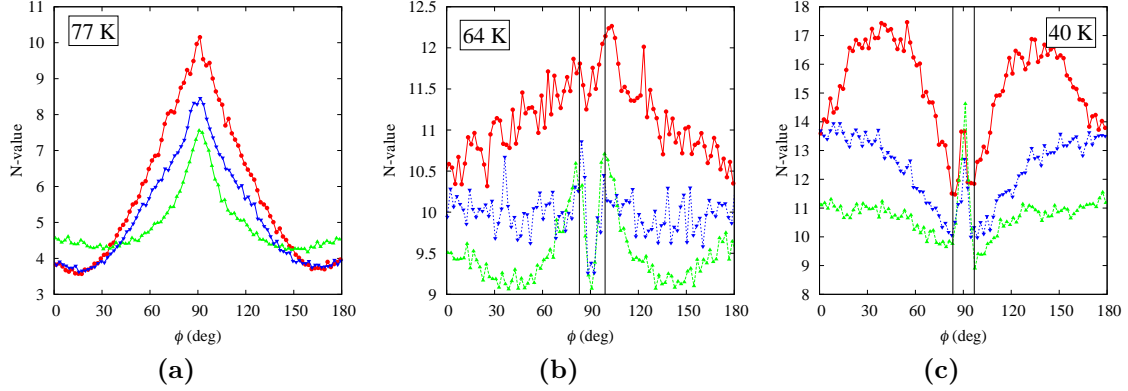


**Figure 6.20:** Angular dependence of the N-value of the three samples at (a) 77 K, (b) 64 K and (c) 40 K and  $\mu_0 H_{\text{app}} = 5$  T. The vertical lines denote the onset of  $\phi_k$  and  $\phi_T$  in (b) and (c), respectively.

## 6.6 Summary

In this chapter, the effects on the anisotropy and value of  $J_c$  in PLD-YBCO tapes with BHO or BYNTO precipitates were presented. The YBCO-SS samples have sharp texture that correlates to a homogenous field profile that represents a uniform current flow. A manifestation of GB limitation is not found within the field and temperature range of the measurements. Therefore, it is easy to discern the effects of the BHO and BYNTO precipitates to vortex pinning. BHO was found to cause larger enhancement in  $J_c$  than BYNTO down to 5 K.

A direct correlation between  $J_c(\phi)$  and  $N(\phi)$  at 77 K, an inverse correlation at 64 K and an appearance of a narrow sharp peak in  $N(\phi)$  at the direction of  $H_{\text{app}} \parallel ab$  at 40 K, were observed consistently in the pure and doped samples. This serves as an experimental evidence of different vortex states in the presence of correlated defects including the weakly superconducting layer of YBCO. The formation of a kinked vortex at angles of about  $7^\circ$  towards the  $ab$ -plane direction is visible at 64 K and 55 K while the quasi-locked in state is manifested at 40 K as thermal activation is diminished. It is remarkable that the onset of the kinked and the quasi-lock-in states does not show a quantitative difference for doped tapes despite the presence of the nanocolumns. Only the values of  $N$  were found to be lower in the doped samples than in the pure YBCO films. This indicates that the nanocolumns promote a higher creep rate. In YBCO+BHO-SS, the vortices are efficiently pinned around the  $H_{\text{app}} \parallel c$  due to the presence of long BHO columns thus a corresponding peak in the  $N(\phi)$  is observed. A valley at intermediate angles signify that the vortices have higher creep rate if they are not aligned to any correlated pinning centers. On the other hand, the shorter and larger BYNTO nanocolumns contribute to pinning in a wider angular range despite the payoff of a higher creep rate.

Because of the granular morphology of the YBCO layer in CCs on RABiTS NiW template, the onset of the kinked and pseudo-lock in states is visible in the angle-dependence of the N-value only at the field range where  $J_c$  is limited by vortex pinning. The same enhancement in  $J_c$  caused by the BHO and BYNTO phases as in the ABAD-textured tape was observed in the PLD-YBCO films on NiW. This gives further evidence that the appearance of the peak in the field-dependence of  $J_c$  is indeed the transition point from the GB-limited to grain-limited regime.



# Chapter 7

## Conclusions and further work

### 7.1 Conclusions

The magnetic and transport properties of different coated conductors were studied in this thesis at different temperatures and applied magnetic fields. The investigated samples include CCs on a low-cost RABiT NiW template and medium cost templates containing textured buffer layers by ABAD and ISD techniques. The study done on a wide variety of tape architectures provides an analysis of the performance of coated conductors produced nowadays with a particular emphasis on the current-limiting mechanisms.

One of the most important results from this thesis is the demonstration of the persisting grain boundary limitation to the current transport in CCs on RABiT NiW especially for pulsed laser deposited YBCO. The granular morphology was initially confirmed by the SHPM images of the field distribution. With the local orientation mapping done alongside the field maps, it was found that despite a successful production of the NiW template with GB angles confined to less than  $10^\circ$ , the misorientation and porosity of the YBCO grains above each NiW grain also contribute to the spatial inhomogeneity of the critical current density. The observed granularity manifests at all temperatures and applied fields – from 4 K to 77 K and fields of up to 5 T. Such granular morphology was found to have drastic effects also in transport measurements. The occurrence of a peak in the field-dependence of  $J_c$  due to weak pinning of vortices in the grain boundaries was first reported in bi-crystal samples where it usually appears at a few tens of millitesla. It was found for the first time that the peak occurs at 1-1.5 T at 40 K, demonstrating a defined transition from the GB-limited to pinning-limited  $J_c$ . Such cross-over is also dependent on the angle of the applied field with respect to the tape surface such that the peak in  $J_c(B)$  occurs at a higher field parallel to the  $ab$ -planes than along the  $c$ -axis. The field range of the GB-limited regime increases as the temperature decreases, therefore, it can be expected to shift to a few more Teslas down to 4.2 K. However, the granularity was observed to be significantly reduced if YBCO is grown by CSD. The formation of meandering GBs and a possibility of a better grain connectivity have contributed to the suppression



of the GB limitation. Initial investigations have shown that the homogeneity of the superconducting layer in PLD-grown YBCO on NiW is also improved by adding secondary phases such as hafnates, tantalates and niobates.

In the case of CCs with textured buffer layer such as the PLD-YBCO on ABAD-YSZ/SS and ISD-MgO buffered GdBCO film on Hastelloy, the GB limitation does not manifest at least within the field and temperature range of the measurements. Therefore, the  $J_c$  limitation is mostly attributed to the mechanism of vortex pinning and has enabled the analysis of the dynamics of vortices.

The technology of ISD-buffered CC is still not widely utilized although it has been demonstrated in lab-scale production in the past. So far, only the company THEVA GmbH has been able to show its prospect for a large-scale production. Therefore, almost no published data and extensive analysis of its anisotropy with applied field exists. Due to the tilted crystallographic axes of GdBCO,  $J_c$  turns out to have a very interesting anisotropic behavior at various field and current orientations. In principle, the tilted geometry of the crystal structure in the superconducting layer basically leads to the appearance of the  $ab$ -peak at intermediate angle between the main axes of the macroscopic surface of the tape. The asymmetric effect in the anisotropy of  $J_c$  is due to kinked vortex states and different synergies of defects on different sides of the correlated defects. The phenomenon of vortex channeling, which is characterized by a minimum in the anisotropy of  $J_c$  and a manifestation of a kinked vortex state in a layered superconductor, was found in this tape at temperatures as high as 77 K. The vortex channeling minimum was only observed at temperatures below 50 K and vicinal angles of  $2^\circ$ - $10^\circ$  in previous works on YBCO films on a vicinal substrate.

On the other hand, the additional pinning by the correlated defects formed either by the hafnate phase or the tantalate and niobate phases in PLD grown YBCO on ABAD-YSZ buffered tapes was determined. When the applied field is aligned to the nanorods roughly parallel to the  $c$ -axis, the samples with the BHO phase has the largest enhancement of up to thrice the value of  $J_c$  of the pure YBCO film down to 5 K. The analysis of the angle dependence of the N-value alongside  $J_c$  has enabled the identification of the dominant pinning mechanism at different temperatures. In the direction parallel to the  $ab$ -planes, the direct correlation between  $N(\phi)$  and  $J_c(\phi)$  at 77 K, the inverse correlation at 64 K and the appearance of a narrower peak at 40 K were observed consistently in the pure and doped samples as well as in the ISD-buffered CC and even in PLD-YBCO on RABiTS NiW in the grain-limited regime. These depict the formation of a kinked vortex state and quasi lock-in state when the field is oriented nearly parallel to the planes as a consequence of the layered structure of YBCO. One remarkable information gained from the N-value is the similarity of the onset of the kinked and lock-in state of all the samples despite the presence of correlated defects perpendicular to the  $ab$ -planes in the BHO- and BYNTO doped CCs. Only the values of N are lower in the doped samples indicating a higher creep rate induced by the presence of the nanorods.

## 7.2 Future outlook

The significance of grain boundary limitation in PLD-grown YBCO on RABiTS NiW may come as a disadvantage for this material compared with other tape architecture such as the ones with textured buffer layer. However, the improvement of the homogeneity by doping of BHO and BYNTO phases indicate a promising solution to this. Further work is still needed such as a systematic study on the microstructural and superconducting properties to confirm the initial results presented in this thesis and to identify the mechanism that leads to the improvement of the electromagnetic properties.

The ISD-buffered tapes has also shown a promising current-carrying performance since  $J_c$  is not degraded with increasing thickness unlike in conventional YBCO films. It also has interesting  $J_c$  anisotropy that enables further understanding of the vortex dynamics in layered superconductor. The thickness of the GdBCO layer investigated in this thesis was only 2  $\mu\text{m}$ , therefore, if applications require production of this tape with a thicker layer, it is important to analyze further such films with a thicker layer.

All the transport measurements presented in this thesis were obtained at a lowest temperature of 40 K due to limitations coming from the current supply and sample heating since the needed current increases as the temperature decreases. The 5 K values of  $J_c$  in the pure YBCO and doped samples were obtained by magnetization measurements which can only provide limited angular range due to inaccessible information in the direction parallel to the  $ab$ -planes. Aside from that, the analysis of the N-values at lower temperatures would also be most interesting to get a whole picture of the effectiveness of the secondary phases as pinning centers down to a possible operating temperature of 4.2 K. As also mentioned in section 6.4, strain induced by the nanorods may be the possible mechanism that enhances vortex pinning at low temperatures. However, further microstructural analysis is needed for a confirmation.



# Bibliography

- [1] AABDIN, Z., DUERRSCHNABEL, M., BAUER, M., SEMERAD, R., PRUSSEIT, W., AND EIBL, O. Growth behavior of superconducting  $\text{DyBa}_2\text{Cu}_3\text{O}_{7-x}$  thin films deposited by inclined substrate deposition for coated conductors. *Acta Materialia* 25 (2012), 6592–6600.
- [2] AREPOC, S. R. O. High linearity Hall probes for room and cryogenic temperatures. <http://www.arepoc.sk>, 2010.
- [3] BAUER, M., SEMERAD, R., AND KINDER, H. YBCO films on metal substrates with biaxially aligned MgO buffer layers. *IEEE Trans. Appl. Supercond.* 9, 2 (1999), 1502–1505.
- [4] BERGHUIS, P., BARTOLOMEO, E. D., WAGNER, G. A., AND EVETTS, J. E. Intrinsic channeling of vortices along the *ab*-plane in vicinal YBCO films. *Phys. Rev. Lett.* 79 (1997), 2332–2335.
- [5] BLATTER, G., FEIGEL'MAN, M. V., GESHKENBEIN, V. B., LARKIN, A. I., AND VINOKUR, V. M. Vortices in high temperature superconductors. *Rev. Mod. Phys.* 66 (1994), 1125–1388.
- [6] BLATTER, G., GESHKENBEIN, V. B., AND LARKIN, A. I. From isotropic to anisotropic superconductors: A scaling approach. *Phys. Rev. Lett.* 68 (1992), 875–878.
- [7] BRANDT, E. H. The flux-line lattice in superconductors. *Reports on Progress in Physics* 58, 11 (1995), 1465–1594.
- [8] BRETOS, I., SCHNELLER, T., FALTER, M., BÄCKER, M., HOLLMANN, E., WÖRDENWEBER, R., MOLINA-LUNA, L., TENDELOO, G. V., AND EIBL, O. Solution-derived  $\text{YBa}_2\text{Cu}_3\text{O}_{7-\delta}$  (YBCO) superconducting films with  $\text{BaZrO}_3$  (BZO) nanodots based on reverse micelle stabilized nanoparticles. *J. Mater. Chem. C* 3 (2015), 3971–3979.
- [9] CAI, X. Y., GUREVICH, A., TSU, I.-F., KAISER, D. L., BABCOCK, S. E., AND LARBALESTIER, D. C. Large enhancement of critical-current density due to vortex matching at the periodic facet structure in  $\text{YBa}_2\text{Cu}_3\text{O}_{7-\delta}$  bicrystals. *Phys. Rev. B* 57 (1998), 10951–10958.
- [10] CANTONI, C., VEREBELI, D. T., SPECHT, E. D., BUDAI, J., AND CHRISTEN, D. K. Anisotropic nonmonotonic behavior of the superconducting critical

- current in thin  $\text{YBa}_2\text{Cu}_3\text{O}_{7-\delta}$  films on vicinal  $\text{SrTiO}_3$  surfaces. *Phys. Rev. B* **71** (2005), 054509.
- [11] CARDWELL, D., AND GINLEY, D. *Handbook of Superconducting materials, Volume I: Superconductivity, Materials and Processes*, vol. 1. Institute of Physics Publishing, Dirac House, Temple Back, Bristol BS1 6BE, UK, 2003.
- [12] CHAUDHARI, P., MANNHART, J., DIMOS, D., TSUEI, C. C., CHI, J., OPRYSKO, M. M., AND SCHEUERMANN, M. Direct measurement of the superconducting properties of single grain boundaries in  $\text{YBa}_2\text{Cu}_3\text{O}_{7-\delta}$ . *Phys. Rev. Lett.* **60** (1988), 1653–1656.
- [13] CIVALE, L. Vortex pinning and creep in high-temperature superconductors with columnar defects. *Supercond. Sci. Technol.* **10** (1997), A11–A18.
- [14] CIVALE, L., MAIOROV, B., MACMANUS-DRISCOLL, J. L., WANG, H., HOLESINGER, T. G., FOLTYN, S. R., SERQUIS, A., AND ARENDT, P. N. Identification of intrinsic ab-plane pinning in  $\text{YBa}_2\text{Cu}_3\text{O}_7$  thin films and coated conductors. *IEEE Trans. Appl. Supercond.* **15**, 2 (2005), 2808–2811.
- [15] CLEM, J. R. Spiral vortex expansion instability in type-II superconductors. *Phys. Rev. Lett.* **38** (1977), 1425–1428.
- [16] CLEM, J. R. Anisotropy and two-dimensional behaviour in the high-temperature superconductors. *Supercond. Sci. Technol.* **11** (1998), 909–914.
- [17] DEW-HUGHES, D. The critical current of superconductors: an historical review. *Low. Temp. Phys.* **27**, 9 (2001), 713–722.
- [18] DIMOS, D., CHAUDHARI, P., MANNHART, J., AND LEGOUES, F. K. Orientation dependence of grain-boundary critical currents in  $\text{YBa}_2\text{Cu}_3\text{O}_{7-\delta}$  bicrystals. *Phys. Rev. Lett.* **61** (1988), 219–222.
- [19] DJUPMYR, M., CRISTIANI, G., HABERMEIER, H.-U., AND ALBRECHT, J. Anisotropic temperature-dependent current densities in vicinal  $\text{YBa}_2\text{Cu}_3\text{O}_{7-\delta}$ . *Phys. Rev. B* **72** (2005), 220507.
- [20] DURRELL, J. H., BURNELL, G., TSANEVA, V. N., BARBER, Z. H., BLAMIRE, M. G., AND EVETTS, J. E. Critical currents in vicinal  $\text{YBa}_2\text{Cu}_3\text{O}_{7-\delta}$  films. *Phys. Rev. B* **70** (2004), 214508.
- [21] DURRELL, J. H., MENNEMA, S. H., JOOSS, C., GIBSON, G., BARBER, Z. H., ZANDBERGEN, H. W., AND EVETTS, J. E. Flux line lattice structure and behavior in antiphase boundary free vicinal  $\text{YBa}_2\text{Cu}_3\text{O}_{7-\delta}$  thin films. *J. Appl. Phys.* **93**, 12 (2003), 9869–9874.
- [22] DURRELL, J. H., AND RUTTER, N. A. Importance of low-angle grain boundaries in  $\text{YBa}_2\text{Cu}_3\text{O}_{7-\delta}$  coated conductors. *Supercond. Sci. Technol.* **22** (2009), 013001.

- [23] DÜRRSCHNABEL, M., AABDIN, Z., BAUER, M., SEMERAD, R., PRUSSEIT, W., AND EIBL, O. DyBa<sub>2</sub>Cu<sub>3</sub>O<sub>7-x</sub> superconducting coated conductors with critical currents exceeding 1000 A cm<sup>-1</sup>. *Supercond. Sci. Technol.* *25* (2012), 105007.
- [24] ERBE, M., HÄNISCH, J., HÜHNE, R., FREUDENBERG, T., KIRCHNER, A., MOLINA-LUNA, L., DAMM, C., TENDELOO, G. V., KASKEL, S., SCHULTZ, L., AND HOLZAPFEL, B. BaHfO<sub>3</sub> artificial pinning centres in TFA-MOD-derived YBCO and GdBCO thin films. *Supercond. Sci. Technol.* *28* (2015), 114002.
- [25] ERCOLANO, G., BIANCHETTI, M., SAHONTA, S.-L., KURSUMOVIC, A., LEE, J. H., WANG, H., AND MACMANUS-DRISCOLL, J. L. Strong correlated pinning at high growth rates in YBa<sub>2</sub>Cu<sub>3</sub>O<sub>7-δ</sub> thin films with Ba<sub>2</sub>YNbO<sub>6</sub> additions. *J. Appl. Phys.* *116*, 3 (2014), 033915.
- [26] ERCOLANO, G., BIANCHETTI, M., WIMBUSH, S. C., HARRINGTON, S. A., WANG, H., LEE, J. H., AND MACMANUS-DRISCOLL, J. L. State-of-the-art flux pinning in YBa<sub>2</sub>Cu<sub>3</sub>O<sub>7-δ</sub> by the creation of highly linear, segmented nanorods of Ba<sub>2</sub>(Y/Gd)(Nb/Ta)O<sub>6</sub> together with nanoparticles of (YGd)<sub>2</sub>O<sub>3</sub> and (Y/Gd)Ba<sub>2</sub>Cu<sub>4</sub>O<sub>8</sub>. *Supercond. Sci. Technol.* *24* (2011), 095012.
- [27] FARRELL, D. E., RICE, J. P., GINSBERG, D. M., AND LIU, J. Z. Experimental evidence of a dimensional crossover in YBCO. *Phys. Rev. Lett.* *64* (1990), 1573–1576.
- [28] FELDMANN, D. M., HOLESINGER, T. G., FEENSTRA, R., AND LARBALESTIER, D. C. A review of the influence of grain boundary geometry on the electromagnetic properties of polycrystalline YBa<sub>2</sub>Cu<sub>3</sub>O<sub>7-δ</sub> films. *J. Am. Ceram. Soc.* *91*, 6 (2008), 1869–1882.
- [29] FELDMANN, D. M., HOLESINGER, T. G., MAIOROV, B., FOLTYN, S. R., COULTER, J. Y., AND APODACA, I. Improved flux pinning in YBa<sub>2</sub>Cu<sub>3</sub>O<sub>7</sub> with nanorods of the double perovskite Ba<sub>2</sub>YNbO<sub>6</sub>. *Supercond. Sci. Technol.* *23*, 9 (2010), 095004.
- [30] FELDMANN, D. M., REEVES, J. L., POLYANSKII, A. A., KOZLOWSKI, G., BIGGERS, R. R., NEKKANTI, R. M., MAARTENSE, I., TOMSIC, M., BARNES, P., OBERLY, C. E., PETERSON, T. L., BABCOCK, S. E., AND LARBALESTIER, D. C. Influence of nickel substrate grain structure on YBa<sub>2</sub>Cu<sub>3</sub>O<sub>7-δ</sub> supercurrent connectivity in deformation-textured coated conductors. *Appl. Phys. Lett.* *77*, 18 (2000), 2906–2908.
- [31] FERNÁNDEZ, L., HOLZAPFEL, B., SCHINDLER, F., DE BOER, B., ATTENBERGER, A., HÄNISCH, J., AND SCHULTZ, L. Influence of the grain boundary network on the critical current of YBa<sub>2</sub>Cu<sub>3</sub>O<sub>7</sub> films grown on biaxially textured metallic substrates. *Phys. Rev. B* *67* (2003), 052503.

- [32] FLÜKIGER, R. Low temperature superconductors. WE-Heraeus-Seminar - Superconducting materials on their way from physics to applications, February 2016.
- [33] FOLTYN, S. R., CIVALE, L., MACMANUS-DRISCOLL, J. L., XIA, Q. X., MAIOROV, B., WANG, H., AND MALEY, M. Material science challenges for high-temperature superconducting wire. *Nat. Mater.* 6 (2007), 631–642.
- [34] FUGER, R., HENGSTBERGER, F., EISTERER, M., AND WEBER, H. Scan techniques for coated conductors. *IEEE Trans. Appl. Supercond.* 17, 2 (2007), 3753–3756.
- [35] GAITZSCH, U., HÄNISCH, J., HÜHNE, R., RODIG, C., FREUDENBERGER, J., HOLZAPFEL, B., AND SCHULTZ, L. Highly alloyed Ni-W substrates for low AC loss applications. *Supercond. Sci. Technol.* 26 (2013), 085024.
- [36] GAPUD, A. A., CHRISTEN, D. K., FEENSTRA, R., III, F. A. L., AND KHAN, A. On narrowing coated conductor film: the emergence of granularity-induced field hysteresis of transport critical current. *Supercond. Sci. Technol.* 21 (2008), 075016.
- [37] GUREVICH, A. Non-local Josephson electrodynamics and pinning in superconductors. *Phys. Rev. B* 46 (1992), 3187–3190.
- [38] GUREVICH, A., AND COOLEY, L. D. Anisotropic flux pinning in a network of planar defects. *Phys. Rev. B* 50 (1994), 13563–13576.
- [39] HABERMEIER, H.-U. Functional substrates – a novel approach to tailor transport properties and flux-line pinning in  $\text{YBa}_2\text{Cu}_3\text{O}_{7-x}$  thin films. *Z. Metallkond.* 93, 10 (2002), 1052–1056.
- [40] HÄNISCH, J. *Strombegrenzende Mechanismen in  $\text{YBa}_2\text{Cu}_3\text{O}_{7-\delta}$  Dünnschichten und -Quasimultilagen*. PhD thesis, Technischen Universität Dresden, October 2005.
- [41] HÄNISCH, J., CAI, C., STEHR, V., HÜHNE, R., LYUBINA, J., NENKOV, K., FUCHS, G., SCHULTZ, L., AND HOLZAPFEL, B. Formation and pinning properties of growth-controlled nanoscale precipitates in  $\text{YBa}_2\text{Cu}_3\text{O}_7$  / transition metal quasi-multilayers. *Supercond. Sci. Technol.* 19 (2006), 534–540.
- [42] HÄNISCH, J., KOZLOVA, N., CAI, C., NENKOV, K., FUCHS, G., AND HOLZAPFEL, B. Determination of the irreversibility field of YBCO thin films from pulsed high-field measurements. *Supercond. Sci. Technol.* 20 (2007), 228–231.
- [43] HARRINGTON, S. A., DURRELL, J. H., MAIOROV, B., WANG, H., WIMBUSH, S. C., KURSUMOVIC, A., LEE, J. H., AND MACMANUS-DRISCOLL, J. L. Self-assembled, rare earth tantalate pyrochlore nanoparticles for superior flux pinning in  $\text{YBa}_2\text{Cu}_3\text{O}_{7-\delta}$  films. *Supercond. Sci. Technol.* 22 (2009),

- 022001.
- [44] HARRINGTON, S. A., MACMANUS-DRISCOLL, J. L., AND DURRELL, J. H. Practical vortex diodes from pinning enhanced YBCO. *Appl. Phys. Lett.* *95*, 2 (2009), 022518.
  - [45] HECHER, J. *Current transport in polycrystalline iron based superconductors*. PhD thesis, Technische Universität Wien, June 2016.
  - [46] HEINIG, N. F., REDWING, R. D., J. E. NORDMAN, J. E., AND LARBALESTIER, D. C. Strong to weak coupling transition in low misorientation angle thin film  $\text{YBa}_2\text{Cu}_3\text{O}_{7-x}$  bicrystals. *Phys. Rev. B* *60* (1999), 1409–1417.
  - [47] HELD, R., SCHNEIDER, C. W., MANNHART, J., ALLARD, L. F., MORE, K. L., AND GOYAL, A. Low-angle grain boundaries in  $\text{YBa}_2\text{Cu}_3\text{O}_{7-\delta}$  with high critical current densities. *Phys. Rev. B* *79* (2009), 014515.
  - [48] HENGSTBERGER, F., EISTERER, M., AND WEBER, W. Magnetic measurement of the critical current anisotropy of coated conductors. *Supercond. Sci. Technol.* *24* (2011), 045002.
  - [49] HENGSTBERGER, F., EISTERER, M., ZEHETMAYER, M., AND WEBER, H. W. Assessing the spatial and field dependence of the critical current density in YBCO bulk superconductors by scanning Hall probes. *Supercond. Sci. Technol.* *22* (2009), 025011.
  - [50] HILGENKAMP, H., AND MANNHART, J. Grain boundaries in high- $T_c$  superconductors. *Rev. Mod. Phys.* *74* (2002), 485–549.
  - [51] HILTON, D. K., GAVRILIN, A. V., AND TROCIEWITZ, U. P. Practical fit functions for transport critical current versus field magnitude and angle data from (RE)BCO coated conductors at fixed low temperatures and in high magnetic fields. *Supercond. Sci. Technol.* *28* (2015), 074002.
  - [52] JIA, Y., HUA, J., CRABTREE, G. W., KWOK, W. K. K., WELP, U., MALOZEMOFF, A. P., RUPICH, M., AND FLESHLER, S. C-axis critical current density of second-generation YBCO tapes. *Supercond. Sci. Technol.* *23* (2010), 115017.
  - [53] JOOSS, C., WARTHMAN, R., AND KRONMÜLLER, H. Pinning mechanism of vortices at antiphase boundaries in  $\text{YBa}_2\text{Cu}_3\text{O}_{7-\delta}$ . *Phys. Rev. B* *61* (2000), 12433–12446.
  - [54] KIM, D., BERGHUIS, P., FIELD, M. B., MILLER, D. J., GRAY, K. E., FEENSTRA, R., AND CHRISTEN, D. K. Evidence for pinning of grain-boundary vortices by Abrikosov vortices in the grains of  $\text{YBa}_2\text{Cu}_3\text{O}_{7-\delta}$ . *Phys. Rev. B* *62* (2000), 12505–12508.
  - [55] KIM, S. I., FELDMANN, D. M., VEREBELYI, D. T., THIEME, C., LI, X.,



- POLYANSKII, A. A., , AND LARBALESTIER, D. C. Influence of the grain boundary network on the critical current density of deformation-textured  $\text{YBa}_2\text{Cu}_3\text{O}_{7-\delta}$  coated conductors made by metal-organic deposition. *Phys. Rev. B* 71 (2005), 104501.
- [56] KWOK, W. K., WELP, U., VINOKUR, V. M., FLESHLER, S., DOWNEY, J., AND CRABTREE, G. W. Direct observation of intrinsic pinning by layered structure in single crystal  $\text{YBa}_2\text{Cu}_3\text{O}_7$ . *Phys. Rev. Lett.* 67 (1991), 390–393.
- [57] LAO, M., BERNARDI, J., BAUER, M., AND EISTERER, M. Critical current anisotropy of GdBCO tapes grown on ISD-MgO buffered substrate. *Supercond. Sci. Technol.* 28 (2015), 124002.
- [58] LAO, M., HECHER, J., SIEGER, M., PAHLKE, P., BAUER, M., HÜHNE, R., AND EISTERER, M. Planar current anisotropy and field dependence of  $J_c$  in coated conductors assessed by scanning Hall probe microscopy. *Supercond. Sci. Technol.* 30 (2017), 024004.
- [59] LARBALESTIER, D. Superconductors for the future – from the perspective of the past. ASC 2016 - Plenary Talk, September 2016.
- [60] LARBALESTIER, D., GUREVICH, A., FELDMANN, D. M., AND POLYANSKII, A. High-Tc superconducting materials for electric power applications. *Nature* 414 (2001), 368–377.
- [61] LLORDES, A., PALAU, A., GAZQUEZ, J., COLL, M., VLAD, R., POMAR, A., ARBIOL, J., GUZMAN, R., YE, S., RUOCO, V., SANDIUMENGE, F., RICART, S., PUIG, T., VARELA, M., CHATEIGNER, D., VANACKEN, J., GUTIERREZ, J., MOSCHALOV, V., DEUTSCHER, G., MAGEN, C., AND OBRADORS, X. Nanoscale strain-induced pair suppression as a vortex-pinning mechanism in high-temperature superconductors. *Nat. Mater.* 11 (2012), 329–336.
- [62] LONG, N. J. Model for the angular dependence of critical currents in technical superconductors. *Supercond. Sci. Technol.* 21 (2008), 025007.
- [63] LYKOV, N. A. Magnetic flux creep in HTSC and Anderson-Kim theory (Review Article). *Low. Temp. Phys.* 40, 9 (2014), 773–795.
- [64] MACMANUS-DRISCOLL, J. L., FOLTYN, S. R., JIA, Q. X., WANG, H., SERQUIS, A., CIVALE, L., MAIOROV, B., HAWLEY, M. E., MALEY, M. P., AND PETERSON, D. E. Strongly enhanced current densities in superconducting coated conductors of  $\text{YBa}_2\text{Cu}_3\text{O}_{7-\delta} + \text{BaZrO}_3$  (BZO). *Nat. Mater.* 3 (2004), 439–443.
- [65] MAIOROV, B., GIBBONS, B. J., V., S. K., G., M. T., HOLESINGER, AND CIVALE, L. Effect of the misalignment between the applied and internal magnetic fields on the critical currents of tilted coated conductors. *Appl. Phys. Lett.* 86, 13 (2005), 132504.

- [66] MATSUSHITA, T., KIUCHI, M., AND OTABE, E. S. Innovative superconducting force-free cable concept. *Supercond. Sci. Technol.* *25* (2012), 125009.
- [67] MATSUSHITA, T., NAGAMIZU, H., TANABE, K., KIUCHI, M., OTABE, E. S., TOBITA, H., YOSHIZUMI, M., IZUMI, T., SHIOHARA, Y., YOKOE, D., KATO, T., AND HIRAYAMA, T. Improvement of flux pinning performance at high magnetic fields in  $\text{GdBa}_2\text{Cu}_3\text{O}_y$  coated conductors with BHO nano-rods through enhancement of  $B_c2$ . *Supercond. Sci. Technol.* *25* (2012), 125003.
- [68] MISHEV, V., SEEBOECK, W., EISTERER, M., IIDA, K., KURTH, F., HÄNISCH, J., REICH, E., AND HOLZAPFEL, B. One-dimensional pinning behavior in co-doped  $\text{BaFe}_2\text{As}_2$  thin films. *Appl. Phys. Lett.* *103* (2013), 232601.
- [69] OPPERDEN, L., SIEGER, M., PAHLKE, P., HÜHNE, R., SCHULTZ, L., MELEDIN, A., TENDELOO, G. V., NAST, R., HOLZAPFEL, B., BIANCHETTI, M., MACMANUS-DRISCOLL, J. L., AND HÄNISCH, J. Large pinning forces and matching effects in  $\text{YBa}_2\text{Cu}_3\text{O}_{7-\delta}$  thin films with  $\text{Ba}_2\text{Y}(\text{Nb}/\text{Ta})\text{O}_6$  nanoprecipitates. *Sci. Rep.* *6* (2016), 21188.
- [70] PAHLKE, P., HERING, M., SIEGER, M., LAO, M., EISTERER, M., USOSKIN, A., STRÖMER, J., HOLZAPFEL, B., SCHULTZ, L., AND HÜHNE, R. Thick high  $J_c$  YBCO films on ABAD-YSZ templates. *IEEE Trans. Appl. Supercond.* *25* (2015), 6603804.
- [71] PAHLKE, P., SIEGER, M., CHEKHONIN, P., SKROTZKI, W., HÄNISCH, J., USOSKIN, A., STRÖMER, J., SCHULTZ, L., AND HÜHNE, R. Local orientation variations in YBCO films on technical substrates - a combined SEM and EBSD study. *IEEE Trans. Appl. Supercond.* *26* (2016), 7201505.
- [72] PALAU, A., PUIG, T., OBRADORS, X., AND JOOSS, C. Simultaneous determination of grain and grain-boundary critical currents in  $\text{YBa}_2\text{Cu}_3\text{O}_7$  coated conductors by magnetic measurements. *Phys. Rev. B* *75* (2007), 054517.
- [73] PARDO, E., DURRELL, J. H., AND BLAMIRE, M. G. Vortex deformation and breaking in superconductors in microscopic description. *Philosophical Magazine* *87* (2007), 4359–4381.
- [74] PINCUS, P., GOSSARD, A., JACCARINO, V., AND WERNICK, J. NMR measurements of the flux distribution in type ii superconductors. *Physics Letters* *13*, 1 (1964), 21–22.
- [75] POLYANSKII, A., EMERGO, R. L. S., WU, J. Z., AYTUG, T., CHRISTEN, D. K., PERKINS, G. K., AND LARBALESTIER, D. Magneto-optical imaging and electromagnetic study of  $\text{YBa}_2\text{Cu}_3\text{O}_7$  vicinal films of variable thickness. *Phys. Rev. B* *72* (2005), 174509.
- [76] PROZOROV, R., AND GIANNETTA, R. W. Magnetic penetration depth in unconventional superconductors. *Supercond. Sci. Technol.* *19* (2006), R41–R67.

- [77] PROZOROV, R., GIANNETTA, R. W., CARRINGTON, A., FOURNIER, P., GREENE, R. L., GUPTASARMA, P., HINKS, D. G., AND BANKS, A. R. Measurements of the absolute value of the penetration depth in high-Tc superconductors using a low-Tc superconductive coating. *Appl. Phys. Lett.* *77*, 25 (2000), 4202–4204.
- [78] PRUSSEIT, W., HOFFMANN, C., NEMETSCHKE, R., SIGL, G., HANDKE, J., AND KINDER, A. L. H. Reel to reel coated conductor fabrication by evaporation. *IEEE Trans. Appl. Supercond.* *16* (2006), 996–998.
- [79] PRUSSEIT, W., HOFFMANN, C., NEMETSCHKE, R., SIGL, G., HANDKE, J., LÜMKEMANN, A., AND KINDER, H. Long length coated conductor fabrication by inclined substrate deposition and evaporation. *Journal of Physics: Conference Series* *43*, 1 (2006), 215–218.
- [80] PRUSSEIT, W., SIGL, G., NEMETSCHKE, R., HOFFMANN, C., HANDKE, J., LÜMKEMANN, A., AND KINDER, H. Commercial coated conductor fabrication based on inclined substrate deposition. *IEEE Trans. Appl. Supercond.* *15* (2005), 2608–2610.
- [81] ROAS, B., SCHULTZ, L., AND SAEMANN-ISCHENKO, G. Anisotropy of the critical current density in epitaxial  $\text{YBa}_2\text{Cu}_3\text{O}_x$  films. *Phys. Rev. Lett.* *64*, 4 (1990), 479–482.
- [82] SCHÖPPL, R. *Grain boundaries in high-temperature superconductors*. PhD thesis, Technische Universität Wien, May 2009.
- [83] SCHUSTER, T., KUHN, H., BRANDT, E. H., INDENBOM, M. V., KLÄSER, M., MÜLLER-VOGT, G., HABERMEIER, H.-U., KRONMÜLLER, H., AND FORKL, A. Current and field pattern in rectangular and inhomogeneous superconductors. *Phys. Rev. B* *52* (1995), 10375.
- [84] SCHUSTER, T., KUHN, H., BRANDT, E. H., AND KLAUMÜNZER, S. Flux penetration into flat rectangular superconductors with anisotropic critical current. *Phys. Rev. B* *56* (1997), 3413.
- [85] SENATORE, C., BARTH, C., BONURA, M., KULICH, M., AND MONDONICO, G. Field and temperature scaling of the critical current density in commercial REBCO coated conductors. *Supercond. Sci. Technol.* *29* (2016), 014002.
- [86] SIEGER, M., HÄNISCH, J., PAHLKE, P., SPARING, M., GAITZSCH, U., IIDA, K., NAST, R., REICH, E., SCHULTZ, L., HOLZAPFEL, B., AND HÜHNE, R.  $\text{BaHfO}_3$ -doped thick  $\text{YBa}_2\text{Cu}_3\text{O}_{7-\delta}$  films on highly alloyed textured ni-w tapes. *IEEE Trans. Appl. Supercond.* *25* (2015), 6602604.
- [87] SIEGER, M., PAHLKE, P., LAO, M., EISTERER, M., MELEDIN, A., TENDELOO, G. V., OTTOLINGER, R., HÄNISCH, J., HOLZAPFEL, B., USOSKIN, A., KURSUMOVIC, A., MACMANUS-DRISCOLL, J. L., STAFFORD, B. H., BAUER, M., NIELSCH, K., SCHULTZ, L., AND HÜHNE, R. Tai-

- loring microstructure and superconducting properties in thick BaHfO<sub>3</sub> and Ba<sub>2</sub>Y(Nb/Ta)O<sub>6</sub> doped YBCO films on technical templates. *IEEE Trans. Appl. Supercond.* *27* (2016), 6601047.
- [88] SILHANEK, A. V., CIVALE, L., AND AVILA, M. A. Columnar defects acting as passive internal field detectors. *Phys. Rev. B* *65* (2002), 174525.
- [89] TACHIKI, M., AND TAKAHASHI, S. Effect of intrinsic pinning on critical current in cuprate superconductors. *Cryogenics* *32*, 11 (1992), 923–929.
- [90] TALLON, J. L., BERNHARD, C., BINNINGER, U., HOFER, A., WILLIAMS, G. V. M., ANSALDO, E. J., BUDNICK, J. I., AND NIEDERMAYER, C. In-plane anisotropy of the penetration depth due to superconductivity on the Cu-O chains in YBa<sub>2</sub>Cu<sub>3</sub>O<sub>7- $\delta$</sub> , Y<sub>2</sub>Ba<sub>4</sub>Cu<sub>7</sub>O<sub>15- $\delta$</sub> , and YBa<sub>2</sub>Cu<sub>4</sub>O<sub>8</sub>. *Phys. Rev. Lett.* *74* (1995), 1008–1011.
- [91] TARANTINI, C., IIDA, K., HÄNISCH, J., KURTH, F., JAROSZYNSKI, J., SUMIYA, N., CHIHARA, M., HATANO, T., IKUTA, H., SCHMIDT, S., SEIDEL, P., HOLZAPFEL, B., AND LARBALESTIER, D. C. Intrinsic and extrinsic pinning in NdFeAs(O,F): vortex trapping and lock-in by the layered structure. *Sci. Rep.* *6* (2016), 36047.
- [92] USOSKIN, A., KIRCHHOFF, L., KNOKE, J., PRAUSE, B., RUTT, A., SELSKIJ, V., AND FARRELL, D. E. Processing of long-length YBCO coated conductors based on stainless steel tapes. *IEEE Trans. Appl. Supercond.* *17* (2007), 3235–3238.
- [93] VEREBELYI, D. T., CHRISTEN, D. K., FEENSTRA, R., CANTONI, C., GOYAL, A., LEE, D. F., PARANTHAMAN, M., ARENDT, P. N., DEPAULA, R. F., GROVES, J. R., AND PROUTEAU, C. Low angle grain boundary transport in YBa<sub>2</sub>Cu<sub>3</sub>O<sub>7- $\delta$</sub>  coated conductors. *Appl. Phys. Lett.* *76*, 13 (2000), 1755–1757.
- [94] WEIGAND, M. Temperature dependence of pinning near  $H \parallel ab$  in YBCO thin films. ASC 2012, October 2012.
- [95] WEIGAND, M., RUTTER, N. A., SAHONTA, S. L., AND DURRELL, J. H. Critical current densities of MOCVD tapes for different current directions. *IEEE Trans. Appl. Supercond.* *21* (2011), 3347–3351.
- [96] ZEHETMAYER, M. Simulation of the current dynamics in superconductors: Application to magnetometry measurements. *Phys. Rev. B* *80* (2009), 104512.
- [97] ZHENG, D. N., CAMPBELL, A. M., JOHNSON, J. D., COOPER, J. R., BLUNT, F. J., PORCH, A., AND FREEMAN, P. A. Magnetic susceptibilities, critical fields, and critical currents of co- and zn-doped YBa<sub>2</sub>Cu<sub>3</sub>O<sub>7</sub>. *Phys. Rev. B* *49* (1994), 1417–1426.

# Curriculum Vitae

Full Name            Mayraluna Lao  
Date of birth        5 May 1987  
Citizenship         Filipino

## Educational background

Jun 2009 – Oct 2011        **MASTER OF SCIENCE IN PHYSICS**  
National Institute of Physics, College of Science,  
University of the Philippines, Diliman, Quezon City  
Thesis title: *“Inter- and intragranular response in the complex magnetic susceptibility of  $YBa_2Cu_3O_{7-\delta}$  superconductor under superimposed AC and DC magnetic field”*

Jun 2004 - Apr 2009        **BACHELOR OF SCIENCE IN PHYSICS**  
National Institute of Physics, College of Science,  
University of the Philippines, Diliman, Quezon City  
Thesis title: *“Low field AC Magnetic susceptibility of Pb-doped Bi-2223”*

1994 - 2004                 Primary and secondary education  
Colegio de Sta. Cecilia  
Valenzuela City, Philippines

## Awards

**Best Student Paper in Materials - 3rd Prize**, ASC 2016, Denver, Colorado, USA, September 2016.

**2015 European Society for Applied Superconductivity (ESAS) Young Researcher Prize in Materials**, EUCAS 2015, Lyon, France, September 2015.

**Cum Laude**, Bachelor of Science in Physics, University of the Philippines, Diliman, Quezon City, April 2009.

## Publications:

**M. Lao**, J. Hecher, M. Sieger, P. Pahlke, M. Bauer, R. Huehne and M. Eisterer, "Planar current anisotropy and field dependence of  $J_c$  in coated conductors assessed by scanning Hall probe microscopy", *Supercond. Sci. Technol.: Focus on Magnetic Properties of Superconductors: Modelling, Experiment and Theory*, **30** 024004, 2017.

**M. Lao**, M. Bauer, J. Bernardi and M. Eisterer, "Critical current anisotropy of GdBCO tapes grown on ISD-MgO buffered substrate", *Supercond. Sci. Technol.: Focus issue on current developments in HTSC coated conductors for applications*, **28**, 124002, 2015.

**M. Lao**, M. Eisterer, O. Stadel, A. Meledin and G. van Tendeloo, "The effect of  $Y_2O_3$  and  $YFeO_3$  additions on the critical current density of YBCO coated conductors", *J. Phys.: Conf. Ser.* 507, 022012, 2014.

M. Sieger, P. Pahlke, **M. Lao**, M. Eisterer, A. Meledin, G. van Tendeloo, R. Ottolinger, J. Hänisch, B. Holzapfel, A. Usoskin, A. Kursumovic, J. MacManus-Driscoll, B. Stafford, M. Bauer, K. Nielsch, L. Schultz and R. Hühne, "Tailoring microstructure and superconducting properties of thick  $BaHfO_3$  and  $Ba_2Y(Nb/Ta)O_6$  doped YBCO films on technical templates", (invited paper), *IEEE Trans. Appl. Supercond.*, **27**, 6601407, 2017.

M. Sieger, P. Pahlke, R. Ottolinger, B. H. Stafford, **M. Lao**, A. Meledin, M. Bauer, M. Eisterer, G. Van Tendeloo, L. Schultz, K. Nielsch, R. Huehne, "Influence of substrate tilt angle on the incorporation of  $BaHfO_3$  in thick  $YBa_2Cu_3O_{7-\delta}$  films", *IEEE Trans. Appl. Supercond.*, **27**, 7500504, 2017.

P. Pahlke, **M. Lao**, M. Eisterer, A. Meledin, G. Van Tendeloo, M. Sieger, J. Hänisch, P. Sun, A. Usoskin, J. Strömer, B. Holzapfel, L. Schultz, R. Hühne, "Reduced  $J_c$ -anisotropy and enhanced in-field performance in thick  $BaHfO_3$  doped  $YBa_2Cu_3O_{7-\delta}$  films on ABAD-YSZ templates", *IEEE Trans. Appl. Supercond.*, **26**, 6603104, 2016.

M. Sieger, P. Pahlke, J. Hänisch, L. Opherden, P. Bergelt, K. Iida, M. Sparing, M. Bianchetti, J. MacManus-Driscoll, **M. Lao**, M. Eisterer, A. Meledin, G. Van Tendeloo, R. Nast, L. Schultz, B. Holzapfel, R. Hühne, " $Ba_2Y(Nb/Ta)O_6$ -Doped YBCO Films on Biaxially Textured Ni-5at.%W Substrates", *IEEE Trans. Appl. Supercond.*, **26**, 7500305, 2016.

P. Pahlke, M. Hering, M. Sieger, **M. Lao**, M. Eisterer, A. Usoskin, J. Stroemer, B. Holzapfel, L. Schultz and R. Huehne, "Thick High  $J_c$  YBCO Films on ABAD-YSZ Templates", *IEEE Trans. Appl. Supercond.*, vol 25, no. 3, 2015.